UNIVERSITY OF CALIFORNIA, SAN DIEGO

# The influence of microorganisms on the atmosphere and tools for the study of transacylase domains

A dissertation submitted in partial satisfaction
of the requirements for the degree of
Doctor of Philosophy

in

Chemistry

by

Jennifer Michelle Michaud

Committee in charge:

Professor Michael D. Burkart, Chair
Professor Christopher L. Dupont
Professor James W. Golden
Professor Vicki H. Grassian
Professor Thomas C. Hermann
Professor Navtej Toor

2017

This dissertation of Jennifer Michelle Michaud is approved, and it is acceptable in quality and form for publication on microfilm and electronically:

Chair

University of California, San Diego

2017

DEDICATION

To my father who taught me to always aspire to be better

EPIGRAPH

"Never, never, never give up."

Winston Churchill

"It ain't about how hard you hit. It's about how hard you can get hit and keep moving forward. How much you can take and keep moving forward. That's how winning is done!"

Rocky

TABLE OF CONTENTS

LIST OF ABBREVIATIONS

Sea spray aerosol ..... SSA
Sea surface microlayer ..... SSML
Ice nucleation ..... IN
Marine aerosol reference tank ..... MART
Minature marine aerosol reference tank ..... miniMART
Scanning molbility particle sizer ..... SMPS
Aerodynamic particle sizer ..... APS
Chemical ionization time-of-flight mass spectrometry ..... CI-ToFMS
Aerosol time-of-flight mass spectrometry ..... ATOFMS
High-resolution mass spectrometry ..... HRMS
Scanning transmission electron microscopy ..... STEM
Cyrogenic electron microscopy ..... cryo-TEM
Graphene oxide ..... GOx
Energy dispersive spectrometer ..... EDS
High angle annular dark field ..... HADDF
Filtered autoclaved seawater ..... FASW
Aerosolization factor ..... AF
High-resolution rapid refresh atmospheric model ..... HRRR
Flexible particle dispersion model ..... FLEXPART
Primary biological aerosol particles ..... PBAP
Fatty acid synthase ..... FAS
Polyketide synthase ..... PKS
Non-ribosomal synthetase ..... NRPS
Acyl-carrier protein ..... ACP
Acyltraferase ..... AT
*Escherichia coli* fatty acid synthase acyl carrier protein ..... AcpP
4' Phosphopantetheinyl transferase ..... PPTase
Coenzyme A ..... CoA
*E. coli* pantothenate kinase ..... CoaA
*E. coli* phosphopantetheine adenylyl transferase ..... CoaD
*E. coli* dephosphocoenzyme A kinase ..... CoaE

LIST OF FIGURES

LIST OF SCHEMES

LIST OF TABLES

ACKNOWLEDGEMENTS

I would like to acknowledge Professor Michael D. Burkart for his support and mentorship throughout graduate school. His encouragement and guidance has been invaluable.

Additionally, I would like to acknowledge the mentorship of Christopher L. Dupont and Kimberly A. Prather who opened new areas of science and research to me that have shaped my scientific interests and future career goals. I would also like to extend my gratitude to my committee members.

I would also like to acknowledge Jim La Clair, Andrew Allen, Ariel Rabines, Kristen Jepsen, Daniel Yee, Raffaela Abbriano Burke, Mark Hildebrand, Karen Selph, Tom Hill, Yongxuan Su, Anthony Mrse, Xuemei Huang, Yi Tang, Michael Thomas, CAICE members, and Scripps Institution of Oceanography Hydraulics Laboratory staff, all other collaborators for their valuable contributions

Finally, I acknowledge the past and present members of the Burkart Laboratory and everyone has supported me personally and scientifically. The Burkart Laboratory is a supportive and fun group to be a part of.

Chapter 1 is material prepared for this dissertation. J.M. Michaud. "Introduction to the influence of microorganisms on the atmosphere and tools for the study of transacylase domains". The dissertation author is the primary author of this chapter supported by M. D. Burkart.

Chapter 2, in full, is a reprint of material as it appears: M. J. Kim, J. M. Michaud, R. Williams, B. P. Sherwood, R. Pomeroy, F. Azam, M. D. Burkart, and T.

H. Bertram. "Bacteria-driven production of alkyl nitrates in seawater." *Geophys. Res. Lett.* **42**, 597–604 (2015). The dissertation author is a contributing author of this manuscript. The dissertation author assisted in experimental design, cultured bacteria, prepared and sampled experiments, and performed growth measurements.

Chapter 3, is material currently being prepared for submission: J.M. Michaud, O. S. Ryder, J. S. Sauer, C. Lee, M. D. Burkart, K. A. Prather. "Enzymatic processing by lipase in seawater determines sea spray aerosol composition". The dissertation author, O. S. Ryder, J. S. Sauer, and C. Lee are co-primary authors of the work under the supervision of M. D. Burkart and K. A. Prather. The dissertation author devised original concept of experiments, performed bulk sampling and system maintenance, conducted enzymatic assays, and prepared diatom lysate. The dissertation author wrote the chapter with contributions from co-primary authors.

Chapter 4, in full, is a reprint of material as it appears: J. P. Patterson, D. B. Collins, J. M. Michaud, J. L. Axson, C. M. Sultana, T. Moser, A. C. Dommer, J. Conner, V. H. Grassian, M. D. Stokes, G. B. Deane, J. E. Evans, M. D. Burkart, K. A. Prather, N. C. Gianneschi. "Sea spray aerosol structure and composition using cryogenic transmission electron microscopy." *ACS Cent. Sci.* **2**(1*)*, 40–47 (2016). The dissertation author is a contributing author of this manuscript. The dissertation author contributed experimental design, set-up, and bacterial culturing to the work outlined in this chapter.

Chapter 5 is material that has been submitted for publication: J. M. Michaud, L. R. Thompson, D. Kaul, J. L. Espinoza, R. A. Richter, Z. Z. Xu, C. Lee, K. M. Pham, C. M. Beall, F. Malfatti, F. Azam, R. Knight, M. D. Burkart, C. L. Dupont, K. A. Prather. "Selective transfer of bacteria and viruses from the ocean to the atmosphere". The dissertation author is the primary author of the work under the supervision of M. D. Burkart, C. L. Dupont, and K. A. Prather. The dissertation author devised experiment and strategy for analyses and performed aerosol and bulk sampling with assistance from co-authors. Additionally, she extracted, purified, prepared DNA samples for sequencing, performed aerosolization calculations and analysis, and prepared manuscript and chapter.

Chapter 6, is material currently being prepared for submission: C. M. Beall, J.M. Michaud, M. Fish, M. D. Stokes, M. D. Burkart, K. A. Prather. "Cultivable halotolerant bacteria and fungi from precipitation and sea spray aerosols indicate a possible missing marine source of atmospheric ice nucleating particles". The dissertation author and C. M. Beall and co-primary authors of this work under the supervision of M. D. Burkart and K. A. Prather. The dissertation author devised isolation and testing strategy, performed isolation of bacterial and fungal species with assistance of C. M. Beall, extracted DNA from isolates, performed species identification and phylogenetic analyses, and prepared manuscript and chapter with assistance from C. M. Beall.

Chapter 7, is material currently being prepared for submission: T. D. Davis, J. M. Michaud, M. D. Burkart. "Fluorescent probes to profile fatty acid and

polyketide acyl-carrier protein transacylase domains". T. D. Davis is the primary author of the work reported, supported by the dissertation author and under the supervision of M. D. Burkart. The dissertation author performed site-directed mutagenesis and cloning of *E. coli* strains, performed docking analyses, expressed and isolated protein samples with assistance from T. D. Davis, and assisted with manuscript and chapter preparation.

## VITA

| | |
|---|---|
| 1998 - 2001 | Research Assistant, Boston University, Boston, MA. |
| 2000 | Bachelor of the Arts, Biochemistry and Molecular Biology, Boston University. Boston, MA. |
| 2000 - 2007 | Laboratory Supervisor, Biology Teaching Laboratories. Boston University, Boston, MA |
| 2008 | Research Associate II, GreenFuel Technologies, Cambridge, MA |
| 2009 - 2011 | Lead Biologist, Element Cleantech/ APS, Newark, DE/ Phoenix, AZ |
| 2011 - 2013 | Teaching Assistant, Department of Chemistry & Biochemistry, University of California, San Diego |
| 2013 | Master of Science, University of California, San Diego |
| 2017 | Doctor of Philosophy in Chemistry, University of California, San Diego |

## PUBLICATIONS

**Michaud, J.M.,** Thompson, L.R., Kaul, D*, Espinoza, J.L.*, Richter, R. A., Xu, Z.Z., Lee, C., Pham, K.M., Beall, C.M., Malfatti, F., Azam, F., Knight, R., Prather, K.A., Dupont, C.L., Burkart, M.D. Taxon-specific aerosolization of bacteria and viruses in sea spray. *Submitted*.

McCluskey, C.S., Hill, T.C.J., Sultana, C.M., Laskina, O., Trueblood, J., Santander, M. V., Beall, C.M., **Michaud, J.M.,** Prather, K.A., Grassian, V., Demott, P.J. A mesocosm double feature: Insights into the chemical make-up of marine ice nucleating particles. *In review. J. Atmos. Sci.*

Patterson, J.P., Collins, D.B., **Michaud, J.M.,** Axson, J.L., Burkart, M.D., Prather, K.A., & Gianneschi, N.C. Sea Spray Aerosol Structure and Composition Using Cryogenic Transmission Electron Microscopy. ACS Cent. Sci. **2**(1), 40-47 (2016).

Kim, M.J., **Michaud, J.M**., Williams, R., Sherwood, B. P., Pomeroy, R., Azam, F., Burkart, M. D., & Bertram, T.H. Bacterial-driven production of nitrates in seawater. Geophys. Res. Lett. **42,** 1-8 (2015).

Blatti, J.L., **Michaud, J.M.,** & Burkart, M.D. Engineering fatty acid biosynthesis in microalgae for sustainable biodiesel. Curr. Opin. Chem. Biol. **17**, 496 -505 (2013).

ABSTRACT OF THE DISSERTATION

The influence of microorganisms on the atmosphere and tools for the study of transacylase domains

by

Jennifer Michelle Michaud

Doctor of Philosophy in Chemistry

University of California, San Diego, 2017

Professor Michael D. Burkart, Chair

Specific biochemical influences on sea spray aerosol (SSA) are not well characterized and are vital to understanding the complex and variable chemical composition and atmospheric properties of SSA. Several studies reported in this thesis explore how microorganisms affect SSA both by examining their metabolic products in seawater and how they transfer from the seawater to aerosol, as well as the impacts of airborne microbes on SSA properties.

To investigate the influence of microbial metabolism on aerosol composition, direct measurements of aerosols revealed a correlation between marine bacteria in seawater and the production of gas-phase even-chain (C:2, C:4) alkyl nitrates ($RONO_2$). Alkyl nitrates are a large contributor to the production of tropospheric ozone and prior to these studies generally thought to originate from anthropogenic sources and produced through *uv*-dependent mechanisms. The results show that bacterial metabolism can contribute to the production of climate warming ozone and demonstrate an important biochemical influence on atmospheric processes. In separate studies, we explored the role of enzymatic processing of lipid metabolites by lipase in seawater and the resulting changes to aerosol morphology and composition. We observed that lipase driven digestion of lipids in seawater vastly changes the composition of SSA in simple triacylglycerol and diatom lysate systems, identifying a possible mechanism for organismal control of aerosolization.

The structural organization within SSA, taxon-specificity of air-sea transfer, and ice nucleation (IN) characteristics of whole bacteria, viruses, and vesicles was explored in several studies. One study elucidated the detailed composition of seawater (bulk), SSML, and SSA using cryogenic transmission electron microscopy. The unique technique allowed the preservation and detailed examination of soft biological particles, facilitating observations of complex structures of diatoms, bacteria, viruses, and vesicles, their hydration state, and their orientation within particles. SSML derived vesicles had a more multi-lamellar

structure in contrast to bulk and aerosol samples. This was the first demonstration of vesicles within SSA, indicating a possible role of these structures in climate processes. Another study examined bacterial and viral transfer across the air-sea interface using metagenomics, revealing marine bacteria aerosolize more efficiently than viruses and taxon-specific properties governing selective transfer of viruses and bacteria delineated by class and order. Several species of bacteria and viruses were consistently enriched in aerosols, and hydrophobic cell- and virus- surfaces positively influenced aerosolization. The results provide a genomic framework to elucidate aerosolization mechanisms and like the lipase studies, identify additional microbial controls of SSA composition and properties. Lastly, we examined the IN properties of halotolerant bacteria and fungi isolated from rain and SSA samples collected from Scripps Pier in La Jolla, CA. Most rain isolates possess moderate IN activity, and reveal that a possible unidentified source of marine IN activity contributing to precipitation. The studies together have yielded important information of how microbial biochemistry and aerosolization influences SSA composition and properties. This work will serve as a foundation to examine the biochemical mechanisms of SSA composition, SSA properties, climate relevant biomarkers, and aerosolization mechanisms that will inform climate models, civil engineering, and public health.

Acyltransferase (AT) domains are serine hydrolases and vital enzymes in the biosynthesis of fatty acids, polyketides and hybrid polyketide nonribosomal peptides. Experiments utilizing broad activity-based serine hydrolase probes to

label cells surface proteases and lipases of marine microbial membranes, provoked development of specific probes for the study of AT domains. To date, inhibitors and probes specific to AT domains have not been reported in literature. AT specific probes have proven challenging to develop due to their characteristically small and restrictive active sites. This dissertation details the design, synthesis, and testing of five activity-based AT probes. Comparisons of these five probes by binding efficacy, specificity, optimization, and competition in FAS and PKS systems provides a basis for future development of crosslinking probes to examine carrier protein-AT interactions and AT inhibitors. These small molecules will permit the study of specific AT-carrier protein interactions in a variety of systems and will provide possible novel therapeutics against drug-resistant bacteria.

# Chapter 1. Introduction to the influence of microorganisms on the atmosphere and tools for the study of transacylase domains

## Section 1.1 Main text

Aerosols are suspended particles in the air, and in the atmosphere, are vital to climate and air quality. Aerosols influence climate directly by scattering sunlight or indirectly by providing surfaces for water and ice deposition central to cloud formation and precipitation [1–3]. Aerosol particles of different composition have vastly different atmospheric properties[2,4,5]. As the ocean covers the majority of the planet, sea spray aerosol (SSA) represents a dominant pool of climate-influencing aerosols[6–8], but the details of SSA composition, reactivity, and effect on atmospheric processes are not well understood[9].

SSA is formed and released from seawater and the sea surface microlayer (SSML) through the process of wave breaking[10], and the composition of nascent SSA is determined by the composition of its source seawater and molecules enriched in the SSML[11–14]. The ocean represents diverse ecologies that have changing composition controlled by the microbial loop and biochemical processes[15–18]. Organic molecules, cells, and detritus from microorganisms may combine with salts, and are released as bioaerosols[19,20]. Connecting the biochemistry and aerosolization of bioaerosols is an important aspect of understanding how the chemistry of SSA changes and how these alterations impact atmospheric properties.

Marine microorganisms can affect SSA in two ways. First, their metabolic products and enzymes can alter the composition of the seawater and SSML that form aerosols[15–18], and second, they can be released intact to act as surfaces themselves for atmospheric processes and chemistry[21–24]. However, the connection of microbial processing and biogeochemical cycles is not well understood[25,26]. Insight into the variation and specific composition of seawater and how it is affected by specific organisms and enzymatic processing in differing marine ecologies is needed to understand SSA composition and will inform climate models. Characterizing the airborne microbial community, its variation, and the taxonomic specificity of microbial transfer from the sea to the atmosphere is also necessary to determine the role of bioaerosols on cloud condensation and ice nucleation.

Fatty acid, polyketide, and non-ribosomal peptide biosynthetic pathways are responsible for producing fatty acids and a variety of valuable natural products[27]. They are multimodular synthases that tether growing intermediates to carrier proteins to facilitate productive interactions with various partner domains and create diverse molecules[28,29]. Processivity is achieved by the transient nature of these protein-protein interactions. As type II fatty acid synthases (FAS) are unique to prokaryotes and vital for fatty acid production, type II FAS domains are a target for novel antibiotics[30,31], and a variety of polyketide synthase (PKS) and non-ribosomal peptide synthetases produce natural products with antibiotic, antitumor, and antiviral activities[32–35]. Domains in these systems utilize highly

specific interactions with the carrier protein and attached substrate, limiting the creation of off target products[28,29]. These interactions are just beginning to be understood[36–39] and are key to understanding these systems, designing better inhibitors, and engineering these systems to create custom products with potentially new or modulated activities.

Transacylase, or acyltransferase (AT) domains are in the serine hydrolase family of enzymes and initiate and propagate PKS and FAS pathways. ATs transfer acyl and other groups from acyl-CoA to *holo*-acyl carrier proteins (*holo*-ACPs) via a transacylation reaction[40,41]. Malonyl-CoA AT (MCAT) domains are responsible for providing malonyl-CoA extender units to growing fatty acids or polyketides[42]. The FAS AT domain from *Esherichia coli*, FabD, like many other FAS enzymes is essential for survival making AT domains a prime target for therapeutic inhibition and ACP-AT protein-protein interaction studies. To date, few inhibitors and probes for AT domains and probes have been identified and substrate specificity has not been attained. Potent inhibitors with high AT specificity would facilitate development of crosslinkers that permit the study of specific ACP-AT interactions in a variety of FAS and PKS systems via trapping of these transient states. They also will provide potential novel therapeutics against the growing multi-drug resistance threat.

**Acknowledgements.**

Chapter 1 is material prepared for this dissertation. J.M. Michaud. "Introduction to the influence of microorganisms on the atmosphere and tools for the study of transacylase domains". The dissertation author is the sole author of this chapter.

**Section 1.2 References**

1. Boucher, O. Atmospheric Aerosols. in *Atmospheric Aerosols* 9–24 (Springer Netherlands, 2015). doi:10.1021/bk-2009-1005

2. Pöschl, U. Atmospheric aerosols: Composition, transformation, climate and health effects. *Angew. Chemie - Int. Ed.* **44,** 7520–7540 (2005).

3. Andreae, M. O. Atmospheric Aerosols: Biogeochemical Sources and Role in Atmospheric Chemistry. *Science.* **276,** 1052–1058 (1997).

4. Saxena, P., Hildemann, L. M., McMurray, P. H. & Seinfeld, J. H. Organics alter hygroscopic behavior of atmospheric particles. *J. Geophys. Res.* **100,** 18,755-18,770 (1995).

5. Nguyen, Q. T., Kjær, K. H., Kling, K. I., Boesen, T. & Bilde, M. Impact of fatty acid coating on the CCN activity of sea salt particles. *Tellus, Ser. B Chem. Phys. Meteorol.* **69,** 1–15 (2017).

6. de Leeuw, G., Andreas, E. L., Anguelova, M. D., Fairall, C. W., Ernie, R., Dowd, C. O., Schulz, M. & Schwartz, S. E. Production Flux of Sea-Spray Aerosol. **80,** 1–39 (2011).

7. Liu, X., Penner, J. E., Das, B., Bergmann, D., Rodriguez, J. M., Strahan, S., Wang, M. & Feng, Y. Uncertainties in global aerosol simulations: Assessment using three meteorological data sets. *J. Geophys. Res. Atmos.* **112,** 1–41 (2007).

8. Struthers, H., Ekman, A. M. L., Glantz, P., Iversen, T., Kirkevåg, A., Seland, O., Mårtensson, E. M., Noone, K. & Nilsson, E. D. Climate-induced changes in sea salt aerosol number emissions: 1870 to 2100. *J. Geophys. Res. Atmos.* **118,** 670–682 (2013).

9. Cochran, R. E., Ryder, O. S., Grassian, V. H. & Prather, K. A. Sea Spray Aerosol: The Chemical Link between the Oceans, Atmosphere, and Climate. (2017). doi:10.1021/acs.accounts.6b00603

10. Leck, C. & Bigg, E. K. Source and evolution of the marine aerosol—A new perspective. *Geophys. Res. Lett.* **32,** L19803, doi:10.1029/2005GL023651 (2005).

11. Cunliffe, M., Engel, A., Frka, S., Gašparović, B., Guitart, C., Murrell, J. C., Salter, M., Stolle, C., Upstill-Goddard, R. & Wurl, O. Sea surface microlayers: A unified physicochemical and biological perspective of the air-ocean interface. *Prog. Oceanogr.* **109,** 104–116 (2013).

12. Wurl, O., Miller, L., Rüttgers, R. & Vagle, S. The distribution and fate of surface-active substances in the sea-surface microlayer and water column. *Mar. Chem.* **115,** 1–9 (2009).

13. Leck, C. & Bigg, E. K. Biogenic particles in the surface microlayer and overlaying atmosphere in the central Arctic Ocean during summer. *Tellus, Ser. B Chem. Phys. Meteorol.* **57,** 305–316 (2005).

14. Sieburth, J., Willis, P.-J., Johnson, K. M., Burney, C. M., Lavoie, D. M., Hinga, K. R., Caron, D. A., French, F. W., Johnson, P. W. & Davis, P. G. Dissolved Organic Matter and Heterotrophic Microneuston in the Surface Microlayers of the North Atlantic. *Science.* **194,** 1415–1418 (1976).

15. Azam, F., Fenchel, T., Field, J. G., Gray, J. S., Meyer-Reil, L. A. & Thingstad, F. The Ecological Role of Water-Column Microbes in the Sea. *Mar. Ecol. Prog. Ser.* **10,** 257–263 (1983).

16. Pomeroy, L. R., Williams, P. J., Azam, F. & Hobbie, J. E. The Microbial Loop. *Oceanography* **20,** 28–33 (2007).

17. Fenchel, T. The microbial loop - 25 years later. *J. Exp. Mar. Bio. Ecol.* **366,** 99–103 (2008).

18. Arnosti, C. Microbial extracellular enzymes and the marine carbon cycle. *Ann. Rev. Mar. Sci.* **3,** 401–425 (2011).

19. Fröhlich-nowoisky, J., Kampf, C. J., Weber, B., Huffman, J. A., Pöhlker, C., Andreae, M. O., Lang-yona, N., Burrows, S. M., Gunthe, S. S., Elbert, W., Su, H., Hoor, P., Thines, E., Hoffmann, T., Després, V. R. & Pöschl, U. Bioaerosols in the Earth system : Climate , health , and ecosystem interactions. *Atmos. Res.*

**182,** 346–376 (2016).

20. Després, V. R., Alex Huffman, J., Burrows, S. M., Hoose, C., Safatov, A. S., Buryak, G., Fröhlich-Nowoisky, J., Elbert, W., Andreae, M. O., Pöschl, U. & Jaenicke, R. Primary biological aerosol particles in the atmosphere: A review. *Tellus B* **64,** (2012).

21. Creamean, J. M., Suski, K. J., Rosenfeld, D., Cazorla, A., Demott, P. J., Sullivan, R. C., White, A. B., Ralph, F., Minnis, P., Comstock, J. M., Tomlinson, J. M. & Prather, K. A. Dust and Biological Aerosols. *Science* **339,** 1572–1578 (2013).

22. Fröhlich-Nowoisky, J., Kampf, C. J., Weber, B., Huffman, J. A., Pöhlker, C., Andreae, M. O., Lang-Yona, N., Burrows, S. M., Gunthe, S. S., Elbert, W., Su, H., Hoor, P., Thines, E., Hoffmann, T., Després, V. R. & P?öschl, U. Bioaerosols in the Earth system: Climate, health, and ecosystem interactions. *Atmos. Res.* **182,** 346–376 (2016).

23. Bauer, H., Giebl, H., Hitzenberger, R., Kasper-Giebl, A., Reischl, G., Zibuska, F. & Puxbaum, H. Airborne bacteria as cloud condensation nuclei. *J. Geophys. Res.* **108,** 1–5 (2003).

24. Morris, C. E., Conen, F., Alex Huffman, J., Phillips, V., Pöschl, U. & Sands, D. C. Bioprecipitation: A feedback cycle linking Earth history, ecosystem dynamics and land use through biological ice nucleators in the atmosphere. *Glob. Chang. Biol.* **20,** 341–351 (2014).

25. Azam, F. & Malfatti, F. Microbial structuring of marine ecosystems. *Nat. Rev. Microbiol.* **5,** 782–791 (2007).

26. Arndt, S., Jørgensen, B. B., LaRowe, D. E., Middelburg, J. J., Pancost, R. D. & Regnier, P. Quantifying the degradation of organic matter in marine sediments: A review and synthesis. *Earth-Science Rev.* **123,** 53–86 (2013).

27. Newman, D. J. & Cragg, G. M. Natural Products as Sources of New Drugs from 1981 to 2014. *J Nat Prod* **79,** 629–661 (2016).

28. Meier, J. L. & Burkart, M. D. The chemical biology of modular biosynthetic enzymes. *Chem. Soc. Rev.* **38,** 2012–45 (2009).

29. Beld, J., Lee, D. J. & Burkart, M. D. Fatty acid biosynthesis revisited: structure elucidation and metabolic engineering. *Mol. BioSyst.* **11,** 38–59 (2015).

30. Wright, H. T. & Reynolds, K. A. Antibacterial targets in fatty acid biosynthesis. *Curr. Opin. Microbiol.* **10,** 447–453 (2007).

31. Waller, R. F., Ralph, S. a, Reed, M. B., Su, V., Douglas, J. D., Minnikin, D. E., Cowman, A. F., Besra, G. S. & McFadden, G. I. A Type II Pathway for Fatty Acid Biosynthesis Presents Drug Targets in Plasmodium falciparum A Type II Pathway for Fatty Acid Biosynthesis Presents Drug Targets in Plasmodium falciparum. *Antimicrob Agents Chemother* **47,** 297–301 (2003).

32. Aggarwal, A., Parai, M. K., Shetty, N., Wallis, D., Woolhiser, L., Hastings, C., Dutta, N. K., Galaviz, S., Dhakal, R. C., Shrestha, R., Wakabayashi, S., Walpole, C., Matthews, D., Floyd, D., Scullion, P., Riley, J., Epemolu, O., Norval, S., Snavely, T., Robertson, G. T., Rubin, E. J., Ioerger, T. R., Sirgel, F. A., van der Merwe, R., van Helden, P. D., Keller, P., Bottger, E. C., Karakousis, P. C., Lenaerts, A. J. & Sacchettini, J. C. Development of a Novel Lead that Targets M. tuberculosis Polyketide Synthase 13. *Cell* **170,** 249–259 e25 (2017).

33. Hughes, D. Microbial genetics: Exploiting genomics, genetics and chemistry to combat antibiotic resistance. *Nat. Rev. Genet.* **4,** 432–441 (2003).

34. Shen, B., Du, L., Sanchez, C., Edwards, D. J., Chen, M. & Murrell, J. M. The biosynthetic gene cluster for the anticancer drug bleomycin from Streptomyces verticillus ATCC15003 as a model for hybrid peptide-polyketide natural product biosynthesis. *J. Ind. Microbiol. Biotechnol.* **27,** 378–385 (2001).

35. Ma, G., Zancanella, M., Oyola, Y., Richardson, R. D., Smith, J. W. & Romo, D. Total synthesis and comparative analysis of orlistat, valilactone, and a transposed orlistat derivative: Inhibitors of fatty acid synthase. *Org. Lett.* **8,** 4497–4500 (2006).

36. Nguyen, C., Haushalter, R. W., Lee, D. J., Markwick, P. R., Bruegger, J., Caldara-Festin, G., Finzel, K., Jackson, D. R., Ishikawa, F., O'Dowd, B., McCammon, J. A., Opella, S. J., Tsai, S. C. & Burkart, M. D. Trapping the dynamic acyl carrier protein in fatty acid biosynthesis. *Nature* **505,** 427–431 (2014).

37. Tang, Y., Chen, A. Y., Kim, C.-Y., Cane, D. E. & Khosla, C. Structural and mechanistic analysis of protein interactions in module 3 of the 6-deoxyerythronolide B synthase. *Chem. Biol.* **14,** 931–43 (2007).

38. Barajas, J. F., Finzel, K., Valentic, T. R., Shakya, G., Gamarra, N., Martinez, D., Meier, J. L., Vagstad, A. L., Newman, A. G., Townsend, C. A., Burkart, M. D. & Tsai, S. C. Structural and Biochemical Analysis of Protein-Protein Interactions Between the Acyl-Carrier Protein and Product Template Domain. *Angew Chem Int Ed Engl* **55,** 13005–13009 (2016).

39. Finzel, K., Lee, D. J. & Burkart, M. D. Using modern tools to probe the structure-function relationship of fatty acid synthases. *Chembiochem* **16,** 528–547 (2015).

40. Wong, F. T., Chen, A. Y., Cane, D. E. & Khosla, C. Protein-protein recognition between acyltransferases and acyl carrier proteins in multimodular polyketide synthases. *Biochemistry* **49,** 95–102 (2010).

41. Oefner, C., Schulz, H., D'Arcy, A. & Dale, G. E. Mapping the active site of Escherichia coli malonyl-CoA-acyl carrier protein transacylase (FabD) by protein crystallography. *Acta Crystallogr. D. Biol. Crystallogr.* **62,** 613–8 (2006).

42. Chan, Y. A. & Thomas, M. G. *Chapter 7 Formation and Characterization of Acyl Carrier Protein-Linked Polyketide Synthase Extender Units*. *Methods in Enzymology* **459,** (Elsevier Inc., 2009).

# Chapter 2. Bacteria-driven production of alkyl nitrates in seawater

AGU PUBLICATIONS

Geophysical Research Letters

RESEARCH LETTER
10.1002/2014GL062865

**Key Points:**
- Trace gas emissions from a controlled mesocosm experiment
- Estimates of biotic oceanic alkyl nitrate production rates
- Bacteria-driven production of short chain alkyl nitrates

**Supporting Information:**
- Text S1, Table S1, and Figures S1–S8

**Correspondence to:**
T. H. Bertram,
thbertram@ucsd.edu

**Citation:**
Kim, M. J., J. M. Michaud, R. Williams, B. P. Sherwood, R. Pomeroy, F. Azam, M. Burkart, and T. H. Bertram (2015), Bacteria-driven production of alkyl nitrates in seawater, *Geophys. Res. Lett.*, *42*, doi:10.1002/2014GL062865.

Received 15 DEC 2014
Accepted 29 DEC 2014
Accepted article online 6 JAN 2015

## Bacteria-driven production of alkyl nitrates in seawater

**Michelle J. Kim[1], Jennifer M. Michaud[2], Renee Williams[2], Byron Pedler Sherwood[1,3], Robert Pomeroy[2], Farooq Azam[1], Michael Burkart[2], and Timothy H. Bertram[2]**

[1]Scripps Institution of Oceanography, University of California, San Diego, La Jolla, California, USA, [2]Department of Chemistry and Biochemistry, University of California, San Diego, La Jolla, California, USA, [3]Now at Center for Microbial Oceanography: Research and Education, School of Ocean and Earth Science and Technology, Department of Oceanography, University of Hawai'i at Mānoa, Honolulu, Hawaii, USA

**Abstract** Aircraft- and ship-borne measurements have shown that the ocean is a large, diffuse source for short chain ($C_1$–$C_3$) gas phase alkyl nitrates ($RONO_2$). Photochemical production of $RONO_2$ has been demonstrated previously as a viable mechanism in surface waters; however, it cannot account for the observed depth profile of $RONO_2$, suggesting an additional, dark $RONO_2$ production mechanism. We present measurements of gas phase $C_1$–$C_5$ alkyl nitrates emitted from seawater in a controlled mesocosm experiment conducted under low-light conditions in a glass-walled wave channel. Ethyl and butyl nitrate emission rates from seawater are strongly correlated with the abundance of heterotrophic bacteria ($R^2 \geq 0.89$) and show no correlation to chlorophyll *a* concentration. Controlled flask experiments conducted using ambient and sterile seawater, inoculated with a heterotrophic bacterium, confirm that bacterial driven production of select $RONO_2$ can proceed efficiently in the absence of light.

### 1. Introduction

The production rate of tropospheric ozone ($O_3$), a potent greenhouse gas and radical precursor, is critically dependent on the abundance of nitrogen oxides ($NO_x \equiv NO + NO_2$). In remote regions, the photolysis, chemical processing, and thermal decomposition of reactive nitrogen ($NO_y \equiv NO_x$ + alkyl nitrates ($RONO_2$) + peroxynitrates ($RO_2NO_2$) + nitric acid ($HNO_3$) + others) act to control $NO_x$ loadings and in turn, $O_3$ production rates. Aircraft observations in the equatorial and southern Pacific Ocean have revealed that alkyl nitrates can contribute to as much as 80% of the total $NO_y$ budget in these regions [*Talbot et al.*, 2000], where $O_3$ production rates are $NO_x$ limited. The lifetime of alkyl nitrates in the troposphere is between days and months depending on the alkyl chain length [*Talukdar et al.*, 1997a, 1997b]. Atmospheric production of alkyl nitrates is known to proceed through the reaction of alkyl peroxy radicals ($RO_2$) with nitric oxide (NO), representing a chain termination reaction through the sequestration of both $RO_2$ and NO.

Aircraft- and ship-borne observations in the equatorial and South Pacific Ocean suggest a diffuse oceanic source for short chain ($C_1$–$C_4$) alkyl nitrates [*Atlas et al.*, 1993; *Blake et al.*, 1999, 2003]. Direct measurements of alkyl nitrates in seawater indicate that $C_1$–$C_3$ alkyl nitrates can be supersaturated, confirming that the ocean is source for alkyl nitrates to the atmosphere [*Chuck et al.*, 2002; *Dahl et al.*, 2005; *Moore and Blough*, 2002]. Chemical transport modeling, constrained by atmospheric alkyl nitrate measurements, predict a globally, annually averaged oceanic emission rate of methyl and ethyl alkyl nitrates of 0.35 Tg N $yr^{-1}$. This equates to approximately 1 Dobson unit of $O_3$ and a 2.4% reduction in the lifetime of methane ($CH_4$) [*Neu et al.*, 2008]. Recently, *Williams et al.* [2014] suggested that oceanic emissions of methyl nitrate could be as large as 0.57 Tg N $yr^{-1}$ and emission of higher-order alkyl nitrates could be as large as 0.17 Tg N $yr^{-1}$. The increased emission rate is balanced in part by a larger dry deposition velocity to the ocean in the source region.

A complete mechanism for oceanic production of alkyl nitrates in seawater that replicates seawater observations has remained elusive. Laboratory and field measurements have demonstrated aqueous photochemical pathways for alkyl nitrate formation, where alkyl peroxy radicals, produced following the photolysis of colored dissolved organic matter (CDOM) react with dissolved NO [*Dahl et al.*, 2003]. *Dahl and Saltzman* [2008], through ship-based incubation studies, demonstrated that $C_1$–$C_3$ alkyl nitrates could be

formed from irradiated seawater, where NO concentrations are sustained by the photolysis of nitrite ($NO_2^-$). Comparing alkyl nitrate production rates in coastal waters with those previously reported in the North Pacific, *Dahl et al.* [2012] suggested that the molecular nature of CDOM controls relative alkyl nitrate production rates by regulating the relative abundances of their respective peroxy radical precursors. The photochemical production channel has proven to be a viable production mechanism for low molecular weight alkyl nitrates. However, this mechanism cannot explain the vertical distribution of alkyl nitrates observed in seawater. Specifically, *Chuck et al.* [2002] and *Dahl et al.* [2007] report $C_1$–$C_3$ alkyl nitrate depth profiles, where elevated alkyl nitrate concentrations are observed down to several hundred meters, where neither local production via photochemical pathways nor transport of surface produced alkyl nitrates can sustain the observed concentrations [*Dahl et al.*, 2007]. These results suggest a parallel, dark alkyl nitrate production mechanism that may be enzymatically mediated.

Here we report gas phase measurements of $C_1$–$C_5$ alkyl nitrates made in: (1) an enclosed wave channel during a simulated 5 day mesocosm experiment [*Prather et al.*, 2013] and (2) controlled flask experiments conducted with ambient and sterile seawater, inoculated with the heterotrophic bacterium *Alteromonas* sp. strain Scripps Institution of Oceanography (AltSIO). While the experiments were not designed to directly quantify waterside alkyl nitrate production rates, the results permit qualitative exploration of the role of phytoplankton and bacteria in the dark production of $C_1$–$C_5$ alkyl nitrates at this location.

## 2. Experiment

### 2.1. Scripps Institution of Oceanography Wave Channel and Mesocosm Experiment

The experiment was conducted in the 33 × 0.5 × 1 m (length × width × height) glass-walled wave channel in the Hydraulics Laboratory at the Scripps Institution of Oceanography (SIO). Seawater was pumped directly from the Pacific Ocean to fill the wave channel. Here we describe a 5 day mesocosm experiment where on day 1, the wave channel was filled with fresh seawater pumped directly from the SIO pier. During the mesocosm experiment, the wave channel was sequentially inoculated with four separate additions of varying combinations of the following: (1) heterotrophic bacteria isolates (*Alteromonas* sp. AltSIO and TW7, and *Pseudoalteromonas* TW2 and *P. atlantica*, strain 19262), (2) bacterial growth medium (ZoBell 2216E), and (3) a monoculture of marine algae (*Dunaliella tertiolecta*). The timing of the additions and a detailed description of the operation of the wave channel can be found in the supporting information.

### 2.2. Flask Experiments With Monocultures of Heterotrophic Bacteria

Controlled flask studies were conducted to complement the wave channel experiments and study alkyl nitrate production under more controlled seawater conditions. Here *Alteromonas* sp. AltSIO was inoculated into to an 2.8 L culture flask containing either 1.0 L of sterile seawater or seawater collected from the SIO pier in La Jolla, CA. ZoBell medium concentrate was added (20 mL) to make a 1X final solution (approximately 4.8 g C $L^{-1}$). Sterile seawater was prepared from plumbed sand/diatomaceous earth-filtered seawater described in the supporting information, which was then filtered with 0.2 μm polycarbonate disk filters, bubbled with $CO_2$ (30 s $L^{-1}$), and autoclaved. Pier water was filtered through a 50 μm Nitex mesh upon collection. The flask and tubing was autoclaved then jacketed to prevent photo-initiated radical production mechanisms. The head space of the flask was monitored continuously in real time using chemical ionization time-of-flight mass spectrometer CI-ToFMS (as described below in section 2.3). In a subsequent small flask experiment, gas phase headspace samples were drawn from the reaction flask for offline confirmation of the presence of alkyl nitrates using Gas chromatography-mass spectrometry (Figure S7 in the supporting information).

### 2.3. Gas Phase Measurements of Alkyl Nitrates

Short chain alkyl nitrates ($C_1$–$C_5$) were measured in real time at 2 Hz via chemical ionization time-of-flight mass spectrometry (CI-ToFMS), using protonated water clusters as the reagent ion. The instrument hardware has been described in detail previously, as applied to the selective detection of organic and inorganic acids using acetate ion chemistry [*Bertram et al.*, 2011]. In addition to $C_1$–$C_5$ alkyl nitrates, hydrogen sulfide ($H_2S$) was detected as $H^+$-$H_2S$ and ammonia ($NH_3$) as $H^+$-$NH_3$ and $H^+(H_2O)_n$-$NH_3$. Mixing ratios for $H_2S$ and $NH_3$ are not reported here due to the lack of an in house calibration standard, but the unit mass resolution signal intensity at 35 Th (corresponding to $H^+$-$H_2S$) is used as a proxy for bacteria abundance. Further information on the CI-ToFMS measurement can be found in the supporting information.

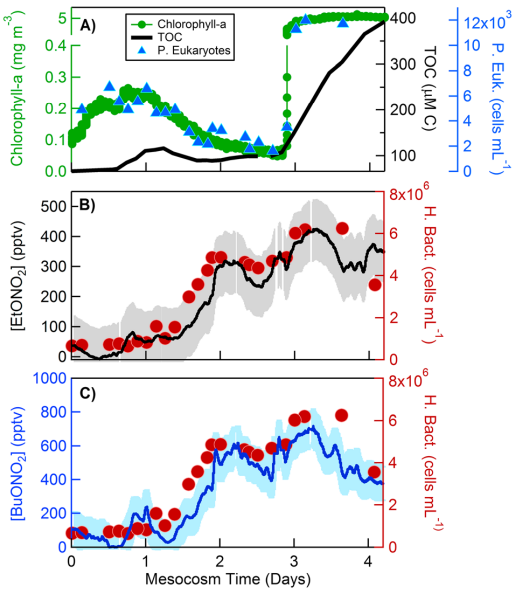


**Figure 1.** (a) Time evolution of chlorophyll *a*, total organic carbon, and photosynthetic eukaryote abundance in the SIO glass-walled wave channel as measured during the November 2011 mesocosm experiment. (b, c) Corresponding time series for ethyl nitrate ($EtONO_2$) and butyl nitrate ($BuONO_2$), respectively. The solid line in Figures 1b and 1c is the 30 min running median and the shaded region represents the variance in the 1 Hz measurements. Waterside concentrations of heterotrophic bacteria (red circles) are shown alongside the $EtONO_2$ and $BuONO_2$ concentration measurements.

## 3. Results

### 3.1. Alkyl Nitrate Production During a Controlled Mesocosm Experiment

Figure 1a depicts the biological evolution of seawater in the wave channel, and its response to the sequential additions described in Table S1 in the supporting information. The experiment commenced with filling the wave channel with coastal seawater (day 0). Prior to the first addition at day 0.6, the mean chlorophyll *a* concentration was $0.18 \pm 0.04$ mg m$^{-3}$, mean total organic carbon (TOC) was $69.1 \pm 2.9$ μM C, mean photosynthetic eukaryotes was $7.8 \times 10^3 \pm 4.4 \times 10^3$ cells mL$^{-1}$, and mean heterotrophic bacteria was $7.1 \times 10^5 \pm 4.3 \times 10^4$ cells mL$^{-1}$. Approximately 1 day following the first addition (approximately $1 \times 10^{10}$ cells of the heterotrophic bacteria *Alteromonas* and 18 g C of ZoBell growth media), the measured bacteria number concentrations in the wave channel doubled (from $7.1 \times 10^5$ to $1.6 \times 10^6$ cells mL$^{-1}$), before peaking on day 3 at $6.2 \times 10^6$ cells mL$^{-1}$. During this period both chlorophyll *a* and the number concentration of photosynthetic eukaryotes declined steadily, while TOC was slightly enhanced (115.9 μM on day 1). Measured heterotrophic bacteria concentrations responded to the second addition of *Alteromonas* and growth media (day 1.9), displaying a second peak at day 3.5, again approximately 1.5 days after the addition. Since the measurements of the heterotropic bacteria were conducted offline, and thus not available in real time for fine tuning the timing of the additions, two further additions were made to the wave channel before the second peak in heterotrophic bacteria. The third addition (day 2.6) was solely bacteria growth media and the fourth addition (day 2.8) included equal number concentrations of *Pseudoalteromonas atlantica* and *Dunaliella tertiolecta*. The measured chlorophyll *a* and photosynthetic eukaryote concentrations respond promptly, rising to 5.5 mg m$^{-3}$ and $1.1 \times 10^4$ cells mL$^{-1}$ by day 3.5.

The separable enhancements in the concentrations of seawater heterotrophic bacteria and photosynthetic eukaryotes under low-light conditions permits assessment of the potential for enzymatically mediated alkyl nitrate production. The time traces for ethyl and butyl nitrate are shown in Figures 1b and 1c, where the 30 min running median is shown with the solid black and blue lines, respectively. The shaded region in both Figures 1b and 1c represents the variance in the 1 Hz measurements. Time traces for methyl, propyl, and pentyl nitrate are shown in Figure S2 in the supporting information. In both Figures 1b and 1c, the concentration of heterotrophic bacteria is depicted with red circles. Prior to the first addition (day 0.6), the concentration of $C_1$–$C_5$ alkyl nitrates was on average, $40 \pm 20$, $30 \pm 12$, $< 20$, $60 \pm 30$, and $< 20$ parts per trillion by volume (pptv), respectively. The nonzero mixing ratios for $C_1$, $C_2$, and $C_4$ alkyl nitrates reflects either minor breakthrough of the charcoal filter into the wave channel headspace or nonzero emission from coastal seawater.

As shown in Figures 1b and 1c, the ethyl and butyl nitrate mixing ratios track measured heterotrophic bacteria. The mixing ratios for ethyl nitrate ($EtONO_2$) and butyl nitrate ($BuONO_2$) peaked on day 3.25 at 420 and 710 pptv, consistent with peak bacteria concentrations ($6.2 \times 10^6$ cells mL$^{-1}$). In contrast methyl nitrate ($MeONO_2$), propyl nitrate ($ProONO_2$), and pentyl nitrate ($PeONO_2$) showed very little enhancement

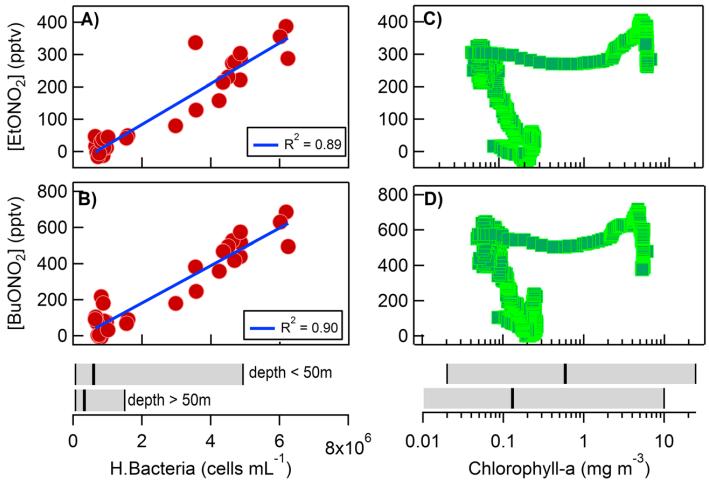


**Figure 2.** Correlation between $EtONO_2$ and $BuONO_2$ with (a, b) heterotrophic bacteria abundance and (c, d) chlorophyll *a* concentration, respectively, as measured in the SIO wave channel during the 2011 mesocosm experiment. Geometric median bacteria and chlorophyll at depths above and below 50 m as reported by *Li et al.* [2004] from a 15 year data set from global cruises ($n = 13{,}973$). The shaded region represents the range in observed concentrations.

through the bacteria growth phase (Figure S2). In what follows, we focus on the emission of ethyl and butyl nitrate and discuss potential biochemical mechanisms that support enhancement of even carbon numbered alkyl nitrate emissions in section 4.

$EtONO_2$ and $BuONO_2$ mixing ratios are shown in Figure 2 as a function of the waterside concentration of heterotrophic bacteria and chlorophyll *a*. A linear least squares regression analysis shows a strong positive correlation between $EtONO_2$ and $BuONO_2$ with heterotrophic bacteria throughout the mesocosm experiment ($R^2$ of 0.89 and 0.9 and *P* values of 0.0088 and 0.0391, respectively). In contrast, there is no observable correlation between $EtONO_2$ or $BuONO_2$ mixing ratios and chlorophyll $\alpha$ or photosynthetic eukaryote abundance. $MeONO_2$, $ProONO_2$, and $PeONO_2$ showed a much weaker correlation with heterotrophic bacteria concentration ($R^2 = 0.53$, 0.47, and 0.57, and *P* values of 0.0462, 0.0939, and 0.4050, respectively) and still no correlation with chlorophyll *a* (Figure S3 in the supporting information).

For comparison, ocean measurements of heterotrophic bacteria abundance and chlorophyll *a* concentration, recently compiled by *Li et al.* [2004], are shown in Figures 2b and 2d. The black line represents the geometric median and the shaded grey region the range in observations for both below and above 50 m. The data shown is a compilation that includes 13,973 concurrent measurements of bacteria abundance and chlorophyll concentration from 15 years of global cruises in the Atlantic, Pacific, Arctic, and Antarctic Oceans. The median values reported for bacteria are $6.0 \times 10^5$ and $3.3 \times 10^5$ cells $mL^{-1}$ for the subset of data above and below 50 m, respectively. As such, it should be noted that the bacteria concentrations measured in the wave channel are as much as a factor of 10 larger than median ocean conditions and exceed the highest bacteria concentrations ($4.94 \times 10^6$ cells $mL^{-1}$) reported in the *Li et al.* [2004] data set.

### 3.2. Time-Dependent Model for Alkyl Nitrate Production From Bacteria

In an attempt to place the measured $RONO_2$ mixing ratios in the context of previously reported seawater production rates, we constructed a 0-D time-dependent box model to simulate water side $RONO_2$ concentrations in the wave channel. We then estimate the emission rate of $C_1$–$C_5$ $RONO_2$ from seawater for comparison with measured $RONO_2$ emission rates calculated from gas phase concentrations.

Modeled seawater concentrations of $EtONO_2$ and $BuONO_2$ (pM) are shown in Figure 3a with black and blue solid lines, respectively, alongside measured heterotrophic bacteria concentrations (red squares). Modeled emission rates are shown in solid lines in Figure 3b, alongside the emission rates calculated from gas phase

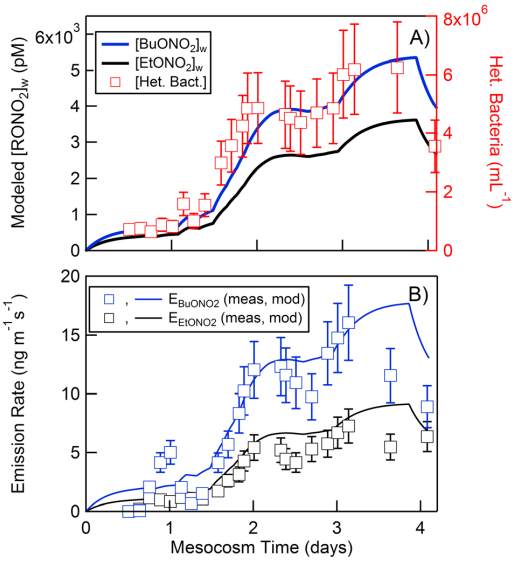


**Figure 3.** (a) Measured heterotrophic bacteria concentration in the SIO wave channel during the 2011 intensive measurement campaign (red). Modeled waterside $EtONO_2$ (black) and $BuONO_2$ (blue) concentrations. (b) Modeled emission rate of $EtONO_2$ (black lines) and $BuONO_2$ (blue lines) from equation (E1), assuming a transfer velocity ($k_w = 10$ cm h$^{-1}$). Emission rates calculated from concentration measurements of $EtONO_2$ and $BuONO_2$ using equation (E2) are shown in black and blue squares, respectively.

measurements of $EtONO_2$ and $BuONO_2$. The best model-measurement agreement was achieved when we held $k_x$ at 10 cm h$^{-1}$ and set $c_f$ at 16 and 24 molecules cell$^{-1}$ s$^{-1}$ for $EtONO_2$ and $BuONO_2$, respectively.

As shown in Figure 3b, the model tends to overestimate $RONO_2$ emission rates following a peak in heterotrophic bacteria concentration (e.g., directly following day 2.0 and day 3.0). This cannot be accounted for in the model with volatilization as the sole loss term. As such, the model-measurement disagreement during these time periods may suggest either (1) consumption of $RONO_2$ in the seawater that is not accounted for here or (2) a reduction in the per cell production rate of $RONO_2$ at periods of high bacteria abundance, suggesting either that alkyl nitrates are not produced directly by bacteria or that a key nutrient for $RONO_2$ production is limited thus slowing $P_{RONO2}$. This will be discussed in detail in section 4.

### 3.3. Alkyl Nitrate Production in Controlled Flask Experiments

As shown in Figure 1, alkyl nitrate production is initiated by the simultaneous addition of *Alteromonas* TW7 and AltSIO, and *Pseudoalteromonas* TW2 to the wave channel, approximately 14 h into the mesocosm experiment. As expected, mixing ratios of hydrogen sulfide ($H_2S$), a known direct by-product of sulfate reducing bacteria [*Barton and Fauque*, 2009], was also strongly correlated with heterotrophic bacteria concentration in the wave channel. As discussed above, the strong correlation ($R^2 > 0.89$) between $EtONO_2$ and $BuONO_2$ with heterotrophic bacteria abundance in the wave channel suggests that bacteria govern alkyl nitrate production in this experiment. The controlled flask studies were conducted to shed light on the mechanism by which heterotrophic bacteria (such as *Alteromonas*) produce alkyl nitrates. Here *Alteromonas* AltSIO and ZoBell growth media were added to the reaction flask containing sterile seawater. Minor, initial off-gassing of $C_1$–$C_5$ alkyl nitrates was observed over the first 6 h but returned to baseline values prior to bacteria growth in the flask. Bacteria growth in the flask was monitored periodically through measurements of optical density, while continuous measurement of $H_2S$ concentration in the headspace proved to be an indirect continuous measure of bacterial activity, likely linearly related to bacteria abundance. In what follows, we focus our analysis on $EtONO_2$.

There was no detectable generation of $EtONO_2$ observed in the sterile seawater matrix doped with *Alteromonas* AltSIO, despite significant production of $H_2S$ (approximately 10X that observed in the wave channel). The null result indicates the heterotrophic bacteria AltSIO is not the primary source for alkyl nitrates and that the bacteria mediated alkyl nitrate production observed in the wave channel experiments is likely to be codependent on the pool of dissolved organic material. To test this, *Alteromonas* AltSIO was added to the reaction flask containing seawater collected from the SIO pier, again under dark conditions. $EtONO_2$ concentrations directly track $H_2S$ through the bacteria growth phase for the first 24 h of the experiment (Figure S6 in the supporting information). At this time $H_2S$ appears to reach steady state, while $EtONO_2$ concentrations decay back to zero over the following 2 days.

To attain a consistent picture of the factors controlling alkyl nitrate production in the wave channel and flask experiments, $EtONO_2$ signal intensities are shown as a function of measured CI-ToFMS $H_2S$ signal intensities in

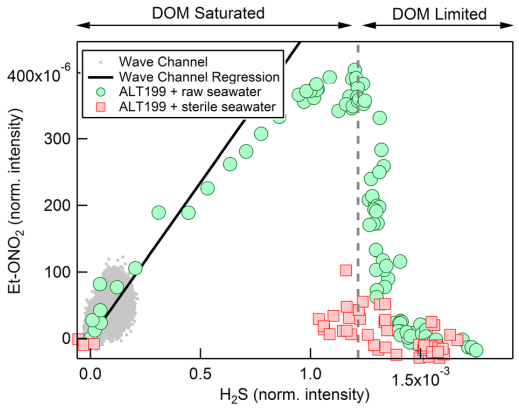


**Figure 4.** Correlation between $H_2S$ and $EtONO_2$ as measured in the wave channel (grey dots) and in the controlled flask experiments using raw, ambient seawater (green circles) and sterilized seawater (red squares) doped with the heterotrophic bacteria *Alteromonas* sp. AltSIO and ZoBell growth media. The solid black line is an extension of the linear regression line for the wave channel mesocosm data to higher $H_2S$ concentrations.

Figure 4. Data from the wave channel comprise most of the low intensity signals yet are highly correlated ($R^2 = 0.98$). The regression line is extrapolated to higher $H_2S$ values for comparison with the flask experiments that span a wider range in $H_2S$ and $EtONO_2$ concentrations. $EtONO_2$ and $H_2S$ are correlated in both the wave channel experiment and for the first 24 h of the flask experiments. Following this, ethyl nitrate concentrations exhibit a steady decline over the remaining 48 h of the experiment, suggesting that either the pool of dissolved organic material has been depleted or that some unknown factor is inhibitory to the production mechanism, thus suppressing alkyl nitrate production. Inhibition might be elicited by a change in chemical conditions such as pH or oxidation-reduction state or by the biochemical production of a molecule that interferes with contributing biosynthetic enzymes, through competitive or regulatory processes. A proposed mechanism, consistent with these results is discussed in section 4.2.

## 4. Discussion

### 4.1. Comparison of Alkyl Nitrate Production Rates With Prior Measurements

A rough comparison of the production rates modeled here can be made with those measured in *Dahl and Saltzman* [2008] during incubation studies performed using seawater samples collected in the North Pacific Ocean, spiked with 1μM nitrite. $EtONO_2$ production rates in that study ranged between $0.6 \pm 1.5$ and $26.1 \pm 8.3$ pM $h^{-1}$ for Warm Pool waters and high chlorophyll *a* waters, respectively. $BuONO_2$ concentrations and production rates were not reported. In comparison, our modeled $EtONO_2$ production rate was 56 pM $h^{-1}$ for a heterotrophic bacteria concentration of $6.0 \times 10^5$ cells $mL^{-1}$. While our model estimate for the dark production rate of $EtONO_2$ in our experiment is of the same order of magnitude of that observed in the *Dahl and Saltzman* [2008] study, our result is not a direct measurement but a best fit to our model. Nonetheless, our observations made in the wave channel highlight that a bacteria mediated production channel for alkyl nitrates is active, and future work to directly quantify the per cell production rate is warranted. In the following section, we discuss a proposed mechanism for bacteria controlled production of $RONO_2$ from seawater.

### 4.2. Proposed Mechanism for Bacteria Generated Alkyl Nitrate Production

Several primary (direct) and secondary (indirect) mechanisms are consistent with the dark production of $RONO_2$ observed in both the wave channel and flask experiments. Our experiments rule out the potential for direct production of $RONO_2$ from *Alteromonas* AltSIO in sterile seawater. However, two potential primary production mechanisms are possible: (1) alkyl nitrates are produced directly by other strain(s) of bacteria that become dominant in the experiment or (2) $RONO_2$ is produced directly by *Alteromonas* sp. AltSIO but requires the pool of dissolved organic material present in seawater to catalyze production. Based on the studies conducted to date, we cannot rule out these primary production mechanisms.

Alternatively, it is also possible that heterotrophic bacteria could produce $RONO_2$ through secondary production channels, where *Alteromonas* AltSIO generates a limited reactant(s) required for in situ production of $RONO_2$ in seawater. We selected *Alteromonas* AltSIO for these studies because its growth and physiology has been studied in coastal waters [*Pedler et al.*, 2014], and the genomes for *Alteromonas* sp. AltSIO, TW7, and

*Pseudoalteromonas* TW2 have been sequenced, thus providing insight on the mechanisms by which $RONO_2$ may be produced. The sequenced genome indicates that AltSIO, like many heterotrophic bacteria, contain nitric oxide synthases [*Crane et al.,* 2010]. Nitric oxide synthases have been shown to catalyze the production of nitric oxide (NO) from amino acids [*Sal Salard-Arnaud et al.,* 2012]. If the necessary genes for NO production are expressed, in situ alkyl nitrate production could follow an analogous pathway to known photochemical mechanisms, where AltSIO produces NO directly, but alkyl nitrate production is limited by either the availability of peroxy radicals generated from the pool of dissolved organic material or the amino acids required to drive bacteria mediated NO production. *Hughes et al.* [2010], using measurements of the vertical distribution of methyl and ethyl nitrate in shallow freshwater lakes, suggested that bacteria may serve as a dark source of NO. Our model predicts that $RONO_2$ production can be rapid (approximately 24 molecules $cell^{-1}$ $s^{-1}$), suggesting that the production rate of NO by heterotrophic bacteria is fast in these experiment. We are not aware of prior direct determinations of NO production rates for *Alteromonas*; however, studies of NO production rates from terrestrial bacteria have shown that bacteria can efficiently produce NO at rates as high as 135 molecules $cell^{-1}$ $s^{-1}$ [*Ren et al.,* 2000].

If the alkyl nitrate production observed in these experiments proceeded through a secondary production mechanism involving NO, a parallel, dark production mechanism for peroxy radicals must also be operational. It was recently demonstrated that heterotrophic bacteria (including *Alteromonas*) are capable of efficient, extracellular production of superoxide ($O_2^-$) and potentially other reactive oxygen species (ROS) [*Diaz et al.,* 2013]. *Diaz et al.* [2013] showed that various strains of *Alteromonas* could produce $O_2^-$ as fast as 200 molecules $cell^{-1}$ $s^{-1}$. In light of this finding, we expect dark production of $O_2^-$, and likely hydroxyl radicals (OH), following known iron catalyzed reactions involving $H_2O_2$ [*Moffett and Zika*, 1987], to be significant in these studies. It follows that bacteria derived ROS may also serve to initiate peroxy radical production following $O_2^-$ and/or OH reactions with the wide range of dissolved organic molecules in surface waters. As such, cogeneration of NO and $O_2^-$ provide the essential initial ingredients to initial prompt alkyl nitrate production in seawater. An interesting result of both the wave channel and flask experiments is that production of even carbon numbered alkyl nitrates ($C_2$ and $C_4$) is significantly favored over the production of odd carbon numbered alkyl nitrates ($C_1$, $C_3$, and $C_5$). This observation may reflect an even carbon number preference in alkyl nitrate assembly implicating the involvement of biochemical pathways including fatty acid synthesis, fatty acid degradation, and polyketide synthesis. All fatty acid synthases and degradation pathways and many PKS synthases add or remove an acetyl two-carbon unit of in modular fashion resulting in products and intermediates with even numbered acyl chains.

Reactions of nitric oxide in biological matrices have received considerable amount of attention, as NO is released by a wide array of mammalian cells and mediates a host of biological actions [e.g., *Nathan,* 1992]. It is believed that bacterial derived NO in the studied bacteria may play similar roles as in mammalian systems but this is not yet well understood [*Coletta et al.,* 2012; *King,* 2013]. Cogeneration of NO and $O_2^-$ has been shown to result in peroxynitrite ($ONOO^-$) production, leading to cytotoxic conditions [*Matheis et al.,* 1992]. It has been shown that the production of alkyl nitrates in the reaction of lipid peroxy radicals with NO can serve to inhibit lipid peroxidation [*O'Donnell et al.,* 1997]. It has also been suggested that NO is utilized in bacterial natural product synthases for nitration reactions as well for recovery or protection from radiation exposure or oxidative stress to support virulence [*Crane et al.,* 2010]. If alkyl nitrates are made as consequence of excess NO it may be that alkyl nitrates are an indicator of a bacterial stress response. Whether alkyl nitrates have dedicated biological functions or are just a by-product of these other processes is not clear at this time.

## 5. Conclusions and Atmospheric Implications

Our measurements of alkyl nitrate emissions from natural and inoculated seawater matrices suggest that heterotrophic bacteria may play a role in the production of alkyl nitrates, particularly at depth where photochemical production is minimized. It is postulated that alkyl nitrate production in seawater could be initiated by the cogeneration of nitric oxide (NO) and superoxide ($O_2^-$) by bacteria. While the results presented here indicate the role for bacteria in the production of alkyl nitrates, they do not explain existing distributions of $RONO_2$ in marine air, where alkyl nitrates larger than $C_3$ are rarely observed. At present it is not clear at this time the extent to which this mechanism competes with known photochemical production pathways in the surface ocean or how widespread bacterial production of nitric oxide is relative to that

generated from nitrite photolysis. Our results highlight the extreme coupling between biological and chemical mechanisms occurring at the ocean surface and suggest that single-component monoculture experiments (either bacteria or phytoplankton) may not capture the mechanisms by which trace gases are produced in the ocean.

**Acknowledgments**
The authors gratefully acknowledge the support of the Scripps Institution of Oceanography Hydraulics Laboratory for helpful discussions and technical development of the sealed wave channel. This overall study was supported by the National Science Foundation (NSF) Center for Chemical Innovation, the Center for Aerosol Impacts on Climate and the Environment (CAICE) under grant CHE1038028. Partial support was provided by an NSF CAREER Award under grant AGS-1151430.

The Editor thanks Elizabeth Dahl and an anonymous reviewer for their assistance in evaluating this paper.

## References

Atlas, E., W. Pollock, J. Greenberg, L. Heidt, and A. M. Thompson (1993), Alkyl nitrates, nonmethane hydrocarbons, and halocarbon gases over the equatorial Pacific Ocean during SAGA 3, *J. Geophys. Res., 98*(D9), 16,933–16,947, doi:10.1029/93JD01005.

Barton, L. L., and G. D. Fauque (2009), Biochemistry, physiology and biotechnology of sulfate-reducing bacteria, *Adv. Appl. Microbiol., 68*, 41–98.

Bertram, T. H., J. R. Kimmel, T. A. Crisp, O. S. Ryder, R. Yatavelli, J. A. Thornton, M. J. Cubison, M. Gonin, and D. R. Worsnop (2011), A field-deployable, chemical ionization time-of-flight mass spectrometer, *Atmos. Meas. Tech., 4*, 1963–1987.

Blake, N. J., et al. (1999), Aircraft measurements of the latitudinal, vertical, and seasonal variations of NMHCs, methyl nitrate, methyl halides, and DMS during the First Aerosol Characterization Experiment (ACE 1), *J. Geophys. Res., 104*(D17), 21,803–21,817, doi:10.1029/1999JD900238.

Blake, N. J., D. R. Blake, A. L. Swanson, E. Atlas, F. Flocke, and F. S. Rowland (2003), Latitudinal, vertical, and seasonal variations of C-1-C-4 alkyl nitrates in the troposphere over the Pacific Ocean during PEM-Tropics A and B: Oceanic and continental sources, *J. Geophys. Res., 108*(D2), 8242, doi:10.1029/2001JD001444.

Chuck, A. L., S. M. Turner, and P. S. Liss (2002), Direct evidence for a marine source of C-1 and C-2 alkyl nitrates, *Science, 297*(5584), 1151–1154, doi:10.1126/science.1073896.

Coletta, C., et al. (2012), Hydrogen sulfide and nitric oxide are mutually dependent in the regulation of angiogenesis and endothelium-dependent vasorelaxation, *Proc. Natl. Acad. Sci. U.S.A., 109*, 9161–9166.

Crane, B. R., J. Sudhamsu, and B. A. Patel (2010), Bacterial nitric oxide synthases, *Annu. Rev. Biochem., 79*, 445–470.

Dahl, E. E., and E. S. Saltzman (2008), Alkyl nitrate photochemical production rates in North Pacific seawater, *Mar. Chem., 112*(3–4), 137–141, doi:10.1016/j.marchem.2008.10.002.

Dahl, E. E., E. S. Saltzman, and W. J. de Bruyn (2003), The aqueous phase yield of alkyl nitrates from ROO + NO: Implications for photochemical production in seawater, *Geophys. Res. Lett., 30*(23), 1271, doi:10.1029/2003GL018686.

Dahl, E. E., S. A. Yvon-Lewis, and E. S. Saltzman (2005), Saturation anomalies of alkyl nitrates in the tropical Pacific Ocean, *Geophys. Res. Lett., 32*, L20817, doi:10.1029/2005GL023896.

Dahl, E. E., S. A. Yvon-Lewis, and E. S. Saltzman (2007), Alkyl nitrate (C-1-C-3) depth profiles in the tropical Pacific Ocean, *J. Geophys. Res., 112*, C01012, doi:10.1029/2006JC003471.

Dahl, E. E., E. M. Heiss, and K. Murawski (2012), The effects of dissolved organic matter on alkyl nitrate production during GOMECC and laboratory studies, *Mar. Chem., 142*, 11–17, doi:10.1016/j.marchem.2012.08.001.

Diaz, J. M., C. M. Hansel, B. M. Voelker, C. M. Mendes, P. F. Andeer, and T. Zhang (2013), Widespread production of extracellular superoxide by heterotrophic bacteria, *Science, 340*, 1223–1226.

Hughes, C., A. J. Kettle, G. A. Unazi, K. Weston, M. R. Jones, and M. T. Johnson (2010), Seasonal variations in the concentrations of methyl and ethyl nitrate in a shallow freshwater lake, *Limnol. Oceanogr., 55*(1), 305–314.

King, S. B. (2013), Potential biological chemistry of hydrogen-sulfide (H2S) with the nitrogen oxides, *Free Radical Biology and Medicine, 55*, 1–7.

Li, W. K. W., E. J. H. Head, and W. G. Harrison (2004), Macroecological limits on heterotrophic bacterial abundance in the ocean, *Deep Sea Res., 51*, 1529–1540.

Matheis, G., M. P. Sherman, G. D. Buckberg, D. M. Haybron, H. H. Young, and L. J. Ignarro (1992), Role L-arginine-nitric oxide pathway in myocardial reoxygenation injury, *Am. J. Physiol., 262*(2 Part 2), H616-20.

Moffett, J. W., and R. G. Zika (1987), Reaction kinetics of hydrogen peroxide with copper and iron in seawater, *Environ. Sci. Tech., 21*(8), 804–810.

Moore, R. M., and N. V. Blough (2002), A marine source of methyl nitrate, *Geophys. Res. Lett., 29*(15), 1737, doi:10.1029/2002GL014989.

Nathan, C. (1992), Nitric oxide as a secretory product of mammalian cells, *FASEB J., 6*(12), 3051–3064.

Neu, J. L., M. J. Lawler, M. J. Prather, and E. S. Saltzman (2008), Oceanic alkyl nitrates as a natural source of tropospheric ozone, *Geophys. Res. Lett., 35*, L13814, doi:10.1029/2008GL034189.

O'Donnell, V. B., P. H. Chumley, N. Hogg, A. Bloodsworth, V. M. Darley-Usmar, and B. A. Freeman (1997), Nitric oxide inhibition of lipid peroxidation: Kinetics of reaction with lipid radicals and comparison with α-Tocopherol, *Biochemistry, 36*, 15,216–15,223.

Pedler, B. E., L. I. Aluwihare, and F. Azam (2014), Single bacterial strain capable of significant contribution to carbon cycling in the surface ocean, *Proc. Natl. Acad. Sci. U.S.A., 111*(20), 7202–7207.

Prather, K. A., et al. (2013), Bringing the ocean into the laboratory to probe the chemical complexity of sea spray aerosol, *Proc. Natl. Acad. Sci. U.S.A., 110*(19), 7550–7555, doi:10.1073/pnas.1300262110.

Ren, T., R. Roy, and R. Knowles (2000), Production and consumption of nitric oxide by three methanotrophic bacteria, *Appl. Environ. Microbiol., 66*(9), 3891–3897.

Sal Salard-Arnaud, I., D. Stuehr, J.-L. Boucher, and D. Mansuy (2012), Spectroscopic, catalytic and binding properties of bacillus subtilis NO synthase-like protein: Comparison with other bacterial and mammalian NO synthases, *J. Inorg. Biochem., 106*, 164–171.

Talbot, R. W., J. E. Dibb, E. M. Scheuer, J. D. Bradshaw, S. T. Sandholm, H. B. Singh, D. R. Blake, N. J. Blake, E. Atlas, and F. Flocke (2000), Tropospheric reactive odd nitrogen over the South Pacific in austral springtime, *J. Geophys. Res., 105*(D5), 6681–6694, doi:10.1029/1999JD901114.

Talukdar, R. K., S. C. Herndon, J. B. Burkholder, J. M. Roberts, and A. R. Ravishankara (1997a), Atmospheric fate of several alkyl nitrates .1. Rate coefficients of the reactions alkyl nitrates with isotopically labelled hydroxyl radicals, *J. Chem. Soc. Faraday Trans., 93*(16), 2787–2796.

Talukdar, R. K., J. B. Burkholder, M. Hunter, M. K. Gilles, J. M. Roberts, and A. R. Ravishankara (1997b), Atmospheric fate of several alkyl nitrates .2. UV absorption cross-sections and photodissociation quantum yields, *J. Chem. Soc. Faraday Trans., 93*(16), 2797–2805, doi:10.1039/A701781b.

Williams, J. E., G. Le Bras, A. Kukui, H. Ziereis, and C. A. M. Brenninkmeijer (2014), The impact of the chemical production of methyl nitrate from the NO + $CH3O_2$ reaction on the global distributions of alkyl nitrates, nitrogen oxides and tropospheric ozone: A global modelling study, *Atmos. Chem. Phys., 14*, 2363–2382, doi:10.5194/acp-14-2363-2014.

*Geophysical Research Letters*

Supporting Information for

# Bacteria driven production of alkyl nitrates in seawater

Michelle J. Kim[1], Jennifer M. Michaud[2], Renee Williams[2], Byron Pedler Sherwood[1,3], Robert Pomeroy[2], Farooq Azam[1], Michael Burkart[2], and Timothy H. Bertram[*2]

[1]Scripps Institution of Oceanography, University of California San Diego, La Jolla, CA 92093
[2]Department of Chemistry and Biochemistry, University of California San Diego, La Jolla, CA 92093
[3]Current address: Center for Microbial Oceanography: Research and Education, School of Ocean and Earth Science and Technology, Department of Oceanography, University of Hawai'i at Mānoa, Honolulu, HI, 96822
[*]Corresponding author: thbertram@ucsd.edu

## Contents of this file



## Introduction

In what follows we describe important supplementary information on: 1) The SIO wave channel, 2) Chemical Ionization Mass Spectrometric Measurements of alkyl nitrates, 3) GC/MS measurements of alkyl nitrates, and 4) Time dependent box model used to track the temporal evolution of alkyl nitrate production. This information is supported by one table and 8 figures.

## Text S1.

### SIO wave channel and mesocosm experiment

The wave channel was filled to 0.6 m. The seawater intake is 300m offshore, and 2m above the ocean floor. Seawater is first pumped through two consecutive coarse filter beds (30cm of No. 12 crystal sand, 20cm of pea gravel, and 45cm of rock) prior to being delivered to three $2.2 \times 10^5$ L holding tanks. Seawater is then delivered to the SIO campus, including

the Hydraulics lab, where it is again filtered by inline sand and diatomaceous earth filters prior to being added to the wave channel. During the course of experiments, breaking waves were generated continuously (0.6Hz) *via* a hydraulic paddle within the wave channel. The primary purpose of wave breaking was for a concurrent study on sea-spray aerosol production.

The headspace of the wave channel was fully sealed and equipped with an air handling and filtration system to eliminated background aerosol as well as volatile organic compounds (VOC), nitrogen and sulphur oxides. The filtration system consists of four stages: 1) a prefilter, 2) 4mm coal-based, pellet activated charcoal, 3) potassium permanganate ($KMnO_4$), and 4) a 30 x 30 x 29cm HEPA filter. Filter breakthrough was monitored continuously with a condensation particle counter (CPC, TSI 3010), and a commercial ozone ($O_3$) and nitrogen oxide ($NO_x$) detector (Horiba APOA-370 and APNA-370, respectively). The air flow velocity over the wave channel was held to 12.2 cm $s^{-1}$, equating to a volumetric flow rate in excess of 1400 sLpm. The light intensity in the wave channel was not quantified, however we expect the UV light intensity in the wave channel to be small as: 1) the wave channel is located indoors where the primary light source is the overhead fluorescent lights, 2) the lid is completely opaque, and 3) the glass walls of the wave channel effectively attenuate light up to approximately 350 nm, which would reduce seawater nitrite photolysis as a source for nitric oxide in these experiments [*Chu and Anastasio*, 2007].

Chlorophyll-a concentration was determined in real-time using a WET Labs ECO Triplet fluorometer. Seawater samples were taken every 3-4 hours during the 5-day mesocosm experiment for the offline determination of total organic carbon (TOC) concentrations and number concentrations of heterotrophic bacteria and photosynthetic eukaryotes *via* flow cytometry. Seawater samples collected for flow cytometry were collected in 1 mL polypropylene cryogenic vials, fixed with 50mL of GF/F filtered 10% paraformaldehyde and flash frozen in liquid $N_2$ before being transferred to a -80°C freezer. Flow cytometry analysis was conducted at the School of Ocean, Earth Science, and Technology (SOEST) Flow Cytometry Facility at the University of Hawaii at Manoa.

**CI-ToFMS measurements of alkyl nitrates**

In this application, air is drawn from the headspace of the wave channel at 10 slpm through ¼" OD PFA tube, where it is sub-sampled at 1.7 slpm into the ion-molecule reaction chamber of the CI-ToFMS. Protonated water clusters ($H^+(H_2O)_n$) were generated by passing 1.5 slpm of ultra high purity $N_2$, saturated with water vapour, through a Po-210 radioactive source (NRD P-2021). Under all conditions sampled here, the primary ion count rate was maintained at >90% of the total ion count rate to suppress the potential for secondary ion chemistry.

As a result of the high IMR pressure (70 mbar) and low collisional energies, $C_1$-$C_5$ alkyl nitrates in our instrument were detected with minimal fragmentation at the protonated parent ion (e.g., methyl nitrate was detected as $H^+$-$CH_3ONO_2$ at 78 m/*Q*) and with either one or two attached water molecules ($H^+(H_2O)_n$-$CH_3ONO_2$). This is in contrast to the extensive fragmentation of alkyl nitrates observed in traditional proton transfer reaction mass spectrometry [*Aoki et al.*, 2007]. Alkyl nitrate mixing ratios were determined through direct calibration of the instrument with an n-butyl and an n-propyl nitrate standard. The concentrations of the nitrate standards were determined following catalytic conversion of the alkyl nitrate to $NO_x$, which was subsequently detected *via* chemiluminescence (Thermo Environmental 42C NO-$NO_2$-$NO_x$ analyzer). Due to the very limited availability of methyl and ethyl nitrate standard, coupled with their instability, we do not have a direct calibration for methyl, ethyl, or pentyl nitrate. As such, we applied the average of the calibration factors retrieved for the n-butyl and n-propyl nitrate standards. The water cluster ion chemistry used here was shown to be much less sensitive toward alkyl nitrates than it is toward other more polar analytes (e.g., dimethyl sulfoxide, ammonia, and acetone). As such, we do not expect this ion chemistry to be particularly useful for ambient determinations of alkyl nitrates, although it was well suited for the experiments described here at higher alkyl nitrate mixing ratios. In addition to the $C_1$-$C_5$ alkyl nitrates, hydrogen sulphide ($H_2S$) was detected as $H^+$-$H_2S$ and ammonia ($NH_3$) as $H^+$-$NH_3$ and $H^+(H_2O)_n$-$NH_3$. Mixing ratios for $H_2S$ and $NH_3$ are not reported here due to the lack of an in house calibration standard, but the unit mass resolution signal intensity at 35 Th is used as a proxy

for the concentration. Baseline measurements were made by overflowing the instrument inlet with ultra-high purity zero air. Further information potential interferences in the CI-ToFMS measurement can be found in the supplemental information.

Given that the CI-ToFMS used for these experiments has low resolving power ($m/\Delta m$ = 1100) and the ion chemistry that was employed is not exceptionally specific toward a given class of molecules, there is a possibility that the molecular assignments we have made to the observed ions (78, 92, 106, 120, and 134 Th) is incorrect or incomplete. To assess this possibility, we have scanned all possible molecular matches for the ions observed. Our assignments for the five studied ions was: $H^+$-$CH_3ONO_2$, $H^+$-$CH_3CH_2ONO_2$, $H^+$-$CH_3(CH_2)_2ONO_2$, $H^+$-$CH_3(CH_2)_3ONO_2$, and $H^+$-$CH_3(CH_2)_2ONO_2$ corresponding to protonated $C_1$-$C_5$ alkyl nitrates. The vast majority of the molecules with the same nominal mass as those detected are either non-volatile or would not be ionized by $H^+(H_3O)_n$ ion chemistry. A select few amines would be detected if present in the experiment. These include: 2-aminoethanethiol (detected as $H^+$-$HS(CH_2)_2NH_2$ at 78 Th), trimethylamine (detected as $H_3O^+$-$N(CH_3)_3$ at 78 Th), 2-(methylthio)-ethylamine (detected as $H^+$-$CH_3S(CH_2)_2NH_2$ at 92 Th), 3-(methylthio)-propylamine (detected as $H^+$-$CH_3S(CH_2)_3NH_2$ at 106 Th), 4-(methylthio)-butylamine (detected as $H^+$-$CH_3S(CH_2)_4NH_2$ at 120 Th), triethylamine (detected as $H_3O^+$-$N(CH_2CH_3)_3$ at 120 Th), and 5-(methylthio)-pentylamine (detected as $H^+$-$CH_3S(CH_2)_5NH_2$ at 134 Th). The primary evidence that the aforementioned amines did not contribute to the signal intensities that we measured comes from the time response of our inlet during background determinations (Fig. S1). The inlet used during these experiments was not designed for high transmission of reactive and/or highly polar molecules. As such, the inlet will yield poor time response to such molecules due to inlet wall effects. As shown in Fig. S1, the decay in the ammonia signal (detected as $H^+NH_3$) can be best modelled as bi-exponential decay with a fast time constant depicting the gas-exchange time of the inlet (ca. 1-2 s) and a slow time constant (minutes) that describes the inlet equilibration. In contrast, the decay of the signal at 120 Th (which we have assigned to butyl nitrate) shows only a fast time constant indicating the molecule is not strongly interacting with the inlet. This is inconsistent with the behaviour of the alkyl

amines listed above. As such, we conclude that the ions detected at 78, 92, 106, 120, and 134 correspond to the series of $C_1$-$C_5$ alkyl nitrates.

Indication of a diel dependence is shown in the time series of $MeONO_2$ (Fig. S2). At presence, the source of this is not known. It is likely either a result of the diel temperature fluctuations of the wave channel, temperature driven fluctuations in the air flow rate (driven by fan speed), or a temperature dependence in the CIMS.

**GC/MS Measurements of alkyl nitrates**

An Agilent 7820A gas chromatographer (GC) was used with a 5975 mass selective detector (MSD) system for the identification of alkyl nitrates. The analytes were collected from the headspace with an air-tight syringe and injected into the GC port with an inlet temperature of 150°C. Separation took place on an Agilent J&W HP-PLOT Q (30 m x 320 μm x 20 μm) column with helium as the carrier gas (flow rate: 0.7 ml/min) in split mode (75:1). The GC method was initiated with an oven temperature of 100°C for 2 min. The temperature was then ramped at 2°C /min until it reached 200°C, and was held at that temperature for 2 min before ramping down to 100°C at 10°C/min (total run time: 65 min). The mass spectrometer was used in full scan mode (range 42:150) with the source and quadrupole temperatures set at 230°C and 150°C, respectively. A sample chromatogram is shown in Fig. S7 and the background subtracted, selected ion chromatogram in Fig. S8.

**Time-dependent model for alkyl nitrate production from bacteria**

There are two adjustable parameters in the model: 1) the production rate for $C_1$-$C_5$ alkyl nitrates in seawater ($P_{RONO2}$), and 2) the gas transfer coefficient for air-sea exchange ($k_x$). It is important to note that neither of these are measured in this experiment. In the model, we relate the water-side production rate of $RONO_2$ to the measured abundance of heterotrophic bacteria, assuming a linear relationship. The conversion factor ($c_f \equiv P_{RONO2}$ / [heterotrophic bacteria]) is expressed in units of molecules $cell^{-1}s^{-1}$ and unique to each alkyl nitrate studied ($C_1$-$C_5$). The conversion factors used in this study are shown in Fig. S5. The model assumes there are no waterside losses for $RONO_2$ other than emission to the atmosphere. We calculate the emission rate (or flux) using Equation 1 (E1):

$$E_C = \alpha_C k_x \left( [C]_{water} / \alpha_C - [C]_{air} \right) \quad \text{(E1)}$$

where $\alpha_C$ is the dimensionless solubility of the gas in seawater, $k_x$ is the transfer velocity (cm $s^{-1}$), and $[C]_{water}$ and $[C]_{air}$ are the concentrations of molecule C in the water and air, respectively. Despite very low wind velocities in the wave channel (U = 0.122 m $s^{-1}$) the transfer coefficient ($k_x$) is not constrained in this experiment due to continuous wave breaking in the wave channel that disrupts air-sea exchange and sub-surface turbulence. As such, we initially set $k_x$ at 10 cm $hr^{-1}$ broadly consistent with gas transfer parameterizations at low wind speeds [*Johnson,* 2010]. We then iterate to find values for $c_f$ and $k_x$ that best fit the measurements.

To compare with the model calculations, $RONO_2$ mixing ratios as measured in the wave channel were converted to emission rates using a puff model of the wave channel [*Jacob*, 1999]. Here, we integrate the mass balance equation for the time rate of change in the gas-phase concentration of compound C to obtain an analytical expression (E2) for $[C]_x$ as a function of: the initial concentration at the entry point to the wave channel ($[C]_{x0}$), the first order loss rate of C in the channel (k, here taken to be zero), the emission rate from the water surface (E), the height of the air in the wave channel (h = 0.4 m), the air speed in the wave channel (U = 0.122 m $s^{-1}$), and x the position along the wave channel.

$$[C]_x = [C]_{x_0} e^{-k/U(x-x_0)} + \frac{E}{hk}\left(1 - e^{-k/U(x-x_0)}\right) \quad \text{(E2)}$$

We then solve for the emission rate (E, ng $m^{-2}$ $s^{-1}$) as a function of time during the mesocosm experiment for comparison with the 0-D box model.

| Addition # | Time (days) | Material Added | Quantity |
|---|---|---|---|
| 1 | 0.6 | Seawater | 100 L |
| | | ZoBell media | 18 g C |
| | | *Alteromonas* TW2, TW7, AltSIO | $1x10^{10}$ cells |
| 2 | 1.9 | ZoBell media | 13.5 g C |
| | | *Alteromonas* TW2, TW7, AltSIO | $4.5x10^{12}$ cells |
| 3 | 2.6 | ZoBell media | 15 g C |
| 4 | 2.8 | ZoBell media | 15 g C |
| | | *Pseudoalteromonas atlantica* | $1x10^{11}$ cells |
| | | *Dunaliella tertiolecta* | $1x10^{11}$ cells |

**Table S1:** Timing of the four sequential additions of heterotrophic bacteria, green algae, and bacterial growth medium to the wave channel during the 5-day mesocosm experiment. The approximate quantities of each addition are reported in the right column. At the beginning of the experiment (time = 0 days), fresh seawater, pumped directly from the Scripps Pier was used to fill the wave channel.

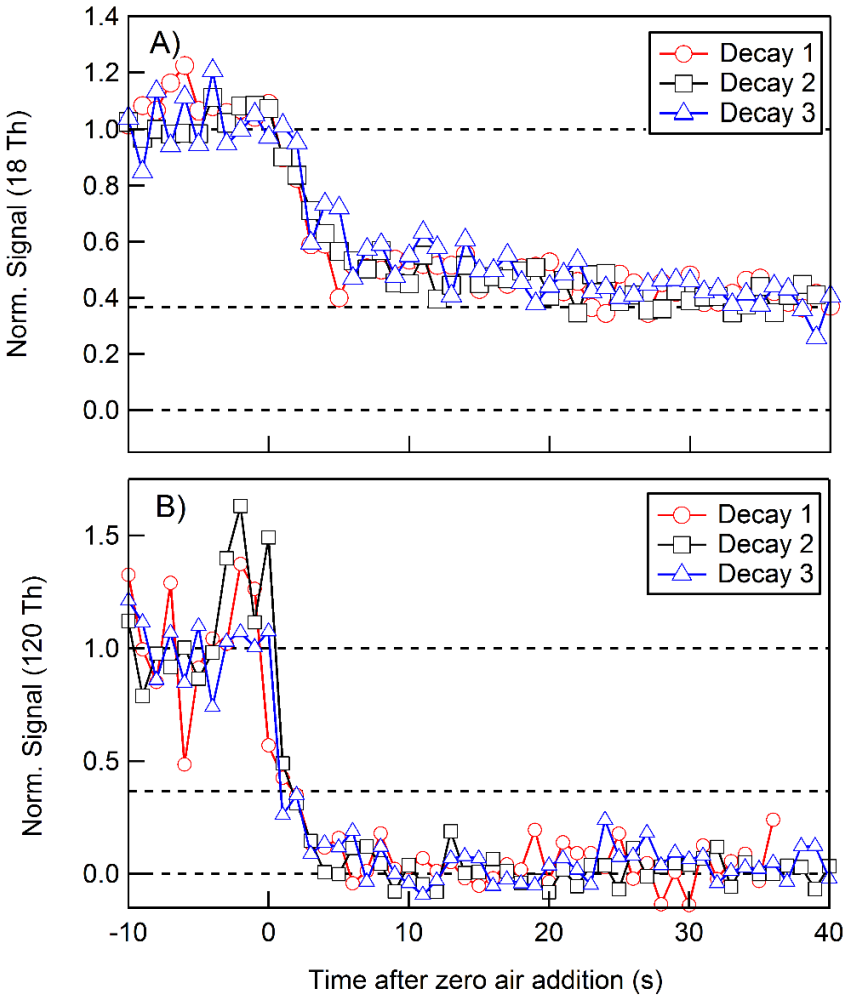


**Figure S1:** A, B) Decay in count rate at 18 Th (assigned as $H^+NH_3$) and 120 Th ($BuONO_2$, $H^+$-$CH_3(CH_2)_3ONO_2$) following the injection of dry zero air to the inlet manifold. The decay in the $H^+NH_3$ signal can be best described by biexponential decay, where the fast time constant is attributed to the gas exchange time of the inlet (ca 1-2 s) and the slow time constant to inlet wall effects. This is typical for a highly polar compound such as ammonia or amines. The decay at $H^+$-$CH_3(CH_2)_3ONO_2$ is consistent with that expected for an alkyl nitrates, which should display limited inlet wall effects.

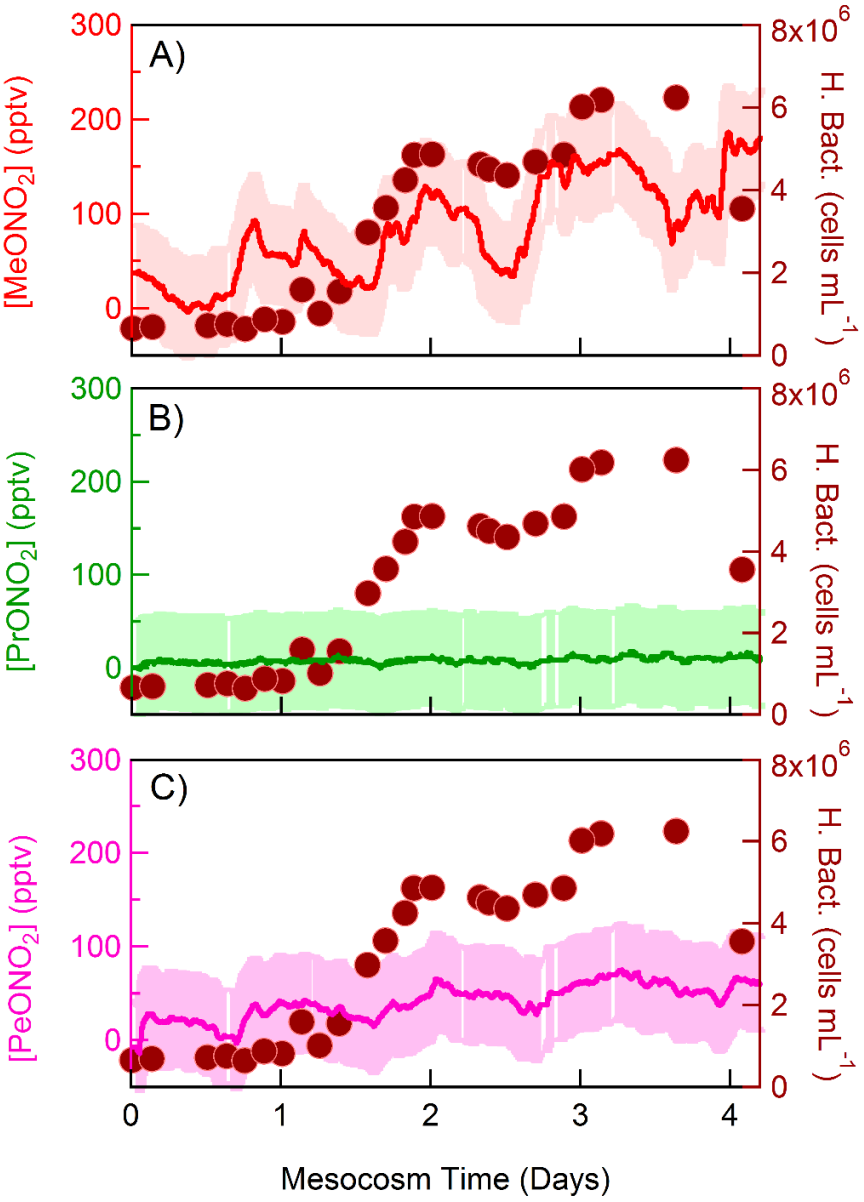


**Figure S2:** Time series for methyl nitrate ($MeONO_2$), propyl nitrate ($ProONO_2$), and pentyl nitrate ($PeONO_2$) during the mesocosm experiment conducted in the SIO wave channel. The solid lines are the 30 minute running median and the shaded region represents the variance in the 1Hz measurements. Waterside concentrations of heterotrophic bacteria (red circles) are shown alongside the $RONO_2$ concentration measurements.

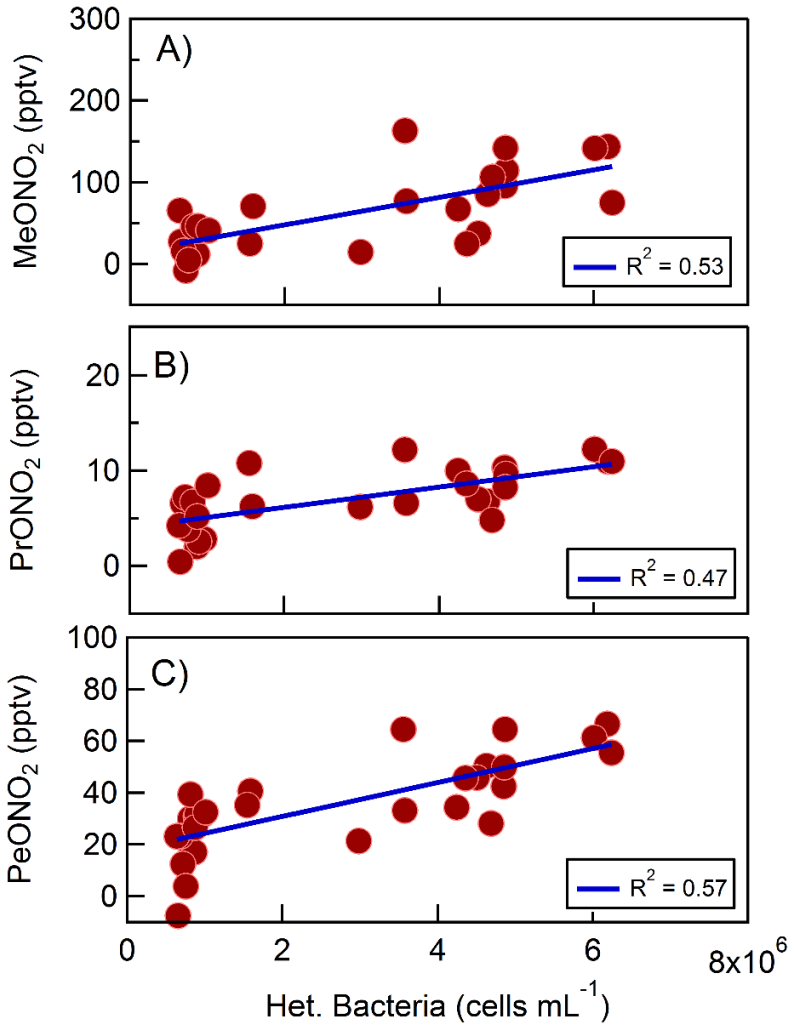


**Figure S3:** Correlation between $MeONO_2$, $ProONO_2$ and $PeONO_2$ with heterotrophic bacteria abundance (A-C) as measured in the SIO wave channel during the 2011 mesocosm experiment.

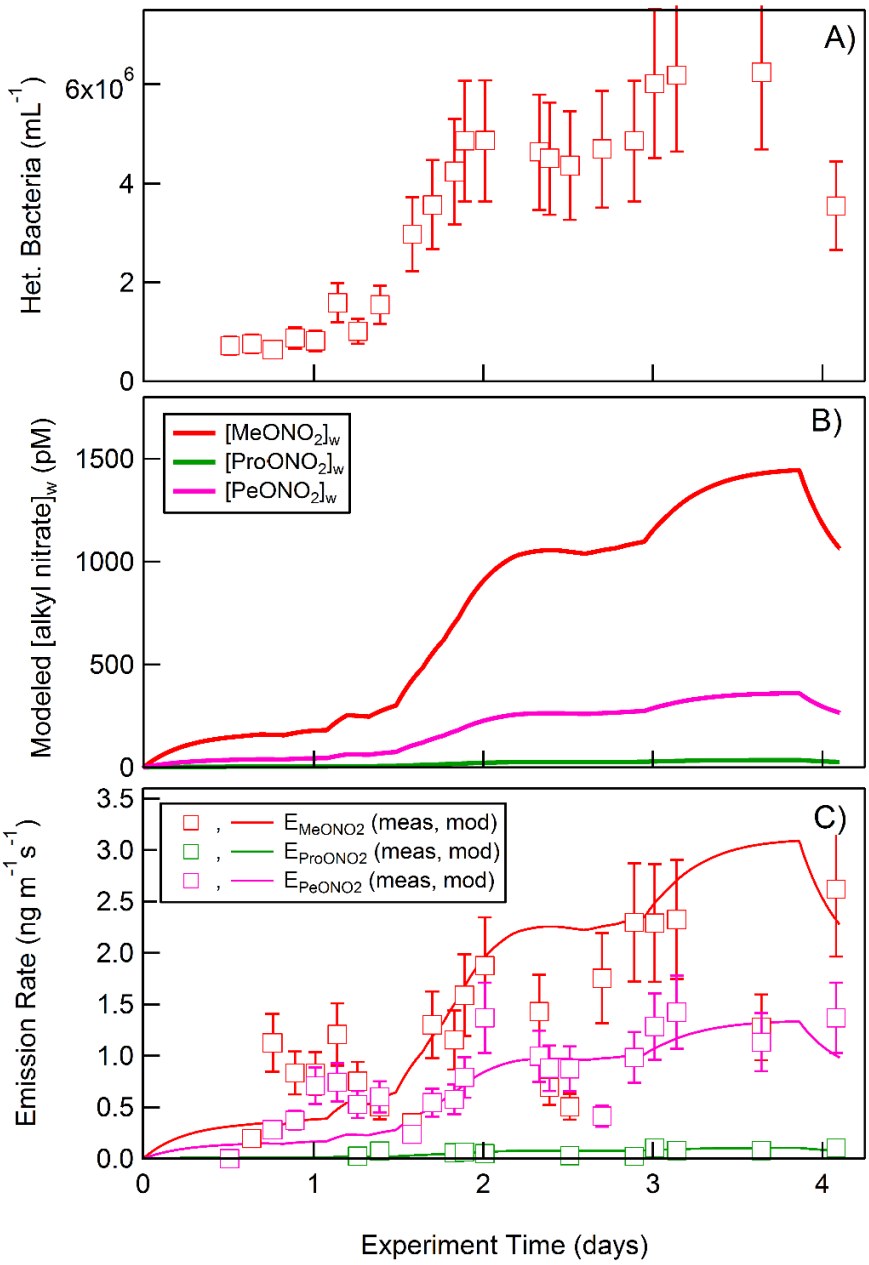


**Figure S4:** A) Measured heterotrophic bacteria concentration in the SIO wave channel during the 2011 intensive measurement campaign. B) Modelled waterside $MeONO_2$ (red), $ProONO_2$ (green), and $PeONO_2$ (pink) concentrations. C) Modelled emission rate of $MeONO_2$ (red lines), $ProONO_2$ (green lines), and $PeONO_2$ (pink lines) from equation E1, assuming a transfer velocity ($k_w$ = 10 cm $hr^{-1}$). Emission rates calculated from concentration measurements of $MeONO_2$, $ProONO_2$, and $PeONO_2$ using equation E2 are shown in black and blue squares, respectively.

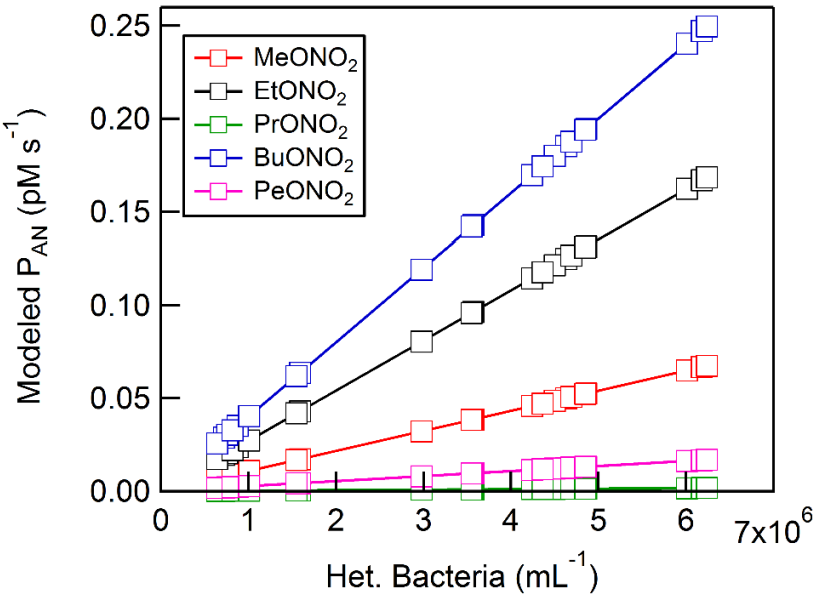


**Figure S5:** Relationship between heterotrophic bacteria concentration and waterside $RONO_2$ production rate (pM $s^{-1}$) used in the model to match the observed $RONO_2$ emission rates. The slope of each line is the per cell alkyl nitrate production rate (molecules $s^{-1}$ $cell^{-1}$), corresponding to 6.5, 16.3, 0.17, 24.1, and 1.63 for $C_1$ to $C_5$ $RONO_2$ respectively.

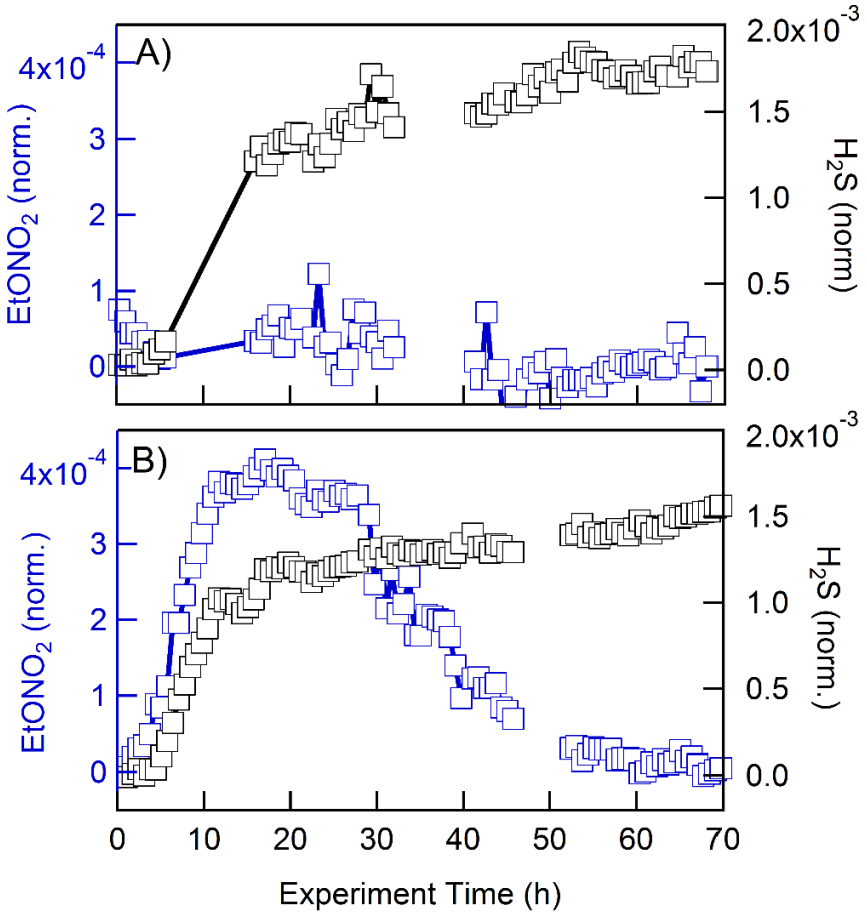


**Figure S6:** Time evolution of $EtONO_2$ and hydrogen sulphide ($H_2S$) over the course of the controlled flask experiment where the heterotrophic bacteria *Alteromonas* sp. AltSIO and ZoBell growth media was added to sterile seawater (A) and ambient seawater collected from surface waters at the end of the SIO pier. The $EtONO_2$ and $H_2S$ signal intensities have been baseline corrected and normalized to the reagent count rate.

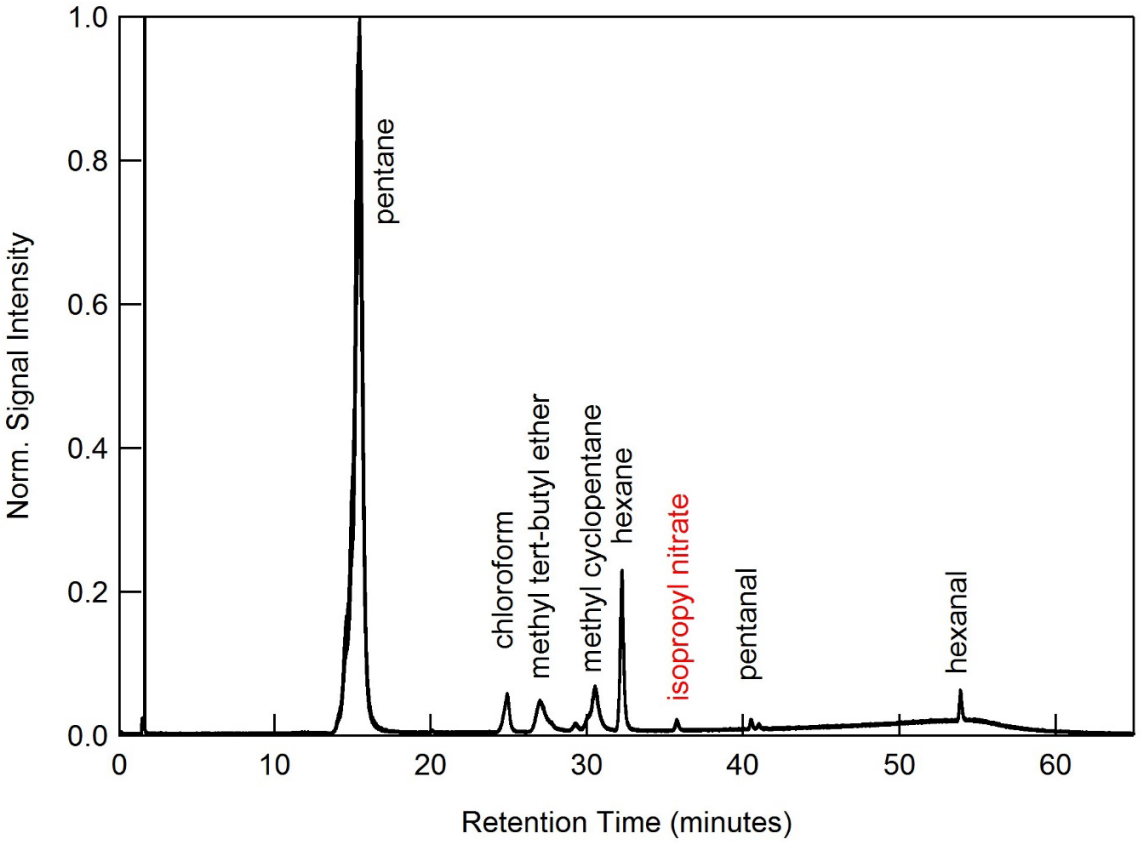


**Figure S7:** Chromatograph from GC/MS for a select unfiltered seawater sample, doped with ZoBell media. This specific sample shows the presence of isopropyl nitrate, alongside a host of other small organic molecules.

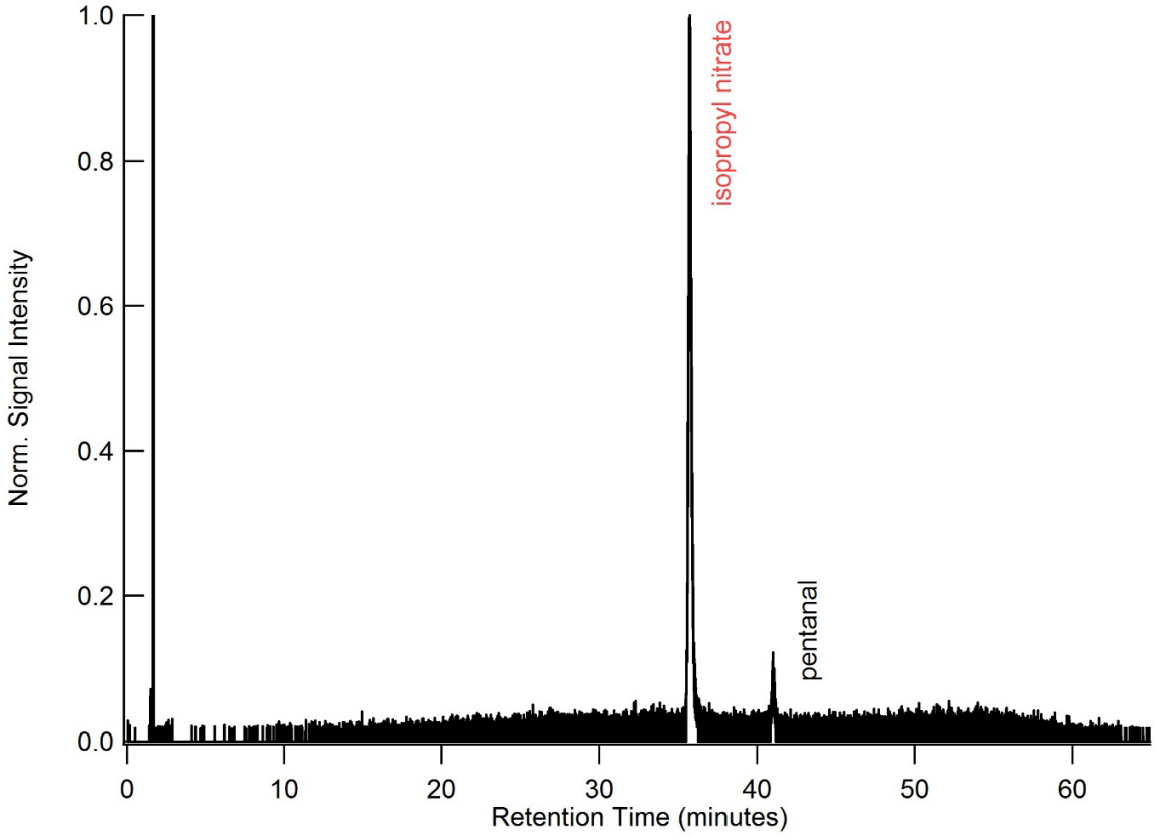


**Figure S8:** Background subtracted selected ion chromatograph from GC/MS for the same sample as Fig. S7, highlighting the enhancement of isopropyl nitrate above a control chromatogram.

**Acknowledgements.**

Chapter 2, in full, is a reprint of material as it appears: M. J. Kim, J. M. Michaud, R. Williams, B. P. Sherwood, R. Pomeroy, F. Azam, M. D. Burkart, and T. H. Bertram. "Bacteria-driven production of alkyl nitrates in seawater." *Geophys Res Lett* (2015), *42*, 597–604. The dissertation author is a contributing author of this manuscript. The dissertation author assisted in experimental design, cultured bacteria, prepared and sampled experiments, and performed growth measurements.

# Chapter 3. Enzymatic processing by lipase in seawater determines sea spray aerosol composition

## Section 3.1 Introduction

The composition of seawater is controlled by enzymatic processes described by the microbial loop[1–4]. As sea spray aerosol (SSA) is derived from seawater, its composition is dependent upon the chemical makeup of its source water. However, the link between enzymatic activity in seawater and the composition of SSA has not been examined. Because the ocean provides a significant proportion of atmospheric aerosols[5–7] and the composition of SSA determines its atmospheric properties, understanding significant processes that affect chemical makeup and atmospheric properties is crucial. Unraveling the chemical complexity of both SSA and seawater for accurate predictions of SSA properties and their effects on climate-influencing properties such as cloud condensation and ice nucleation is the aim of numerous studies.

Marine bacteria cannot utilize macromolecules or detritus larger than 600 Da as they are not able to cross bacterial membranes[8]. To break molecules and cells down, bacteria use extracellular enzymes to digest them into small molecules able to pass into bacterial cells[4,8]. By virtue of these processes, bacteria are responsible for the carbon recycling and degradation of decaying organisms particularly relevant in the processing of phytoplankton blooms[9,10]. The specific contribution of microbial processing to biogeochemical cycles and atmospheric

carbon are not well understood[11,12]. However, biomolecules prevalent in phytoplankton and bacteria are often used as model molecules in atmospheric and biogeochemical studies. As enzymatic activity is a dominant process and bacteria possess diverse enzymes of variable activity[9,13–15], the alterations to biomolecules by extracellular enzymes in marine systems need to be both considered and determined.

A previous study of nutrient-stimulated phytoplankton blooms correlated a loss in submicron SSA organic enrichment to increased seawater lipase activity and heterotrophic bacterial concentrations[16]. Lipase activity has also been correlated to increases in marine dissolved organic carbon[17]. To examine if lipase activity would directly influence SSA composition, we sought to examine resulting changes to SSA composition with lipase treatment in simplified laboratory-scale seawater systems. The miniature marine aerosol reference tank (miniMART), a small volume apparatus that produces SSA in ocean-relevant size distributions[18], was selected for controlled studies of lipase treatment of simple substrates. The substrates triolein and diatom lysate were treated with lipase and SSA composition was determined by high-resolution mass spectrometry (HRMS) and aerosol time-of-flight mass spectrometry (ATOFMS).

## Section 3.2 Results and Discussion

*Lipase processing of triolein*

Triolein is a triacylglycerol with three oleic acids (C18:1) attached to a glycerol backbone. It is selected as a model lipid in these studies due to its similarity to fatty acid-based lipids including triacylglycerols, phospholipids, wax esters, and glycolipids which are commonly found in marine ecosystems. These lipids are predominantly appended with combinations of C16:0, C16:1, C18:0, and C18:1 fatty acids[19–21]. The expected processing of triolein to diolein and monolein is shown in Figure 3.1a. Due to its bacterial origin and validation against triolein, lipase from *Pseudomonas cepacia* (MilliporeSigma 62309) was selected. The experimental set-up is shown in Figure 3.2b-c. For online measurements, nascent SSA is dried and split for particle counts by a scanning mobility particles sizer (SMPS) and aerodynamic particle sizer (APS). Single particle composition was measured using ATOFMS. Additionally, primary SSA generated from the miniMART was directed onto two separate PTFE filters collecting either the entire aerosol size range (supermicron mass dominated) or submicron aerosol size fraction for subsequent offline HRMS analysis. Enzymatic activity was tracked using a fluorogenic substrate assay (see methods).

Seawater was used to establish a baseline for measurements; then triolein was added and measured. This was followed by the addition of 70 U of lipase (end concentration 0.01 U $mL^{-1}$) for additional composition measurement. The activity of the lipase in this seawater system was confirmed and max turnover of

a oleate-fluorophore substrate determined to be between 2 - 27 μM $hr^{-1}$ (Figure S3.1). Expected products of triolein, diolein, and monolein, as well as a variety of molecules expected from the fragmentation and oxidation of these products were observed by HRMS (Section 2.5, Figures S3.2-3.3).

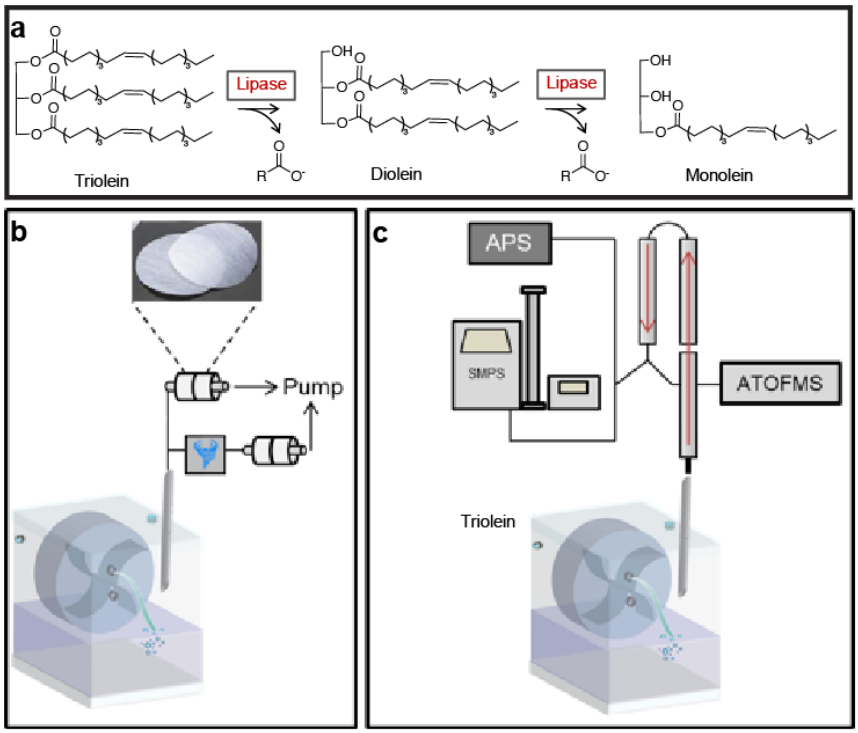


Figure 3.1 (a) Enzymatic processing of triolein by lipase. (b, c) Offline and online SSA measurement methods utilizing a miniMART system. (b) PTFE filter collection for offline HRMS analysis of entire size distribution and submicron SSA using an aerosol cyclone, and (c) online measurements of composition by ATOFMS: aerosol time-of-flight mass spectrometer, and particle counts by SMPS: scanning mobility particle sizer and APS: aerodynamic particle sizer.

*Triolein and lipase-treated triolein effects on SSA*

Ratios of diolein to triolein and monolein to triolein are shown in Figure 3.2. Addition of triolein to the Mini-MART tank resulted in particles in both size ranges containing triolein in excess ratios to the enzymatic products. After lipase addition,

the ion current ratio of triolein digestion products, diolein and monolein, decreased to ~1 in the supermicron particles (Figure 3.2a), but not in the submicron particles (Figure 3.2b). The ion intensities of diolein and monolein, obtained from integrated peak areas, were compared to the intensity of triolein in each filter sample obtained for both the full size distribution and submicron SSA filter samples. Prior to lipase treatment, both the ratios of diolein to triolein and monolein to triolein are dominated by the intensity of triolein. This result indicates that the majority of the triolein did not undergo significant autohydrolysis in the miniMART system before lipase was added. Following the addition of the enzyme, it is evident that the diolein:triolein and monolein:triolein ratios significantly increase, caused by the digestion of triolein and the transfer of enzyme products to the aerosol phase in the supermicron mass dominated regime of the full size distribution. In the submicron filter samples (Figure 3.2b), the ratios of enzyme products to substrate did not show a notable change after addition of lipase. We hypothesize that this effect could be caused by the increased solubility of diolein and monolein versus triolein, which would result in a seawater interface composed of primarily triolein with the digestion products more soluble in the bulk. In Cochran et al., the selectivity of organic molecules for the aerosol phase in submicron film drops was shown to be related to alkanoic acid chain length and their solubility in the bulk phase, with more insoluble material showing higher enrichment factors in the aerosol phase[22]. This effect could also be occurring in

the triolein system, with differences in solubility between triolein, diolein, and monolein mediating their transfer to the aerosol phase in a size selective manner.

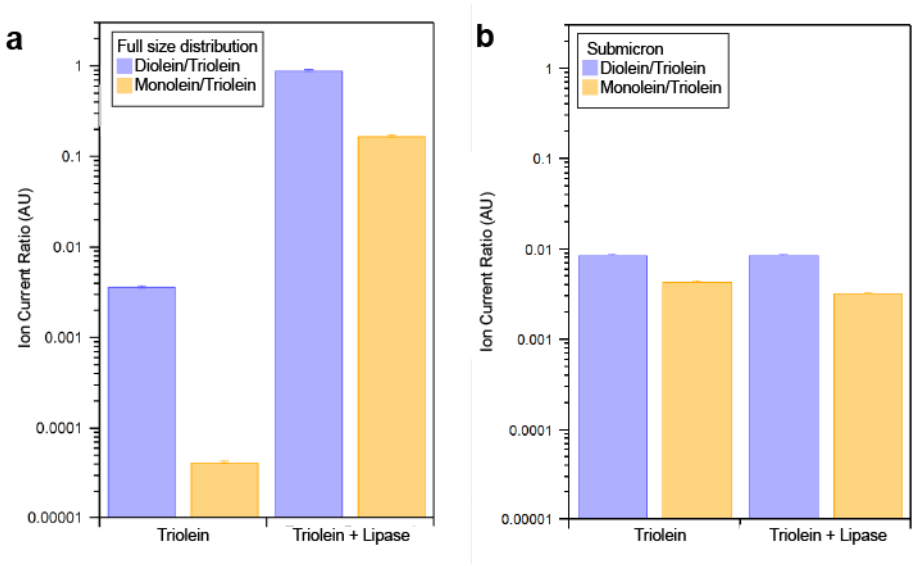


Figure 3.2 Changes in SSA speciation in (a) full size distribution (supermicron mass dominated) and (b) <1 μm size fraction by HRMS.

ATOFMS analysis was performed to determine size-resolved single particle chemical composition of aerosols of aerodynamic size range of 0.3 to 3.0 μm over the course of sequential additions of triolein and lipase to seawater (Figure 3.3). The change in the proportions of particle types showed remarkable change over the course of the experiment. Representative ATOFMS spectra is shown in Figure S3.4a. As triolein was added, significant fraction of Organic Carbon (OC) particle type increased, and as the lipase enzyme was added, the OC fraction decreased, with increase in fractions of Sea Salt mixed with Organic Carbon (SSOC) that showed dominant markers of magnesium and calcium. In addition, after 2 days after the addition of lipase, the particle type proportions returned to

the state observed in the Filtered Autoclaved SeaWater (FASW) control, illustrating the significant role lipase plays in influencing the chemical composition of the observable particles. Lipase treatment liberates oleate which we propose is then able to coordinate with $Mg^{2+}$ and $Ca^{2+}$ ions altering solubility, surface properties, and aerosolization.

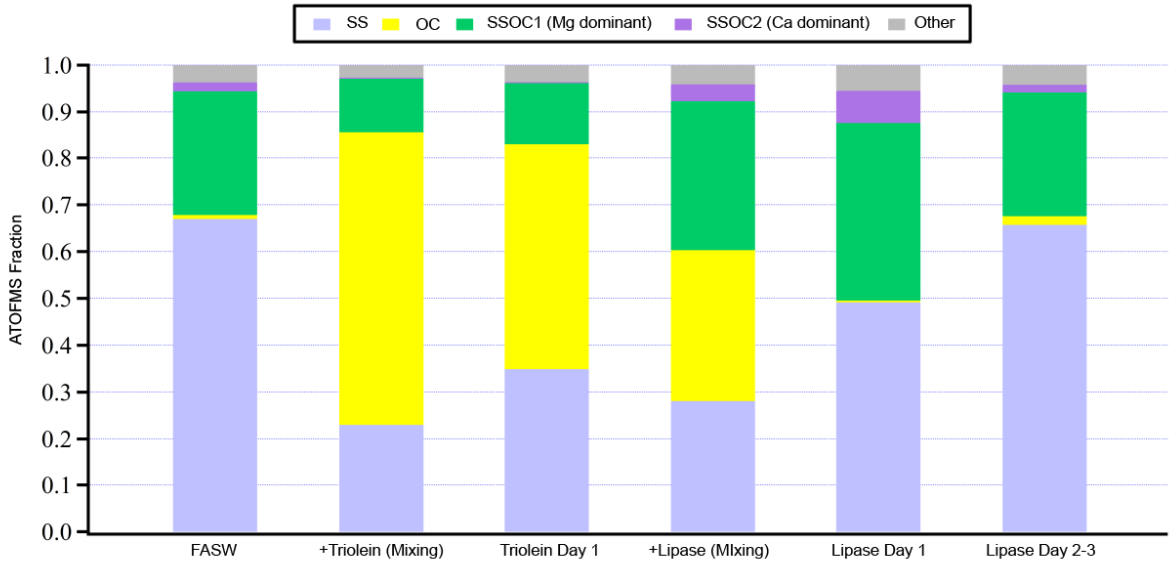


Figure 3.3 Evolution of SSA composition upon sequential addition of triolein and lipase to seawater (FASW: filtered autoclaved seawater). Mixing indicates first hour post-addition.

To further examine the role of calcium in the observed changes, the intensity of calcium($^{40}Ca^{+}$) signals relative to carbon marker ($^{37}C_3H^{+}$ and $^{43}C_3H_7^{+}$) signals were compared across the sequential additions (Figure 3.4). The intensity of the calcium signal does not vary relative to the carbon markers in baseline seawater or triolein treated water, but calcium increases significantly relative to both $^{37}C_3H^{+}$ and $^{43}C_3H_7^{+}$ upon lipase treatment demonstrating an emerging enrichment of organic particles containing calcium. The enhancement of

calcium and magnesium are similar to published observations of preferential binding of $Ca^{2+}$ and then $Mg^{2+}$ to lipids and salt-influenced deprotonation of phosphaditic acid monolayers at the sea interface[23–25]. Thus, findings from these studies can be used to explain the single particle observations in this study, where freed oleic acid from triolein is likely being deprotonated to oleate to bond with calcium and produce population of SSA containing both organic and calcium ion markers. These enzyme driven alterations to SSA can have profound implications for surface-sensitive processes such as heterogeneous chemistry[26,27], and ability to form cloud droplets[28].

*Lipase processing of diatom lysate*

To assess whether seawater lipase processing would have similar effects in a more complex and biologically relevant system we sought to mimic the peak of a phytoplankton bloom at the point when phytoplankton death prompts bacterial-mediated degradation. *Thalassiosira pseudonana,* a marine, centric diatom, was selected as it is well-characterized and has a rich lipid and fatty acid composition[29], and diatoms are prominent in phytoplankton blooms[30]. Cultured cells were collected and lysed to initiate cell death; this lysate was added to the miniMART system. After baseline and lysate only measurements were collected lipase was added to the mixture (0.01 U $mL^{-1}$).

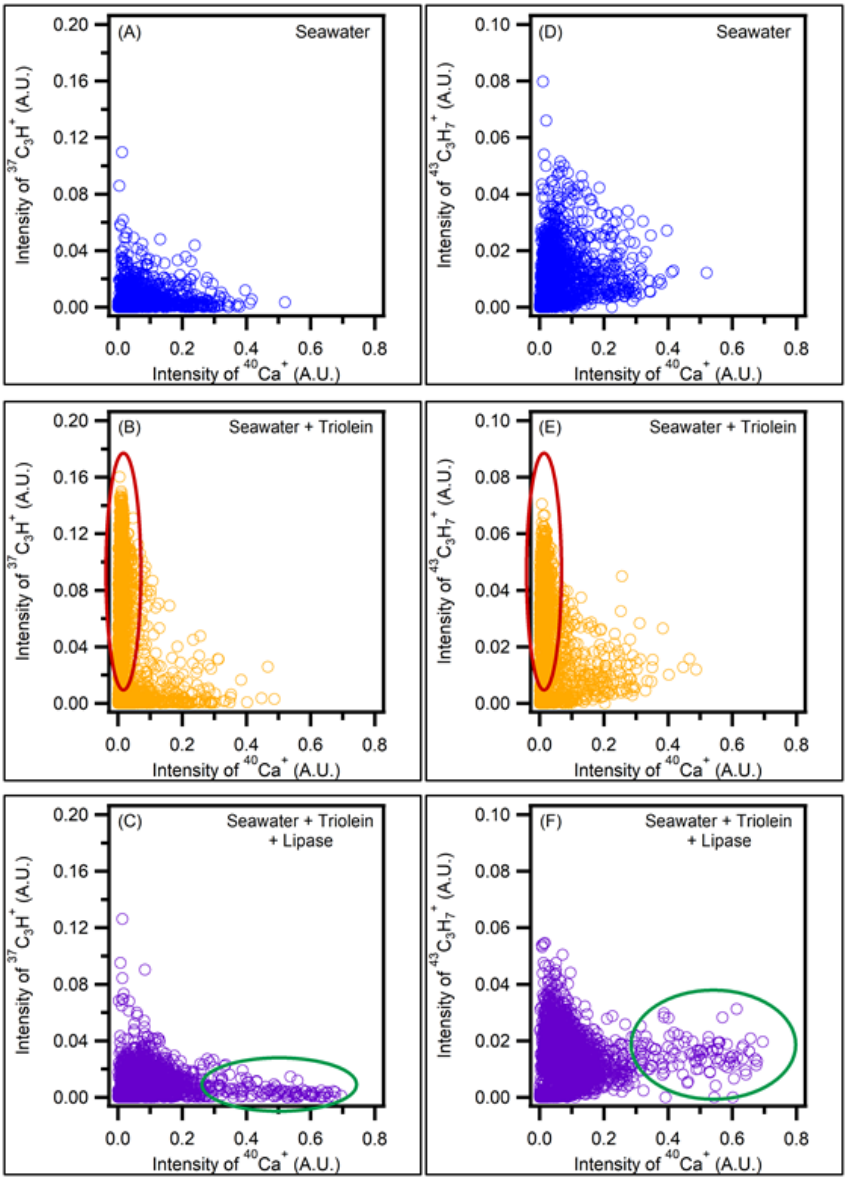


Figure 3.4 Intensity of $^{37}C_3H^+$ and $^{43}C_3H_7^+$ vs Intensity of $^{40}Ca^+$ plots for seawater background (a, d), seawater + triolein (b, e), and seawater + triolein + lipase (c, f), respectively, by ATOFMS. Red circles highlight the organic enriched SSA due from triolein addition. Green circles highlight the emergence of particles with organic enriched, high intensity of $^{40}Ca^+$ containing particles from the lipase cleavage of triolein.

Post addition of lysate to the system, seawater was tested for protease, lipase, phosphatase, and β-glucosidase activities (Figure S3.1b). The lysate had detectable, endogenous activity that could contribute to diatom self-degradation. Protease activity was detected in the range of 14 – 438 nM $hr^{-1}$;

lipase activity was not detected(ND) to 500 nM $hr^{-1}$. Phosphatase and β-glucosidase activities were also detected at ND to 350 nM $hr^{-1}$ and ND to 35 nM $hr^{-1}$ respectively. The addition of lipase solution to the system generally caused a ten-fold or greater increase in lipase activity and modest increases in the other enzyme activities, presumably from contaminants in the lipase or from increased availability of substrates. Lipase activity in the lysate varied but was seemingly sufficiently low to allow for discernable differences from lipase treatment.

HRMS of pure diatom lysate was performed as the concentration of lysate collected on aerosol filters was found to be near or below the dynamic range of the HRMS system. Cellular lysate was found to be composed of a wide variety of triglycerides and fatty acids, with the most instrument intensity originating from several unsaturated palmitic acids (16:0-16:4) and tripalmitate species (Figure 3.5, S3.5). These results are in general agreement with lipid speciation of *T. pseudonana* in other studies[31,32]. To better understand the change in lipid composition of the cellular lysate after the addition of lipase, the following calculation was performed to normalize the intensity of negative-mode palmitic acids to the intensity of the tripalmitate ions observed in the same sample in positive mode.

$$Normalized\ Fatty\ Acid\ Intensity = \frac{Individual\ Palmitic\ Acid\ Intensity}{Summed\ Tripalmitate\ Species\ Intensity} \quad \text{(Eq. 1)}$$

Figure 3.5 shows the results of this calculation for analyzed samples of diatom lysate before and after addition of lipase. Notably, the ratio of fatty acid intensity significantly increases for all the fatty acids after the addition of lipase.

This result informs the analysis of SSA produced from the mini-MART containing cellular lysate pre- and post-digestion by lipase, confirming the likely transfer of lipase-generated fatty acids to the aerosol phase. The processing by the enzyme also correspondingly significantly decreases the amount of triacylglycerols present (Figure S3.5b).

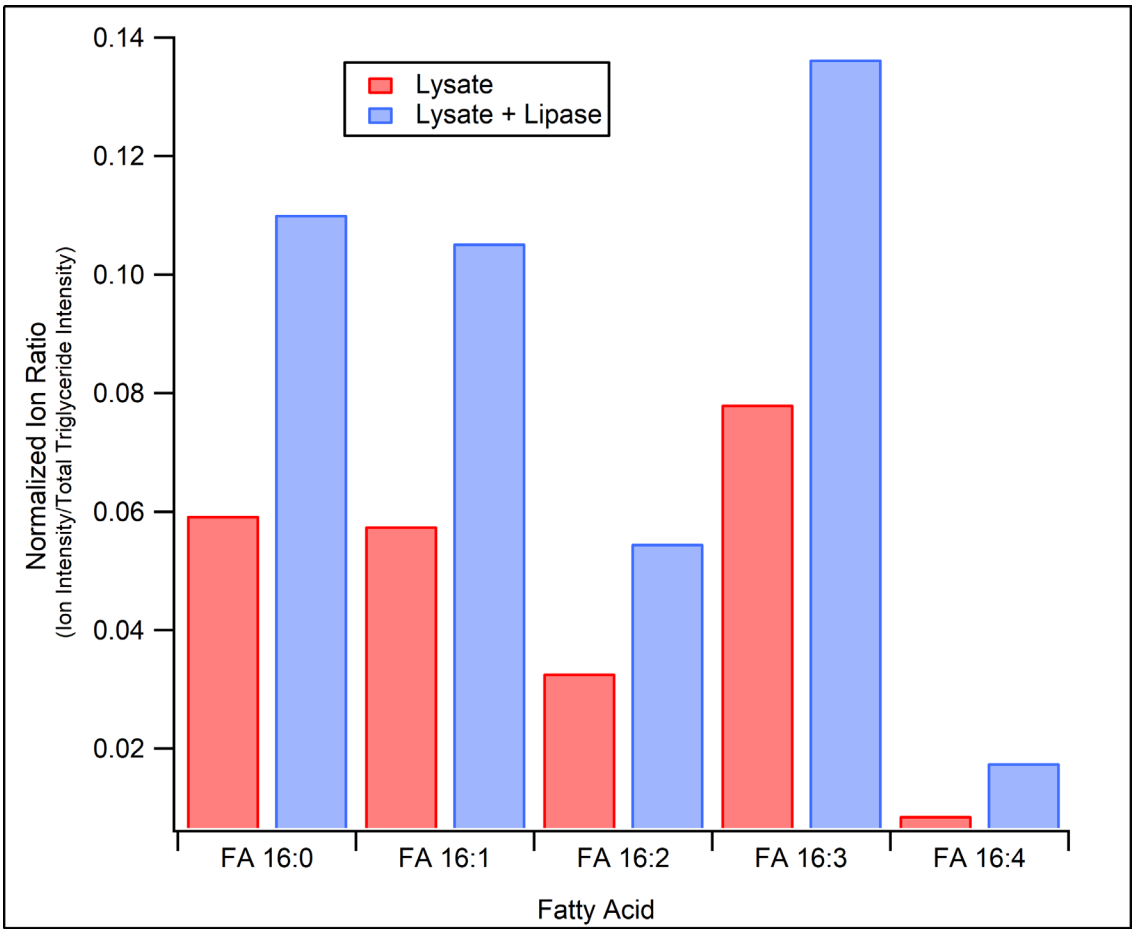


Figure 3.5 Normalized ion ratios for fatty acids identified in diatom lysate prior to and after lipase addition by HRMS.

*Diatom lysate and lipase-treated lysate effects on SSA*

The ATOFMS results from the lysate is shown in Figure 3.6 and demonstrated very similar patterns to the triolein experiment. Representative ATOFMS spectra is shown in Figure S3.4b. Diatom lysate added to synthetic seawater (reef salt) resulted in a drastic increase in organic particles associated with iron and phosphate markers (FePhosOrg). The association of phosphate and iron is likely due to phospholipids arising from cell membranes and iron containing ferroproteins[33]. Upon lipase treatment, this organic fraction is drastically diminished, again returning to a baseline seawater state and demonstrating replacement with a salt containing organic fraction.

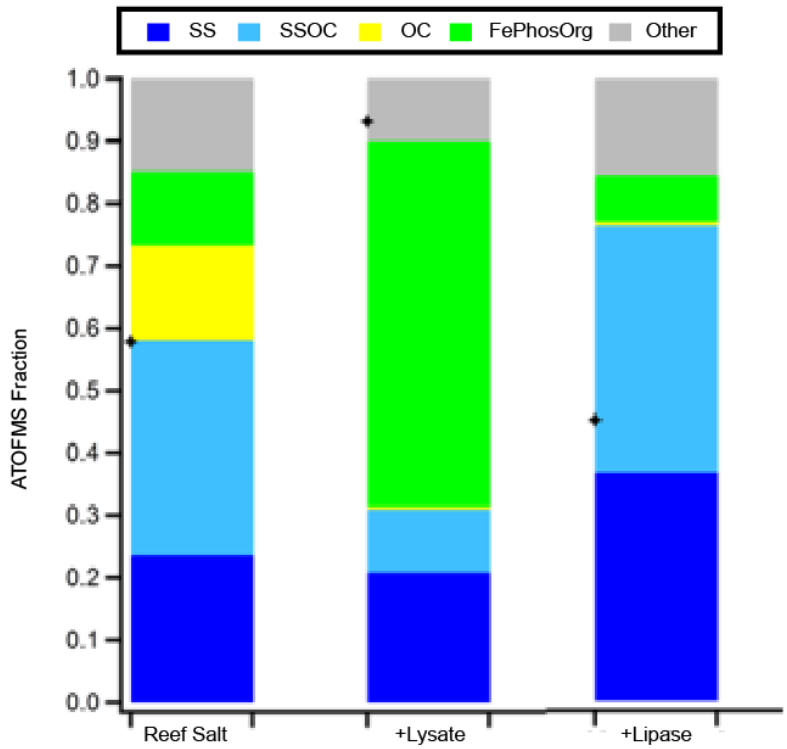


Figure 3.6 Evolution of SSA composition upon sequential addition of *T. pseudonana* (diatom) lysate and lipase to seawater.

**Section 3.3 Conclusions**

The results of these studies demonstrate that lipase activity significantly alters the composition of lipid-based SSA in the model systems tested. In the case of triolein, lipase treatment decreases the amount of carbon-rich SSA particles to be more salt ($Mg^{2+}$, $Ca^{2+}$) associated and for total composition to return to a baseline-like state. The addition of lysate generates organic SSA particles with a high content of iron and phosphate that with lipase treatment again return to a more baseline state.

A phytoplankton bloom often is initiated by an influx of nutrients such as nitrate and phosphate that stimulate the growth of photoautotrophs but not heterotrophs. Wang et al. found a phytoplankton peak with low bacteria counts and low lipase activity had organic SSA enrichment and a second phytoplankton peak with high bacterial counts and high lipase activity connected to the loss of the organic SSA enrichment[16]. In marine ecosystems bacterial extracellular enzymes are responsible for carbon degration[9,14] and here, lipase activity was low in untreated lysate, emphasizing the importance of bacteria in lipid processing. Putting these results together suggests that bacteria-poor, lipid-rich oceans will generate highly organic submicron particles, and regions with high bacteria and lipid concentrations will give rise to saltier, much less-organic enriched particles. Lipase processing will also generally solubilize fatty acid based lipids and attenuate their transfer to SSA. This could be a phenomenon especially relevant in area of differing microbial communities with different enzymatic capacities[34].

These results also imply that phytoplankton blooms can have very immediate and rapid changes on the composition of SSA during different stages of a bloom dependent upon bacterial communities present. This could correspond to sudden and drastic changes to atmospheric properties and air quality. These findings warrant the opening of new avenues of research into the specific enzymes and enzyme activities common to specific marine ecosystems to better understand the extent and kinetics of hydrolysis of common metabolites. Additionally, atmospheric SSA studies that use intact biomolecules as model substrates should also consider the effects enzymatic processing in their selection of model substrates.

**Section 3.4 Methods**

*Experimental setup and sequential addition of reagents*

A miniature Marine Aerosol Reference Tank (miniMART) was utilized throughout this study as the SSA generation method. Details of operating principle can be found elsewhere[18], but in brief, the tank utilizes a rotating water wheel to intermittently produce a plunging waterfall into an approximately 7 L reservoir that mimics the bubble size distribution of breaking waves[18,35]. Mimicking the bubble size distribution replicates the size and physicochemical composition of the produced SSA[36,37]. The smaller reservoir of the miniMART allows better control of the reagent amounts. The headspace of the miniMART was purged using particle free air (Sabio Instruments, Model 1001) at always 1 standard liters per

minute (SLPM) greater than the sampling flow rate of the instruments and apparatus. This overflow of 1 SLPM ensured positive pressurization of the headspace, preventing any accidental back-sampling of room air. Under normal operation conditions, the headspace had relative humidity (RH) of > 90 % (Vaisala, HMP110).

Prior to beginning of the experiments, all surfaces, including the rotating wheel were cleaned using ethanol (90 % v/v) and rinsed with ultra-pure water. Seawater used in this study was obtained either through 1) filtering natural seawater collected at Scripps Pier (La Jolla, CA; 32° 52' 00'' N, 117° 15' 21'' W) using a 0.7 μm filter (Whatman GF/F Z242489) to remove most of the particulate organic matter (POM) then autoclaved (121 °C for 90 min), or 2) synthesizing artificial seawater by dissolving reef salt mix (Brightwell Aquatics, NēoMarine, 35.53 g $L^{-1}$) in ultra-pure water followed by autoclaving the seawater at 121 °C for 90 min). After baseline seawater measurements were taken (ATOFMS, particle counts, and HRMS, described below), 500 mg of triolein (MilliporeSigma T7140) was added and measurements were repeated. 70 U of lipase (end concentration 0.01 U $mL^{-1}$) (lipase from *Pseudomonas cepacia*, MilliporeSigma 62309) was then added and the measurements were again repeated. Experiments involving diatom lysate were conducted similarly. After baseline measurements of seawater, lysate was added and measured. Lipase was added (0.01 U $mL^{-1}$) and measurements were repeated.

*Filter collection for offline analysis*

MART generated SSA particles were collected onto 0.2 µm PTFE 47 mm filters (Whatmann) encased in aluminum or polypropylene filter cartridges. For each sampling period, 13 hours overnight, SSA were collected into two size fractions by splitting the air stream, the first stream consisting of the entire aerosol size distribution passed at 1.2 LPM through a filter. The second air stream, composed of aerosols < 1.0 µm aerodynamic diameter (Da), was facilitated by passing through a cyclone separator (BGI - SCC 0.695) at 1.2 LPM. After collection, filters were stored in muffled aluminum foil at -20 °C for later analysis. Filters were subsampled by using a clean razor blade to cut out ½ of the filter, with the residual half reserved for repeat analyses. Subsampled filters were extracted by sonication in 1 mL of $CHCl_3$ for 30 minutes, the liquid was moved to a separate vial, and extraction was repeated 2 more times. The final 3 mL of $CHCl_3$ was evaporated to dryness under a gentle stream of $N_2$. Extracted organics were redissolved in 1 mL of ACN and transferred to glass vials for LC/MS analysis. 1 mL liquid samples of diatom lysate were liquid-liquid extracted by 1 mL of $CHCl_3$ after 30 min sonication. The extraction was performed 3 times, with the extracted 3 mL of $CHCl_3$ evaporated to dryness under a gentle stream of $N_2$. Extracted organics were resuspended in 1 mL of ACN and transferred to glass vials. Standards of triolein, diolein, and monolein (Sigma Aldrich > 99%) were solubilized in ACN in combusted glass vials.

*Orbitrap Ultra High Resolution Mass Spectrometry (HRMS)*

Ten µL samples were injected onto a Thermo Scientific (Vanquish) ultra-high pressure liquid chromatograph utilizing a Accucore C18 3 x 50 cm 2.6 µm column on an empirically determined 22 min gradient elution with solvent A: Acetonitrile with 2.5 mM $NH_4Ac$, solvent B: Isopropanol with 2.5 mM $NH_4Ac$, solvent C: $H_2O$ with 2.5 mM $NH_4Ac$. Details on the gradient profile can be found in Table 3.1. Column eluent was passed into an electrospray ionization mass spectrometer (Orbitrap Elite); positive mode settings: Spray voltage 3.5 kV(+), 2.6V (-), ESI temperature 350C, mass range 100-1500 Da, Capillary Temperature 350C. Data files produced by the instrument were processed in the Thermo Excalibur data analysis software in which operations such as extracted ion chromatograms and background subtraction were evaluated.

Table 3.1 LC Gradient elution profile for Orbitrap HRMS for both positive and negative mode analysis of filter collected aerosols and bulk cellular lysate.

| Time (min) | % A | % B | % C |
|---|---|---|---|
| 0.00 | 10.0 | 0.0 | 90.0 |
| 2.50 | 10.0 | 0.0 | 90.0 |
| 4.00 | 50.0 | 50.0 | 0.0 |
| 7.50 | 50.0 | 50.0 | 0.0 |
| 10.00 | 0.0 | 100.0 | 0.0 |
| 14.00 | 0.0 | 100.0 | 0.0 |
| 15.00 | 50.0 | 50.0 | 0.0 |
| 17.00 | 50.0 | 50.0 | 0.0 |
| 18.00 | 10.0 | 0.0 | 90.0 |
| 22.00 | 10.0 | 0.0 | 90.0 |

*Total flow remained at 0.500 L/min for entirety of run

*Chemical composition of individual sea spray aerosols*

An aerosol time-of-flight mass spectrometer (ATOFMS) was used to better understand the chemical differences of individual SSA particles. ATOFMS provides real-time measurements of single particle size and chemical composition of aerosol particles between 0.3-3.5 μm vacuum aerodynamic diameter (Dva). Detailed instrument design and operating principle is previously reported[38,39]. In brief, aerosol particles dried using diffusion driers (RH < 10 %) and drawn into the nozzle inlet of the instrument and accelerated through two stages of differential pumping. During this process, each particle reaches its size-dependent terminal velocity, which is measured when the particle pass through two orthogonally positioned continuous wave solid-state lasers (diode-pumped Nd:YAG, 532 nm, 50 mW) set 6 cm apart. Dva of the particles are calculated using an external calibration curve generated using polystyrene latex spheres of known density and diameter. The velocity of the particles is then used to trigger the third laser (Quantel, pulsed Q-switched Nd:YAG, 266 nm, 8 ns pulse width, 700 μm spot size, 3 × 107 W $cm^{-2}$) that simultaneously desorb and ionize each particles. Produced positive and negative ions are simultaneously detected using a dual-polarity reflectron time-of-flight mass spectrometer with microchannel plate detectors (MCP, Photonis, 931377). Collected data were imported into MATLAB (The MathWorks, Inc.) with software toolkit FATES[40].

In addition to single particle chemical composition measurements, SSA number size distributions were monitored to track the changes over the course of the sequential addition experiment. The sample flow was split between the ATOFMS, aerodynamic particle sizer (APS, TSI Model 3321, sample flow rate of 1 SLPM) and scanning mobility particle sizer (SMPS, TSI Model 3080, sample/sheathe flow rate of 0.3/3.0 SLPM) (Figure 3.1c). APS and SMPS provided number size distribution of the SSA particles generated from the miniMART in the size ranges of approximately 0.5-20 μm aerodynamic diameter (Da) and 13-750 nm mobility diameter (Dm), respectively.

*Enzymatic activity assays*

To assess lipase, protease, phosphatase, or glucosidase enzymatic activity assays described by Hoppe were performed[41]. This methodology uses model substrates attached to a fluorophore: MUF (4-methylumbelliferone, MilliporeSigma M1381) or MCA (4-rnethylcoumarinyl-7-amide, MilliporeSigma A9891). Enzymatic activity is demonstrated by cleavage of the fluorophore from the attached substrate detectable by fluorescence at $\lambda_{ex}$ 360 nm / $\lambda_{em}$ 465 nm. An oleate substrate (MUF-oleate, MilliporeSigma 75164) is used to detect lipase activity. A glucose substrate (MUF-β-D-glucopyranoside, MilliporeSigma M3633) is used to detect β-glucosidase activity. A phosphate substrate (MUF-phosphate, MilliporeSigma M8883) is used to detect phosphatase activity. A leucine substrate (L-leucine-MCA, MilliporeSigma L2145) is used to detect protease activity.

*Preparation of diatom lysate*

Cultures of *T. pseudonana* were grown at 18 °C in artificial seawater medium[42] to late exponential phase, ~5 x $10^6$ cells / mL. Cells were harvested via centrifugation and filtration on 3 µm polycarbonate filters (Whatman Nucleopore®) to maximize cell recovery. Lysis was performed by triplicate passes through a French press at ~20,000 psi. Lysate is added directly to miniMART providing ~1 x $10^6$ lysed cells $mL^{-1}$.

**Section 3.5 Supplementary Information**

*HRMS analysis*

Figure S3.2 shows mass spectra, corresponding to aerosols collected after triolein addition and after lipase addition. In Figure S.2a, a mass spectrum of a full size distribution (predominantly superrmicron) SSA sample post triolein addition is dominated by the presence of intact triolein m/z 902.81 $(M+NH_4)^+$ as well as a small contribution from a fragment ion corresponding to loss of an oleic acid from triolein m/z 603.53 $(M-OA)^+$, diolein. Differentiation of ionization-induced fragmentation of triolein from enzymatic digestion of triolein was determined by retention time of the ion observed as well as complexation with ammonium present in the eluent. Diolein and monolein were both observed to elute at separate times in the chromatographic separation than triolein. These ions also appeared as ammonium adducts m/z 638.57 and m/z 374.32 when ionized by electrospray, but not when generated as fragments from triolein (Figure S3.2c). This was used to distinguish enzyme treated products from triolein fragments as shown in Figure 3.2. The HRMS results are in line with observations in the literature[43]. Figure S3.2c-d qualitatively illustrate the impact of lipase, showing an increase in diolein and monolein observed. Other ions, likely also products of digestion were present in the spectra and the structures of molecules detected are shown in Figure 3.3, however the masses of some of these ions do not match known fragmentation or degradation products of triolein.

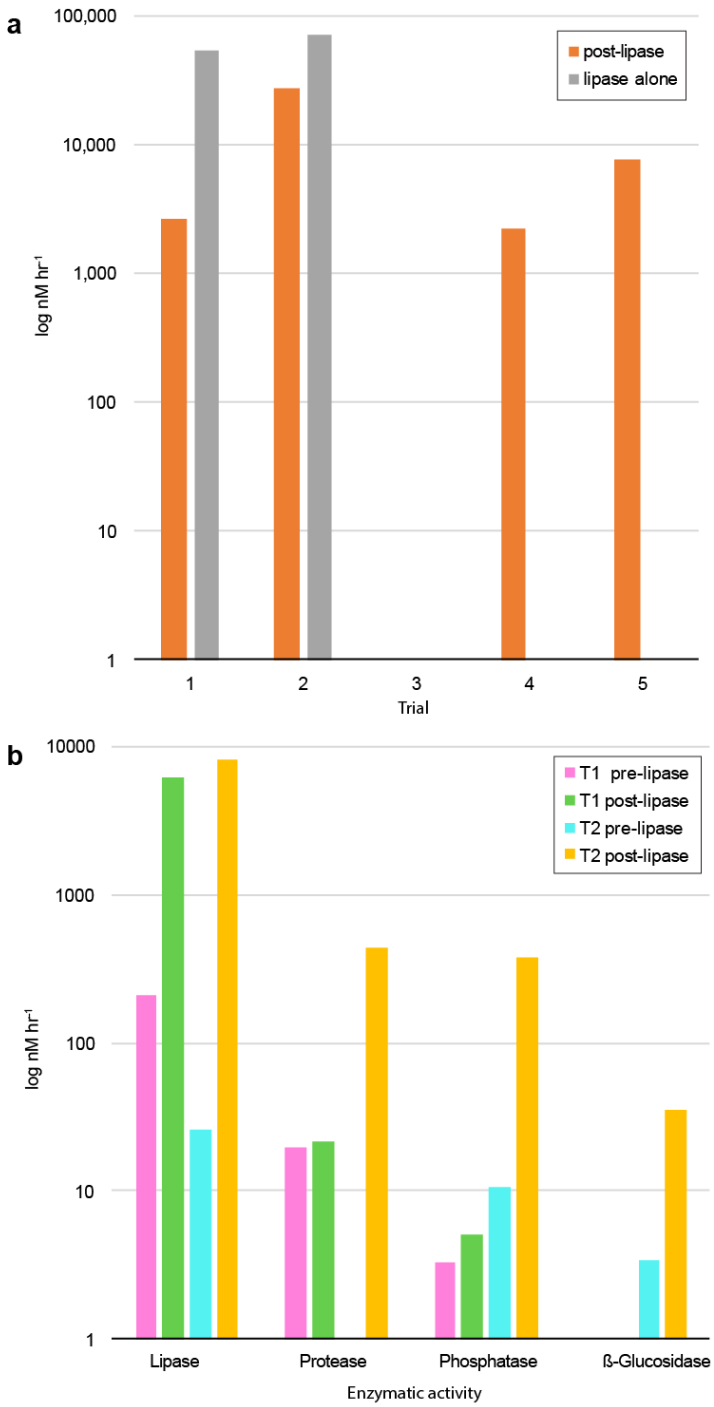


Figure S3.1 Results of enzyme assays across experiments. (a) Lipase activity by cleavage of MUF-oleate substrate across triolein runs. The activity post-lipase addition (orange) is shown and enzyme solution activity (gray) is shown for trials 1-3. Trial 3 utilized heat-killed enzyme sample and measurements verified a loss of activity. (b) Lipase (MUF-oleate), protease (MCA-Leucine), phosphatase (MUF-phosphate), and glucosidase (MUF glucose) activity are shown for *T. pseudonana* (diatom) lysate and lipase treated lysate in seawater studies. Two separate lysate experiment trials (T1, T2) are shown pre- and post- lipase addition.

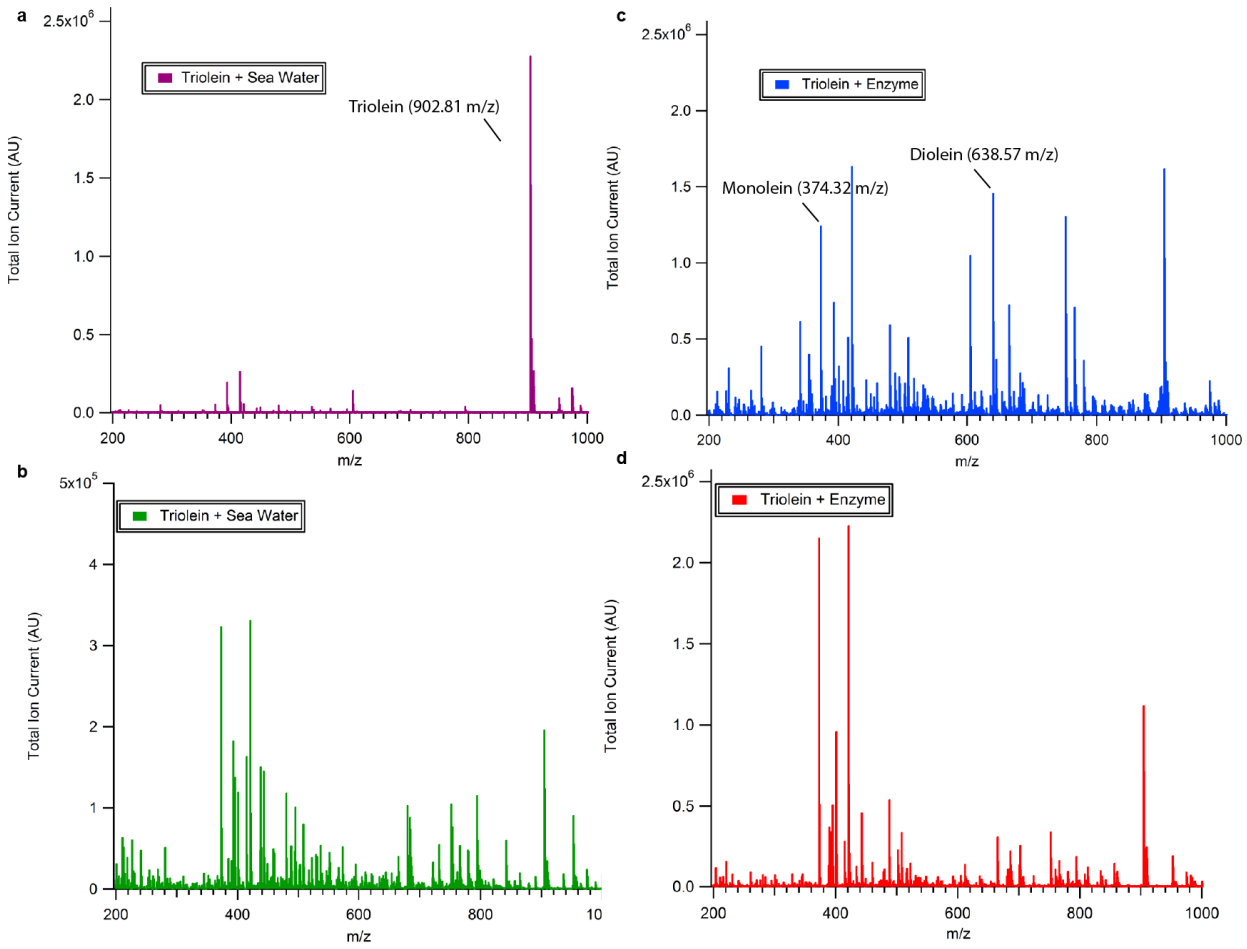


Figure S3.2 Representative HRMS spectra of SSA from triolein in seawater for full size distribution (a, c) and submicron particle sizes (b, d) for pre-lipase (a, b) and post- lipase (c, d) treatment.

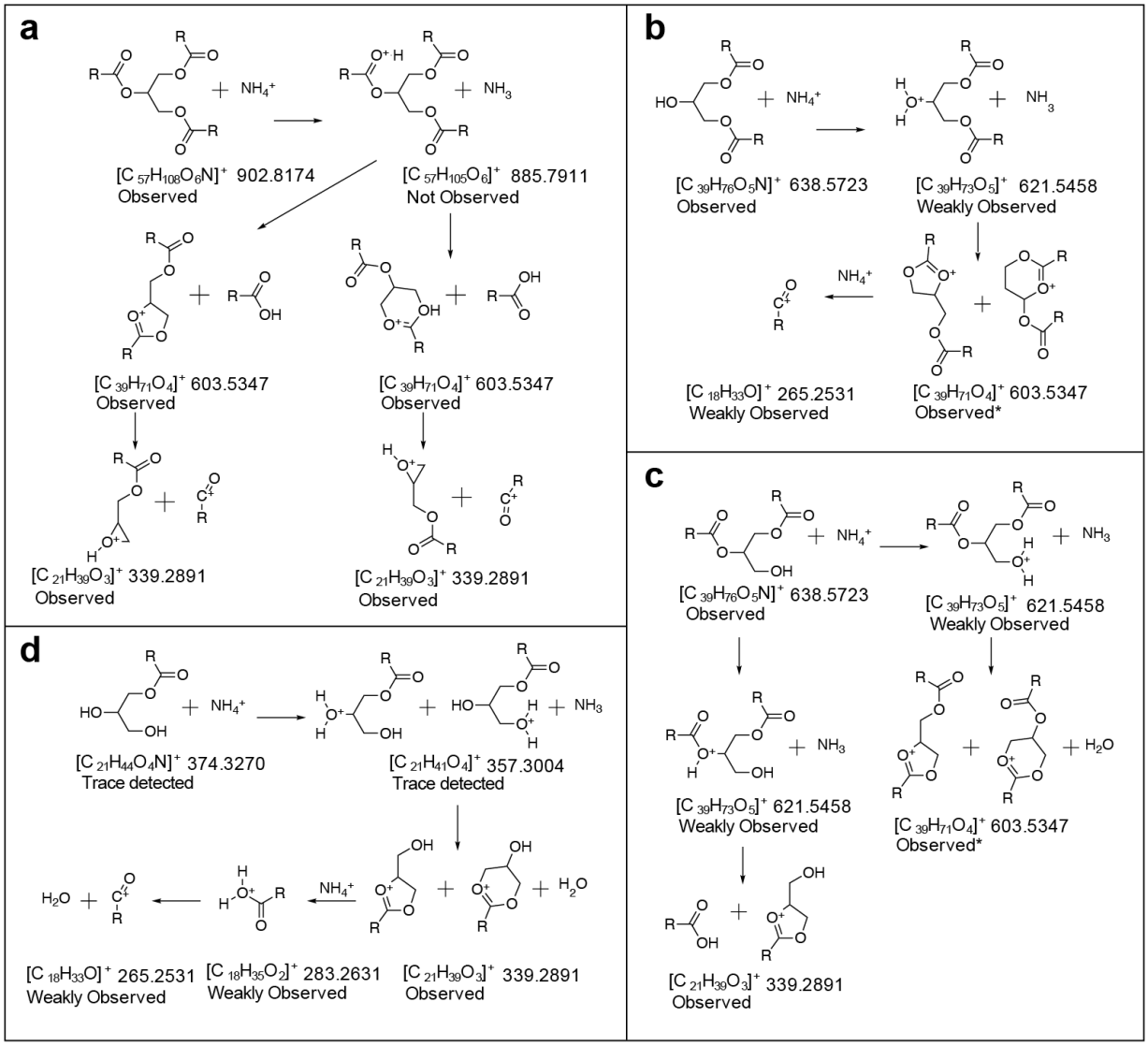


Figure S3.3 Fragmentation patterns and molecules detected by HRMS for triolein (a), diolein (b, c) and monolein (d). Fragmentation patterns are adapted from Kalo et al. 2006[43]. The molecular formula, mass (m/z), and whether it was detected by HRMS is indicated. *These fragments derived from diolein and were able to be separated from the similar products of triolein fragmentation due to different retention times.

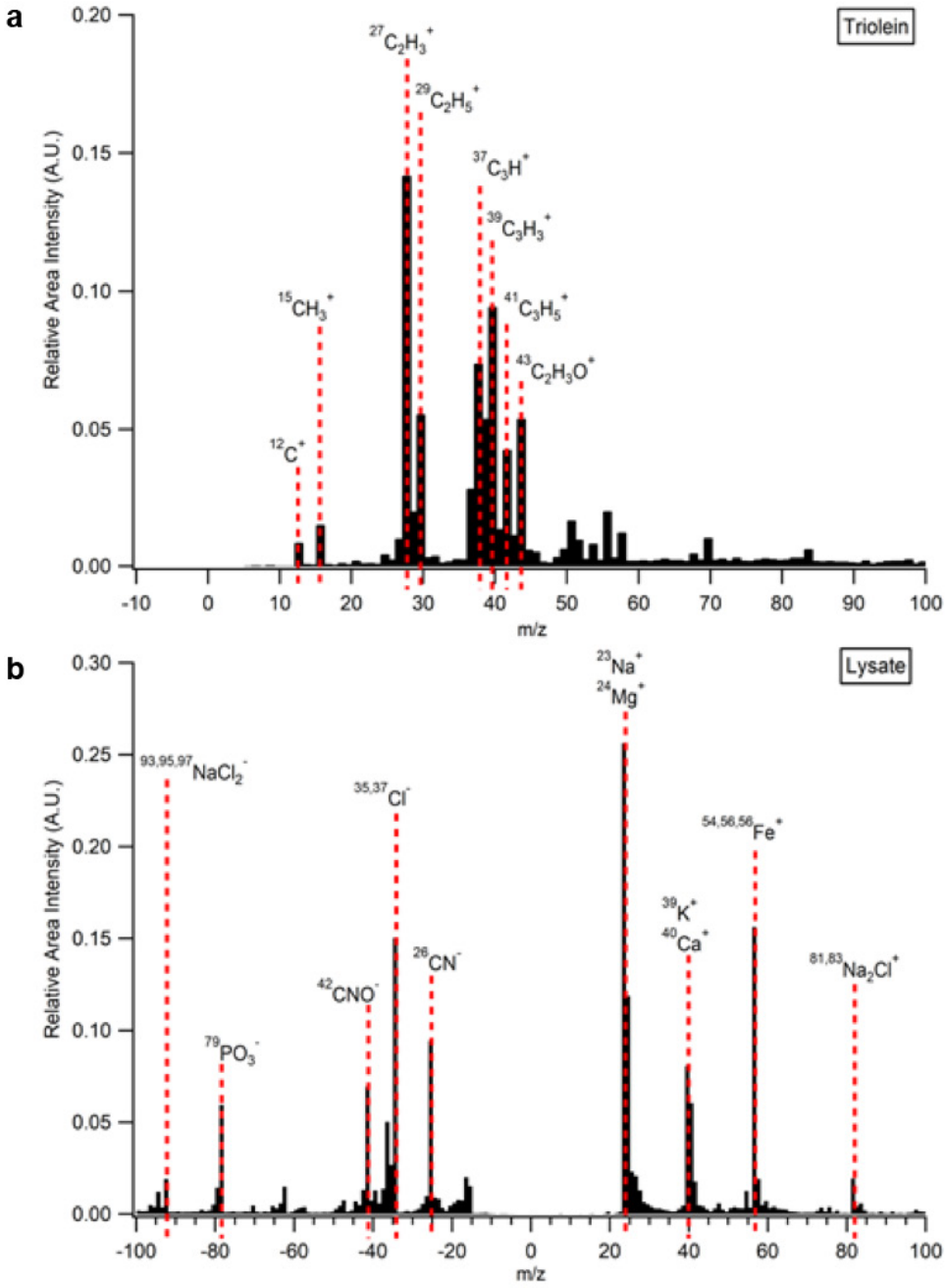


Figure S3.4 Averaged ATOFMS mass spectra of organic-enriched SSA upon triolein addition (a) and lysate (b).

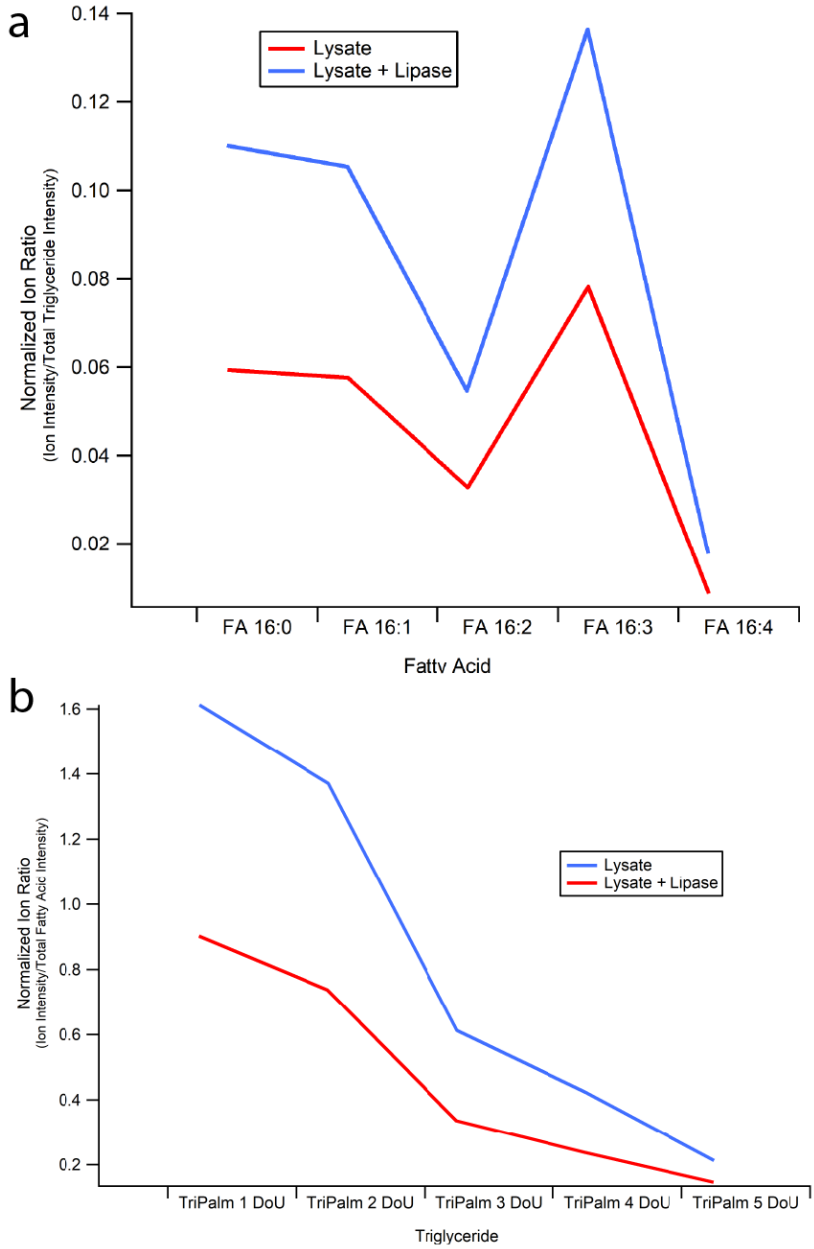


Figure S3.5 Normalized ion intensities for triglycerides and fatty acids for diatom lysate and lysate after lipase addition. Predominant fatty acid abundance (a) and triglycerides (b) are depicted. Tripalmitate and palmitic acid species are both separated by their degrees of unsaturation (DoU).

**Acknowledgements.**

Chapter 3, is material currently being prepared for submission: J.M. Michaud, O. S. Ryder, J. S. Sauer, C. Lee, M. D. Burkart, K. A. Prather. "Enzymatic

processing by lipase in seawater determines sea spray aerosol composition". The dissertation author, O. S. Ryder, J. S. Sauer, and C. Lee are co-primary authors of the work under the supervision of M. D. Burkart and K. A. Prather. The dissertation author devised original concept of experiments, performed bulk sampling and system maintenance, conducted enzymatic assays, and prepared diatom lysate. The dissertation author wrote the chapter with contributions from co-primary authors.

**Section 3.6 References**


1. Azam, F., Fenchel, T., Field, J. G., Gray, J. S., Meyer-Reil, L. A. & Thingstad, F. The Ecological Role of Water-Column Microbes in the Sea. *Mar. Ecol. Prog. Ser.* **10,** 257–263 (1983).

2. Pomeroy, L. R., Williams, P. J., Azam, F. & Hobbie, J. E. The Microbial Loop. *Oceanography* **20,** 28–33 (2007).

3. Fenchel, T. The microbial loop - 25 years later. *J. Exp. Mar. Bio. Ecol.* **366,** 99–103 (2008).

4. Arnosti, C. Microbial extracellular enzymes and the marine carbon cycle. *Ann. Rev. Mar. Sci.* **3,** 401–425 (2011).

5. de Leeuw, G., Andreas, E. L., Anguelova, M. D., Fairall, C. W., Ernie, R., Dowd, C. O., Schulz, M. & Schwartz, S. E. Production Flux of Sea-Spray Aerosol. **80,** 1–39 (2011).

6. Liu, X., Penner, J. E., Das, B., Bergmann, D., Rodriguez, J. M., Strahan, S., Wang, M. & Feng, Y. Uncertainties in global aerosol simulations: Assessment using three meteorological data sets. *J. Geophys. Res. Atmos.* **112,** 1–41 (2007).

7. Struthers, H., Ekman, A. M. L., Glantz, P., Iversen, T., Kirkevåg, A., Seland, O., Mårtensson, E. M., Noone, K. & Nilsson, E. D. Climate-induced changes in sea salt aerosol number emissions: 1870 to 2100. *J. Geophys. Res. Atmos.* **118,** 670–682 (2013).

8. Weiss, M. S., Abele, U., Weckesser, J., Welte, W., Schiltz, E. & Schulz, G. E. Molecular architecture and electrostatic properties of a bacterial porin. *Science* **254,** 1627–30 (1991).

9. Buchan, A., LeCleir, G. R., Gulvik, C. a & González, J. M. Master recyclers: features and functions of bacteria associated with phytoplankton blooms. *Nat. Rev. Microbiol.* **12,** 686–98 (2014).

10. Riemann, L., Steward, G. F. & Azam, F. Dynamics of Bacterial Community Composition and Activity during a Mesocosm Diatom Bloom. *Appl. Environ. Microbiol.* **66,** 578–587 (2000).

11. Azam, F. & Malfatti, F. Microbial structuring of marine ecosystems. *Nat. Rev. Microbiol.* **5,** 782–791 (2007).

12. Arndt, S., Jørgensen, B. B., LaRowe, D. E., Middelburg, J. J., Pancost, R. D. & Regnier, P. Quantifying the degradation of organic matter in marine sediments: A review and synthesis. *Earth-Science Rev.* **123,** 53–86 (2013).

13. Pedler, B. E., Aluwihare, L. I. & Azam, F. Single Bacterial Strain Capable of Significant Contribution to Carbon Cycling in the Surface Ocean. *Proc. Natl. Acad. Sci. U. S. A.* **111,** 7202–7207 (2014).

14. Arnosti, C., Bell, C., Moorhead, D. L., Sinsabaugh, R. L., Steen, a. D., Stromberger, M., Wallenstein, M. & Weintraub, M. N. Extracellular enzymes in terrestrial, freshwater, and marine environments: Perspectives on system variability and common research needs. *Biogeochemistry* **117,** 5–21 (2014).

15. Zimmerman, A. E., Martiny, A. C. & Allison, S. D. Microdiversity of extracellular enzyme genes among sequenced prokaryotic genomes. *ISME J.* **7,** 1187–99 (2013).

16. Wang, X., Sultana, C. M., Trueblood, J., Hill, T. C. J., Malfatti, F., Lee, C., Laskina, O., Moore, K. a., Beall, C. M., McCluskey, C. S., Cornwell, G. C., Zhou, Y., Cox, J. L., Pendergraft, M. a., Santander, M. V., Bertram, T. H., Cappa, C. D., Azam, F., DeMott, P. J., Grassian, V. H. & Prather, K. a. Microbial Control of Sea Spray Aerosol Composition: A Tale of Two Blooms. *ACS Cent. Sci.* **1,** 124–131 (2015).

17. Bourguet, N., Goutx, M., Ghiglione, J. F., Pujo-Pay, M., Mével, G., Momzikoff, A., Mousseau, L., Guigue, C., Garcia, N., Raimbault, P., Pete, R., Oriol, L. & Lefèvre, D. Lipid biomarkers and bacterial lipase activities as indicators of organic matter and bacterial dynamics in contrasted regimes at the DYFAMED site, NW Mediterranean. *Deep. Res. Part II Top. Stud. Oceanogr.* **56,** 1454–1469 (2009).

18. Stokes, M. D., Deane, G., Collins, D. B., Cappa, C., Bertram, T., Dommer, A., Schill, S., Forestieri, S. & Survilo, M. A miniature Marine Aerosol Reference Tank ( miniMART ) as a compact breaking wave analogue. 5194 (2016). doi:10.5194/amt-9-4257-2016

19. Parrish, C. C. Lipids in Marine Ecosystems. *ISRN Oceanogr.* **2013,** 1–16 (2013).

20. Hama, T. Fatty acid composition of particulate matter and photosynthetic products in subarctic and subtropical Pacific. *J. Plankton Res.* **21,** 1355–1372 (1999).

21. Kattner, G., Gercken, G. & Hammer, K. DEVELOPMENT OF LIPIDS DURING A SPRING PLANKTON BLOOM IN THE NORTHERN NORTH SEA. *Mar. Chem.* **14,** 163–173 (1983).

22. Cochran, R. E., Jayarathne, T., Stone, E. A. & Grassian, V. H. Selectivity Across the Interface: A Test of Surface Activity in the Composition of Organic-Enriched Aerosols from Bubble Bursting. *J. Phys. Chem. Lett.* **7,** 1692–1696 (2016).

23. Zhang, T., Cathcart, M. G., Vidalis, A. S. & Allen, H. C. Cation effects on phosphatidic acid monolayers at various pH conditions. *Chem. Phys. Lipids* **200,** 24–31 (2016).

24. Adams, E. M., Casper, C. B. & Allen, H. C. Effect of cation enrichment on dipalmitoylphosphatidylcholine (DPPC) monolayers at the air-water interface. *J. Colloid Interface Sci.* **478,** 353–364 (2016).

25. Adams, E. M. & Allen, H. C. Palmitic acid on salt subphases and in mixed monolayers of cerebrosides: Application to atmospheric aerosol chemistry. *Atmosphere (Basel)*. **4,** 315–336 (2013).

26. Abbatt, J. P. D., Lee, A. K. Y. & Thornton, J. A. Quantifying trace gas uptake to tropospheric aerosol: recent advances and remaining challenges. *Chem. Soc. Rev.* **41,** 6555 (2012).

27. Zahardis, J. & Petrucci, G. A. The oleic acid-ozone heterogeneous reaction system: products, kinetics, secondary chemistry, and atmospheric implications of a model system – a review. *Atmos. Chem. Phys. Discuss.* **6,** 11093–11179 (2006).

28. Nguyen, Q. T., Kjær, K. H., Kling, K. I., Boesen, T. & Bilde, M. Impact of fatty acid coating on the CCN activity of sea salt particles. *Tellus, Ser. B Chem. Phys. Meteorol.* **69,** 1–15 (2017).

29. Hildebrand, M., Davis, A. K., Smith, S. R., Traller, J. C. & Abbriano, R. The place

of diatoms in the biofuels industry. *Biofuels* **3,** 221–240 (2012).

30. Kooistra, W. H. C. F., Gersonde, R., Medlin, L. K. & Mann, D. *The origin and evolution of the diatoms: their adaptation to a planktonic existence*. *Evolution of planktonic photoautotrophs* (Elsevier Academic Press, 2007). doi:10.1016/B978-0-12-370518-1.50012-6

31. Tonon, T., Harvey, D., Larson, T. R. & Graham, I. a. Long chain polyunsaturated fatty acid production and partitioning to triacylglycerols in four microalgae. *Phytochemistry* **61,** 15–24 (2002).

32. Zendejas, F. J., Benke, P. I., Lane, P. D., Simmons, B. a & Lane, T. W. Characterization of the acylglycerols and resulting biodiesel derived from vegetable oil and microalgae (Thalassiosira pseudonana and Phaeodactylum tricornutum). *Biotechnol. Bioeng.* **109,** 1146–54 (2012).

33. Groussman, R. D., Parker, M. S. & Armbrust, E. V. Diversity and evolutionary history of iron metabolism genes in diatoms. *PLoS One* **10,** 1–25 (2015).

34. Arnosti, C., Durkin, S. & Jeffrey, W. H. Patterns of extracellular enzyme activities among pelagic marine microbial communities: Implications for cycling of dissolved organic carbon. *Aquat. Microb. Ecol.* **38,** 135–145 (2005).

35. Deane, G. B. & Stokes, M. D. Scale dependence of bubble creation mechanisms in breaking waves. *Nature* **418,** 839–844 (2002).

36. Collins, D. B., Zhao, D. F., Ruppel, M. J., Laskina, O., Grandquist, J. R., Modini, R. L., Stokes, M. D., Russell, L. M., Bertram, T. H., Grassian, V. H., Deane, G. B. & Prather, K. A. Direct aerosol chemical composition measurements to evaluate the physicochemical differences between controlled sea spray aerosol generation schemes. *Atmos. Meas. Tech.* **7,** 3667–3683 (2014).

37. Lewis, E. R. & Schwartz, S. E. Sea Salt Aerosol Production: Mechanisms, Methods, Measurements and Models - A Critical Review. *Am. Geophys. Union* (2013). doi:10.1029/GM152

38. Gard, E., Mayer, J. E., Morrical, B. D., Dienes, T., Fergenson, D. P. & Prather, K. a. Real-time analysis of individual atmospheric aerosol particles: Design and performance of a portable ATOFMS. *Anal. Chem.* **69,** 4083–4091 (1997).

39. Prather, K. A., Nordmeyer, T. & Salt, K. Real-Time Characterization of Individual Aerosol Particles Using Time-of-Flight Mass Spectrometry. *Anal. Chem.* **66,** 1403–1407 (1994).

40. Sultana, C. M., Cornwell, G. C., Rodriguez, P. & Prather, K. A. FATES: A flexible

analysis toolkit for the exploration of single-particle mass spectrometer data. *Atmos. Meas. Tech.* **10,** 1323–1334 (2017).

41. Hoppe, H.-G. *Use of fluorogenic model substrates for extracellular enzyme activity (EEA) measurement of bacteria*. *Handbook of methods in aquatic microbial ecology* (1993).

42. Darley, W. M. & Volcani, B. E. Role of silicon in diatom metabolism: A silicon requirement for deoxyribonucleic acid synthesis in the diatom Cylindrotheca fusiformis Reimann and Lewin. *Exp. Cell Res.* **58,** 334–342 (1969).

43. Kalo, P. J., Ollilainen, V., Rocha, J. M. & Malcata, F. X. Identification of molecular species of simple lipids by normal phase liquid chromatography-positive electrospray tandem mass spectrometry, and application of developed methods in comprehensive analysis of low erucic acid rapeseed oil lipids. *Int. J. Mass Spectrom.* **254,** 106–121 (2006).

# Chapter 4. Sea spray aerosol structure and composition using cryogenic transmission electron microscopy

## Sea Spray Aerosol Structure and Composition Using Cryogenic Transmission Electron Microscopy

Joseph P. Patterson,[*,†] Douglas B. Collins,[†] Jennifer M. Michaud,[†] Jessica L. Axson,[†] Camile M. Sultana,[†] Trevor Moser,[‡] Abigail C. Dommer,[†] Jack Conner,[†] Vicki H. Grassian,[§] M. Dale Stokes,[∥] Grant B. Deane,[∥] James E. Evans,[‡] Michael D. Burkart,[†] Kimberly A. Prather,[†,∥] and Nathan C. Gianneschi[†]

[†]Department of Chemistry & Biochemistry and [∥]Scripps Institution of Oceanography, University of California, San Diego, La Jolla, California 92093, United States

[‡]Environmental Molecular Science Laboratory, Pacific Northwest National Laboratory, 3335 Innovation Boulevard, Richland, Washington 99354, United States

[§]Department of Chemistry, University of Iowa, Iowa City, Iowa 52242, United States

*S* *Supporting Information*

**ABSTRACT:** The composition and surface properties of atmospheric aerosol particles largely control their impact on climate by affecting their ability to uptake water, react heterogeneously, and nucleate ice in clouds. However, in the vacuum of a conventional electron microscope, the native surface and internal structure often undergo physicochemical rearrangement resulting in surfaces that are quite different from their atmospheric configurations. Herein, we report the development of cryogenic transmission electron microscopy where laboratory generated sea spray aerosol particles are flash frozen in their native state with iterative and controlled thermal and/or pressure exposures and then probed by electron microscopy. This unique approach allows for the detection of not only mixed salts, but also soft materials including whole hydrated bacteria, diatoms, virus particles, marine vesicles, as well as gel networks within hydrated salt droplets—all of which will have distinct biological, chemical, and physical processes. We anticipate this method will open up a new avenue of analysis for aerosol particles, not only for ocean-derived aerosols, but for those produced from other sources where there is interest in the transfer of organic or biological species from the biosphere to the atmosphere.

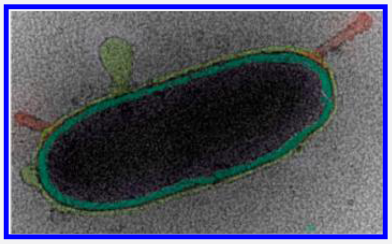

### ■ INTRODUCTION

Our understanding of how complex atmospheric aerosols are impacting clouds and climate will depend on our ability to obtain detailed information on aerosol three-dimensional (3D) structure, morphology, and composition under controlled and variable environmental conditions. Electron microscopy (EM) has provided insight into both aerosol structure and composition, taking advantage of high spatial resolution, elemental analysis capabilities via energy dispersive X-ray spectroscopy, and 3D imaging using electron tomography.[1] However, native structures are difficult to study with EM due to the high vacuum requirements of the microscope, which are known to affect particle structure, particularly hydrated or soft matter.[2] For particles in solution, cryogenic transmission electron microscopy (cryo-TEM) has revolutionized the study of dynamic, soft, and biological particles,[2,3] through the use of cryofixation, whereby the solution is cooled at a rate of $10^4$ to $10^6$ K per second resulting in a liquid to solid phase transition, fast enough to avoid any organization of the water molecules and consequently resulting in the trapping of amorphous ice.[3a,4] Consequently, we hypothesized that this same approach could be applied to trap the native or nascent structure of aerosol particles. Therefore, we report the first cryo-TEM experiments of hydrated aerosol particles demonstrating the power and utility of this technique through the study of laboratory generated sea spray aerosols (SSA).

SSA are generated through wave action and bubble bursting at the air−sea interface[5] and have been shown to be highly complex systems consisting of both sea salt and organic components. To date, dry-state electron microscopy has led to the conclusion that these important environmental nanoparticles are phase separated.[6] Thorough investigation of particle size, morphology, phase separation, and composition is considered critical because these properties will profoundly influence their behavior and the climate through their ability to serve as seeds upon which liquid and ice clouds form and to directly scatter solar radiation.[7] In contrast to previous analyses, our observations by cryo-TEM reveal previously undetected phases of SSA, yield unprecedented images of biological structures inside SSA particles, and show that without cryogenic methods, significant reorganization of SSA morphology is observed when samples are aged under laboratory conditions or exposed to high vacuum in conventional EM. Conventionally,

**Received:** October 19, 2015
**Published:** January 15, 2016



DOI: 10.1021/acscentsci.5b00344
*ACS Cent. Sci.* 2016, 2, 40−47

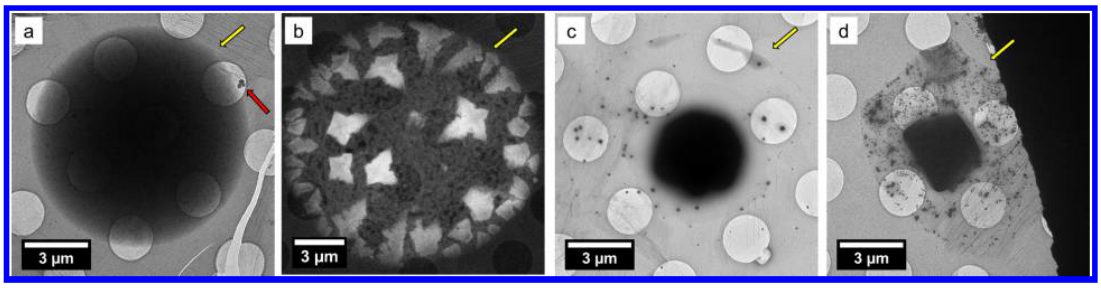


**Figure 1.** (S)TEM images representative of >1 $\mu$m particles collected after different stages of reorganization. (a) TEM image at stage 1, nascent SSA, (b) HADDF STEM image at stage 2, efflorescence, (c) TEM image at stage 3, after laboratory drying and aging (note: the large salt crystal appears out of focus as it is too thick to image through), and (d) TEM image at stage 4 after exposure to high vacuum. Yellow arrows indicate the edge of the SSA, and the red arrow indicates contamination from the cryo-TEM preparation.

SSA particle analysis by EM has been conducted by collection of particles either in liquid form using an impinger—whereby aerosols are collected into an aqueous medium (which can later be applied to a TEM grid),[8] or via direct impaction onto TEM grids,[6b,9] using, for example, a micro-orifice uniform-deposit impactor (MOUDI) for size separation.[6a] In previous studies, there has been no mention of, and indeed little attention paid to, particle aging time or storage conditions before insertion into the electron microscope,[9,10] at which point they are exposed to high vacuum conditions. Freedman et. al have explored the use of cold holders to reduce aerosol damage under the electron beam.[11] However, in this study, samples were inserted into the microscope at room temperature, and then exposed to a vacuum.[11,12] There have been several reports of aerosols being imaged using environmental scanning electron microscopy (E-SEM) and environmental transmission electron microscopy (E-TEM), which allow for particles to be imaged under hydrated conditions. However, the conditions are representative only of water saturated conditions and not a natural representation of a liquid environment. Furthermore, prior to imaging, particle aging and exposure to high vacuum occur,[9b,13] which, as we have discovered in this work, prevents the imaging of nascent SSA.

## RESULTS AND DISCUSSION

**SSA Generation and Collection.** Several stages of reorganization can occur following the generation of nascent SSA before they are imaged, including depositions onto a substrate (stage 1), dehydration and efflorescence (stage 2), particle drying and aging under laboratory conditions (stage 3), and exposure to vacuum upon insertion into the microscope (stage 4). To date, particles have been imaged by EM at stage 4, after drying and aging under laboratory conditions and exposure to high vacuum; consequently we lack a thorough investigation of the transformations that occur prior to these stages and the ability to trap the nascent hydrated structure of SSA. While it is currently impossible to image an airborne particle inside an electron microscope, we hypothesized that by using cryo-TEM it would be possible to investigate the sequential stages of reorganization within a few seconds of deposition onto a substrate and trap the hydrated structure of the particles, which in this paper we consider to be nascent SSA. In this study, SSA was generated using state-of-the-art laboratory production mechanisms using a wave channel[14] and marine aerosol reference tanks (MART).[15] However, the techniques presented here could readily be applied to those collected in field studies. Furthermore, the SSA generated by MART and wave channel systems have been shown to be representative of those formed from breaking waves in the open ocean,[15] over a wide size and range of compositions. SSA was produced from natural seawater, collected from the surface ocean at Scripps Pier (32° 52.0′ N, 117° 15.4′ W) approximately 275 m from shore. Figure 1 shows S/TEM images for SSA generated from natural sea water using a MART and processed according to procedures laid out in the Supporting Information. Briefly, aerosols are passively adhered to either graphene oxide ($GO_x$) or carbon coated TEM grids (used only for the images in Figure S9),[16] vitrified by plunging into either liquid ethane or nitrogen, and kept at < −170 °C while being inserted into the microscope and during imaging. Control samples were collected by placing the grids inside the wave channel or the MART in the absence of the wave breaking mechanism, thereby negating SSA production; images are shown in Figure S1. TEM and STEM Images were recorded on either an FEI Titan operating at 300 keV with spherical aberration corrected TEM and STEM with a Si(Li) X-ray energy dispersive spectrometer (EDS) or an FEI Sphera microscope operated at 200 keV. Low dose imaging procedures were used in order to prevent beam damage to the particles. Sommerdijk and co-workers have described in detail the artifacts and image interpretation associated with cryo-TEM images;[3a] here, we will indicate SSA particles with a blue arrow, biological structures with a green arrow and contamination with a red arrow. Imaging SSA by cryo-TEM presents certain challenges; in particular, for SSA particles ≫1 $\mu$m, there were often very thin as well as very thick regions within the sample particle. Consequently, a variety of imaging conditions, e.g., bright field TEM, bright field STEM, and high angle annular dark field (HADDF) STEM, were used in order to obtain the relevant information for each particle; the specific imaging conditions is noted in the figure caption for each image.

**SSA: Nascent Structure, Efflorescence and Aging.** The images in Figure 1 are representative cryo-(S)TEM or TEM images collected from multiple grids where >50 particles were imaged in each case, and the images are representative of the general morphology observed in each case; additional images are provided in the Supporting Information. Vitrification of SSA at stage (1) (Figure 1a, Figure S2) shows wet aerosol droplets adhered to the grid. No phase separation was observed, and energy dispersive X-ray spectroscopy (EDS) showed a similar Na/Mg ratio when measuring at both the center and the edge of the particle. (Figure S3).The particles shown were trapped as quickly as 30 s after production, so these represent images of truly nascent SSA after deposition

DOI: 10.1021/acscentsci.5b00344
ACS Cent. Sci. 2016, 2, 40−47

onto a substrate. Droplets with diameters between 100 nm and 20 $\mu$m were observed. However, as prepared $GO_x$ is significantly hydrophilic and has been shown to give water contact angles of ca. 12°,[17] this means a significant wetting of the surface will occur, flattening out the particle. Furthermore, using the electron energy loss spectroscopy (EELS) log-ratio method for thickness measurements,[18] we estimate that the center of 15−20 $\mu$m particles has a rough liquid thickness of 550 nm, which indicates that the wet aerosol diameter was around a factor of 6 smaller than the measured TEM diameter. Given these considerations, we estimate a particle diameter range of 20 nm to 10 $\mu$m in this study. For larger particles, this spreading is extremely beneficial in order to create liquid layers thin enough to achieve high resolution imaging. However, it has been observed that substrate hydrophobicity is extremely important for some aerosol measurements (e.g., water uptake properties).[19] When necessary, the hydrophobicity of the $GO_x$-TEM grids can be tuned accordingly.[17] After adherence to the grid, if SSA particles are subjected to low relative humidity (ca. RH = 20%) laboratory conditions for 30−60 s before vitrification, the initial stages of particle dehydration and efflorescence can be observed by cryo-TEM (stage 2, Figure 1b and Figure S4). Here, we observe an early stage of salt crystallization where dendrites appear to form on the particle surface. Indeed, in other work, a similar "nonspatially homogeneous" efflorescence was also observed for ammonium sulfate water aerosols with glutaric acid, by surface aerosol microscopy.[20] EDS analysis of the particle type in Figure 1b reveals the dendrites are rich in Na and that there is a distinct lack of Na present in the center of the aerosol (Figure S5). The 3D interpretation of this information is that during the initial stages of dehydration, NaCl begins to crystallize at the particle surface, leaving a Na depleted particle core. Na, Mg phase separation has been previously reported for SSA and shown to be affected when SSA undergo reactions with nitric acid at 60% RH;[6a] therefore, cryo-TEM could provide key insights into the mechanism of these surface active processes. If these particles are not subjected to vitrification prior to insertion into the microscope, significant structural reorganization occurs upon exposure to a vacuum, which typically results in Na-rich salt crystals surrounded by a ring of particle residue. This was observed when warming the cryo-TEM samples to room temperature within the microscope, which itself results in little deformation of the particles. However, removal from the microscope after warming, followed by reinsertion (after 2 min) at room temperature causes significant rearrangement (Figure S6). Therefore, cryo-TEM is essential for imaging the hydrated surface structure of SSA, which is of paramount importance to understanding their impact on the environment. If particles are allowed to age on the grid (ca. 3 h, ambient laboratory conditions) prior to vitrification (stage 3, Figure 1c and Figure S7), their structure appears similar to those which are not vitrified before imaging and subjected to high vacuum (HV) (stage 4, Figure 2d and Figure S8). Here, it can be seen that >1 $\mu$m particles typically contain a large salt crystal, which is occasionally surrounded by a residue of mixed organic/salt species, similar to previous observations.[6a,c,10] A similar experiment was performed on hydrophobic amorphous carbon TEM grids, and again similar results were obtained, inducing the observation of small dendrite salt crystals on the particle surface and a reorganization after aging or exposure to high vacuum (Figure S9). However, it was noted qualitatively that fewer particles adhered to the hydrophobic grids and that particles of a similar diameter appeared to be high contrast on the carbon grids (indicating they were thicker and less spread out), both of which are consistent with $GO_x$ being hydrophilic.[16a,17] Efflorescence is an extremely important phenomenon in atmospheric science,[21] and therefore the ability to trap particles during the first efflorescent event after aerosol production can provide unique insights. While there have been numerous investigations into particle efflorescence by electron microscopy,[9b,22] these studies have only examined SSA efflorescence after particles have been created, dehydrated, and then rehydrated, rather than the very first efflorescence event. Substrate deposited SSA storage (over weeks or months) and imaging methods have recently been investigated,[23] and it was concluded that ambient imaging conditions provide the most relevant particle size measurement. Here, we trap the ambient structure by vitrification, and use this process to investigate aging over short time periods (minutes to seconds) and by exposure to high vacuum. We have shown that the phase and organization of salt crystals in SSA can be greatly affected by exposure to HV (Figure 1 and Figure S6). Work is ongoing in our lab to fully utilize cryo-TEM in order to study efflorescence for a range of complex aerosol particle compositions.

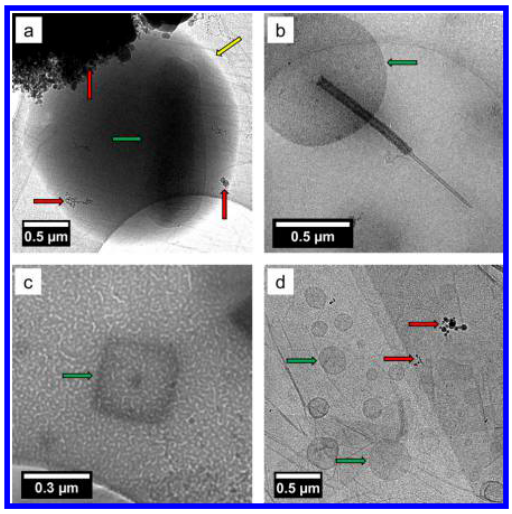


**Figure 2.** Bright field TEM images of SSA prepared by cryo-TEM showing (a) a whole bacterium inside a wet SSA droplet (note: the image contrast and brightness was adjusted to aid the observation of the cell, the original image is shown in Figure S11), (b) an intact diatom, (c) a virus particle, and (d) marine membrane vesicles. The biological structures were identified according to their size, shape, and morphology (see Supporting Information for more details). Yellow arrows indicate the edge of the SSA, the red arrows indicate contamination from the cryo-TEM preparation, and the green arrows indicate the biological particles.

**Biological Structures in SSA.** Next we sought to investigate the morphology and composition of nascent SSA by cryo-TEM as a function of biologically mediated changes in seawater chemical composition.[24] This was achieved through the addition of Guillard's f/2 growth medium plus sodium metasilicate and continuous illumination (5700 K fluorescent lamps; ~100 $\mu$E $m^{-1}$ $s^{-2}$), to induce a phytoplankton bloom, in both the MART and wave flume. Over the course of the bloom, many biological structures were observed inside wet SSA particles (Figure 2), including whole bacteria (Figure 2a), diatoms (Figure 2b), viruses (Figure 2b), and membrane

DOI: 10.1021/acscentsci.5b00344
ACS Cent. Sci. 2016, 2, 40−47

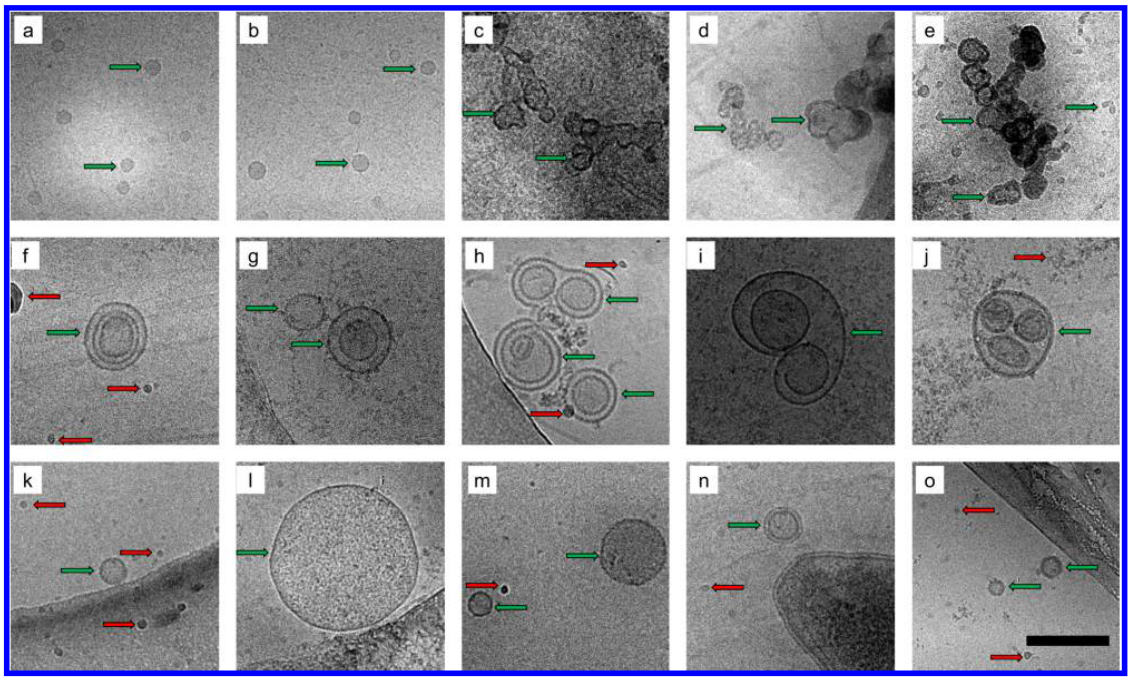


**Figure 3.** Bright field TEM images of membrane vesicles from aerosols (top row, a–e), SSML (middle row f–j) and bulk (bottom row, k–o blue), were collected from a MART experiment during a phytoplankton bloom. Scale bar = 200 nm. The red arrows indicate contamination from the cryo-TEM prepration, and the green arrows indicate the membrane vesicles.

vesicles (Figure 2d). Importantly, these images demonstrate that cryo-TEM can be used to preserve soft biological structures within SSA, as well as provide direct evidence that whole intact biological structures and cells can be ejected into the atmosphere in hydrated form (i.e., in a salt containing sea spray aerosol particle). Biological particles have been detected previously in SSA.[6b,c,9a,10,25] However, with conventional TEM it is impossible to probe the hydrated nature of the SSA droplets within which they exist. In addition, the vacuum of the microscope induces changes to their delicate structures,[2] which makes distinguishing between different types of biological particles (e.g., vesicles, marine nanogels, bacteria cells) extremely difficult. Therefore, our observations suggest that cryo-TEM has the potential to be used to characterize particles harboring hydrated life forms from one aqueous environment to another while traveling over significant distances as hydrated aerosols.[7d] It should be noted that while Raman, optical, and atomic force microscopy techniques can all be performed at ambient pressure and high relative humidity, the trapping of particles by vitrification prevents any further reorganization or aging of the particles allowing the structure of nascent sea spray to be captured. Furthermore, cryo-TEM has significantly higher spatial resolution than Raman or optical microscopy, allowing the nanoparticles within SSA particles to be easily identified, and in comparison to AFM, cryo-TEM allows the imaging of particle internal structure.

**Membrane Vesicles in SSA.** Recently Chisholm et al. showed, by concentration and purification of large volumes (ca. 90 L) of bulk seawater, that membrane vesicles make up a small but significant component of the oceanic loading of colloidal particles with diameter ($d$) < 200 nm.[26] Furthermore, their production by *Prochlorococcus* (a marine cyanobacterium) was observed from large-scale lab cultures, allowing the presence of DNA, RNA, and proteins within the membrane vesicles to be confirmed.[26] These nanometer-scale vehicles act as concentrating containers for biological species and chemical information in the ocean, but hitherto have never been detected before this study in the aerosol phase. This is likely due to the reorganization that occurs within noncryogenic imaging techniques, thereby obscuring or destroying the soft nanostructures. Figure 3 shows cryo-TEM images for membrane vesicles collected from the aerosol (Figure 3a–e), the sea surface microlayer (SSML) (Figure 3f–j), and the bulk seawater (Figure 3k–o), revealing the structural variability and complexity of these vesicles. Chisholm et al. reported an increase in vesicle concentration with decreasing depth in the ocean from $10^4$ (500 m depth) to $10^6$ (surface).[26] Here, we show similar concentrations for bulk surface seawater (approximately 0.5 m depth) and approximately a 3-fold increase for the SSML, (ca. $10^7$ vesicles $mL^{-1}$ Table S1) collected via a glass plate method, whereby glass substrates are dipped into the surface of the water and removed in order to capture the top hydrophobic layer onto the glass substrate. Furthermore, we find a remarkably high fraction (20%) of complex multilamellar vesicles (MLVs) in the SSML when compared to the bulk, where a low fraction of MLVs (<5%) were observed. The structural differences between membrane vesicles observed in aerosols (Figure 3a–e), which are more aggregated or have a narrower size distribution (Figure S5) compared to the SSML/bulk samples (Figure 3f–o), indicate that these vesicles might not simply be ejected as intact structures like bacteria shown in Figure 2a. We contend that rather than being ejected as already intact structures from seawater, we propose that the shear forces associated with

DOI: 10.1021/acscentsci.5b00344
*ACS Cent. Sci.* 2016, 2, 40–47

bubble bursting at the surface promote self-assembly of these structures in the lipid-salt matrix.[27] Vesicles could conceivably influence aqueous phase reactivity by providing an interface within the hydrated droplet or act as a container for larger biomolecules, which would influence their availability at the gas-particle interface. Indeed, the formation of membrane vesicles in aerosols has previously been proposed by Dobson et al. as an important step in abiogenesis.[28] Our observation that these types of structures can indeed be formed during aerosol production and remain stable within aerosols strongly supports this theory. The membrane vesicles in Figure 3a,b were obtained from impinged solutions collected at the same time as particles shown in the images in Figure 3c−e collected as aerosols by cryo-TEM. The obvious structural differences between particles seen in Figure 3a,b, which show discrete uniform vesicles versus particles seen in Figure 3c−e, which show disperse aggregated vesicles, indicate a further rearrangement upon re-entry into a dilute continuous liquid phase. This result opens up many questions about which additional chemical species they contain and transfer processes at play between the ocean and the atmosphere. Membranes act as barriers for smaller biogenic species such as proteins, enzymes, and DNA. The morphology, composition, and phase state of particles have been shown to affect processes such as gas-particle mass transfer,[29] and gas-particle reactions,[30] and therefore this structural rearrangement may have profound consequences for the chemistry of the aerosol particles as they travel through the atmosphere and undergo changes in hydration, temperature, pressure, oxidation, and UV radiation exposure.

**Marine Gels in SSA.** Marine gels are also important biological entities for the storage and transfer of biological and organic material in the marine environment.[31] A gel can be defined as a nonfluid colloidal network or polymer network that is expanded throughout its whole volume by a fluid.[32] Therefore, direct evidence of a gel should include an observation of the network structure or physical testing of mechanical properties. Several working definitions serve as indirect evidence for marine gels, such as a spontaneous self-assembly,[7c,31] disassembly in the presence of EDTA (which binds the divalent $Ca^{2+}$ and $Mg^{2+}$ metals holding the network structure together),[7c,31] and staining with Alcian blue for acidic polysaccharides, Coomassie Blue for amino acids and chlortetracycline for $Ca^{2+}$,[7c,33] all of which are known to be components of marine gels. While there have been numerous studies on marine gels in the seawater,[31,34] there have been very few reports of marine gels in aerosols. Orellana et al. found indirect evidence for gels in high Arctic cloudwater using chlortetracycline, EDTA disassembly, and pH responsive swelling.[7c] Bigg and Leck have observed gel-like aggregates in aerosol particles by TEM.[25a,b] However, the network structure was not clear, and as pointed out by Verdugo,[35] conventional electron microscopy is not suitable for studying these structures as it can readily lead to network-like artifacts. For cryo-TEM, the combination of low dose imaging and the trapping of hydrated particles will prevent these network-like artifacts from forming during sample preparation, thereby allowing the observation of the native network of the gels. Furthermore, it should be noted that cryo-TEM is an established method for imaging the network structure of synthetic hydrogels.[36] Here, we directly observe the network structure of marine gels throughout the entire volume of wet aerosol particles collected after the senescence phase of a laboratory phytoplankton bloom (Figure 4). Under cryogenic imaging conditions (Figure 4a,b and S13a), the particles typically appear to have no significant phase separation; however, some network-like structures can be observed at particle edges (Figure 4b). EDS analysis for these particles shows a significant lack of Na and Mg signals when compared to the particles shown in Figure S3, indicating their salt concentration is significantly lower than for the typical SSA discussed previously. Bigg and Leck have discussed a film drop formation mechanism by which SSA particles can become significantly depleted of salts,[6b,c] and therefore it is possible these gels were formed through such a film drop mechanism. The sample was then selectively dehydrated inside the microscope, by raising the temperature of the holder to ca. −135 °C, at which point a sharp pressure increase in the microscope column was observed. Post dehydration, the network structure of the gel-type particles was revealed and shown to have been present throughout the entire the liquid aerosol droplet (Figure 4c,d) and S13c). EDS spectra recorded after dehydration (Figure S13d) shows a large decrease in the O signal, due to loss of water, and reveals the presence of weak Na, Mg, and Cl signals, which were previously obscured. This is the first observation of an SSA gel particle and shows that the network structure presents on the surface of the particle and therefore interfaces with the atmosphere, which could affect the climate-relevant properties of these aerosols.

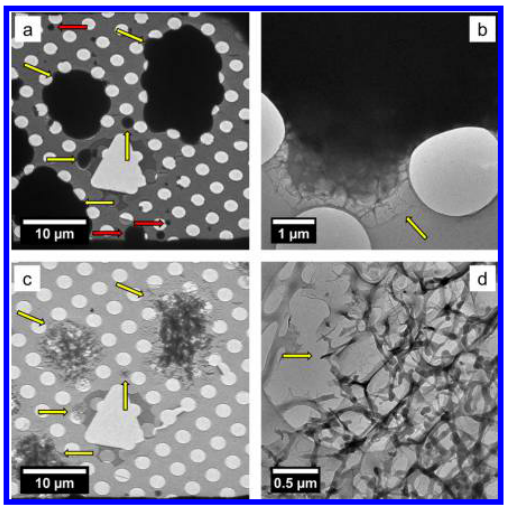


**Figure 4.** Bright field TEM images of gel SSA particles, (a) and (b) show hydrated particles, which are too thick to observe any internal morpgology; however a network structure is observed at the edge; the particles in (b−d) show images after controlled dehydration inside the microscope, which reveals a network structure that was present thought the entire liquid aerosol droplet. The yellow arrows indicate the edges of the SSA and the red arrow show contamination from the cryo-TEM preparation.

## CONCLUSIONS

Sea spray aerosol is a mixture of biological and chemical constituents that are often external mixtures of particle types. The use of cryo-TEM allows us to measure these different chemical and biological components intact for the first time leading to an unprecedented understanding of these particles and their nanostructures. Through laboratory studies, we have

DOI: 10.1021/acscentsci.5b00344
ACS Cent. Sci. 2016, 2, 40−47

demonstrated that this approach allows investigations into the chemical and morphological changes that occur when particles are exposed to various environmental (for example, changing humidity) or nonenvironmental (for example, high vacuum) conditions. For SSA, we observed that, upon ejection, most nascent SSA are essentially homogeneous water droplets, which then rapidly reorganize and phase separate upon exposure in a lower relative humidity environment. This reorganization involves the formation of NaCl dendrites on the surface of the particle as well as a phase separation of salts within the bulk of the particle. We report the first observation of marine vesicles within aerosols, which have important implications for carbon/biomolecule cycling, cloud formation, as well as the study of abiogenesis. Furthermore, we have imaged the network structure of marine gels in aerosols for the first time, showing that they can penetrate through an entire aerosol droplet. With the ability to trap aerosols under environmentally relevant hydrated conditions, studies can now begin to address many of the questions posed about the chemical complexity and structure of aerosol particles and how they impact climate and the environment for both laboratory and field studies.

## ■ ASSOCIATED CONTENT

### Supporting Information

The Supporting Information is available free of charge on the ACS Publications website at DOI: 10.1021/acscentsci.5b00344.

Additional S/TEM images, including EDS analysis, experimental information detailing the synthesis of the GO grids, aerosol production methods, and the calculations for vesicle concentration (PDF)

## ■ AUTHOR INFORMATION


### Corresponding Author

*E-mail: jppatterson@ucsd.edu.


### Notes

The authors declare no competing financial interest.

## ■ ACKNOWLEDGMENTS

This work was conducted within the Center for Aerosol Impacts on Climate and the Environment (CAICE), an NSF Center for Chemical Innovation and supported by the NSF (CHE-1305427). We acknowledge use of the UCSD Cryo-Electron Microscopy Facility, which is supported by NIH Grant R37 GM-03350 to Dr. Timothy S. Baker and a gift from the Agouron Institute to UCSD. A portion of the cryo-S/TEM work was performed using the Environmental Molecular Sciences Laboratory (EMSL), a national scientific user facility sponsored by the Department of Energy's Office of Biological and Environmental Research and located at PNNL.

## ■ REFERENCES


(1) (a) Goodhew, P. J.; Humphreys, F. J.; Beanland, R. *Electron Microscopy and Analysis*; Taylor & Francis Group: New York, 2001. (b) Williams, D. B.; Carter, C. B. *The Transmission Electron Microscope*; Springer: Berlin, 1996.

(2) Adrian, M.; Dubochet, J.; Lepault, J.; McDowall, A. W. Cryo-electron microscopy of viruses. *Nature* **1984**, *308* (5954), 32−36.

(3) (a) Friedrich, H.; Frederik, P. M.; de With, G.; Som-merdijk, N. A. J. M. Imaging of Self-Assembled Structures: Interpretation of TEM and Cryo-TEM Images. *Angew. Chem., Int. Ed.* **2010**, *49* (43), 7850−7858. (b) Nudelman, F.; de With, G.; Sommerdijk, N. A. J. M. Cryo-electron tomography: 3-dimensional imaging of soft matter. *Soft Matter* **2011**, *7* (1), 17−24. (c) Newcomb, C. J.; Moyer, T. J.; Lee, S. S.; Stupp, S. I. Advances in cryogenic transmission electron microscopy for the characterization of dynamic self-assembling nanostructures. Current Opinion in Colloid &. *Curr. Opin. Colloid Interface Sci.* **2012**, *17* (6), 350−359.

(4) Almgren, M.; Edwards, K.; Karlsson, G. Cryo transmission electron microscopy of liposomes and related structures. *Colloids Surf., A* **2000**, *174* (1−2), 3−21.

(5) O'Dowd, C. D.; De Leeuw, G. Marine aerosol pro-duction: a review of the current knowledge. *Philos. Trans. R. Soc., A* **2007**, *365* (1856), 1753−1774.

(6) (a) Ault, A. P.; Guasco, T. L.; Ryder, O. S.; Baltrusaitis, J.; Cuadra-Rodriguez, L. A.; Collins, D. B.; Ruppel, M. J.; Bertram, T. H.; Prather, K. A.; Grassian, V. H. Inside versus Outside: Ion Redistribution in Nitric Acid Reacted Sea Spray Aerosol Particles as Determined by Single Particle Analysis. *J. Am. Chem. Soc.* **2013**, *135* (39), 14528−14531. (b) Bigg, E. K.; Leck, C. The composition of fragments of bubbles bursting at the ocean surface. *J. Geophys. Res.* **2008**, *113* (D11), No. D11209, DOI: 10.1029/2007JD009078. (c) Leck, C.; Bigg, E. K. Source and evolution of the marine aerosol—A new perspective. *Geophys. Res. Lett.* **2005**, *32* (19), L19803. (d) Ault, A. P.; Moffet, R. C.; Baltrusaitis, J.; Collins, D. B.; Ruppel, M. J.; Cuadra-Rodriguez, L. A.; Zhao, D.; Guasco, T. L.; Ebben, C. J.; Geiger, F. M.; Bertram, T. H.; Prather, K. A.; Grassian, V. H. Size-Dependent Changes in Sea Spray Aerosol Composition and Properties with Different Seawater Conditions. *Environ. Sci. Technol.* **2013**, *47* (11), 5603−5612. (e) Ault, A. P.; Zhao, D.; Ebben, C. J.; Tauber, M. J.; Geiger, F. M.; Prather, K. A.; Grassian, V. H. Raman microspectroscopy and vibrational sum frequency generation spectroscopy as probes of the bulk and surface compositions of size-resolved sea spray aerosol particles. *Phys. Chem. Chem. Phys.* **2013**, *15* (17), 6206−6214.

(7) (a) Schill, S. R.; Collins, D. B.; Lee, C.; Morris, H. S.; No-vak, G. A.; Prather, K. A.; Quinn, P. K.; Sultana, C. M.; Tivanski, A. V.; Zimmermann, K.; Cappa, C. D.; Bertram, T. H. The Impact of Aerosol Particle Mixing State on the Hygroscopicity of Sea Spray Aerosol. *ACS Cent. Sci.* **2015**, *1* (3), 132−141. (b) Langmann, B.; Scannell, C.; O'Dowd, C. New Directions: Organic matter contribution to marine aerosols and cloud condensation nuclei. *Atmos. Environ.* **2008**, *42* (33), 7821−7822. (c) Orellana, M. V.; Matrai, P. A.; Leck, C.; Rauschenberg, C. D.; Lee, A. M.; Coz, E. Marine microgels as a source of cloud condensation nuclei in the high Arctic. *Proc. Natl. Acad. Sci. U. S. A.* **2011**, *108* (33), 13612−13617. S13612/1-S13612/4 (d) Konstantinidis, K. T. Do airborne microbes matter for atmospheric chemistry and cloud formation? *Environ. Microbiol.* **2014**, *16* (6), 1482−1484. (e) Adler, G.; Koop, T.; Haspel, C.; Taraniuk, I.; Moise, T.; Koren, I.; Heiblum, R. H.; Rudich, Y. Formation of highly porous aerosol particles by atmospheric freeze-drying in ice clouds. *Proc. Natl. Acad. Sci. U. S. A.* **2013**, *110* (51), 20414−20419. S20414/1-S20414/10 (f) Farmer, D. K.; Cappa, C. D.; Kreidenweis, S. M. Atmospheric Processes and Their Controlling Influence on Cloud Condensation Nuclei Activity. *Chem. Rev.* **2015**, *115* (10), 4199−4217.

(8) Verreault, D.; Moineau, S.; Duchaine, C. Methods for Sampling of Airborne Viruses. *Microbiology and Molecular Biology Reviews* **2008**, *72* (3), 413−444.

(9) (a) Leck, C.; Bigg, E. K. New Particle Formation of Marine Biological Origin. *Aerosol Sci. Technol.* **2010**, *44* (7), 570−577. (b) Wise, M. E.; Freney, E. J.; Tyree, C. A.; Allen, J. O.; Martin, S. T.; Russell, L. M.; Buseck, P. R. Hygroscopic behavior and liquid-layer composition of aerosol particles generated from natural and artificial seawater. *J. Geophys. Res.* **2009**, *114* (D3), No. D03201.

(10) Bigg, E. K.; Leck, C. Properties of the aerosol over the central Arctic Ocean. *Journal of Geophysical Research: Atmospheres* **2001**, *106* (D23), 32101−32109.

(11) Veghte, D. P.; Bittner, D. R.; Freedman, M. A. Cryo-Transmission Electron Microscopy Imaging of the Morphology of Submicrometer Aerosol Containing Organic Acids and Ammonium Sulfate. *Anal. Chem.* **2014**, *86* (5), 2436−2442.

(12) Veghte, D. P.; Altaf, M. B.; Freedman, M. A. Size De-pendence of the Structure of Organic Aerosol. *J. Am. Chem. Soc.* **2013**, *135* (43), 16046−16049.
(13) Laskina, O.; Morris, H. S.; Grandquist, J. R.; Qin, Z.; Stone, E. A.; Tivanski, A. V.; Grassian, V. H. Size Matters in the Water Uptake and Hygroscopic Growth of Atmospherically Relevant Multicompo-nent Aerosol Particles. *J. Phys. Chem. A* **2015**, *119* (19), 4489−4497.
(14) Wernand, M. R.; van der Woerd, H. J.; Gieskes, W. W. C. Trends in Ocean Colour and Chlorophyll Concentration from 1889 to 2000, Worldwide. *PLoS One* **2013**, *8* (6), e63766.
(15) (a) Prather, K. A.; Bertram, T. H.; Grassian, V. H.; Deane, G. B.; Stokes, M. D.; DeMott, P. J.; Aluwihare, L. I.; Palenik, B. P.; Azam, F.; Seinfeld, J. H.; Moffet, R. C.; Molina, M. J.; Cappa, C. D.; Geiger, F. M.; Roberts, G. C.; Russell, L. M.; Ault, A. P.; Baltrusaitis, J.; Collins, D. B.; Corrigan, C. E.; Cuadra-Rodriguez, L. A.; Ebben, C. J.; Forestieri, S. D.; Guasco, T. L.; Hersey, S. P.; Kim, M. J.; Lambert, W. F.; Modini, R. L.; Mui, W.; Pedler, B. E.; Ruppel, M. J.; Ryder, O. S.; Schoepp, N. G.; Sullivan, R. C.; Zhao, D. Bringing the ocean into the laboratory to probe the chemical complexity of sea spray aerosol. *Proc. Natl. Acad. Sci. U. S. A.* **2013**, *110* (19), 7550−7555. S7550/1-S7550/10 (b) Stokes, M. D.; Deane, G. B.; Prather, K.; Bertram, T. H.; Ruppel, M. J.; Ryder, O. S.; Brady, J. M.; Zhao, D. A Marine Aerosol Reference Tank system as a breaking wave analogue for the production of foam and sea-spray aerosols. *Atmos. Meas. Tech.* **2013**, *6* (4), 1085−1094. (c) Collins, D. B.; Zhao, D. F.; Ruppel, M. J.; Laskina, O.; Grandquist, J. R.; Modini, R. L.; Stokes, M. D.; Russell, L. M.; Bertram, T. H.; Grassian, V. H.; Deane, G. B.; Prather, K. A. Direct aerosol chemical composition measurements to evaluate the physicochemical differences between controlled sea spray aerosol generation schemes. *Atmos. Meas. Technol. Discuss.* **2014**, *7* (7), 6457−6499.
(16) (a) Wilson, N. R.; Pandey, P. A.; Beanland, R.; Young, R. J.; Kinloch, I. A.; Gong, L.; Liu, Z.; Suenaga, K.; Rourke, J. P.; York, S. J.; Sloan, J. Graphene Oxide: Structural Analysis and Application as a Highly Transparent Support for Electron Microscopy. *ACS Nano* **2009**, 3 (9), 2547−2556. (b) Pantelic, R. S.; Meyer, J. C.; Kaiser, U.; Baumeister, W.; Plitzko, J. M. Graphene oxide: A substrate for optimizing preparations of frozen-hydrated samples. *J. Struct. Biol.* **2010**, *170* (1), 152−156. (c) van de Put, M. W. P.; Patterson, J. P.; Bomans, P. H. H.; Wilson, N. R.; Friedrich, H.; van Benthem, R. A. T. M.; de With, G.; O'Reilly, R. K.; Sommerdijk, N. A. J. M. Graphene oxide single sheets as substrates for high resolution cryoTEM. *Soft Matter* **2015**, *11*, 1265−1270.
(17) Patterson, J. P.; Sanchez, A. M.; Petzetakis, N.; Smart, T. P.; Epps, T. H., III; Portman, I.; Wilson, N. R.; O'Reilly, R. K. A simple approach to characterizing block copolymer assemblies: graphene oxide supports for high contrast multi-technique imaging. *Soft Matter* **2012**, *8* (12), 3322−3328.
(18) Malis, T.; Cheng, S. C.; Egerton, R. F. EELS log-ratio technique for specimen-thickness measurement in the TEM. *J. Electron Microsc. Tech.* **1988**, *8* (2), 193−200.
(19) Eom, H.-J.; Gupta, D.; Li, X.; Jung, H.-J.; Kim, H.; Ro, C.-U. Influence of Collecting Substrates on the Characterization of Hygroscopic Properties of Inorganic Aerosol Particles. *Anal. Chem.* **2014**, *86* (5), 2648−2656.
(20) Peckhaus, A.; Grass, S.; Treuel, L.; Zellner, R. Deliques-cence and Efflorescence Behavior of Ternary Inorgan-ic/Organic/Water Aerosol Particles. *J. Phys. Chem. A* **2012**, *116* (24), 6199−6210.
(21) (a) Martin, S. T. Phase Transitions of Aqueous Atmos-pheric Particles. *Chem. Rev. (Washington, DC, U. S.)* **2000**, *100* (9), 3403−3453. (b) Onasch, T. B.; Siefert, R. L.; Brooks, S. D.; Prenni, A. J.; Murray, B.; Wilson, M. A.; Tolbert, M. A. Infrared spectroscopic study of the deliquescence and efflorescence of ammonium sulfate aerosol as a function of temperature. *J. Geophys. Res.* **1999**, *104* (D17), 21317−21326.
(22) Wise, M.; Biskos, G.; Martin, S.; Russell, L.; Buseck, P. Phase Transitions of Single Salt Particles Studied Using a Transmission Electron Microscope with an Environmental Cell. *Aerosol Sci. Technol.* **2005**, *39* (9), 849−856.
(23) Laskina, O.; Morris, H. S.; Grandquist, J. R.; Estillore, A. D.; Stone, E. A.; Grassian, V. H.; Tivanski, A. V. Substrate-Deposited Sea Spray Aerosol Particles: Influence of Analytical Method, Substrate, and Storage Conditions on Particle Size, Phase, and Morphology. *Environ. Sci. Technol.* **2015**, *49* (22), 13447−13453.
(24) Lee, C.; Sultana, C. M.; Collins, D. B.; Santander, M. V.; Axson, J. L.; Malfatti, F.; Cornwell, G. C.; Grandquist, J. R.; Deane, G. B.; Stokes, M. D.; Azam, F.; Grassian, V. H.; Prather, K. A. Advancing Model Systems for Fundamental Laboratory Studies of Sea Spray Aerosol Using the Microbial Loop. *J. Phys. Chem. A* **2015**, *119* (33), 8860−70.
(25) (a) Leck, C.; Bigg, E. K. Biogenic particles in the surface microlayer and overlaying atmosphere in the central Arctic Ocean during summer. *Tellus, Ser. B* **2005**, *57* (4), 2005. (b) Leck, C.; Bigg, E. K. Comparison of sources and nature of the tropical aerosol with the summer high Arctic aerosol. *Tellus, Ser. B* **2008**, *60* (1), 118−126. (c) Leck, C.; Bigg, E. K. Comparison of sources and nature of the tropical aerosol with the summer high Arctic aerosol. *Tellus, Ser. B* **2008**, *60* (1), 10.3402/tellusb.v60i1.16906. (d) Pósfai, M.; Li, J.; Anderson, J. R.; Buseck, P. R. Aerosol bacteria over the Southern Ocean during ACE-1. *Atmos. Res.* **2003**, *66* (4), 231−240.
(26) Biller, S. J.; Schubotz, F.; Roggensack, S. E.; Thompson, A. W.; Summons, R. E.; Chisholm, S. W. Bacterial Vesicles in Marine Ecosystems. *Science* **2014**, *343* (6167), 183−186.
(27) (a) Medronho, B.; Shafaei, S.; Szopko, R.; Miguel, M. G.; Olsson, U.; Schmidt, C. Shear-Induced Transitions between a Planar Lamellar Phase and Multilamellar Vesicles: Continuous versus Discontinuous Transformation. *Langmuir* **2008**, *24* (13), 6480−6486. (b) Guida, V. Thermodynamics and kinetics of vesicles formation processes. *Adv. Colloid Interface Sci.* **2010**, *161* (1−2), 77−88.
(28) (a) Dobson, C. M.; Ellison, G. B.; Tuck, A. F.; Vaida, V. Atmospheric aerosols as prebiotic chemical reactors. *Proc. Natl. Acad. Sci. U. S. A.* **2000**, *97* (22), 11864−8. (b) Griffith, E. C.; Rapf, R. J.; Shoemaker, R. K.; Carpenter, B. K.; Vaida, V. Photoinitiated Synthesis of Self-Assembled Vesicles. *J. Am. Chem. Soc.* **2014**, *136* (10), 3784−3787.
(29) Shiraiwa, M.; Zuend, A.; Bertram, A. K.; Seinfeld, J. H. Gas-particle partitioning of atmospheric aerosols: interplay of physical state, non-ideal mixing and morphology. *Phys. Chem. Chem. Phys.* **2013**, *15* (27), 11441−11453.
(30) Ryder, O. S.; Campbell, N. R.; Shaloski, M.; Al-Mashat, H.; Nathanson, G. M.; Bertram, T. H. Role of Organics in Regulating ClNO2 Production at the Air−Sea Interface. *J. Phys. Chem. A* **2015**, *119* (31), 8519−8526.
(31) Chin, W.-C.; Orellana, M. V.; Verdugo, P. Spontaneous assembly of marine dissolved organic matter into polymer gels. *Nature (London, U. K.)* **1998**, *391* (6667), 568−571.
(32) Alemán, J. V.; Chadwick, A. V.; He, J.; Hess, M.; Horie, K.; Jones, R. G.; Kratochvíl, P.; Meisel, I.; Mita, I.; Moad, G.; Penczek, S.; Stepto, R. F. T. Definitions of terms relating to the structure and processing of sols, gels, networks, and inorganic-organic hybrid materials (IUPAC Recommendations 2007). *Pure Appl. Chem.* **2007**, *79*, 1801.
(33) Wurl, O. *Practical Guidelines for the Analysis of Seawater*; CRC Press: Boca Raton, FL, 2009.
(34) (a) Verdugo, P. The role of marine gel-phase on carbon cycling in the ocean. *Mar. Chem.* **2004**, *92* (1−4), 65−66. (b) Verdugo, P.; Alldredge, A. L.; Azam, F.; Kirchman, D. L.; Passow, U.; Santschi, P. H. The oceanic gel phase: a bridge in the DOM-POM continuum. *Mar. Chem.* **2004**, *92* (1−4), 67−85. (c) Verdugo, P. Dynamics of marine biopolymer networks. *Polym. Bull. (Heidelberg, Ger.)* **2007**, *58* (1), 139−143. (d) Ding, Y.-X.; Chin, W.-C.; Verdugo, P. Development of a fluorescence quenching assay to measure the fraction of organic carbon present in self-assembled gels in seawater. *Mar. Chem.* **2007**, *106* (3−4), 456−462. (e) Cunliffe, M.; Murrell, J. C. The sea-surface microlayer is a gelatinous biofilm. *ISME J.* **2009**, 3 (9), 1001−1003. (f) Verdugo, P.; Santschi, P. H. Polymer dynamics of DOC networks and gel formation in seawater. *Deep Sea Res., Part II* **2010**, *57* (16),

DOI: 10.1021/acscentsci.5b00344
*ACS Cent. Sci.* 2016, 2, 40−47

1486−1493. (g) Radic, T. M.; Svetlicic, V.; Zutic, V.; Boulgaropoulos, B. Seawater at the nanoscale: marine gel imaged by atomic force microscopy. *J. Mol. Recognit.* **2011**, *24* (3), 397−405. (h) Verdugo, P. Marine microgels. *Ann. Rev. Mar Sci.* **2012**, *4*, 375−400.

(35) Verdugo, P. Marine Microgels. *Annu. Rev. Mar. Sci.* **2012**, *4* (4), 375−400.

(36) Krysmann, M. J.; Castelletto, V.; Kelarakis, A.; Hamley, I. W.; Hule, R. A.; Pochan, D. J. Self-Assembly and Hydrogelation of an Amyloid Peptide Fragment. *Biochemistry* **2008**, *47* (16), 4597−4605.

(37) Verdugo, P. Marine Microgels. *Annu. Rev. Mar. Sci.* **2012**, *4* (4), 375−400.

DOI: 10.1021/acscentsci.5b00344
*ACS Cent. Sci.* 2016, 2, 40−47

Supporting Information for: Sea spray aerosol structure and composition using cryogenic transmission electron microscopy'

Joseph P. Patterson,[†*] Douglas B. Collins,[†] Jennifer M. Michaud,[†] Jessica L. Axson, [†] Camile M. Sultana,[†] Trevor Moser,[‡] Abigail C. Dommer,[†] Jack Conner,[†] Vicki, H. Grassian,[§] M. Dale Stokes,[∥] Grant B. Deane,[∥] James E. Evans,[‡] Michael D. Burkart,[†] Kimberly A. Prather,[†,∥] and Nathan C. Gianneschi,[†]

[†]Department of Chemistry & Biochemistry, University of California, San Diego, La Jolla, California, USA, 92093, USA

[‡]Environmental Molecular Science Laboratory, Pacific Northwest National Laboratory, 3335 Innovation Blvd., Richland, WA 99354,

[§]Department of Chemical and Biochemical Engineering and ||Department of Chemistry, University of Iowa, Iowa City, Iowa 52242, United States

**Materials and Methods**

**STEM/TEM imaging:**

TEM and STEM Images were recorded on either an FEI Titan operating at 300 keV with spherical aberration corrected TEM and STEM with a Si(Li) X-ray energy dispersive spectrometer (EDS) with a polymer based windwon and operating with a collection solid angle of <0.1 sr or an FEI Sphera microscope operated at 200 keV. In general the images were recorded at relatively low magnification and electron doses for higher magnification imaging low dose imaging procedures were used in order to prevent beam damage to the particles.

**EDS collection:**

EDS spectra were collected in STEM mode as either point or line scans. The dwell times were varied (typically 1-10 minutes) depending on sample thickness, but were kept consistence for individual particles, in order to obtain a sufficient signal to noise ratio. EDS spectra typically resulted in localized particle damage, in the form of small holes being drilled through the sample, which could be observed afterwards by imaging in TEM or STEM mode. The post EDS collection images show the localization of the damage and the EDS collection. All spectra are presented as background subtracted, and the peaks are assigned to the relevant element K edges.

**Aerosol generation:**

Marine aerosol Reference Tank. Details for the procedure of aerosol generation can be found in reference 1.[1]

Waveflume. Details for the procedure of aerosol generation can be found in reference 2.[2]

**Synthesis of GOx as described previously [3]**

H2SO4 (conc, 170 mL) was added to graphite (5 g) in a 250 mL round bottom flask on ice and stirred for 10 min. KMnO4 (22.5 g) was added over 1 hour and the mixture was stirred for 2 hours on ice. The solution was allowed to warm to room temperature and stirred overnight. The viscous brown liquid was

added to H2SO4 (5 wt%, 500 mL) with continuous stirring for 2 hours. An aqueous solution of H202 (30 wt%, 15 g) was added and stirred for 2 hours. The viscous brown liquid was centrifuged and the supernatant discarded. An aqueous solution (500 mL) of H2SO4 (3 wt%) and H2O2 (0.5 wt%) was added to the precipitate and stirred for 1 min. The centrifugation and washing step was then repeated 5 times with the H2SO4 (3 wt%) and H2O2 (0.5 wt%) solution and 5 times with DI water. After a final centrifuge small portions of GO was stirred in water and freeze dried to obtain brown GO flakes. GO flakes were stirred in a nanopure water over night, sonicated for 30 seconds and left to stand. Any sediment was discarded after one day. Note: the synthesis of graphene oxide involves the use of highly corrosive materials and the appropriate MSDS forms should be consulted.

**Preparation of GOx-TEM grids as described previously [3]**
Quantifoil R2/2 TEM grids were plasma cleaned using an EMITECH K950X for 3 minutes at 20 mAmp and 0.2 mbar. The grids were immediately transferred to a piece of filter paper and one drop (from a 200 µL pipette) of GO solution (ca. 0.1 mg/mL) was dropped from a height of 1 cm onto the TEM grids (allowing the filter paper to wick away most of the solution). The grids were left to dry in air for at least 30 minutes before use. The GOx solution concentration of 0.1 mg/mL was used to obtain high (generally > 90%) coverage on the TEM grids, as it was noticed that when SSA adhered to areas with holes not covered with GOx that these SSA deformed around the holes (see Figure S5)

**Preparation of SSML and bulk samples for GOx-Cryo-TEM**
7 µL of sample was added to GOx-TEM grids and left under high humidity for particles to adsorb to the surface for 20-60 minutes. For studies where per mL concentrations of vesicles were determined the waiting time was held at 30 minutes. After the adherence period the grids were manually blotted with filter paper for 25 seconds and rapidly plunged into liquid ethane. The grids were then transferred to liquid nitrogen for storage and transfer to the microscope where they were imaged at < -170 °C. TEM images were recorded on a FEI Sphera microscope operated at 200 keV using a precooled Gatan 626 cryo-transfer holder. Micrographs were recorded on a 2K X 2K Gatan CCD.

**Preparation of impinged aerosol samples for GOx-Cryo-TEM**
Impinger samples were collected into autoclaved sea water at a flow rate of 1 standard liters per minute over periods of two hours. Multi samples were collected, combined and concentrated approximately 1000x using Amicon Ultra-15 or 0.5 centrifugal filters. Sample were then prepared for GOx-supported cryo-TEM as described above for SSML and bulk samples.

**Preparation of Aerosol-Cryo-TEM samples**
Either Carbon film or GOx-TEM grids were held with a pair of tweezers and placed into MART tanks either during or after plunging cycles and let for a set period of time 20 minutes-12 hours to allow particles to adhere to the grids. The grids were removed from the MART tanks and either directly plunged into liquid ethane or kept under high humidity until they were plunged into liquid ethane or nitrogen. Note: no blotting step was used in the process.

For the carbon film grids (only used for the images in Figure S4) it was observed qualitatively that far fewer particles were adhered to the grids in comparison with the GOx grids despite having the same collections times. Furthermore, for particles of a similar diameter, the particles on the GOx grids appeared to be much thinner (lower contrast) indicating that the SSA are spreading out more on the GOx grids, which is consistent with GOx being hydrohpilic.[3]

Both liquid nitrogen and liquid ethan can be used of vitrification agents, in this study we did not notice any difference between using the two coolants.

**Calculation of SSA thickness at the particle center by EELS**
Particle thickness was estimated using electron energy loss spectroscopy and the log ratio technique,[4] where the relative thickness (t/λ) is a function of the integrated area beneath the zero loss peak and the total spectrum.

Absolute thickness was calculated by estimating the inelastic mean free path (λ) of the particles to be ~152.8 nm, assuming the primary components of the aerosol particles to be water and sea salts λ can be calculated from the following equations .

$$\lambda = \frac{106\mathrm{F}.\,\mathrm{E}(0)}{\mathrm{E}(\mathrm{M})\ln(2\beta\mathrm{E}(0)/\mathrm{E}(\mathrm{M})}$$

E(0) is the accelerating voltage expressed in keV, β is the collection angle in mrad, F is a relativistic factor defined by

$$F = \frac{1 + (E(0)/1022)}{(1 + (E(0)/511))^2}$$

And E(M) is an average energy loss defined by E(M) = 7.6 Z(eff)$^{0.33}$. where Z(eff) is defined by

$$Z(eff) = \frac{\Sigma(f(n)Z(n)^{1.3}}{\Sigma(f(n)Z(n)^{0.3}}$$

Where f is the atomic fraction of the samples and Z is the atomic number. In this case the following atomic fractions were used H (0.110), O (0.883), Na (1.08x10$^{-2}$), Mg (1.29x10$^{-3}$), Cl (1.94x10$^{-2}$)

For a measured log ratio of 3.59, a thickness (t) value of approximately 549 nm is determined.

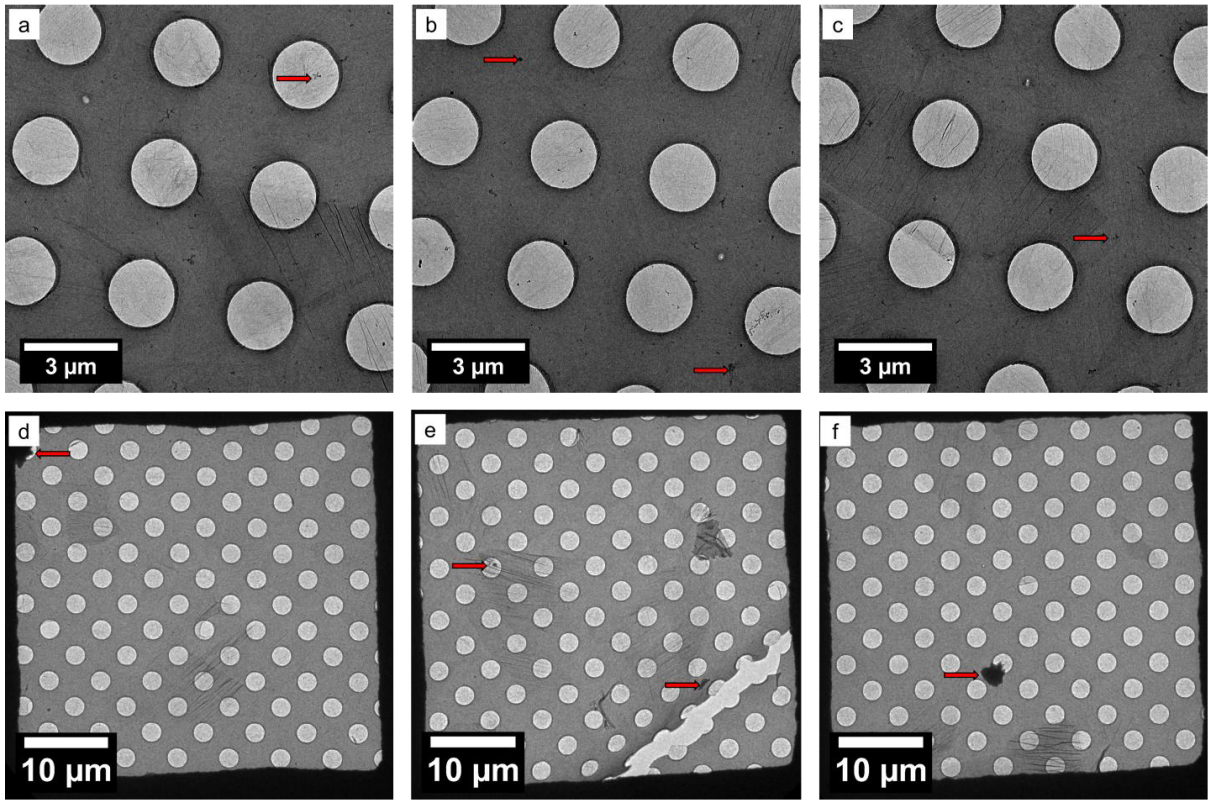


**Figure S1.** Bright field TEM images for a control sample where the GOx TEM grid was placed inside the MART, but without the plunging mechanism, which generates the aerosols. The red arrows indicate contamination from the cryo-TEM preparation method.

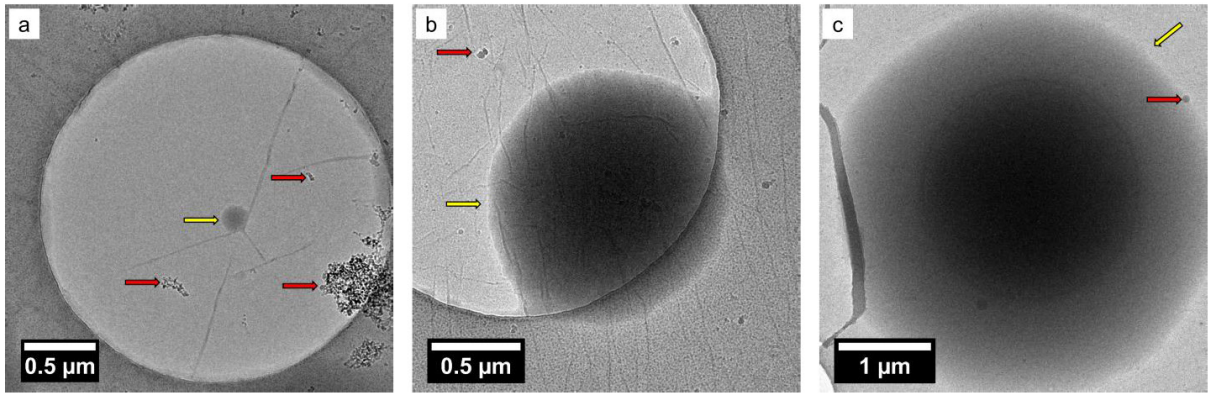


**Figure S2.** Additional bright field TEM images of SSA collected at stage 1. The yellow arrows indicate the edge of the SSA and the red arrows indicate contamination from the cryo-TEM preparation.

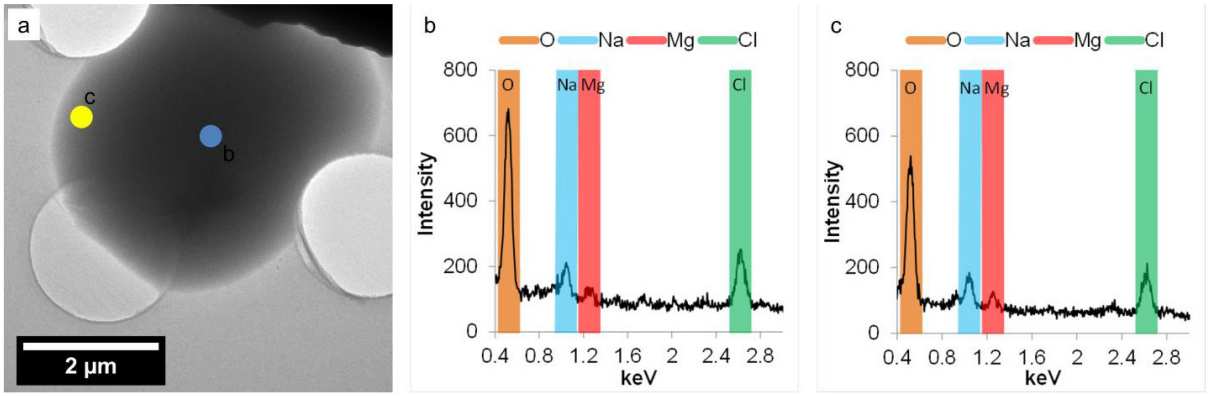


**Figure S3.** cryo-TEM image and EDS spectra for a particle collected at stage 1. a) bright field TEM image, b) EDS spectrum collected at the center of the particle (blue dot) and c) EDS spectrum collected at the edge of the particle (yellow dot).

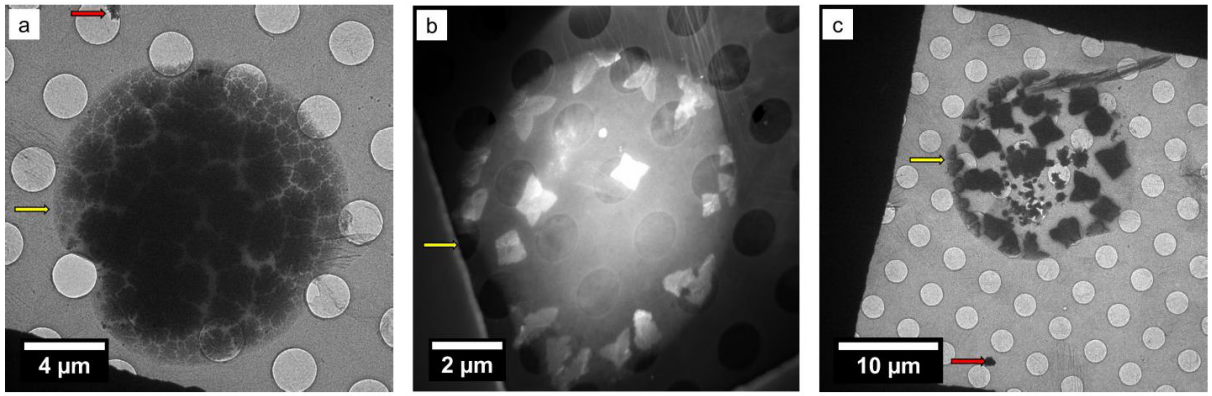


**Figure S4.** Additional (S)TEM images for SSA collected at stage 2. a) bright field TEM, b) HADDF STEM and c) bright field TEM.

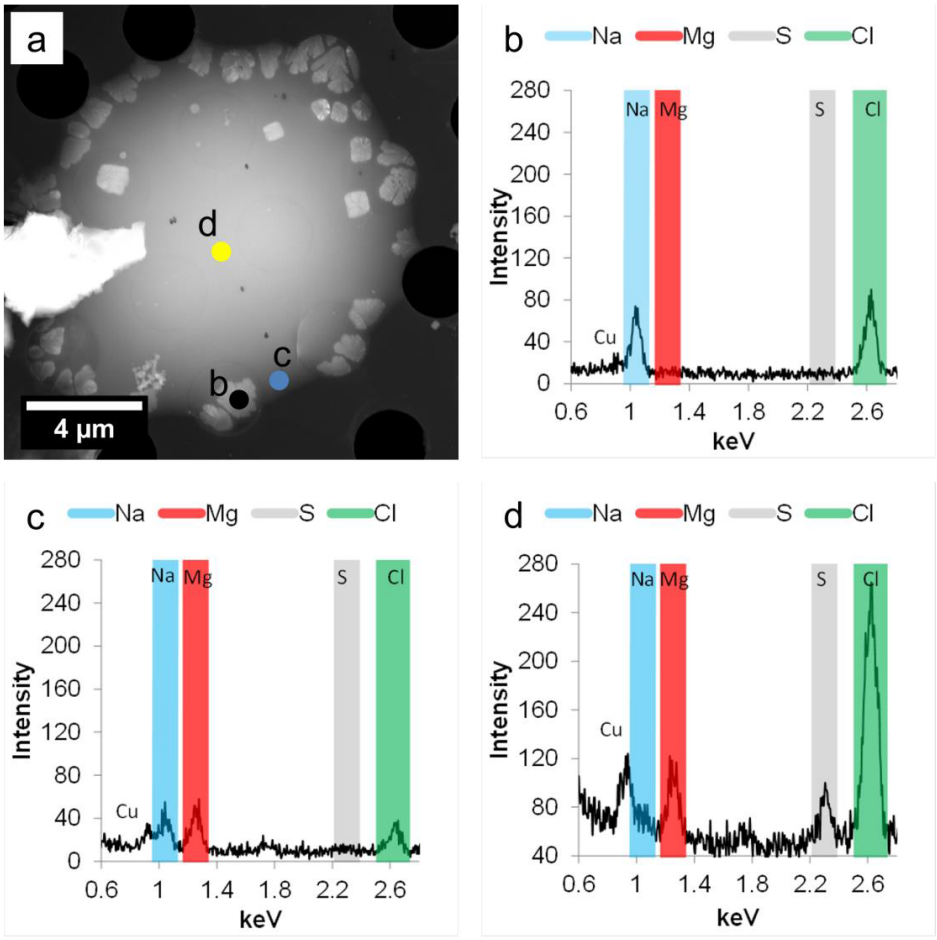


**Figure S5.** HADDF STEM image and EDS spectra for particles collected at stage 2. a) HADDF STEM images where the colored dots and letter show the location of the EDS spectra, b) An EDS spectrum collected from one of the salt crystals at the edge of the SSA showing its composition is NaCl, c) An EDS spectrum collected from the edge of the SSA, but in the continuous phase (i.e. not on a salt crystal) showing a relatively even composition of Na and Mg and d) EDS collected from the center of the particle showing that a high relative amount of Mg over Na. As discussed in the main text, the general conclusion to this data is that, as the particle dehydrate and effloresce, NaCl crystals form on the particle surface, which leads to a depletion of Na from the core of the SSA. As indicated in the spectra there in a slightly overlapping Cu peak from the substrate, which would interfere with quantitative analysis of the Na and Mg ratio, however qualitatively this does not impact the general conclusion.

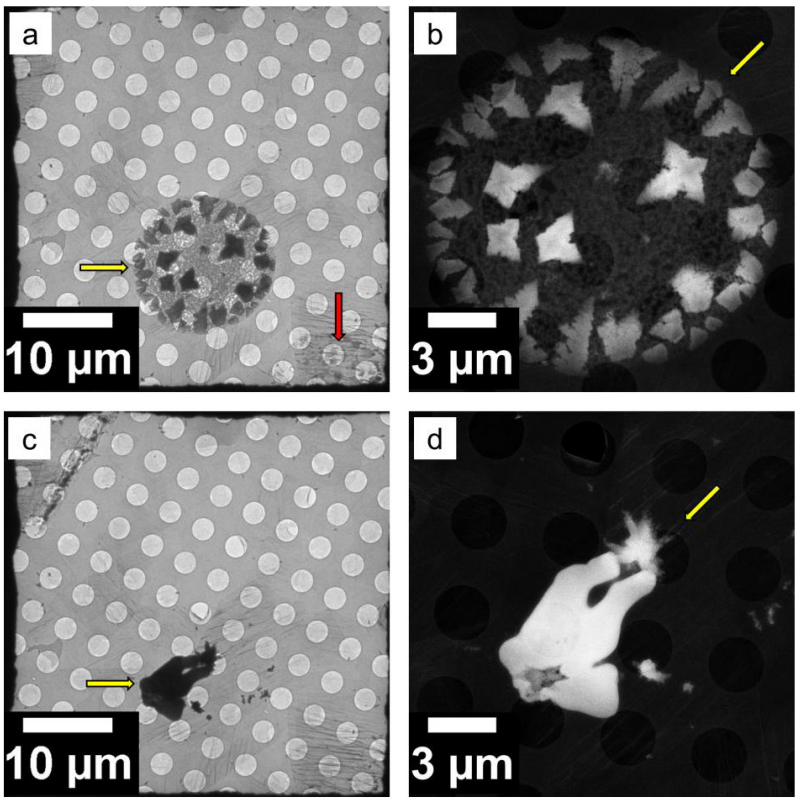


**Figure S6.** (S)TEM images for the SSA collect by cryo-TEM in Figure 1b, a) and b) bright field TEM and HAADF STEM images respectively after warming inside the microscope to room temperature and c) and d) bright field TEM and HAADF STEM images respectively after removing the sample from the microscope and reinserting into the microscope and thereby exposure the sample to high vacuum.

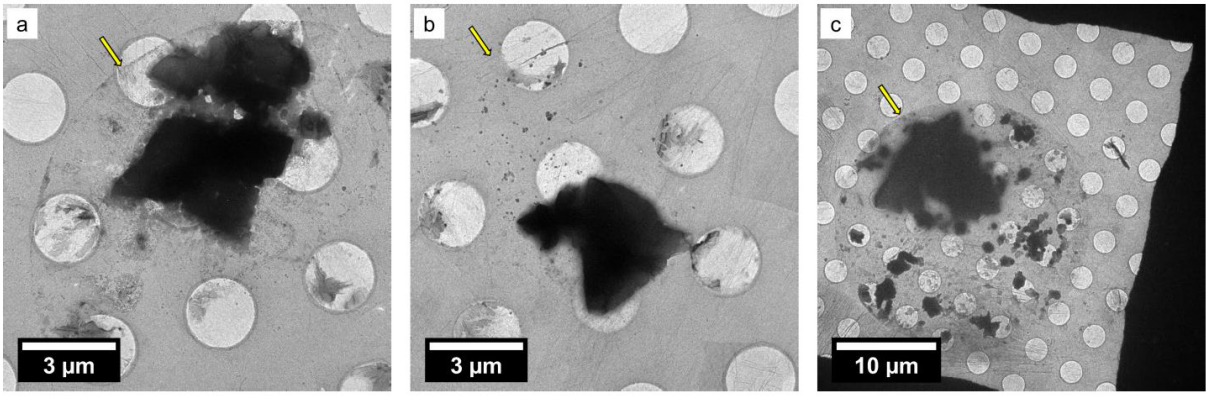


**Figure S7.** Additional bright field TEM images of SSA collected at stage 3. The yellow arrows indicate the edge of the SSA.

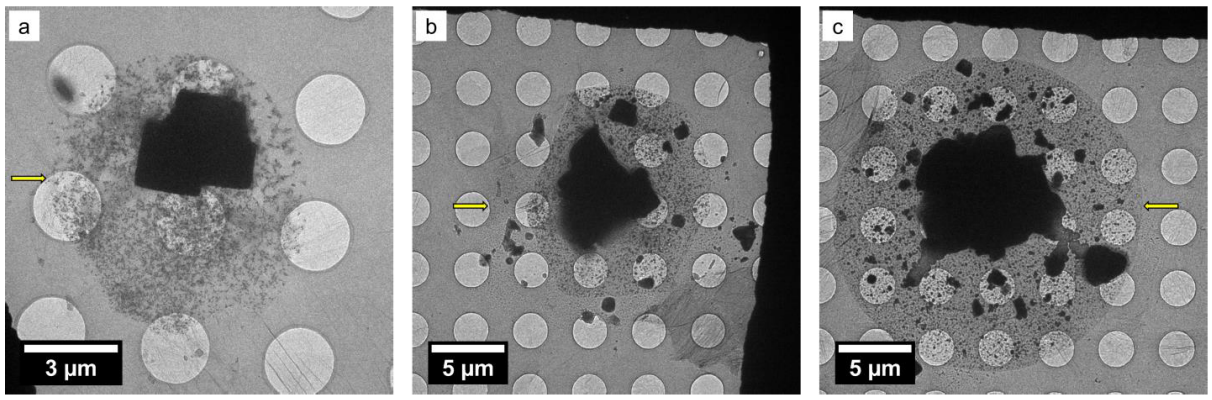


**Figure S8.** Additional bright field TEM images of SSA collected at stage 4. The yellow arrows indicate the edge of the SSA.

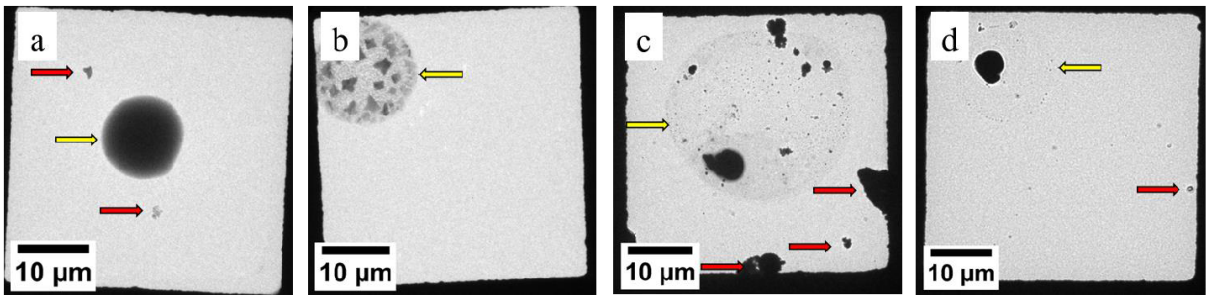


**Figure S9.** Analogous to Figure 1 in the main text, where SSA particles were collected on hydrophobic amorphous carbon grids after different stages of reorganization and images by bright field TEM. a) stage 1, nascent SSA, b) stage 2, efflorescence, c) stage 3, after laboratory drying and aging and d) stage 4 after exposure to high vacuum. The yellow arrows indicate the edge of the SSA and the red arrows indicate contamination from the cryo-TEM preparation.

**Determination of biological structure from the cryo-TEM images:**

The cryo-TEM images give a 2D projection of the SSA particles and consequently the assignment of biological structures inside the SSA is based on their size, shape and morphology. The following is a brief description of the biological structures found inside SSA particles, in the SSML or bulk sea water in this study.

Bacterial cells:[5]

Size Approximately 1-2 microns in length

Shape; Rod like

Morphology: Contains a membrane . A membrane is defined as (in a bright field imaging mode) a dark ring around the particles, indicating an increased mass around the exterior of the particle

Virus:[5]

Size <300 nm

Morphology: faceted features.

Membrane vesicle: [6]

Size < 500 nm,

Shape: Largely spherical, although some membrane vesicles in the SSA appeared to be distorted, Figure 3 a) and b),

Morphology: Contains a membrane structure.

Diatom: [7]

Size > 1 micron

Morphology: A silicon containing cell wall. Note: the presence of Si was determined by EDS analysis, shown in Figure S10. Note, no Si was detected in the background spectra collected for the same dwel time.

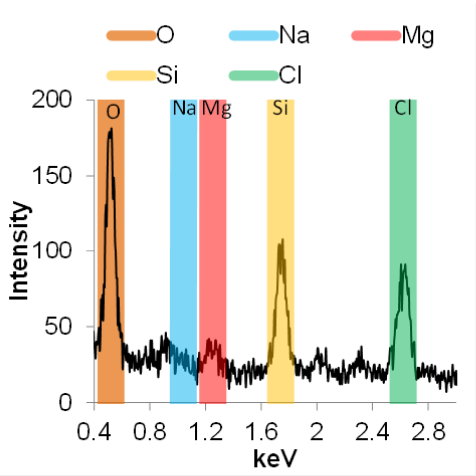


**Figure 10.** EDS spectra for the particle shown in Figure 2b, strong signal from Si indicated this is likely a diatom. Note, no Si was detected in the background spectra collected for the same dwel time.

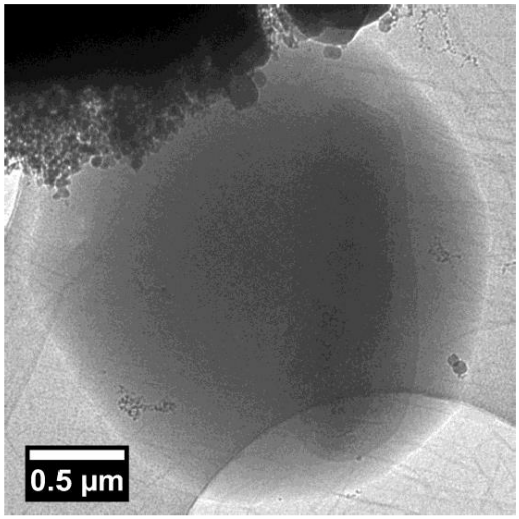


**Figure S11**. Original unprocessed bright field TEM image corresponding to the processed image in Figure 2a.

**Calculation for the number of vesicle per mL by supported cryo-TEM:**

The calculation assumes that all vesicles in the 7 µL drop become attached to the GO surface on the carbon film of the TEM grid. Therefore the concentrations of vesicles are likely an underestimation as it is likely that not all vesicles will become attached.

The calculation can then be performed in two ways:

Method 1:

Concentration of vesicles per mL = calculated total number of vesicles on the TEM grid x 1000/7

Calculated total number of vesicles on the TEM grid = the average number of vesicles found per area x the number of areas per grid square (160) x the number of grid squares (400)

OR

Method 2:

Concentration of vesicles per mL = calculated total number of vesicles on the TEM grid x 1000/7

Calculated total number of vesicles on the TEM grid = the average number of vesicles found per area x the number of areas per grid (4*π*15002/7.4) (based on the total size of the 1.5 mm TEM grid and the area of each image which is 7.4 µm2)

Table S1. Summary of vesicle counting studies by GOx-cryo-TEM for the SSML and bulk samples. For each sample the area size was 3 $\mu m^2$ and 500 areas were imaged

| Sample | Average number of vesicles per area | Vesicles per mL based on method 1 | Vesicles per mL based on method 2 |
|---|---|---|---|
| SSML run 1 | 0.152 | 1.40E+06 | 8.30E+07 |
| SSML run 2 | 0.066 | 6.07E+05 | 3.60E+07 |
| Bulk run 1 | 0.03 | 2.76E+05 | 1.64E+07 |
| Bulk run 2 | 0.04 | 3.68E+05 | 2.18E+07 |

As discussed above it is likely that not all vesicles become attached to the grid and therefore both calculations are likely an underestimate and the real value is probably closer to method 2, which we believe is roughly accurate to within an order of magnitude.

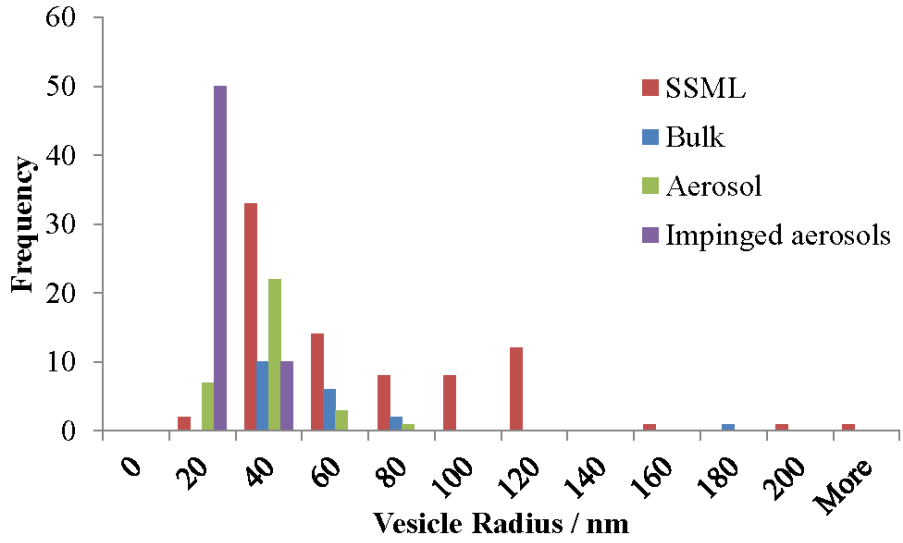


**Figure 12.** Typical size distribution data for vesicles in the SSML (red), bulk (blue), aerosols collected by capturing by cryo-TEM (green) and impinged aerosols (purple).

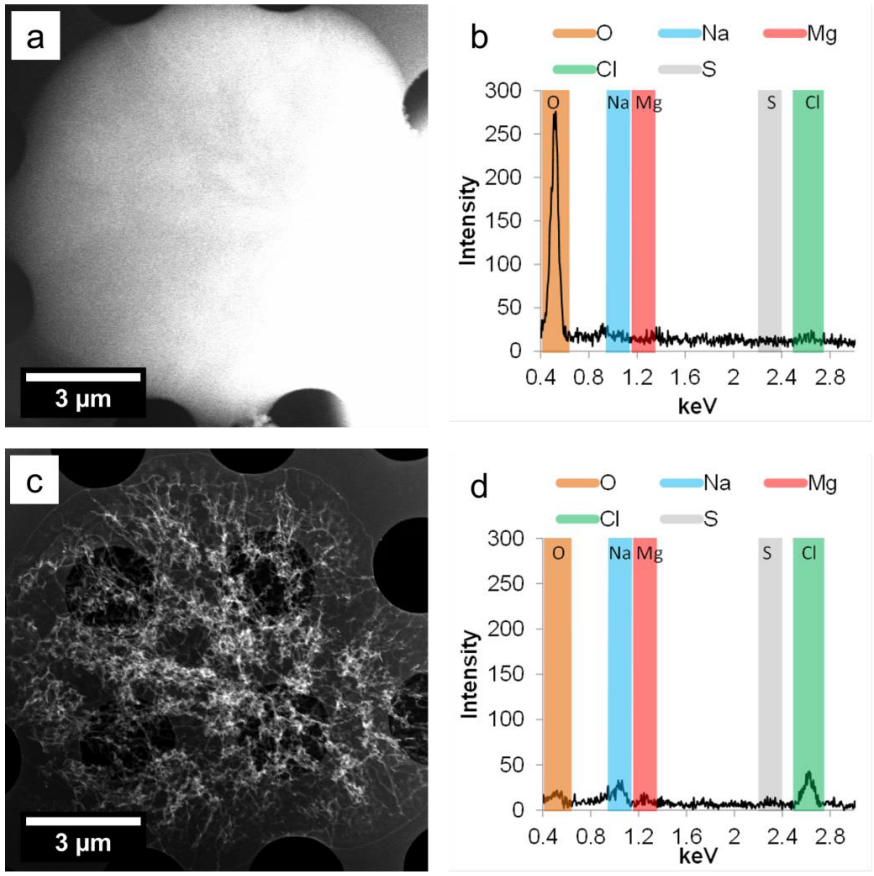


**Figure S13.** HADDF STEM images and EDS spectra for gel SSA particles. A) cryo-HADDF STEM for a wet particles and b) corresponding EDS spectra taken from the center of the particle, c) HADDF-STEM image for the same particle in a) but after selective dehydration and d) corresponding EDS spectra taken from the center for the particle.

**References:**


1. Lee, C.; Sultana, C. M.; Collins, D. B.; Santander, M. V.; Axson, J. L.; Malfatti, F.; Cornwell, G. C.; Grandquist, J. R.; Deane, G. B.; Stokes, M. D.; Azam, F.; Grassian, V. H.; Prather, K. A., Advancing Model Systems for Fundamental Laboratory Studies of Sea Spray Aerosol Using the Microbial Loop. *J Phys Chem A* 2015, *119* (33), 8860-70.
2. Wang, X.; Sultana, C. M.; Trueblood, J.; Hill, T. C. J.; Malfatti, F.; Lee, C.; Laskina, O.; Moore, K. A.; Beall, C. M.; McCluskey, C. S.; Cornwell, G. C.; Zhou, Y.; Cox, J. L.; Pendergraft, M. A.; Santander, M. V.; Bertram, T. H.; Cappa, C. D.; Azam, F.; DeMott, P. J.; Grassian, V. H.; Prather, K. A., Microbial Control of Sea Spray Aerosol Composition: A Tale of Two Blooms. *ACS Central Science* 2015, *1* (3), 124-131.
3. (a) Patterson, J. P.; Sanchez, A. M.; Petzetakis, N.; Smart, T. P.; Epps, I. I. I. T. H.; Portman, I.; Wilson, N. R.; O'Reilly, R. K., A simple approach to characterizing block copolymer assemblies: graphene oxide supports for high contrast multi-technique imaging. *Soft Matter* 2012, *8* (12), 3322-3328; (b) Wilson, N. R.; Pandey, P. A.; Beanland, R.; Young, R. J.; Kinloch, I. A.; Gong, L.; Liu, Z.; Suenaga, K.; Rourke, J. P.; York, S. J.; Sloan, J., Graphene Oxide: Structural Analysis and Application as a Highly Transparent Support for Electron Microscopy. *ACS Nano* 2009, *3* (9), 2547-2556.
4. Malis, T.; Cheng, S. C.; Egerton, R. F., EELS log-ratio technique for specimen-thickness measurement in the TEM. *Journal of Electron Microscopy Technique* 1988, *8* (2), 193-200.

5. Leck, C.; Bigg, E. K., Biogenic particles in the surface microlayer and overlaying atmosphere in the central Arctic Ocean during summer. *Tellus B; Vol 57, No 4 (2005)* 2005.
6. Biller, S. J.; Schubotz, F.; Roggensack, S. E.; Thompson, A. W.; Summons, R. E.; Chisholm, S. W., Bacterial Vesicles in Marine Ecosystems. *Science* 2014, *343* (6167), 183-186.
7. Hevia-Orube, J.; Orive, E.; David, H.; Díez, A.; Laza-Martínez, A.; Miguel, I.; Seoane, S., Molecular and morphological analyses of solitary forms of brackish Thalassiosiroid diatoms (Coscinodiscophyceae), with emphasis on their phenotypic plasticity. *European Journal of Phycology* 2015, 1-20.

**Acknowledgements**

Chapter 4, in full, is a reprint of material as it appears: J. P. Patterson, D. B. Collins, J. M. Michaud, J. L. Axson, C. M. Sultana, T. Moser, A. C. Dommer, J. Conner, V. H. Grassian, M. D. Stokes, G. B. Deane, J. E. Evans, M. D. Burkart, K. A. Prather, N. C. Gianneschi. "Sea spray aerosol structure and composition using cryogenic transmission electron microscopy." *ACS Cent. Sci.* ***2***(1*)*, 40–47 (2016). The dissertation author is a contributing author of this manuscript. The dissertation author contributed experimental design, set-up, and bacterial culturing to the work outlined in this chapter.

## Chapter 5. Selective transfer of bacteria and viruses from the ocean to the atmosphere

Ocean-derived microbes play important roles in Earth's climate system and human health, yet little is known about factors controlling their transfer, or aerosolization, from the ocean to the atmosphere. This study describes the microbiomes of isolated sea spray samples collected in a unique ocean-atmosphere facility that demonstrate taxon-specific transfer across the air-sea interface via common aerosolization patterns between related genomes. These trends were conserved within taxonomic orders and classes, and temporal variation in aerosolization was similarly shared by related taxa. Enhanced transfer into sea spray aerosol (SSA) was observed in Actinobacteria, select Gammaproteobacteria, and lipid-enveloped viruses; conversely, Flavobacteriia, select Alphaproteobacteria, and *Caudovirales* were generally under-represented in SSA. Viruses did not transfer to SSA as efficiently as bacteria. The enrichment of mycolic acid-coated Corynebacteriales and lipid-enveloped viruses suggests hydrophobic properties increase transport to the sea surface and SSA. These results indicate genome-encoded properties influence aerosolization and provide a framework to further elucidate aerosolization mechanisms, which will have ramifications for elucidating airborne transport pathways, ecosystem dynamics, and precipitation processes.

## Section 5.1 Introduction

A fundamental understanding of how bacteria and viruses become airborne remains elusive yet is central to understanding their role in atmospheric processes and the spread of disease. Microbial transmission and survival are influenced by particle size, relative humidity, temperature, environmental composition, and virus type[1–3], yet the mechanisms leading to airborne transmission and adaptations are unknown. The atmosphere contains vast bacterial ($6 \times 10^4$ to $1.6 \times 10^7$ cells $m^{-3}$) and viral populations arising from a wide range of aquatic, terrestrial, and organismal biomes[4–7]. As the ocean covers 71% of the planet and contains 60—90% of the world's prokaryotes (cell abundance in open ocean and sediment)[8], sea spray aerosol (SSA) represents a significant yet largely under-studied source of airborne bacteria and viruses. Bacteria in aerosols can travel as far as 11,000 km, with air residence times of days to weeks[1,5,9], and algal viruses maintain infectivity over several hundred kilometers[10]. Airborne bacteria and viruses influence climate by serving as cloud seeds and inducing ice nucleation[11–14]. Microbes detected in clouds and precipitation have major impacts on ice formation and precipitation efficiency yet their source remains largely unknown[15]. They also impact air quality through transmission of allergens and pathogens[16]. However, identification of species-level contributions of ocean microbes to atmospheric processes and air quality has never been definitely determined.

The production of SSA is a key process connecting the nanobiome of seawater to the atmosphere. SSA is formed through bubble bursting occurring in the sea surface microlayer (SSML), the top 1–1000 μm of seawater. The SSML can act as a concentrator for organic molecules, microbes, and viruses[17,18] prior to their release as SSA[19–23]; however, oceanic observations of bacterial SSML enrichment are inconsistent[24–26] suggesting unknown influences. Jet drops containing bulk seawater can also transfer microbes from the ocean to the atmosphere[27]. Cultivation-based studies have observed differential transfer of bacteria to SSA in lab-scale systems[28,29]. While these studies do not access microbial diversity or produce natural SSA, they suggest taxon-specific aerosolization dynamics.

Studying aerosolization in natural systems is prohibitively difficult because confounding factors such as ocean and atmospheric circulation patterns prevent deconvolution of terrestrial and marine sources of airborne microbes[30]. Until now, most laboratory generation systems that produce isolated sea spray aerosols have not appropriately replicated natural aerosolization processes[31]. Accordingly, an ocean–atmosphere facility, developed collaboratively by chemists, oceanographers, and marine biologists was employed to study microbial aerosolization in a controlled setting using locally-derived seawater and breaking waves[32]. This 13,000 L, enclosed system is supplied with filtered air and is conducive to microbial growth at ocean-relevant concentrations. It was verified experimentally to produce isolated SSA with the same size distributions,

composition, and properties as those occurring in the atmosphere[32]. To examine if transfer was taxon-specific and sensitive to environmental changes, we characterized bacterial and viral communities sampled from bulk (subsurface), SSML, and SSA at several timepoints during a 34-day nutrient-induced bloom event in this simulated natural ecosystem using read- and assembly-based metagenomic approaches.

**Section 5.2 Results and Discussion**

*Mesocosm phytoplankton blooms*

Aerosol transfer of bacteria and viruses was monitored over 34 days of nutrient-stimulated phytoplankton blooms in a 13,000 L mesocosm. Filtered (50 µm) coastal Pacific seawater (32°52'01.4"N 117°15'26.5"W) was supplemented with nitrate, phosphate, and trace metals to induce phytoplankton growth under continuous illumination (45 µE $m^{-2}$ $s^{-1}$) with mixing provided by wavebreaking or bubbling (see methods). Exogenous carbon was not added. The conditions generated two phytoplankton blooms and corresponding heterotrophic bacterial blooms (Figure 5.1a). Growth was monitored using chlorophyll *a* fluorescence to track bulk phytoplankton abundance and cell and virus counts in bulk seawater, SSML, and SSA (Figure 5.1a, Figure S5.1c). Bulk chlorophyll *a* levels, cell counts, and viral counts were representative of natural oceanic bloom concentrations[8,33,34]. Due to the proximity of the SSA collection ports to the breaking waves, the average aerosol bacterial concentrations (1.26

x $10^7$ ± 0.19 x $10^7$ cells $m^{-3}$) were 1000-fold greater than those estimated in natural environments[9]. Aquatic bacterial abundance moderately increased with phytoplankton populations during the first phytoplankton bloom, while the peak for the second bacterial bloom was both larger in intensity and slightly delayed from the phytoplankton peak. The concentrations of bacterial cells in the bulk and SSML were positively correlated, while aerosol abundances were negatively correlated with seawater population. Bacteria were not immediately released into SSA from SSML, suggesting dynamics that depend on growth and accumulation in the bulk seawater and SSML prior to atmospheric release. In seawater, virus concentrations are generally 5 to 25 times greater than bacteria[35], and here we observed 10-fold greater bulk viral concentration by cell and particle counts (Figure 5.1a, Figure S5.1c). However, average SSA concentrations of viruses (1.19 x $10^7$ ± 0.58 cells $m^{-3}$) and bacteria were nearly equivalent indicating preferential aerosolization of bacteria relative to viruses.

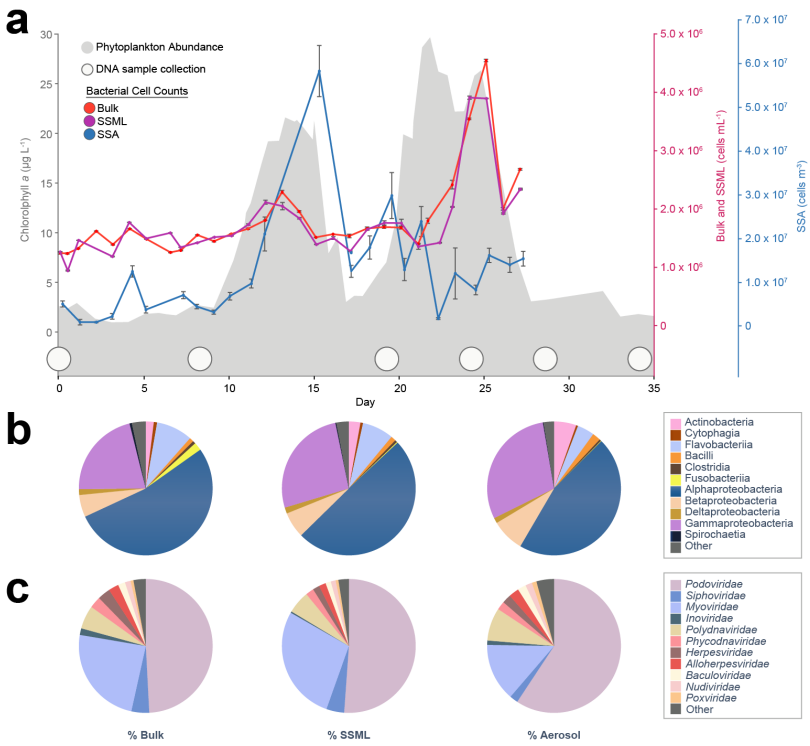


Figure 5.1 Bacterial and viral abundance across phytoplankton blooms. (a) Phytoplankton abundance is indicated by chlorophyll *a* fluorescence (gray). Bacterial cell counts by flow cytometry are shown for bulk (red), sea surface microlayer (SSML) (violet), and sea spray aerosol (SSA) (blue). 1 $m^3$ = $10^6$ mL of air volume. Time points for taxonomic analysis are indicated by white circles. (b) Average percent of dominant bacteria classes and (c) average percent of dominant virus families during the blooms are shown for bulk, SSML, and SSA. Identities are from read–based analysis.

*Genome Assembly and Taxonomic Classification*

Bacterial and viral genomes were identified in bulk seawater, SSML, and SSA at six time points over the course of the experiment using size-fractionated metagenomics (Figure 5.1). Following sequencing, both read-based (Kraken[36]), and assembly-based approaches[37,38] were used to taxonomically characterize microbial communities in the bulk, SSML, and SSA. Comparisons between these methods were used to substantiate read-based annotations and aerosolization trends. Spatial scaffold coverage of detected genomes was inspected, and

genomes below a spatial coverage threshold (0.1%) were removed. Assembly of k-mer and coverage-based binned contigs resulted in 24 draft genomes. These assemblies were also cross-annotated annotated using Kraken, with similar phylogenetic results based on whole genome and read analyses (Table S5.1).

Phytoplankton bloom-associated copiotrophs—Alphaproteobacteria (Roseobacters), Flavobacteriia, and Gammaproteobacteria[39–41]—were proportionately most abundant during the experiment, but comparisons between bulk, SSML, and aerosol community compositions reveal key differences (Figure 5.1b). The aquatic microbial population shifted significantly from the original oceanic composition, but after Day 8 remained relatively constant for the duration of the experiment (Figure S5.1a). The blooms also contained taxa not often found in seawater including an avian strain of *Escherichia coli* and a novel strain of *Legionella,* as revealed by assembly of nearly complete genomes (Table S5.1, Table S5.4, Table S5.5). The novel *Legionella* strain has 70–80% amino acid identity to orthologs in *Legionella pneumophila* (Legionnaires' disease) and *Legionella drancourtii* and has both Type II and Type IV secretion systems typical of pathogenic strains (Table S5.5). *E. coli* and *Legionella* were present in initial samples, suggesting they were native to the coastal community but became enriched in our system during the experiment. The recovery of these genomes is consistent with increasing evidence for enteric contaminants in coastal marine waters[42,43].

*Podovirdae* and *Myoviradae* were the most common viruses identified in raw read assignments, and the viral population varied across the air–sea interface (Figure 5.1c). Populations shifted slightly from the initial community and were more dynamic during the bloom than the bacterial populations (Fig S5.1b). Draft genomes were recovered for several bacteriophage as well as an NCLDV (nucleoplasmic large DNA virus) (Figure S5.6, Table S5.5).

*Bacterial Aerosolization*

To examine the transfer of annotated genomes across the air-sea interface, we compared relative abundances in bulk seawater, SSML, and SSA. The relative enrichment occurring in the sea-to-air exchange process was determined by calculating the aerosolization factor (AF) for each genome in the 0.2–3 μm size fraction for bacteria and 0.025–0.2 μm for viruses. This is defined as the ratio of the fraction in SSA (A) to the fraction in bulk seawater (B) or the fraction in the SSML (S) (Eq. 1). Surface enrichment factors are calculated similarly using the ratio of S to B (S:B).

$$\text{AF (Aerosolization Factor)} = \frac{\text{Species fraction in Aerosol (A)}}{\text{Species fraction in Bulk (B) or SSML (S}} \quad \text{(Eq. 1)}$$

Genomes that contributed less than 0.01% to the population in any sample or less than 0.1% in more than half of samples were omitted. The AFs for bacteria and viruses over the course of the bloom are shown in Figure 4.2a. The top-right quadrants (red) of Figure 5.2 indicate genomes enriched in aerosol relative to both bulk and SSML (A:B and A:S > 1); the bottom-left quadrants (blue) indicate

genomes that are primarily waterborne (A:B and A:S < 1). The upper-left quadrants indicate species enriched relative to bulk but not SSML (A:B > 1, A:S < 1), and the bottom-right indicates species enriched in aerosol relative to the SSML but not bulk (A:B < 1, A:S > 1). A Gaussian distribution of species, centered at (1,1), would be expected if aerosolization was random. However, the "spindle" shaped distribution of the data reveals non-random patterns. The distribution is similar in the genome spatial coverage trimmed data set (Fig S5.2a). Histograms and normality analysis revealed positively skewed data with a non-normal distribution and mean bacterial AF of 0.90 (Figure S5.3a, g). Genomes predominantly exhibit SSA enrichment or depression with respect to both bulk and SSML. While water enriched species (AF values less than 1) represented 52% of the population, aerosol enrichment was much larger in amplitude than diminishment, reflected in a greater extension of data points into the red region compared to the blue region of Figure 5.2a. The average maximum AF value is 2 times larger in amplitude than the average minimum value.

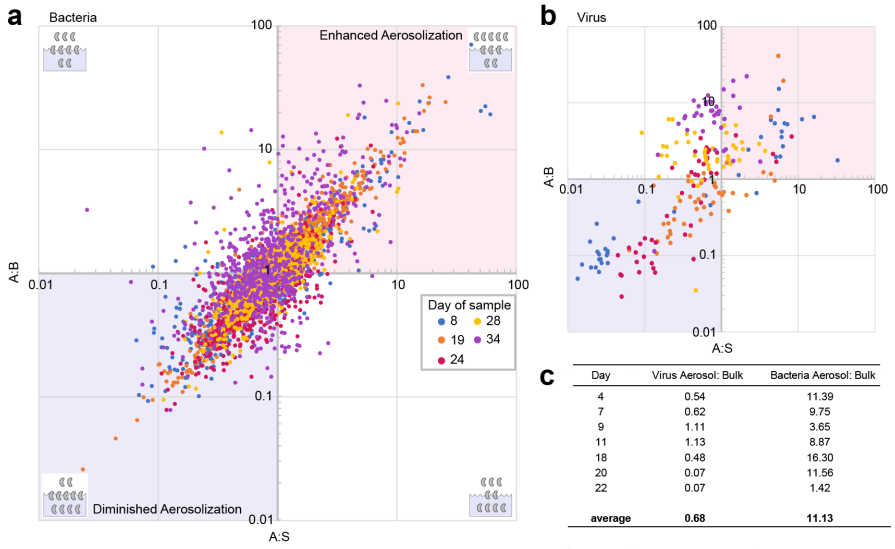


c

| Day | Virus Aerosol: Bulk | Bacteria Aerosol: Bulk |
|---|---|---|
| 4 | 0.54 | 11.39 |
| 7 | 0.62 | 9.75 |
| 9 | 1.11 | 3.65 |
| 11 | 1.13 | 8.87 |
| 18 | 0.48 | 16.30 |
| 20 | 0.07 | 11.56 |
| 22 | 0.07 | 1.42 |
| **average** | **0.68** | **11.13** |

Figure 5.2 Aerosolization of bacterial and viral genomes across the blooms. The ratio of fraction of genomes in aerosols to the fraction in bulk (A:B) plotted against ratio of fraction of genomes in aerosols to those in sea surface microlayer (A:S) is shown for bacteria, (a), and viruses, (b), on select days. The upper right quadrants (red) of (a) and (b) indicate genomes enriched in aerosol relative to both bulk and SSML (A:B and A:S > 1); the lower left quadrants (blue) indicates genomes that are primarily waterborne (A:B and A:S < 1). The upper left quadrants indicates genomes enriched relative to bulk but not SSML (A:B > 1, A:S < 1), and the lower right indicates species enriched in aerosol relative to the surface but not bulk (A:B < 1, A:S > 1). The data sets represent (a), 710 bacterial genomes, and (b), 46 viral genomes identified by read–based taxonomic assignments. Graphics in the corners various quadrants in (a) show examples of expected species ratios in indicated portion of graph. In (c), the fraction of aerosol to bulk virus and bacteria counts by flow cytometry and microscopy on indicated days is shown.

A genetic signal in bacterial AF is evident at fine-scale taxonomic levels when individual genomes are compared (Figure 5.3a, Figure S5.4–5.7). Closely related species have nearly identical aerosolization patterns that are propagated across environmental and enrichment changes. Genomes within the same class (Actinobacteria and Flavobacteriia) or order (Rhodobacteriales, Sphingomonodales, and Alteromonadales) typically have similar aerosolization profiles. Examples of bacterial genomes with consistently high AF values include *Rhodococcus erythropolis*, *Cutibacterium acnes*, and *Methylobacterium radiotolerans*. Conversely, genomes such as *Flavobacterium indicum*,

*Cellulophaga lytica,* and *Erythobacter litoralis* had persistently low AFs. The low AF values of the *Erythobacter* draft genome provide ancillary assembly based evidence for the read based analysis (Figure S5.6).

Comparisons of temporal phylogenetic patterns provide critical information needed to determine aerosolization mechanisms, especially in rare cases where a species' aerosolization departs from other members of its genus, order, or class (Figure 5.3a, i–ii). For example, *Corynebacterium kroppenstedtii* and *C. aurimucosum* are the same genus yet have opposite aerosolization patterns (Figure 5.4a, i). Likewise, the low AF values of *Moraxella catarrhalis*, depart from the other more aerosolized Pseudomonadales members (Figure 5.4a, ii). Direct observations and *in silico* compositional, genomic, and metabolomic studies guided by divergent aerosolization patterns of closely related genera will provide a biochemical basis for aerosolization biases further discussed below.

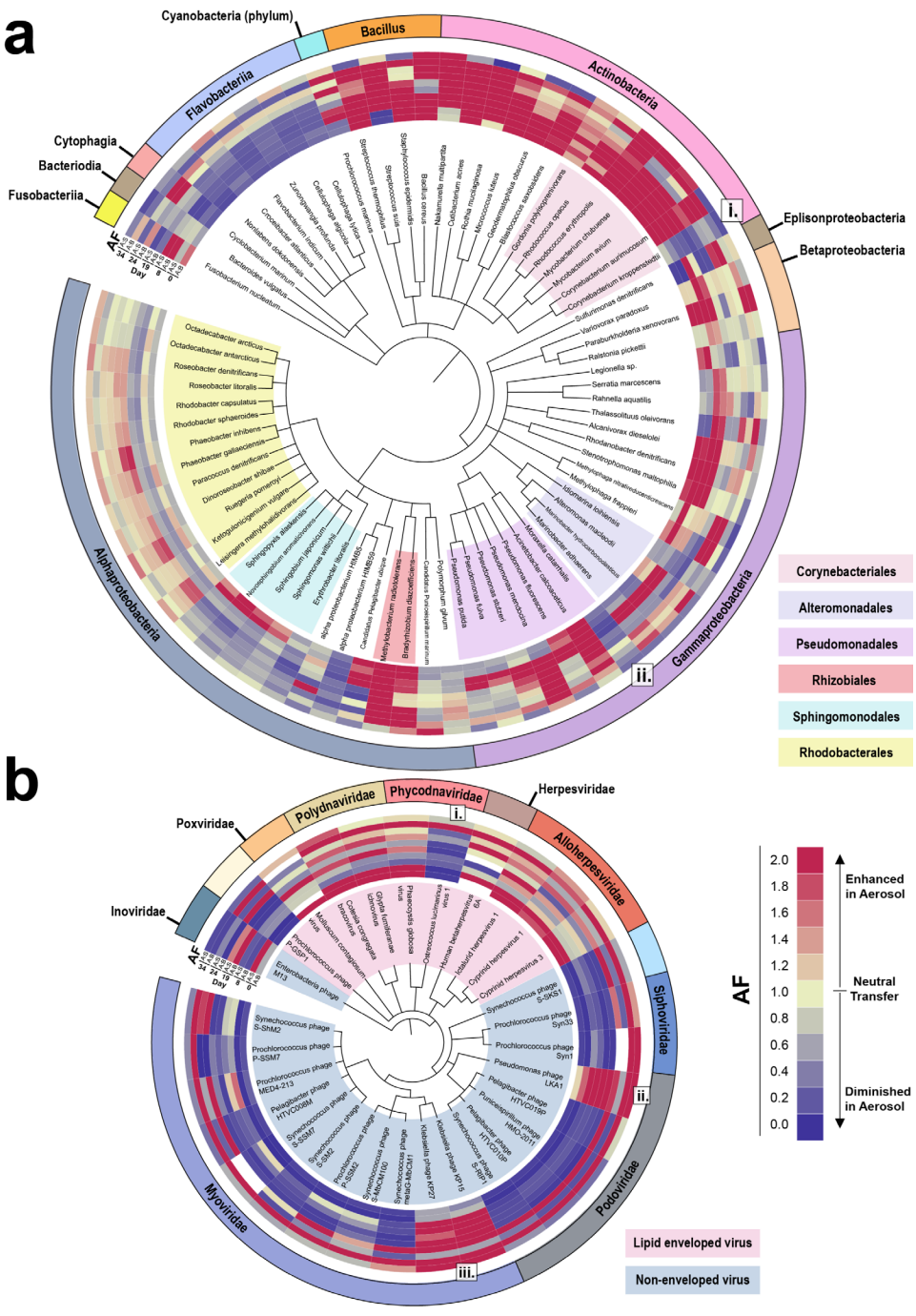


Figure 5.3 The taxonomic basis of bacterial and viral aerosolization. Genome-based phylogenetic trees from read-based annotations trimmed of genomes with low spatial coverage: (a) 76 bacterial genomes and (b) 30 viral genomes. Aerosolization factors (AF), A:B and A:S, on different days are indicated (Blue = Diminished aerosolization; Yellow = Neutral aerosolization; Red = Enhanced aerosolization). Blanks indicate samples below threshold limits. (a) Bacteria class is indicated on outer ring to further indicate species and shading of species names indicate orders of interest. In (b), the outer ring denotes viral family and shading indicates presence or lack of a viral envelope. (a)i., ii. and bi.–iii. Indicate genomes with aerosolization patterns that differ from their closest relatives. Trees generated using phyloT (http://phylot.biobyte.de/) and iTOL (http://itol.embl.de/).

*Viral Aerosolization*

Quantitatively, viruses did not aerosolize as efficiently as bacteria (Figure 5.2c). The ratio of average bacterial count in aerosol (cells $m^{-3}$) to bulk (cells $mL^{-1}$) was 11.13, while the average virus counts in aerosol (particles $m^{-3}$) to bulk (particles $mL^{-1}$) was 0.68. In contrast, surface enrichment is approximately the same for both (0.98 and 1.02 for bacteria and viruses, respectively). In read-based sequence analysis, the proportion of viruses in aerosol at the division level was consistently lower than bulk in all size fractions (Figure S5.1d). Decreased viral transfer is further supported by comparisons of data distributions of viral and bacterial communities (Figure S5.3). Viral distributions were shifted more negative and had lower mean AFs than bacterial populations (viral- 0.72 ± 4.70, bacterial- 0.90 ± 2.32). Studies in pathogen transmission suggest that smaller bioaerosol size leads to increased residence time in the air[1,2]. However, these results indicate that size is not the only contributor to marine viral aerosolization, and active host infection is likely a dominant mechanism.

Despite depressed aerosolization relative to bacteria, differential transfer of select and functionally specific viral genomes into SSA was observed (Figure 5.2b). However, the viral AF factors cluster around different values according to sampling date, indicating broad environmental parameters affect the aerosolization of most viruses; bacterial AFs demonstrate a more linear relationship less dependent on environmental variance (Fig 5.2a, Figure S5.3e).

The temporal clustering (Figure 5.2b) is further observed in shared aerosolization by most taxa on a given day as seen by bands of similar AF intensity in Figure 5.3b.

Taxon-specific patterns were also detected; however, aerosolization differences seem to delineate across the broader physiological trait of viral envelopes in addition to taxonomic order (Figure 5.3b, Figure S5.5–S5.6, S5.8). Non-enveloped viruses are less enriched in aerosol compared to lipid-enveloped species. The tailed bacteriophage, *Caudovirales* (*Myoviridae*, *Podoviradae*, and *Siphoviridae*), were generally waterborne as were phage identified in the binned assemblies (Figure S5.6); lipid-enveloped *Polydnavirdae* and *Alloherpesviridae* were enriched in aerosol. Similar to bacteria, select genomes differed from their closest relatives in their aerosolization behavior. *Ostrecoccus lucimarinus* virus 1 (Figure S5.3b, i) was greatly diminished in aerosol unlike its relatives, while *Pseduomonas* phage LKA1, *Klebsiella* phage KP15, and *Klebsiella* phage KP27 (Figure 5.3b, ii–iii) were consistently aerosol enriched in comparison to the other bacteriophage. These results indicate that many viruses have aerosolization patterns governed by global environmental conditions and general morphological characteristics.

*Temporal Dynamics*

As observed in the AF values of individual genomes, some bacteria and viruses demonstrated consistent behavior (enhanced or diminished) during the

blooms, while others exhibited intermittent aerosolization enrichment patterns (Figure 5.4, Figure S5.4–S5.8). Constitutive aerosolization, defined here as when 80% of a species' observed AF values were either all greater or less than 1, was present in 45% of the bacterial genomes and 35% of viruses. Constitutive aerosolizers like *Rhodococcus erythropolis*, *Flavobacterium indicum*, and *Pseudomonas* phage LKA1 likely have a surface composition that supports or inhibits aerosolization. Intermittent aerosolizers, such as *Dinoroseobacter shibae*, *Legionella* sp., or *Phaeocystis globosa* virus may undergo changes that alter physiological properties. For example, *Legionella pneumophila* is known to have both non-motile non-pathogenic and motile pathogenic phases of its lifecycle[44]. Thus, it could be postulated that such morphological changes dictate aerosolization, and intermittent release might promote host exposure.

Both constitutive and intermittent aerosolizers exhibit some variation in their AFs, indicating that environmental conditions influence aerosolization. The resulting changes in response to these external factors were also correlated across select taxa. This coordination is seen in intermittent Alphaproteobacteria and high AF lipid-enveloped viruses that were generally more waterborne on Day 8 (pre-bloom) while several Gammaproteobacteria genomes were aerosol enriched. During the second bloom (Day 28), when total seawater bacterial counts were high, Flavobacteriia and nearly all viral genomes became enriched in SSA (Figure 5.3). Because viruses were generally more intermittent than bacteria and share aerosolization patterns across taxa during a given time

period, viral aerosolization seems especially sensitive to chemical and biological water composition changes.

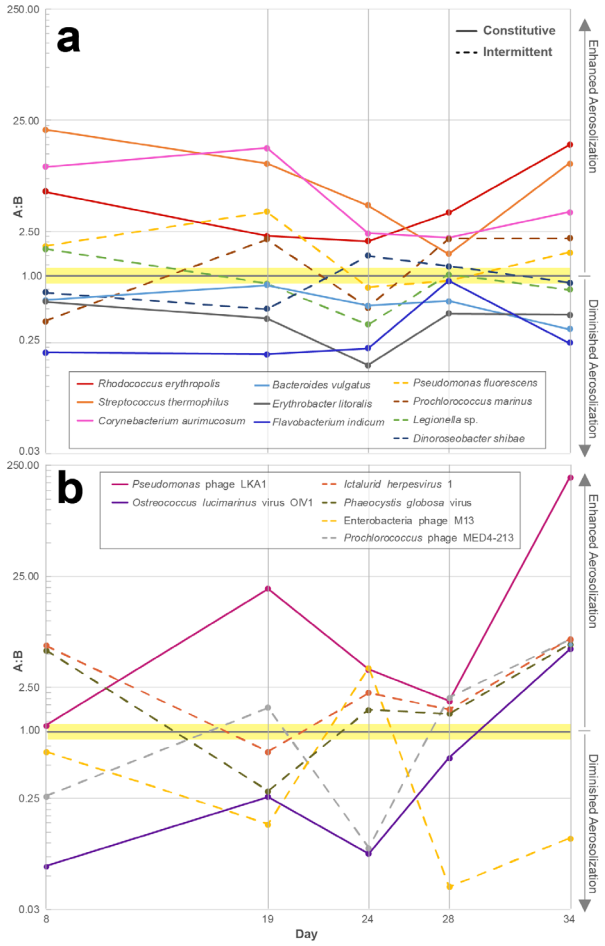


Figure 5.4 Temporal aerosolization dynamics. Intermittent versus constitutive aerosolization patterns are shown for select bacteria, (a), and viruses, (b), across the phytoplankton blooms. Solid lines indicate genomes that are always enriched or always diminished (constitutive). Dashed lines indicate intermittent genomes that demonstrate both states.

*Surface Enrichment*

Taxon-specific variation in surface enrichment demonstrated factors that support SSML accumulation also support aerosolization. Surface enrichment factors (S:B) predominately indicated SSML enrichment or neutral accumulation from bulk water (Figure S5.4, S5.6–S5.8), and the magnitude of the S:B and AF

values were positively correlated. The constitutive, low AF Flavobacteriia were the least surface-enriched with an average S:B of 0.95 compared to 1.92 for all species examined (Figure S5.4). Constitutively high AF Actinobacteria had a corresponding above average S:B of 3.92. Viruses were more surface-enriched than bacteria with an average S:B of 4.70 with a large contribution from global viral surface enrichment on Days 28 and 34 (Figure S5.8). The surface enrichment of most viral taxa on these days corresponded to global viral A:B enrichment (Figure 5.3b). Excluding these days, the average S:B falls to 1.70, low AF non-enveloped viruses have an average S:B of 1.70, and high AF enveloped viruses have an average S:B of 3.69. As SSML is organic-enriched[17], hydrophobic cell surface properties likely promote both surface enrichment and aerosolization. This taxon-specific surface accumulation also helps account for the disparate oceanic observations of microbial sea surface enrichment[24–26].

*Implications of Aerosolization Studies*

Guided by these results, comparative genomics of identified genomes indicate cell surface modifications influence aerosolization. The Gram-positive Actinobacteria had high and constitutive AF values. Within this class, Corynebacterales possess an unusual waxy coat consisting of mycolic acids made of ultra-long chain fatty acids ($C_{25\text{-}30,60\text{-}90}$)[45,46]. In contrast to the rest of its order, *C. kroppenstedtii* (Figure 5.3a, i) lacks mycolic acids[47], and this missing

hydrophobic cell envelope component may explain its reduced aerosolization relative to closely related strains.

The ability to rapidly desiccate and tolerate desiccation are important factors in viral pathogen transmission, as they increase the time particles remain aloft and viable[48,49]. Most respiratory viruses, like influenza and corona viruses, are lipid-enveloped and able to survive longer at low relative humidity (15–40%); non-enveloped viruses require a minimum of 70% humidity for viability[1,3]. Similar trends are echoed in these data (Figure 5.3b). Tailed bacteriophage utilize surface capsid proteins that are likely hydrophilic, while herpesviruses are lipid enveloped[50–52]. Here, *Caudovirales* were generally waterborne while *Herpesvirales* were aerosol enriched. Hydrophobic surface features probably assist in rapid cell desiccation, which is one potential mechanism of aerosolization and surface enrichment.

However, hydrophobicity is likely not the only mechanism of aerosolization and SSML enrichment. *Bacillus* strains, generally encapsulated in hydrated polysaccharide coatings[53], also had consistently high AF and S:B values (Figure 5.3a, Figure S5.4). Some Gammaproteobacteria in Pseudomondales are observed with capsules. *Moraxella catarrhalis* unlike its closest relatives had constitutive, low AFs (Fig 5.3a, ii.), and contradicting reports describe both the presence and lack of a cell capsule[54]. If different strains or growth conditions alter encapsulation states it could elucidate another potential aerosolization mechanism.

## Section 5.3 Conclusions

This study reveals the taxon-specific dynamics of viral and bacterial transfer across the air-sea interface during phytoplankton blooms. The enrichment is dictated by inherent biochemical properties and influenced by environmental conditions. Taxon-specific patterns are applied to reveal different aerosolization mechanisms. Species with enhanced aerosolization likely have a larger influence on climate properties, and studies with relevant isolates will clarify specific contributions to atmospheric processes. Several bacterial lineages of known respiratory and airborne pathogens are identified in this study, including *Legionella*, *E. coli*, *Corynebacterium,* and *Mycobacterium*. Factors that modulate SSA formation likely will apply to other aerosolization processes. Elucidating the specific aerosolization mechanisms of pathogens, either from environmental reservoirs or from hosts themselves, may form the basis of therapeutics that target aerosolization by interaction with surface features or inhibition of relevant biosynthetic pathways. These findings provide a framework to resolve such mechanisms.

## Section 5.4 Methods

*Waveflume mesocosm bloom*

The wavechannel was set up as described in Wang et al.[1]. 13,000 L of ocean water was collected off Scripps Pier in La Jolla, CA (32°52'01.4"N

117°15'26.5"W). Water was filtered using 50 µM Nitex mesh before transfer into the wavechannel tank to remove grazing zooplankton. The wavechannel is a 33 m × 0.5 m × 1 m (0.6 m water depth), enclosed, glass, growth system equipped with a hydraulic pump attached to a vertical paddle at one end. Each pulse created one simulated wave that broke midway through the channel just upstream of sampling ports and is calibrated to mimic aerosol formation that occurs during natural wave breaking[2]. Bloom conditions were initiated by the addition of F/2 medium (Proline, Aquatic Eco-Systems, Apopka, FL) supplemented separately with sodium metasilicate. F/2 is a common marine medium for algae cultivation that provides 880 µM $NaNO_3$, 36 µM $NaH_2PO_4 \cdot H_2O$, 70 µM $Na_2SiO_3 \cdot 9H_2O$ along with trace metals[3]. An additional 9 µM sodium phosphate was added to the wave flume on July 25, 2014 as phosphate was depleted in the system. No exogenous carbon or additional nutritional supplementation was given for bacterial cultivation. The tank was continuously illuminated (45 µE $m^{-2}$ $s^{-1}$). During periods when aerosols were not being collected, additional aeration was provided by bubbling with HEPA-filtered air through perforated tygon tubing at the bottom of the tank.

*Sample collection*

Samples were taken for DNA analysis on six days during the phytoplankton bloom from bulk water (2 L), sea surface microlayer (SSML, 200 mL), and aerosol (collected for 3 hours at a flowrate of 450 L / min) resulting in 18 samples total. Bulk samples were collected via siphon from 3 ft below the water

surface, and SSML samples were collected by the glass-plate method[4]. Aerosols were collected using a SpinCon®PAS 450-10A Portable Air Sampler (Scepter Industries) as described in Yooseph *et al*[5]. Prior to each sample collection, the SpinCon® was disinfected by autoclaving removable parts, soaking and/or spraying parts non-detachable or non-removable components with 70% ethanol where appropriate, and using new anti-microbial tubing. The inlet was plumbed directly to an outlet of the wave flume positioned ~3 ft downfield of the general position of the wave break. Aerosols for DNA anlaysis were concentrated into 7.5–10 mL of sterile PBS (pH 7.4) over 3 h of wave breaking. Samples for bacterial and viral counts were collected similarly, with the exceptions of aerosol, which were collected by impingement at 1 L $min^{-1}$ into sterile seawater. Samples for counts were immediately fixed in 0.05% glutaraldehyde, flash-frozen, and stored at –80 °C. A system flow variance of 10% was accounted for in aerosol standard deviations.

*Phytoplankton, cell and virus abundance*

Phytoplankton growth was monitored using a Turner AquaFluor fluorometer. Bacterial counts were performed at the University of Hawaii Department of Oceanography using Hoeschst 3442 staining and flow cytometry[6]. A Beckman–Coulter Altra flow cytometer (operated by the SOEST Flow Cytometry Facility, www.soest.hawaii.edu/sfcf) was connected to a Harvard Apparatus syringe pump for quantitative analyses. Viral counts were

determined on filtered samples (0.02-µm Anotop, Whatman Nucleopore®) using SYBR Green-I (ThermoFisher) staining and epifluorescence microscopy (Keyence BZ-X700)[7]. It was not possible to perform aerosol virus counts on replicate samples. Standard deviation reported reflects variance in air flows.

*DNA extraction*

Immediately after collection, samples were size fractionated by serially filtering on 3-µm polycarbonate filters (Whatman Nucleopore®), 0.2-µm polyethylsulphone filters (Pall Supor® 200), and then 0.025-µm mixed cellulose filters (MF-Millipore®). Filters were stored at –80 °C until extraction. DNA was extracted from the membranes according to Boström et al[8]. This included overnight lysis, phenol chloroform extraction, and coprecipitation with GlycoBlue™ (ThermoFisher). DNA concentration was quantified by Qubit™ (ThermoFisher).

*Metagenomic sequencing*

Libraries were prepared using a Nextera XT DNA Library kit (Illumina). Sequencing was performed at the Institute for Genomic Medicine at UC San Diego on a HiSeq 4000 DNA sequencer (Illumina). Paired reads were trimmed and quality-filtered using Trimmomatic 0.32[9] in paired-end mode with parameters ILLUMINACLIP:NexteraPE-PE.fa:2:30:10 LEADING:3 TRAILING:3 SLIDINGWINDOW:4:15 MINLEN:36.

*Taxonomic profiling of metagenomes*

Trimmed and quality-filtered metagenomic sequence reads were analyzed using Kraken[10] (v0.10.5) to determine the identity and abundance of eukaryotic, bacterial, archaeal, and viral species present. Kraken was run in paired mode with the full RefSeq database. Genus-level annotations in Kraken are nearly 100% reliable in benchmark studies when the genus is in the database, while species assignments are 89% accurate with human microbiome datasets[10]. This accuracy is much lower in environmental samples because the representation of relevant genomes in the database is much less complete. To prevent errors in calculations the taxonomic data set generated with Kraken was filtered to exclude any species that had any sample containing less than 0.001% of the total population or if 10 or more samples (of 18 total) contained less than 0.01%. Spatial coverage for each genome was calculated by implementing the following pipeline: (1) parsing Kraken label output files to generate individual fastq files for each taxonomy hit; (2) mapping the reads to their respective genome assembly (e.g. full chromosomes, contigs, plasmids, etc.) [HISAT2 v2.0.0][11]; (3) converting the *.sam files to *.bedgraph files [bedtools v2.24.0][12]; and (4) concatenating all sequences in the genome assembly and calculating the proportion of positions that were mapped. The coverage trimmed data set omitted species below 0.1% spatial coverage.

*Draft genome assembly*

Draft genomes were assembled using the pipeline described by Dupont et al[13]. Sixty-two individual shotgun sequenced metagenomes were assembled separately using metaSPAdes[14], with subsequent co-assembly of the assemblies using CLC (QIAGEN) to collapse redundant contigs. Genome quality throughout was assessed using QUAST[15]. Original reads for each sample were mapped to the contigs (CLC) to build sample specific coverage information. All contigs greater than 5 kbp were clustered into genome bins using VizBin[16] and completeness of each of these bins was assessed using CheckM[17] (Supplementary Data Table 2). Subsequently, 14 bins were recovered from a pangenome in the data by utilizing hierarchical clustering and sample specific coverage information. Genome annotations were determined utilizing APIS and manual curation[18]. Read and assembly data deposited to European Nucleotide Archive, accession number PRJEB20421.

*Data analysis*

Aerosolization factor (AF) was calculated as the ratio of the fraction of species in the aerosol compartment to either the bulk water or SSML compartment using both raw-read phylogenies from Kraken for bacteria and virus and additionally for draft genome data for virus. Surface enrichment factors were similarly calculated using species fractions ratios of SSML to bulk seawater. To make comparisons of individual species more manageable, the

free bacteria data set was further trimmed. Species were sorted by AF and twenty species were selected at random for the following values: AF >5, AF 1.5 to 5, AF 1 to 1.5, AF ≈ 1, AF 0.667 to 1, AF 0.20 to 0.667, AF < 0.2. To ensure all abundant species were included, this was amended with the top 50 abundant species resulting in 197 bacteria species. Phylogenetic trees were constructed in PhyloT (http://phylot.biobyte.de/) and visualized in iTOL (http://itol.embl.de/)[19]. Species were annotated with corresponding AF data to compare phylogeny and aerosolization patterns.

## Section 5.5 Supplementary Information

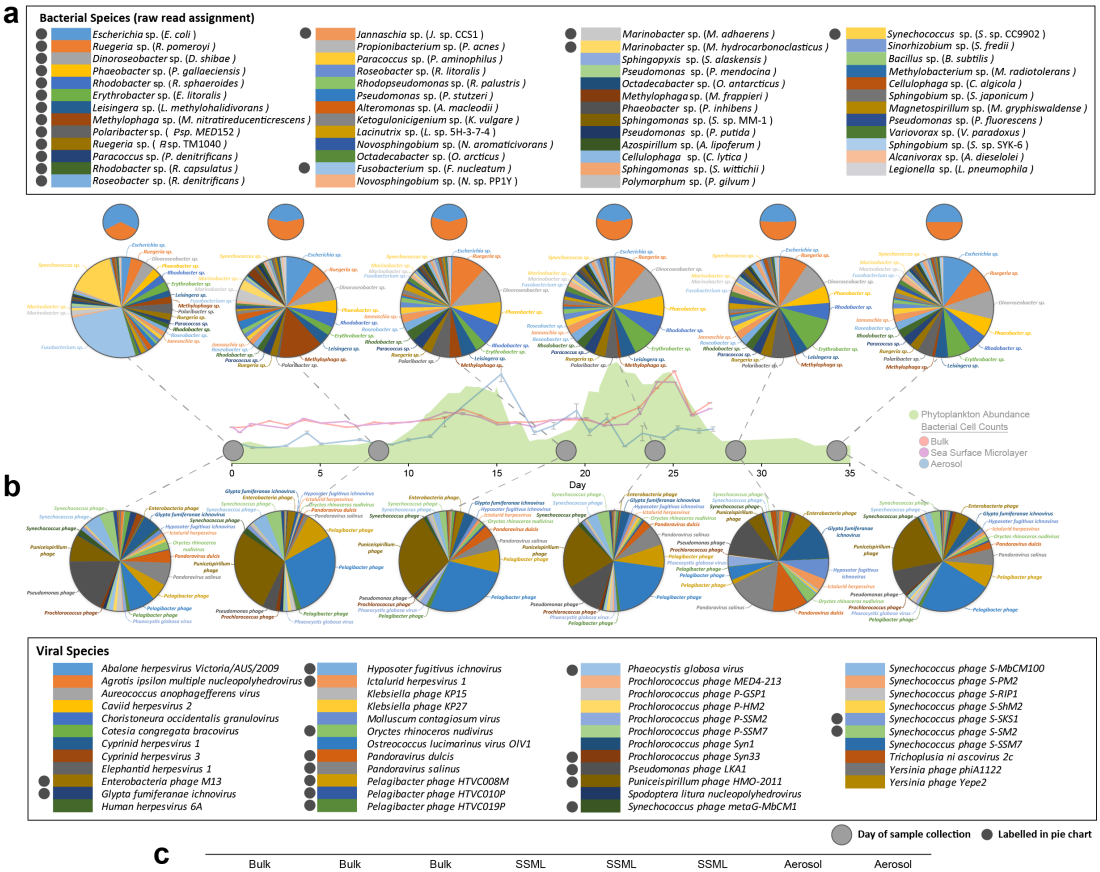


**c**

| Bulk ( x $10^7$) Day | ( vp $mL^{-1}$) | Bulk ( x $10^7$) Day | ( vp $mL^{-1}$) | Bulk ( x $10^7$) Day | ( vp $mL^{-1}$) | SSML ( x $10^7$) Day | ( vp $mL^{-1}$) | SSML ( x $10^7$) Day | ( vp $mL^{-1}$) | SSML ( x $10^7$) Day | ( vp $m^{-3}$) | Aerosol ( x $10^7$) Day | ( vp $m^{-3}$) | Aerosol ( x $10^7$) Day | ( vp $m^{-3}$) |
|---|---|---|---|---|---|---|---|---|---|---|---|---|---|---|---|
| 4 | 1.86 ± 0.40 | 12 | 1.24 ± 0.27 | 21 | 4.36 ± 0.36 | 7 | 1.32 ± 0.19 | 21 | 3.90 ± 0.42 | 35 | 4.06 ± 0.49 | 0 | 1.58 ± 0.18 | 13 | 1.20 ± 0.13 |
| 5 | 1.00 ± 0.29 | 13 | 1.63 ± 0.34 | 22 | 7.97 ± 0.79 | 8 | 1.21 ± 0.22 | 22 | 3.04 ± 0.43 | 36 | 2.95 ± 0.34 | 1 | 0.70 ± 0.08 | 14 | 1.32 ± 0.15 |
| 6 | 2.17 ± 0.52 | 14 | 1.44 ± 0.26 | 23 | 4.76 ± 0.65 | 9 | 1.21 ± 0.22 | 23 | 3.66 ± 0.35 | | | 2 | 0.77 ± 0.09 | 18 | 1.39 ± 0.15 |
| 7 | 1.68 ± 0.32 | 15 | 1.72 ± 0.33 | 24 | 3.63 ± 0.52 | 10 | 1.43 ± 0.28 | 24 | 3.96 ± 0.53 | | | 4 | 1.01 ± 0.11 | 20 | 0.33 ± 0.04 |
| 8 | 5.98 ± 0.10 | 16 | 2.99 ± 0.36 | 25 | 8.01 ± 0.80 | 16 | 2.08 ± 0.27 | 29 | 5.56 ± 0.92 | | | 6 | 2.33 ± 0.26 | 22 | 0.55 ± 0.06 |
| 9 | 1.93 ± 0.21 | 17 | 2.36 ± 0.26 | 26 | 5.50 ± 0.74 | 17 | 3.54 ± 0.42 | 32 | 1.59 ± 0.54 | | | 7 | 1.04 ± 0.12 | | |
| 10 | 1.10 ± 0.38 | 18 | 2.91 ± 0.42 | 27 | 5.07 ± 0.59 | 18 | 3.85 ± 0.51 | 33 | 2.35 ± 0.54 | | | 9 | 2.14 ± 0.24 | | |
| 11 | 1.01 ± 0.23 | 19 | 4.56 ± 0.43 | 28 | 5.26 ± 0.62 | 20 | 3.66 ± 0.57 | 34 | 3.48 ± 0.68 | | | 11 | 1.14 ± 0.13 | | |

**d**

| | Bulk > 3 µm | SSML > 3 µm | Aerosol > 3 µm | Bulk 3 - 0.2 µm | SSML 3 - 0.2 µm | Aerosol 3 - 0.2 µm | Bulk 0.2 - 0.025 µm | SSML 0.2 - 0.025 µm | Aerosol 0.2 - 0.025 µm |
|---|---|---|---|---|---|---|---|---|---|
| Bacteria | 91.45 | 91.13 | 92.50 | 95.13 | 95.91 | 96.49 | 91.49 | 83.01 | 92.25 |
| Viruses | 7.28 | 7.72 | 6.86 | 4.27 | 3.63 | 3.03 | 8.00 | 16.15 | 7.18 |

Figure S5.1 Bacterial and viral genome variation across the phytoplankton blooms. Bacteria (51 most abundant genomes), (a), and viruses, (b), as determined by read based analysis on abundance trimmed data. Legends indicate species represented with dark gray circles denoting those that are labelled in the chart. Light gray circles on middle plot indicate day of sampling. Middle Plot shows phytoplankton abundance and bacterial abundance as reported in Figure 5.1. (a) Orange portion of small pie charts above larger species pie charts represents 51 abundant genomes during the experiment and blue represents the remainder of the population. Abundance determined by number of samples above 0.5% of population and by sum of fraction of samples across blooms. Expanded pie charts demonstrate the identity and abundance of these species. Identities derived from bulk 0.2–3 µm samples. (b) Virus species from 0.025–0.2 µm bulk samples. (c) Virus particle (vp) counts by microscopy in bulk, SSML, and aerosol samples. (d) Percent of population in bacterial and viral divisions in >3 µm, 3–0.2 µm, and 0.2–0.025 µm size fractions in bulk, SSML, and aerosol samples from read-based k-mer sequence analysis.

Table S5.1 Analysis of draft genomes using k-mer based taxonomic profiling.

| Draft genome | Kraken Assignment | Assembly characteristics | Genome size (bp) | No. of Contigs | % complete |
|---|---|---|---|---|---|
| JCVI_CAICE_Erythrobacter_1 | Erythrobacter litoralis | | 2558218 | 49 | 97.96 |
| JCVI_CAICE_Novosphingobium_1 | Novosphingobium aromaticivorans | | 282480 | 44 | 5.8 |
| JCVI_CAICE_Methylophaga_1 | Methylophaga nitratireducenticrescens | Many core methophaga genes | 2541903 | 61 | 100 |
| JCVI_CAICE_Gammaproteobacterium_1 | Gammaproteobacterium HdN1 | Basal gammaproteobacteria, SAR92 | 1709939 | 224 | 29.86 |
| JCVI_CAICE_Escherichia coli_1 | Escherichia coli | | 4486681 | 170 | 96.55 |
| JCVI_CAICE_Legionella_1 | Legionella pneumophila | | 2886101 | 95 | 100 |
| JCVI_CAICE_Polaribacter_1 | Polaribacter sp. MED152 | | 1354003 | 166 | 55.02 |
| JCVI_CAICE_Deltaproteobacterium_1 | Candatus Babela massiliensis | Basal deltaproteobacteria | 746461 | 86 | 46.16 |
| JCVI_CAICE_Diatom_Fragment_1 | Synechococcus sp. PCC_6312 | | 146965 | 19 | 12.93 |
| JCVI_CAICE_Roseobacter_1 | Ruegeria pomeroyi | | 4280636 | 394 | 74.61 |
| JCVI_CAICE_Roseovarius_1 | Ruegeria pomeroyi | | 3387409 | 126 | 80.88 |
| JCVI_CAICE_Roseobacter_fragments_1 | - | | | | |
| JCVI_CAICE_Roseobacter_fragments_2 | Rhodobacter sphaeroides | | | | |
| JCVI_CAICE_Roseobacter_fragments_3 | Dinoroseobacter shibae | | 543659 | 49 | 12.85 |
| JCVI_CAICE_Roseobacter_fragments_4 | Bacillus infantis | Portion of roseobacter | 178918 | 28 | 1.72 |
| JCVI_CAICE_Roseobacter_fragments_5 | Erythrobacter litoralis | | 184708 | 27 | 10.34 |
| JCVI_CAICE_Roseobacter_fragments_6 | Ruegeria pomeroyi | Missing core roseobacter genes | 2970438 | 403 | 19.2 |
| JCVI_CAICE_Roseobacter_fragments_7 | Leisingera methylohalidivorans | | | | |
| JCVI_CAICE_Roseobacter_fragments_contamination | Pseudomonas phage LKA1 | Both alphaproteobacteria and roseobacter | 241080 | 24 | 0 |
| JCVI_CAICE_NCLDV_1 | - | | 545842 | 57 | 1.41 |
| JCVI_CAICE_Phage_1 | Puniceispirillum phage HMO-2011 | Large, T7-like | 977327 | 76 | 0 |
| JCVI_CAICE_Phage_2 | Synecoccus phage ACG-2014c | Probable roseobacteria phage | 356493 | 22 | 0 |
| JCVI_CAICE_Phage_3 | - | | 416069 | 27 | 0 |
| JCVI_CAICE_Phage_4 | Cotesia congregata bracovirus | Possible gammaproteobacteria phage | 490666 | 26 | 0 |
| JCVI_CAICE_Phage_5 | - | | 384320 | 24 | 0 |

Taxonomic assignment of assembled metagenomics scaffolds using k-mer analysis (Kraken) with NCBI Refseq database. Assembled draft genomes identified utilizing APIS and manual curation. The assemblies were analyzed by Kraken to yield taxonomic assignments for comparison to raw read generated assignments. More complete genomes resulted in more accurate Kraken assignments. The diatom fragment derived from a chloroplast genome resulting in a cyanobacterial annotation in Kraken.

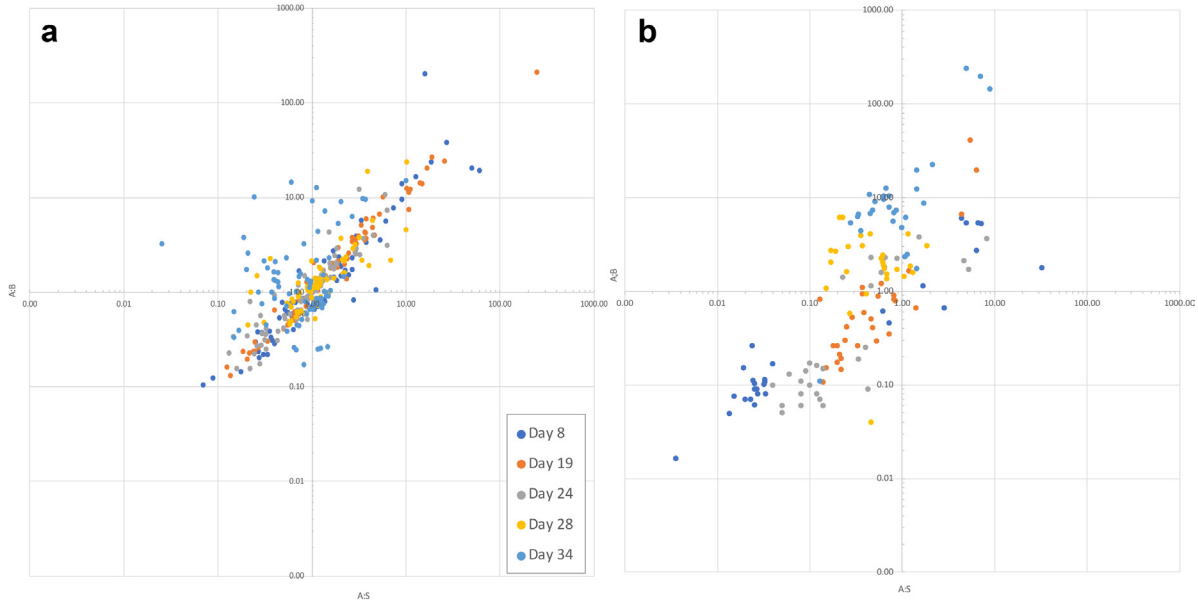


Figure S5.2 Genome spatial coverage trimmed bacterial and viral populations aerosolization distribution. The ratio of fraction of genomes in aerosols to the fraction in bulk plotted against ratio of fraction of genomes in aerosols to those in sea surface is shown for bacteria, (a), and viruses, (b), in genome spatial coverage trimmed data sets on select days. The upper right quadrants of (a) and (b) indicate genomes enriched in aerosol relative to both bulk and SSML (A:B and A:S > 1); the lower left quadrants indicates genomes that are primarily waterborne (A:B and A:S < 1). The upper left quadrants indicates genomes enriched relative to bulk but not SSML (A:B > 1, A:S < 1), and the lower right indicates genomes enriched in aerosol relative to the surface but not bulk (A:B < 1, A:S > 1). The data sets represent, (a), 76 bacterial genomes, and (b), 30 viral genomes identified by read-based taxonomic assignments trimmed of species with low genome spatial coverage.

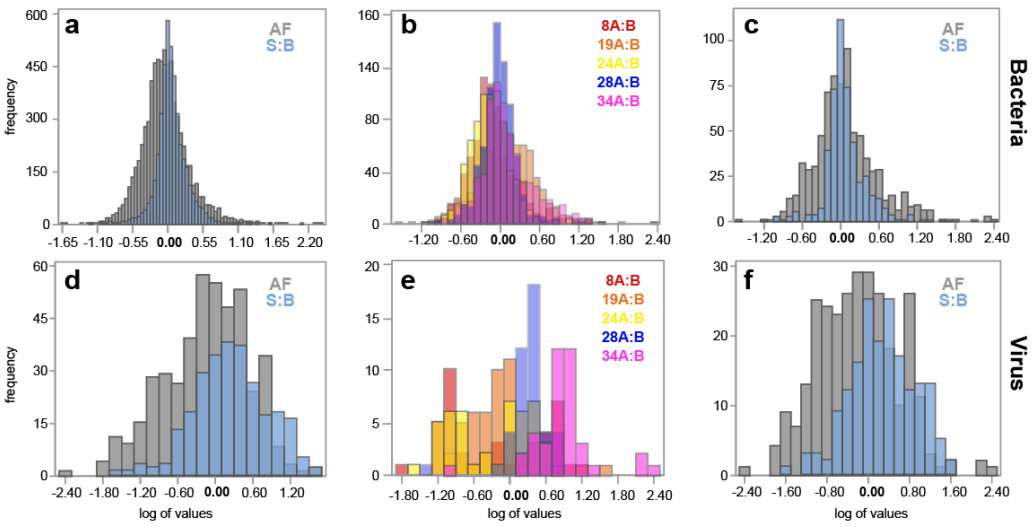


g

| | | AD - Value | P- Value | Skewness | Kurtosis | Mean | Std Dev | CV | Range | Minimum | Median | Maximum | N |
|---|---|---|---|---|---|---|---|---|---|---|---|---|---|
| Bacteria | ALL A:B | 25.91 | <0.0050 | 0.726 | 2.184 | -0.019 | 0.374 | -1985 | 3.91 | -1.59 | -0.05 | 2.33 | 3550 |
| | ALL A:S | 17.25 | <0.0050 | 0.537 | 2.287 | -0.070 | 0.357 | -512 | 4.02 | -1.63 | -0.08 | 2.39 | 3550 |
| | ALL AF | 43.35 | <0.0050 | 0.644 | 2.256 | -0.044 | 0.367 | -828 | 4.02 | -1.63 | -0.07 | 2.39 | 7100 |
| | ALL S:B | - | <0.0050 | 0.328 | 4.848 | 0.057 | 0.243 | 423 | 3.31 | -1.20 | 0.04 | 2.11 | 4260 |
| Bacteria Trimmed | ALL A:B | 4.47 | <0.0050 | 0.945 | 1.765 | 0.097 | 0.501 | 516 | 3.31 | -0.98 | 0.03 | 2.33 | 380 |
| | ALL A:S | 3.54 | <0.0050 | 0.737 | 2.214 | 0.036 | 0.482 | 1352 | 3.99 | -1.60 | 0.02 | 2.39 | 380 |
| | ALL AF | 7.70 | <0.0050 | 0.848 | 1.981 | 0.066 | 0.492 | 742 | 3.99 | -1.60 | 0.02 | 2.39 | 760 |
| | ALL S:B | 14.42 | <0.0050 | 0.914 | 6.551 | 0.072 | 0.325 | 452 | 3.31 | -1.20 | 0.03 | 2.11 | 456 |
| Virus | ALL A:B | 4.85 | <0.0050 | -0.491 | -0.473 | -0.010 | 0.651 | -6508 | 3.40 | -1.78 | 0.21 | 1.62 | 224 |
| | ALL A:S | 1.98 | <0.0050 | -0.300 | 0.257 | -0.285 | 0.665 | -233 | 3.95 | -2.44 | -0.23 | 1.51 | 223 |
| | ALL AF | 2.05 | <0.0050 | -0.380 | -0.161 | -0.147 | 0.672 | -456 | 4.06 | -2.44 | -0.09 | 1.62 | 447 |
| | ALL S:B | 0.39 | 0.3826 | -0.111 | 0.124 | 0.254 | 0.577 | 227 | 3.35 | -1.67 | 0.22 | 1.68 | 263 |
| Virus Trimmed | ALL A:B | 1.58 | <0.0050 | 0.219 | -0.338 | -0.008 | 0.827 | -10183 | 4.16 | -1.78 | 0.11 | 2.38 | 144 |
| | ALL A:S | 1.03 | 0.0101 | -0.128 | 0.068 | -0.410 | 0.701 | -171 | 3.95 | -2.44 | -0.35 | 1.51 | 146 |
| | ALL AF | 0.47 | 0.250 | 0.196 | 0.045 | -0.210 | 0.791 | -376 | 4.82 | -2.44 | -0.21 | 2.38 | 290 |
| | ALL S:B | 0.30 | 0.5706 | -0.204 | 0.034 | 0.276 | 0.629 | 228 | 3.38 | -1.7 | 0.29 | 1.68 | 177 |
| Bacteria A:B | day 8 | 12.53 | <0.0050 | 1.353 | 4.175 | -0.099 | 0.395 | -400 | 3.34 | -1.03 | -0.16 | 2.31 | 710 |
| | day 19 | 0.78 | 0.0434 | 0.122 | 1.290 | 0.092 | 0.436 | 471 | 3.91 | -1.59 | 0.09 | 2.33 | 710 |
| | day 24 | 0.87 | 0.0253 | 0.355 | 1.213 | -0.160 | 0.288 | -180 | 2.19 | -1.10 | -0.17 | 1.09 | 710 |
| | day 28 | 5.46 | <0.0050 | 0.508 | 3.723 | -0.023 | 0.253 | -1106 | 2.39 | -1.02 | -0.03 | 1.37 | 710 |
| | day 34 | 8.40 | <0.0050 | 0.619 | 0.765 | 0.095 | 0.393 | 413 | 2.62 | -1.11 | 0.03 | 1.52 | 710 |
| Bacteria A:S | day 8 | 6.08 | <0.0050 | 0.902 | 2.142 | -0.121 | 0.423 | -348 | 2.96 | -1.18 | -0.17 | 1.78 | 710 |
| | day 19 | 1.35 | <0.0050 | 0.243 | 1.751 | 0.033 | 0.423 | 1264 | 4.02 | -1.63 | 0.01 | 2.39 | 710 |
| | day 24 | 0.68 | 0.0771 | 0.007 | 0.076 | -0.137 | 0.282 | -206 | 1.77 | -0.97 | -0.13 | 0.80 | 710 |
| | day 28 | 1.47 | <0.0050 | 0.331 | 1.595 | -0.060 | 0.247 | -412 | 1.97 | -0.96 | -0.06 | 1.01 | 710 |
| | day 34 | 6.62 | <0.0050 | 0.340 | 1.600 | -0.064 | 0.350 | -550 | 2.78 | -1.60 | -0.09 | 1.19 | 710 |
| Bacteria S:B | day 0 | 7.93 | <0.0050 | -0.861 | 0.995 | 0.090 | 0.343 | 381 | 2.14 | -1.20 | 0.14 | 0.93 | 710 |
| | day 8 | 13.70 | <0.0050 | 1.258 | 6.142 | 0.022 | 0.185 | 822 | 1.76 | -0.66 | 0.01 | 1.11 | 710 |
| | day 19 | 5.46 | <0.0050 | 1.154 | 5.543 | 0.059 | 0.122 | 206 | 1.34 | -0.34 | 0.05 | 1.00 | 710 |
| | day 24 | 8.48 | <0.0050 | 0.317 | 2.347 | -0.023 | 0.179 | -774 | 1.53 | -0.68 | -0.02 | 0.85 | 710 |
| | day 28 | * | <0.0050 | 1.933 | 16.100 | 0.037 | 0.160 | 429 | 2.10 | -0.50 | 0.03 | 1.61 | 710 |
| | day 34 | 3.81 | <0.0050 | 0.286 | 2.932 | 0.159 | 0.332 | 209 | 3.11 | -1.00 | 0.17 | 2.11 | 710 |
| Virus A:B | day 8 | 1.85 | <0.0050 | 0.049 | -1.483 | -0.230 | 0.823 | -358 | 2.96 | -1.78 | -0.29 | 1.18 | 43 |
| | day 19 | 1.64 | <0.0050 | 1.726 | 4.575 | -0.227 | 0.507 | -224 | 2.59 | -0.97 | -0.25 | 1.62 | 44 |
| | day 24 | 1.91 | <0.0050 | -0.244 | -1.519 | -0.322 | 0.648 | -201 | 2.12 | -1.54 | -0.08 | 0.58 | 45 |
| | day 28 | 2.10 | <0.0050 | -2.931 | 14.059 | 0.303 | 0.351 | 116 | 2.24 | -1.45 | 0.31 | 0.79 | 44 |
| | day 34 | 2.40 | <0.0050 | 0.211 | 4.307 | 0.881 | 0.548 | 62 | 3.32 | -0.94 | 0.86 | 2.38 | 41 |
| Virus A:S | day 8 | 2.88 | <0.0050 | -0.020 | -1.703 | -0.417 | 1.168 | -280 | 3.95 | -2.44 | -0.17 | 1.51 | 44 |
| | day 19 | 0.67 | 0.077 | 0.526 | -0.100 | -0.224 | 0.474 | -212 | 2.01 | -1.20 | -0.27 | 0.81 | 45 |
| | day 24 | 0.97 | 0.0135 | 0.398 | 0.170 | -0.483 | 0.538 | -111 | 2.27 | -1.35 | -0.36 | 0.92 | 46 |
| | day 28 | 0.29 | 0.6091 | -0.100 | -0.599 | -0.214 | 0.376 | -176 | 1.61 | -1.04 | -0.21 | 0.57 | 44 |
| | day 34 | 0.91 | 0.019 | 0.695 | 1.589 | -0.080 | 0.367 | -457 | 1.82 | -0.87 | -0.10 | 0.95 | 44 |
| Virus S:B | day 0 | 0.31 | 0.5526 | -0.431 | -0.023 | -0.221 | 0.542 | -245 | 2.43 | -1.67 | -0.22 | 0.76 | 46 |
| | day 8 | 0.79 | 0.0362 | -0.654 | 0.244 | 0.183 | 0.490 | 268 | 2.30 | -1.26 | 0.29 | 1.04 | 42 |
| | day 19 | 0.29 | 0.5923 | 0.333 | 0.720 | 0.000 | 0.327 | $-3.4x10^{18}$ | 1.58 | -0.71 | 0.01 | 0.87 | 45 |
| | day 24 | 0.41 | 0.3244 | -0.372 | -0.447 | 0.172 | 0.352 | 204 | 1.49 | -0.68 | 0.22 | 0.81 | 45 |
| | day 28 | 0.60 | 0.1128 | -0.289 | 1.711 | 0.532 | 0.497 | 93 | 2.77 | -1.12 | 0.50 | 1.65 | 46 |
| | day 34 | 1.68 | <0.0050 | -1.295 | 1.716 | 0.951 | 0.414 | 44 | 1.96 | -0.28 | 1.03 | 1.68 | 39 |

Figure S5.3 Population distribution of aerosolization and surface enrichment data sets. Histograms of all aerosolization factors (AFs) and surface enrichment factors (S:B) for bacteria, (a–c), and viruses, (d–f) given by log values. (a, d) represent pooled AF and S:B values for abundance trimmed but not coverage trimmed data. (b, e) demonstrate day resolved variance in A:B distributions of these partially trimmed data sets. (c, f) show the pooled AF and S:B values for the fully trimmed data sets. In (g), distribution parameters for partially trimmed, fully trimmed, pooled, and day resolved data sets is shown. Normality is tested by the Anderson–Darling (AD) normality test, skewness, kurtosis (excess), and inspection of histograms. For the AD test, p-values below 0.05 demonstrate data is significantly non-normal. Departure from zero indicates increasing non-normality in skewness and kurtosis values.

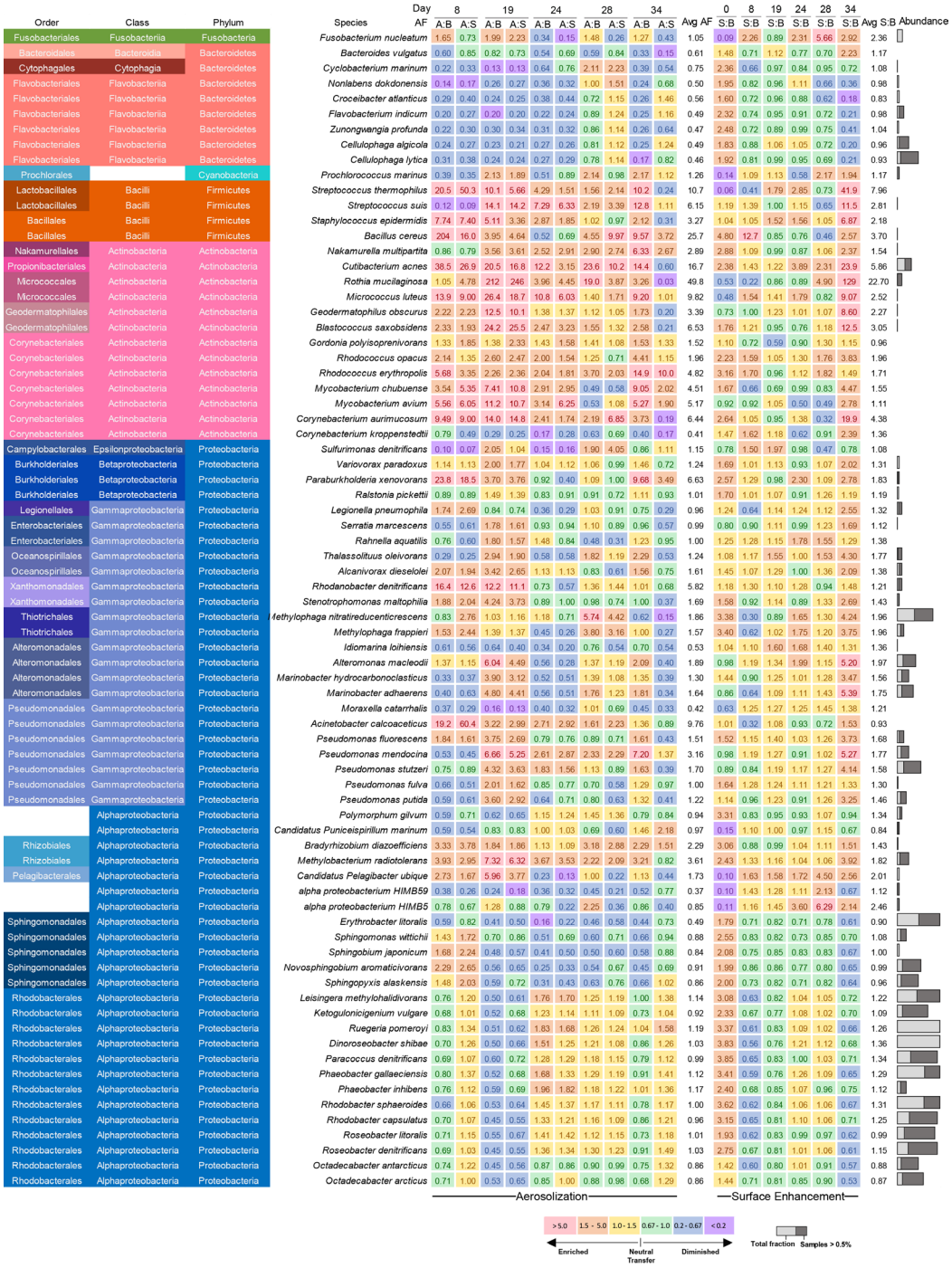


Figure S5.4 Bacterial aerosolization and surface enrichment. Taxonomy, aerosolization factors, and surface enrichment of bacterial genomes of spatial coverage and abundance trimmed data. Phylum, class, and orders are color coded to reflect species relationships. Genome annotation by read-based analysis, Heat map column labels indicate day and measurement. Aerosolization factor is expressed as the fraction of genomes in aerosol to bulk or surface (A:B or A:S). Surface enrichment is the fraction in SSML to the fraction in the bulk (S:B). Heat map values indicate ratio values (bottom legend). Species abundance is reported as the sum of fraction of the population across the experiment and as the number of samples above 0.5% of the population.

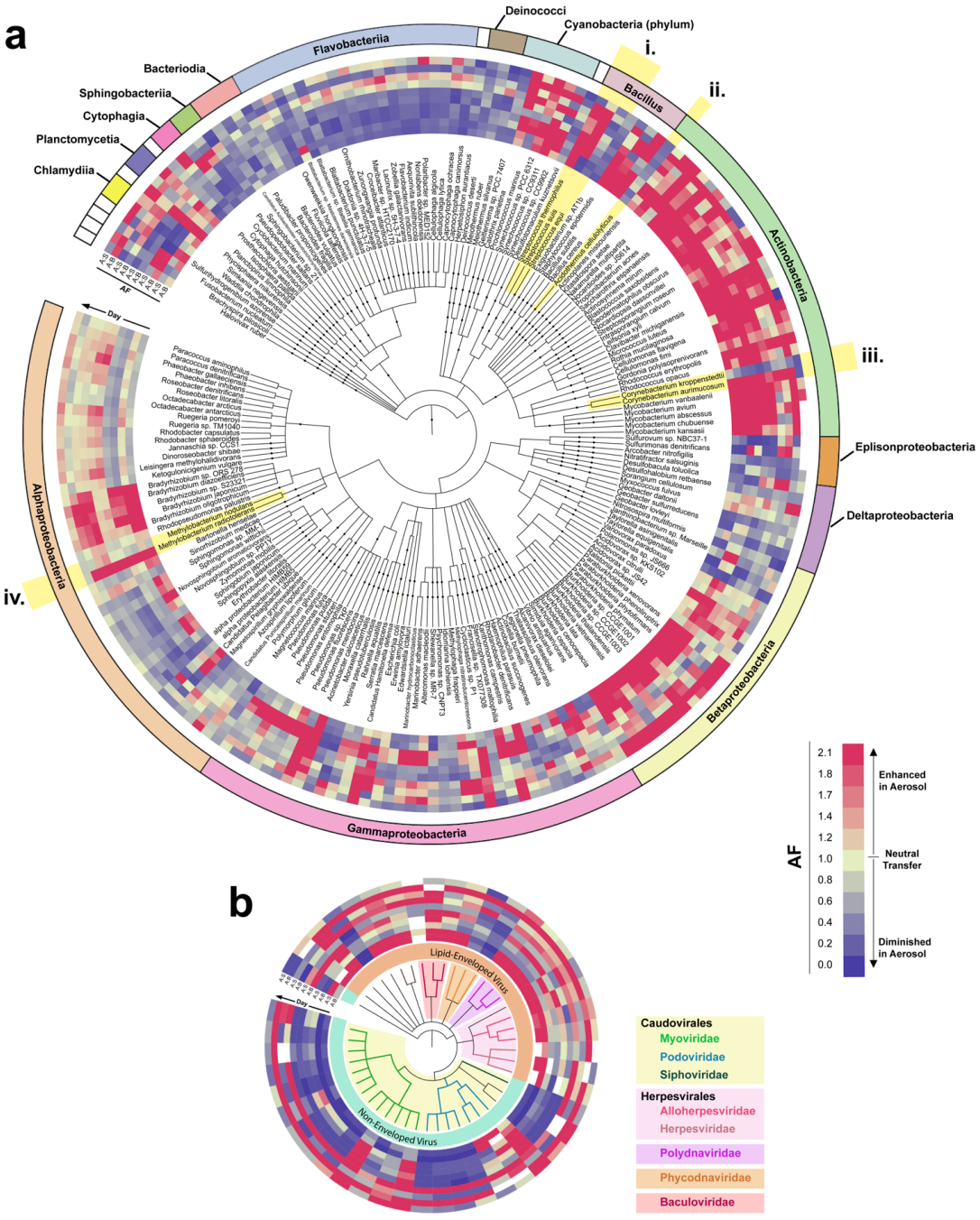


Figure S5.5 The genetic basis of bacterial and viral aerosolization in the abundance trimmed data set. Genome-based phylogenetic trees based on 198 bacterial genome sequences, (a), and 46 viral genomes, (b). Sequences are derived from read-centric analysis of above 0.1% of the population but not trimmed of genomes with low spatial coverage. The bacteria are a subset of this data that contains 710 bacterial genomes total. The heatmaps display aerosolization factor (AF), A:B and A:S, on different days. AF intensity specified by the legend: Blue = Diminished aerosolization; Yellow = Neutral aerosolization; Red = Enhanced aerosolization. (a), Bacteria class is indicated on outer ring to further denote species and aerosolization relationships. Yellow highlights, (i –iv) indicate closely related species with differing aerosolization patterns. (b), Line colors denote viral family and shading indicates order as shown by legend.

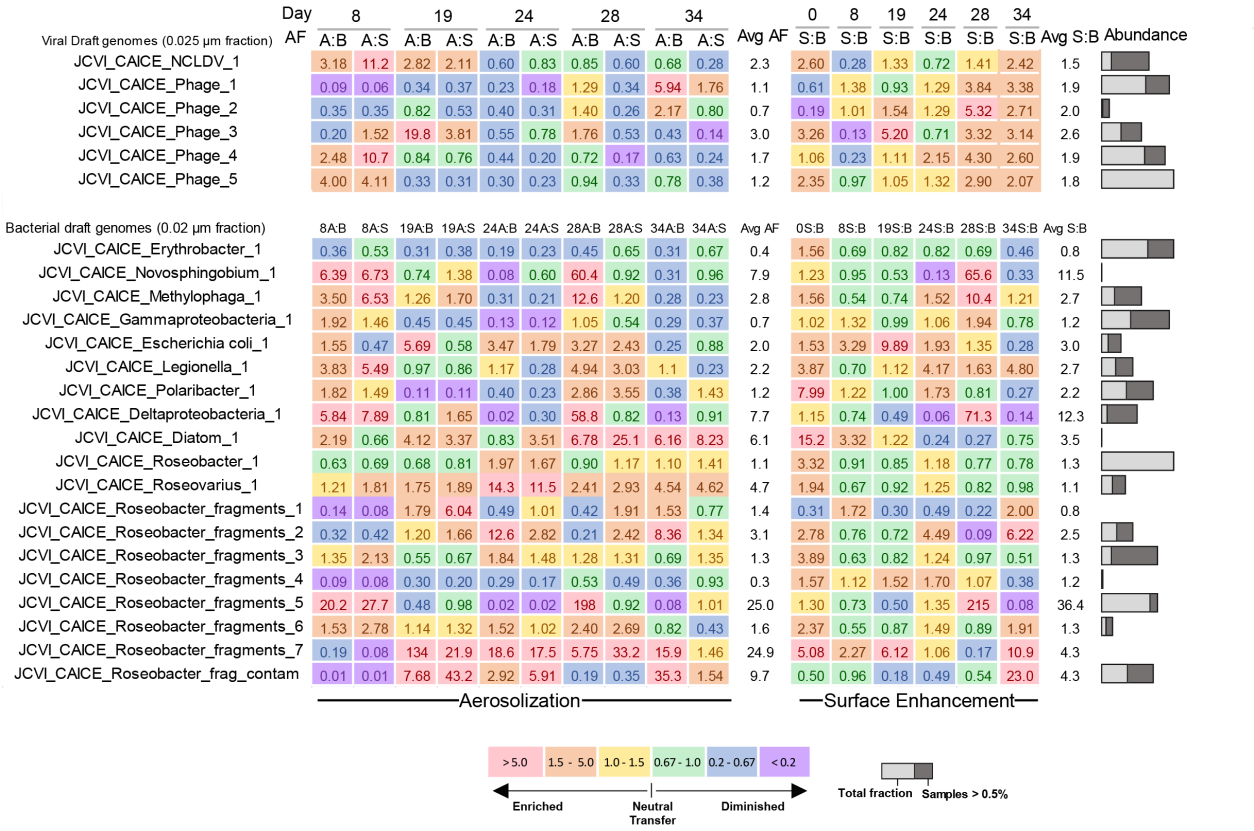


Figure S5.6 Draft genome bacterial and viral aerosolization and surface enrichment. Taxonomy, aerosolization factors, and surface enrichment of assembled draft genomes. Heat map column labels indicate day and measurement. Aerosolization factor is expressed as the fraction of species in aerosol to bulk or surface (A:B or A:S). Surface enrichment is the fraction in SSML to the fraction in the bulk (S:B). Heat map values indicate ratio values (bottom legend). Genome abundance is reported as the sum of fraction of the population across the experiment and as the number of samples above 0.5% of the population.

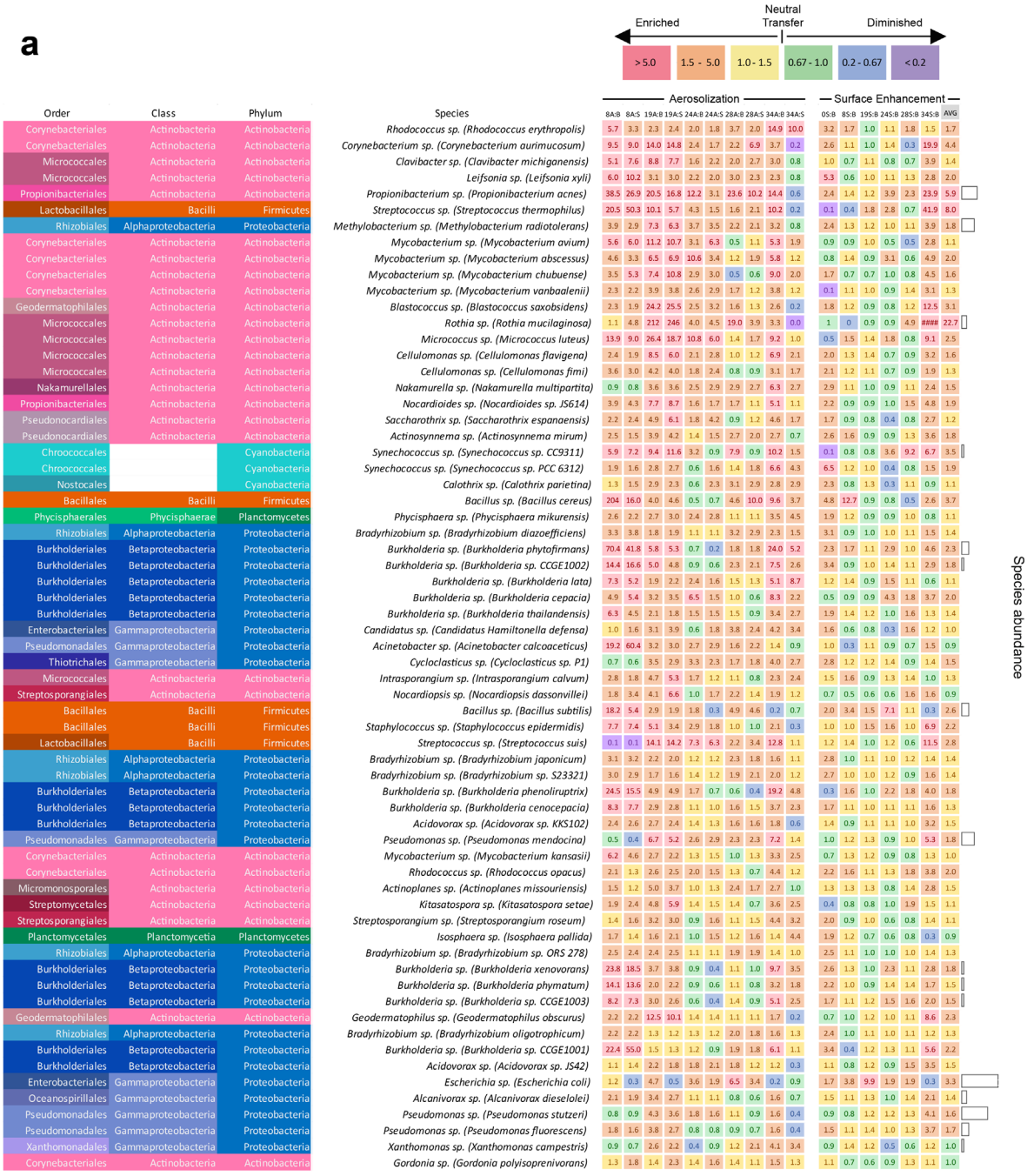


Figure S5.7 Bacterial aerosol and surface enrichment of abundance trimmed data set. Taxonomy, aerosolization factors, and surface enrichment of bacterial genomes from abundance trimmed but not coverage trimmed data presented in three sets, (a, b, c). Phylum, class, and orders are color coded to reflect genome relationships. Genome annotation by read-based analysis, exact assignment in parentheses. Heat map column labels indicate day and measurement as well as enrichment factor. Aerosolization factor is expressed as the fraction of a genome in aerosol to bulk or surface (A:B or A:S). Surface enrichment is the fraction in SSML to the fraction in the bulk (S:B). Heat map values indicate ratio values as given in legend. Bars on right indicate genome abundance (number of samples containing above 0.5% of the total population).

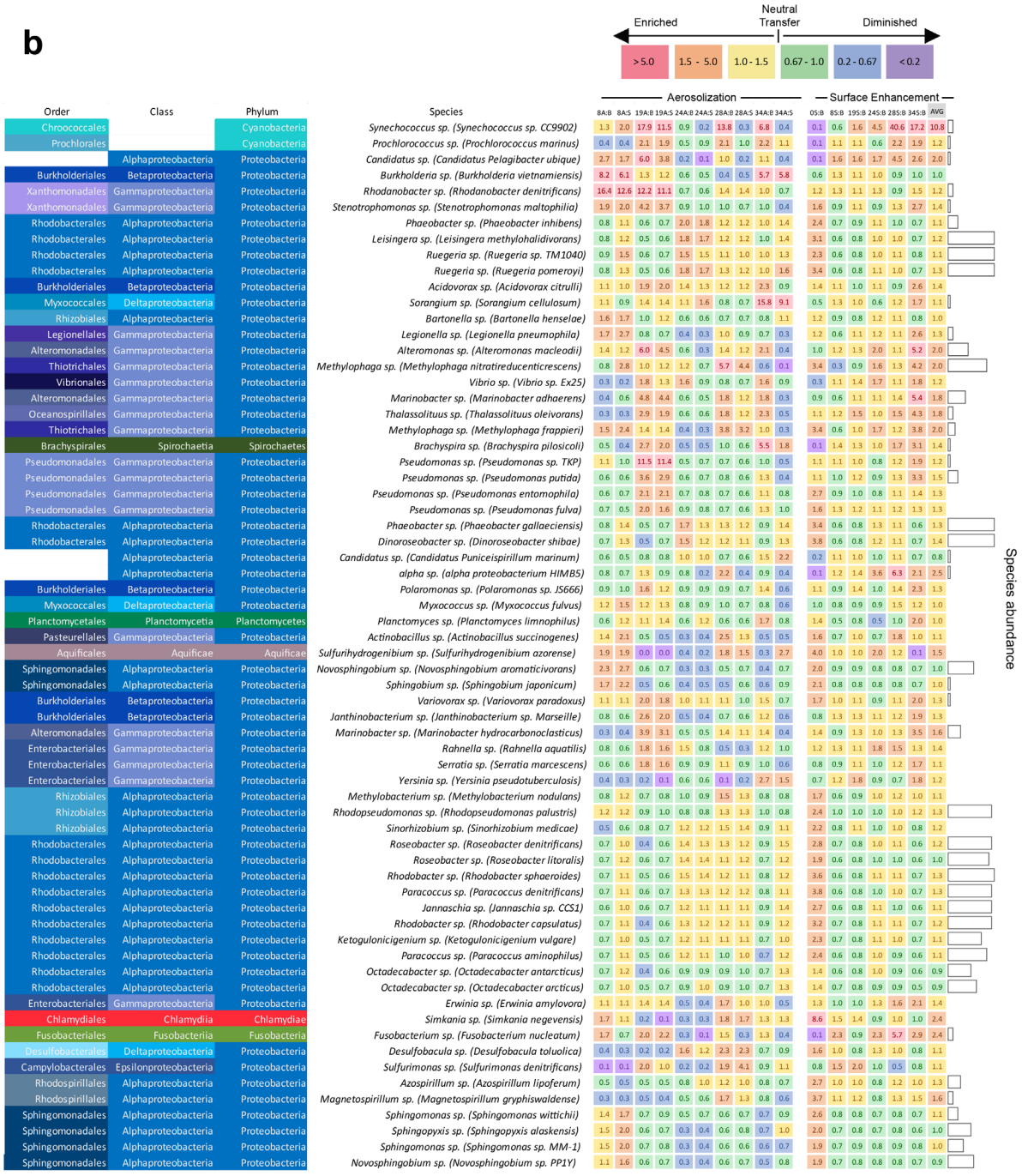


Figure S5.7 Bacterial aerosol and surface enrichment of abundance trimmed data set. (continued)

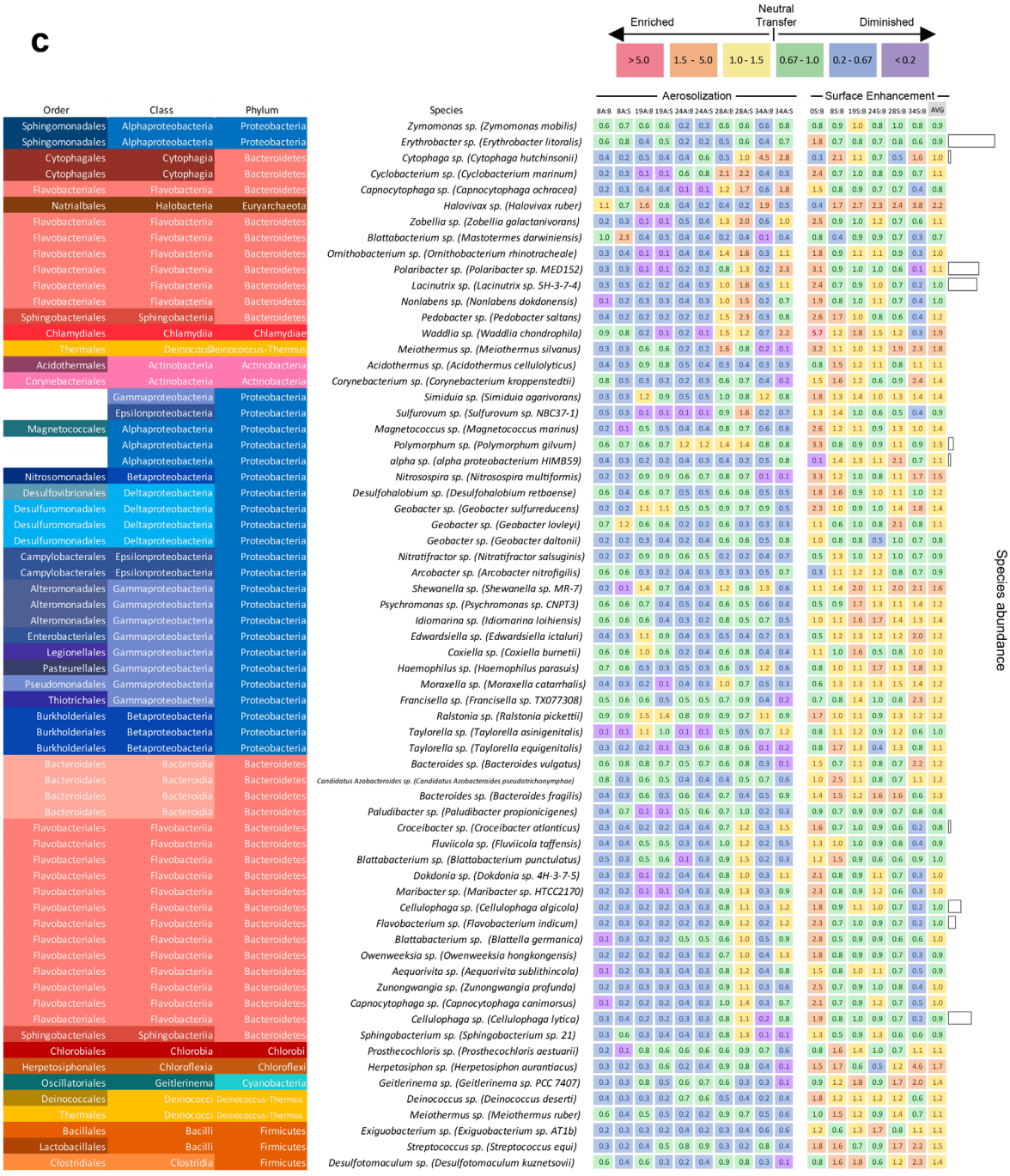


Figure S5.7 Bacterial aerosol and surface enrichment of abundance trimmed data set. (continued)

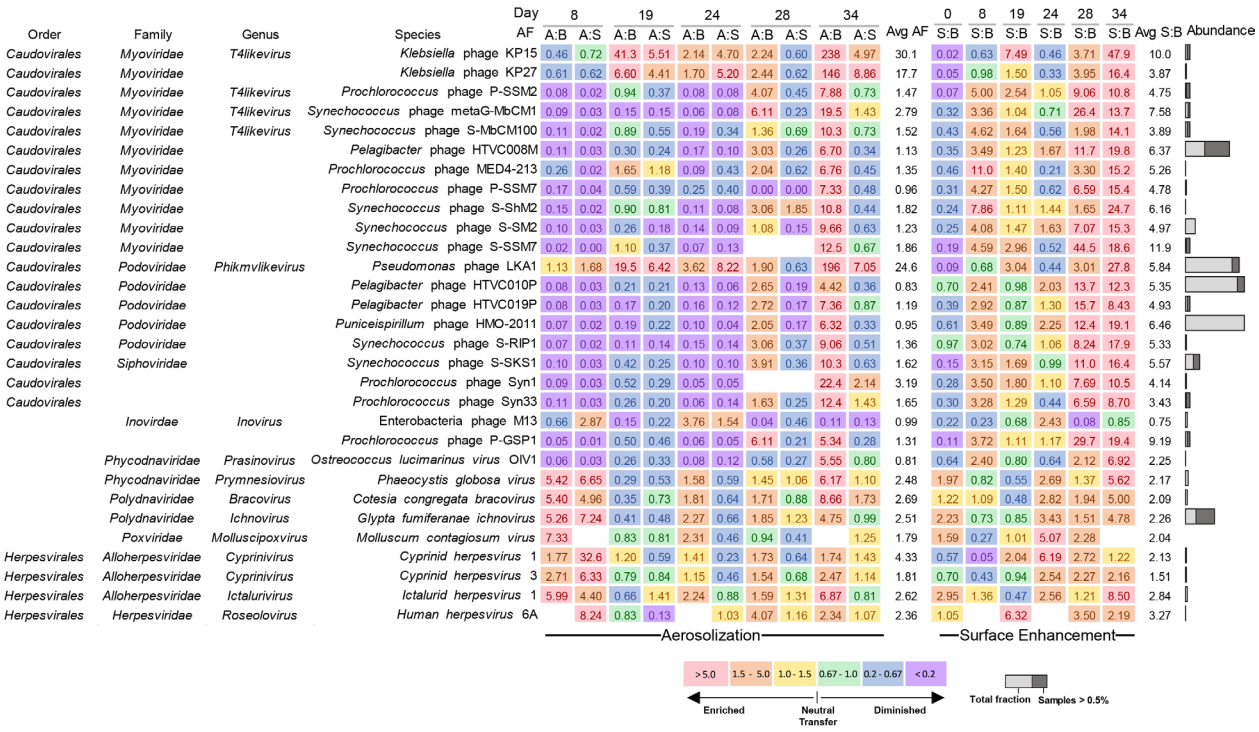


Figure S5.8 Viral aerosolization and surface enrichment. Taxonomy, aerosolization factors, and surface enrichment of viral genomes in the abundance and genome coverage trimmed data set. Heat map column labels indicate day and measurement. Aerosolization factor is expressed as the fraction of genomes in aerosol to bulk or surface (A:B or A:S). Surface enrichment is the fraction in SSML to the fraction in the bulk (S:B). Heat map values indicate ratio values (bottom legend). Genome abundance is reported as the sum of fraction of the population across the experiment and as the number of samples above 0.5% of the population. Blanks indicate samples below threshold limits.

*Bloom dynamics*

Chlorophyll *a* peaked at 21.7 µg $L^{-1}$ for bloom 1 and 30.0 µg $L^{-1}$ for bloom 2 (Figure 5.1, Extended Data Figure 5.1). Major phytoplankton blooms at Scripps Pier generally have chlorophyll *a* levels in the range of 18 – 219 µg/L [1], placing this on the low end of natural major bloom from the same source water. Bacteria counts were found to be in the range of 0.65 X $10^6$ ± 0.01 X $10^6$ to 3.98 X $10^6$ ± 0.02 X $10^6$ cells / mL in bulk water, 0.36 X $10^6$ ± 0.01 X $10^6$ to 3.34 X $10^6$ ± 0.03 X $10^6$ cells / mL in SSML, and 0.09 X $10^7$ ± 0.06X $10^7$ to 5.83 X $10^7$ ± 0.58 X $10^7$ cells /

$m^3$ in aerosol. Oceanic values for bacteria range from $10^4$ to $10^6$ cells / mL [2], making the values here on the high end of ocean concentrations. However, considering bacterial abundance increases linearly with chlorophyll [3] and under certain conditions oceanic concentrations have been found to up to $10^8$ cells / mL [4], these values seem especially relevant. Aerosol bacteria concentrations are estimated to be ~$10^2$ to $10^4$ cells $m^{-3}$ [5]. Virus abundances were found to 1 X $10^7$ to 8 X $10^7$ cells $mL^{-1}$ in bulk and SSML and 0.3 X $10^7$ to 7.7 X $10^7$ (cells $m^{-3}$ ) in aerosol which is ~10-fold higher than water bacteria concentrations and approximately the same as bacterial concentrations in aerosol.

*Genomic data analysis*

*Metagenomic sequencing*

A total of 625 million reads were trimmed and quality filtered generating on average 3.0 million sequence reads with lengths of 2 x 142 bp and GC content of 48% (Table S5.1). Taxonomic profiling generated a total of 700 bacterial, 10 archaeal and 28 viral species in samples from the 0.02–3 μm size fraction after data filtering. The >3 μm and 0.025–0.2 μm fraction were also trimmed similarly to generate 613 species (576 bacteria, 8 archaea, 29 viruses) and 627 species (585 bacteria, 7 archaea, 35 viruses), respectively. The viral species from the three fractions were pooled to yield 46 viral species.

Table S5.2 Trimmed and filtered read statistics

| Sample Name | Sequences (M) | Length (bp) | Percent GC | Sample Name | Sequences (M) | Length (bp) | Percent GC |
|---|---|---|---|---|---|---|---|
| 03B0025_R1 | 1.7 | 138 | 46% | 27B0025_R1 | 1.9 | 138 | 43% |
| 03B0025_R2 | 1.7 | 147 | 46% | 27B0025_R2 | 1.9 | 145 | 43% |
| 03B02_R1 | 4.1 | 147 | 46% | 27B3_R1 | 5.4 | 136 | 48% |
| 03B02_R2 | 4.1 | 137 | 46% | 27B3_R2 | 5.4 | 147 | 48% |
| 03B3_R1 | 4.8 | 147 | 47% | 27S0025_R1 | 4.2 | 137 | 44% |
| 03B3_R2 | 4.8 | 138 | 47% | 27S0025_R2 | 4.2 | 148 | 44% |
| 03S0025_R1 | 1.3 | 136 | 46% | 27S02_R1 | 5.4 | 148 | 51% |
| 03S0025_R2 | 1.3 | 147 | 46% | 27S02_R2 | 5.4 | 138 | 51% |
| 03S02_R1 | 1.5 | 138 | 46% | 27S3_R1 | 5.0 | 137 | 46% |
| 03S02_R2 | 1.5 | 147 | 46% | 27S3_R2 | 5.0 | 147 | 46% |
| 03S3_R1 | 1.1 | 147 | 46% | 31A0025_R1 | 1.1 | 147 | 48% |
| 03S3_R2 | 1.1 | 138 | 46% | 31A0025_R2 | 1.1 | 136 | 48% |
| 05A0025_R1 | 0.8 | 137 | 48% | 31A02_R1 | 1.3 | 147 | 48% |
| 05A0025_R2 | 0.8 | 147 | 48% | 31A02_R2 | 1.3 | 137 | 48% |
| 05A02_R1 | 2.3 | 138 | 48% | 31A3_R1 | 0.7 | 137 | 47% |
| 05A02_R2 | 2.3 | 147 | 48% | 31A3_R2 | 0.7 | 146 | 47% |
| 05A3_R1 | 1.7 | 147 | 45% | 31B0025_R1 | 1.4 | 147 | 47% |
| 05A3_R2 | 1.7 | 137 | 45% | 31B0025_R2 | 1.4 | 137 | 47% |
| 11A0025_R1 | 1.0 | 147 | 46% | 31B02_R1 | 6.4 | 148 | 49% |
| 11A0025_R2 | 1.0 | 137 | 46% | 31B02_R2 | 6.4 | 138 | 49% |
| 11A02_R1 | 6.8 | 148 | 52% | 31B3_R1 | 8.7 | 137 | 48% |
| 11A02_R2 | 6.8 | 139 | 52% | 31B3_R2 | 8.7 | 147 | 48% |
| 11A3_R1 | 3.3 | 147 | 52% | 31S0025_R1 | 2.3 | 136 | 45% |
| 11A3_R2 | 3.3 | 138 | 52% | 31S0025_R2 | 2.3 | 147 | 45% |
| 11B0025_R1 | 0.7 | 138 | 44% | 31S02_R1 | 10.7 | 148 | 51% |
| 11B0025_R2 | 0.7 | 147 | 44% | 31S02_R2 | 10.7 | 139 | 51% |
| 11B02_R1 | 5.3 | 148 | 51% | 31S3_R1 | 1.7 | 146 | 48% |
| 11B02_R2 | 5.3 | 138 | 51% | 31S3_R2 | 1.7 | 134 | 48% |
| 11B3_R1 | 2.0 | 147 | 50% | 86_27B02_R1 | 9.7 | 139 | 51% |
| 11B3_R2 | 2.0 | 138 | 50% | 86_27B02_R2 | 9.7 | 148 | 51% |
| 11S0025_R1 | 5.7 | 148 | 43% | 86A0025_R1 | 1.5 | 147 | 49% |
| 11S0025_R2 | 5.7 | 140 | 43% | 86A0025_R2 | 1.5 | 138 | 49% |
| 11S02_R1 | 1.6 | 147 | 51% | 86A02_R1 | 1.1 | 147 | 50% |
| 11S02_R2 | 1.6 | 135 | 51% | 86A02_R2 | 1.1 | 137 | 50% |
| 11S3_R1 | 1.4 | 137 | 49% | 86A3_R1 | 1.0 | 147 | 49% |
| 11S3_R2 | 1.4 | 147 | 49% | 86A3_R2 | 1.0 | 138 | 49% |
| 18B3_02_R1 | 1.8 | 136 | 47% | 86Ad_R1 | 1.4 | 147 | 48% |
| 18B3_02_R2 | 1.8 | 147 | 47% | 86Ad_R2 | 1.4 | 137 | 48% |
| 22A0025_R1 | 0.7 | 147 | 45% | 86B0025_R1 | 8.6 | 148 | 53% |
| 22A0025_R2 | 0.7 | 137 | 45% | 86B0025_R2 | 8.6 | 140 | 53% |
| 22A02_R1 | 1.0 | 137 | 49% | 86B3_R1 | 6.1 | 136 | 49% |
| 22A02_R2 | 1.0 | 147 | 49% | 86B3_R2 | 6.1 | 147 | 49% |
| 22A3_R1 | 1.0 | 137 | 46% | 86Bd_R1 | 1.1 | 138 | 50% |
| 22A3_R2 | 1.0 | 147 | 46% | 86Bd_R2 | 1.1 | 147 | 50% |
| 22B0025_R1 | 2.5 | 137 | 43% | 86S0025_R1 | 2.1 | 147 | 47% |
| 22B0025_R2 | 2.5 | 148 | 43% | 86S0025_R2 | 2.1 | 138 | 47% |
| 22B02_R1 | 9.3 | 140 | 49% | 86S02_R1 | 1.0 | 138 | 51% |
| 22B02_R2 | 9.3 | 148 | 49% | 86S02_R2 | 1.0 | 147 | 51% |
| 22B3_R1 | 4.6 | 139 | 45% | 86S3_R1 | 1.3 | 146 | 47% |
| 22B3_R2 | 4.6 | 147 | 45% | 86S3_R2 | 1.3 | 135 | 47% |
| 22S0025_R1 | 4.7 | 148 | 43% | 86Sd_R1 | 1.3 | 137 | 48% |
| 22S0025_R2 | 4.7 | 138 | 42% | 86Sd_R2 | 1.3 | 147 | 48% |
| 22S02_R1 | 6.8 | 138 | 48% | 87CA02_R1 | 0.6 | 137 | 46% |
| 22S02_R2 | 6.8 | 148 | 49% | 87CA02_R2 | 0.6 | 146 | 46% |
| 22S3_R1 | 2.1 | 147 | 46% | 87CA3_R1 | 4.7 | 147 | 51% |
| 22S3_R2 | 2.1 | 137 | 46% | 87CA3_R2 | 4.7 | 137 | 51% |
| 27_86B02_R1 | 2.9 | 148 | 51% | 88B02_R1 | 2.5 | 136 | 50% |
| 27_86B02_R2 | 2.9 | 136 | 51% | 88B02_R2 | 2.5 | 147 | 50% |
| 27A0025_R1 | 1.0 | 137 | 47% | 88B3_R1 | 1.0 | 138 | 47% |
| 27A0025_R2 | 1.0 | 147 | 47% | 88B3_R2 | 1.0 | 147 | 47% |
| 27A02_R1 | 3.2 | 137 | 54% | 88BS3_02_R1 | 1.6 | 147 | 48% |
| 27A02_R2 | 3.2 | 147 | 54% | 88BS3_02_R2 | 1.6 | 137 | 47% |
| 27A3_R1 | 0.9 | 138 | 50% | mbla_R1 | 1.7 | 138 | 49% |
| 27A3_R2 | 0.9 | 147 | 50% | mbla_R2 | 1.7 | 147 | 49% |
| | | | | | | | |
| AVERAGE | 3.0 | 142.3 | 47.9% | | | | |
| MIN | 0.6 | 134.0 | 42.0% | | | | |
| MAX | 10.7 | 148.0 | 54.0% | | | | |

*Coverage analysis*

198 bacteria and 46 viral species identified using Kraken were further examined for genomic coverage. Scaffolds from species' assignments were examined against published genomes (Table S5.2). Species below 0.1% spatial coverage were removed resulting in a coverage trimmed set of 76 bacterial and 30 viral species.

Table S5.3 Spatial coverage of scaffolds to Kraken assigned genomes.

| Taxonomy | scaffold size (nts) | spatial coverage (nts) | spatial coverage (%) | Taxonomy | scaffold size (nts) | spatial coverage (nts) | spatial coverage (%) |
|---|---|---|---|---|---|---|---|
| *Acinetobacter calcoaceticus* | 4110074 | 17174 | 0.4% | *Pelagibacter* phage HTVC008M | 147284 | 92310 | 62.7% |
| *Alcanivorax dieselolei* | 4928223 | 203641 | 4.1% | *Pelagibacter* phage HTVC010P | 34892 | 23275 | 66.7% |
| *alpha proteobacterium* HIMB5 | 1343202 | 4965 | 0.4% | *Pelagibacter* phage HTVC019P | 42084 | 16404 | 39.0% |
| *alpha proteobacterium* HIMB59 | 1410127 | 21163 | 1.5% | *Phaeobacter gallaeciensis* | 4061725 | 13031 | 0.3% |
| *Alteromonas macleodii* | 4575623 | 1917348 | 41.9% | *Phaeobacter inhibens* | 2041825.5 | 7261.5 | 0.5% |
| *Bacillus cereus* | 5295158 | 186859 | 3.5% | *Phaeocystis globosa* virus | 459984 | 826 | 0.2% |
| *Bacteroides vulgatus* | 5163189 | 27842 | 0.5% | *Polymorphum gilvum* | 4649365 | 18001 | 0.4% |
| *Blastococcus saxobsidens* | 4875340 | 9395 | 0.2% | *Prochlorococcus marinus* | 1657990 | 296810 | 17.9% |
| *Bradyrhizobium diazoefficiens* | 9105828 | 10991 | 0.1% | *Prochlorococcus* phage MED4-213 | 180977 | 989 | 0.5% |
| *Burkholderia xenovorans* | 3243713 | 13728 | 0.4% | *Prochlorococcus* phage P-GSP1 | 44945 | 1136 | 2.5% |
| *Candidatus Pelagibacter ubique* | 1395018 | 27281 | 2.0% | *Prochlorococcus* phage P-SSM2 | 252407 | 300 | 0.1% |
| *Candidatus Puniceispirillum marinum* | 2753527 | 33134 | 1.2% | *Prochlorococcus* phage P-SSM7 | 182180 | 3175 | 1.7% |
| *Cellulophaga algicola* | 4888353 | 8416 | 0.2% | *Prochlorococcus* phage Syn1 | 191195 | 4277 | 2.2% |
| *Cellulophaga lytica* | 3824196 | 20408 | 0.5% | *Prochlorococcus* phage Syn33 | 174285 | 4976 | 2.9% |
| *Corynebacterium aurimucosum* | 1409613 | 23234 | 4.8% | *Propionibacterium acnes* | 2519002 | 2450832 | 97.3% |
| *Corynebacterium kroppenstedtii* | 2446804 | 4844 | 0.2% | *Pseudomonas fluorescens* | 6143950 | 46014 | 0.7% |
| Cotesia congregata bracovirus | 28766 | 157.5 | 0.7% | *Pseudomonas fulva* | 4920769 | 6930 | 0.1% |
| *Croceibacter atlanticus* | 2952962 | 14005 | 0.5% | *Pseudomonas mendocina* | 5072807 | 428758 | 8.5% |
| *Cyclobacterium marinum* | 6221273 | 15968 | 0.3% | Pseudomonas phage LKA1 | 41593 | 13016 | 31.3% |
| *Cyprinid herpesvirus* 1 | 291144 | 1044 | 0.4% | *Pseudomonas putida* | 6870827 | 408056 | 5.9% |
| *Cyprinid herpesvirus* 3 | 295146 | 316 | 0.1% | *Pseudomonas stutzeri* | 4709064 | 1620871 | 34.4% |
| *Dinoroseobacter shibae* | 869114.4 | 39816.4 | 25.4% | *Puniceispirillum* phage HMO-2011 | 55282 | 5830 | 10.5% |
| Enterobacteria phage M13 | 6407 | 636 | 9.9% | *Rahnella aquatilis* | 2766562 | 3868 | 0.1% |
| *Erythrobacter litoralis* | 3251353 | 3890 | 0.1% | *Ralstonia pickettii* | 1775243 | 10757 | 0.4% |
| *Flavobacterium indicum* | 2993089 | 5620 | 0.2% | *Rhodanobacter denitrificans* | 4225490 | 10225 | 0.2% |
| *Fusobacterium nucleatum* | 2443126 | 3274 | 0.1% | *Rhodobacter capsulatus* | 1935960 | 2742.5 | 0.2% |
| *Geodermatophilus obscurus* | 5322497 | 18786 | 0.4% | *Rhodobacter sphaeroides* | 1461698 | 2004.33 | 0.3% |
| *Glypta fumiferanae ichnovirus* | 3141 | 568 | 18.1% | *Rhodococcus erythropolis* | 3297806 | 18933 | 0.4% |
| *Gordonia polyisoprenivorans* | 2922149.5 | 1953 | 0.2% | *Rhodococcus opacus* | 4229686.5 | 2595.5 | 0.1% |
| *Human herpesvirus* 6A | 156714 | 363 | 0.2% | *Roseobacter denitrificans* | 1081352.5 | 2596.25 | 1.8% |
| *Ictalurid herpesvirus* 1 | 134226 | 321 | 0.2% | *Roseobacter litoralis* | 1550624 | 6759 | 5.2% |
| *Idiomarina loihiensis* | 2839759 | 13167 | 0.5% | *Rothia mucilaginosa* | 2292716 | 311952 | 13.6% |
| *Ketogulonicigenium vulgare* | 1516261 | 4392 | 0.4% | *Ruegeria pomeroyi* | 2300524 | 5500 | 0.2% |
| *Klebsiella* phage KP15 | 174436 | 87598 | 50.2% | *Serratia marcescens* | 5207023 | 16976 | 0.3% |
| *Klebsiella* phage KP27 | 174413 | 73104 | 41.9% | *Sphingobium japonicum* | 884972.4 | 11099.8 | 4.6% |
| *Legionella pneumophila* | 3409143 | 55709 | 1.6% | *Sphingomonas wittichii* | 1971748.7 | 14816 | 4.7% |
| *Leisingera methylohalidivorans* | 1550332 | 5559.67 | 0.2% | *Sphingopyxis alaskensis* | 1686856.5 | 34968.5 | 45.1% |
| *Marinobacter adhaerens* | 2304688 | 488703.5 | 17.6% | *Staphylococcus epidermidis* | 2454929 | 240828 | 9.8% |
| *Marinobacter hydrocarbonoclasticus* | 3989480 | 411335 | 10.3% | *Stenotrophomonas maltophilia* | 4769156 | 56540 | 1.2% |
| *Methylobacterium radiotolerans* | 1685848 | 319342.25 | 10.3% | *Streptococcus suis* | 2028815 | 54495 | 2.7% |
| *Methylophaga frappieri* | 1372645 | 27145 | 3.5% | *Streptococcus thermophilus* | 1796846 | 315319 | 17.5% |
| *Methylophaga nitratireducenticrescens* | 3137191 | 656987 | 20.9% | *Sulfurimonas denitrificans* | 2201561 | 5508 | 0.3% |
| *Micrococcus luteus* | 2501097 | 302946 | 12.1% | *Synechococcus* phage metaG-MbCM1 | 172879 | 132028 | 76.4% |
| *Molluscum contagiosum* virus | 190289 | 709 | 0.4% | *Synechococcus* phage S-MbCM100 | 170438 | 15176 | 8.9% |
| *Moraxella catarrhalis* | 1887974 | 4629 | 0.2% | *Synechococcus* phage S-RIP1 | 44892 | 2746 | 6.1% |
| *Mycobacterium avium* | 5011264 | 12848 | 0.3% | *Synechococcus* phage S-ShM2 | 179563 | 2432 | 1.4% |
| *Mycobacterium chubuense* | 3099500.5 | 1291.5 | 0.2% | *Synechococcus* phage S-SKS1 | 208007 | 44401 | 21.3% |
| *Nakamurella multipartita* | 6060298 | 245383 | 4.0% | *Synechococcus* phage S-SM2 | 190789 | 2506 | 1.3% |
| *Nonlabens dokdonensis* | 3914632 | 8829 | 0.2% | *Synechococcus* phage S-SSM7 | 232878 | 450 | 0.2% |
| *Novosphingobium aromaticivorans* | 1873023 | 17855 | 1.7% | *Thalassolituus oleivorans* | 3764053 | 24088 | 0.6% |
| *Octadecabacter antarcticus* | 4812600 | 5381 | 0.1% | *Variovorax paradoxus* | 5626353 | 6430 | 0.1% |
| *Octadecabacter arcticus* | 5200279 | 5393 | 0.1% | *Zunongwangia profunda* | 5128187 | 52302 | 1.0% |
| *Ostreococcus lucimarinus* virus OlV1 | 194022 | 69241 | 35.7% | | | | |
| *Paracoccus denitrificans* | 2291189.5 | 9244.5 | 0.4% | | | | |

*Genomic assembly and annotation*

Sixty-two metagenomes resulted from assembly of shotgun reads. k-mer based binning (Vizbin) isolated seven bins (Np-bin1, 2, 3, 4, 5, 6, 8) and a mosaic bin (bin7). The remaining bin7 was a mosaic of genomes and thus was examined using sample-specific sequencing coverage vectors and hierarchical clustering, generating a further 14 bins. Completeness of bins was assessed using CheckM (Table S5.3).

Table S5.4 CheckM statistics of genome bins.

| Bin name | Label | BACT completeness | BACT contamination | BACT strain-heterogeneity | genome size (bp) | # scaffolds |
|---|---|---|---|---|---|---|
| np-bin7-pan.bin7_1 | *Legionella* sp. | 100 | 0 | 0 | 2886101 | 95 |
| outliers | Roseobacter fragments | n/a | n/a | n/a | | |
| np-bin4 | *Methylophaga* sp. | 100 | 1.72 | 100 | 2541903 | 61 |
| pangenome_np-bin7_2-pan.bin7_2_14 | Diatom fragment | 12.93 | 0 | 0 | 146965 | 19 |
| pangenome_np-bin7_2-pan.bin7_2_2 | *Polaribacter* sp. | 55.02 | 10.19 | 5.26 | 1354003 | 166 |
| pangenome_np-bin7_2-pan.bin7_2_3 | Phage 1 | 0 | 0 | 0 | 977327 | 76 |
| pangenome_np-bin7_2-pan.bin7_2_13 | Phage 2 | 0 | 0 | 0 | 356493 | 22 |
| pangenome_np-bin7_2-pan.bin7_2_5 | *Erythrobacter* sp. | 97.96 | 0 | 0 | 2558218 | 49 |
| pangenome_np-bin7_2-pan.bin7_2_6 | Roseobacter fragments | 12.85 | 3.45 | 52 | 543659 | 49 |
| np-bin5 | *Escherichia coli* | 96.55 | 0 | 0 | 4486681 | 170 |
| pangenome_np-bin7_2-pan.bin7_2_9 | Roseobacter fragments | 10.34 | 0 | 0 | 184708 | 27 |
| pangenome_np-bin7_2-pan.bin7_2_8 | Phage 3 | 0 | 0 | 0 | 416069 | 27 |
| pangenome_np-bin7_2-pan.bin7_2_0 | Roseobacter fragments | 19.2 | 4.55 | 11.11 | 2970438 | 403 |
| np-bin6 | Delta proteobacteria | 46.16 | 1.72 | 100 | 746461 | 86 |
| np-bin3 | Gamma proteobacteria | 29.86 | 1.72 | 0 | 1709939 | 224 |
| pangenome_np-bin7_2-pan.bin7_2_4 | NCLDV | 1.41 | 0 | 0 | 545842 | 57 |
| pangenome_np-bin7_2-pan.bin7_2_7 | Roseobacter fragments | 1.72 | 0 | 0 | 178918 | 28 |
| np-bin2 | *Novosphingobium* sp. | 5.8 | 0 | 0 | 282480 | 44 |
| pangenome_np-bin7_2-pan.bin7_2_12 | Roseobacter frags + contamination | 0 | 0 | 0 | 241080 | 24 |
| pangenome_np-bin7_2-pan.bin7_2_10 | Phage 4 | 0 | 0 | 0 | 490666 | 26 |
| np-bin1 | *Roseovarius* sp. | 80.88 | 1.72 | 100 | 3387409 | 126 |
| pangenome_np-bin7_2-pan.bin7_2_11 | Phage 5 | 0 | 0 | 0 | 384320 | 24 |
| pangenome_np-bin7_2-pan.bin7_2_1 | *Roseobacter* sp. | 74.61 | 0 | 0 | 4280636 | 394 |
| np-bin8 | Roseobacter fragments | | | | | |
| np-bin9 | Roseobacter fragments | | | | | |

Genome bins, while mostly not complete, were recovered for Bacteria, Eukarya, and multiple viral lineages. The completeness appears to be mostly due to more conserved regions of the genome fragmenting during the secondary co-assembly, which did decrease large contigs. The low completeness (CheckM) for several genomes rather large in size is consistent

with this. Annotation of genomes was performed by APIS and manual curation[6]. Summaries of genome bins are given in Table S5.5.

Table S5.5 Genome bin summaries

| Genome bin | Annotation | Genome summary |
|---|---|---|
| NP1 | *Roseovarius* sp. | The assembly is consistently annotated at *Roseovarius* based on ribosomal proteins and other conserved genes. The organism possesses microcompartments (ethanolamine) co-localized with polyamine uptake, which appears to be a novel system. Formate dehydrogenase suggests some C1 metabolism. This is the most abundant draft genome and is enriched in several aerosol samples. |
| NP2 | *Novosphingobium* sp. | The assembly is consistently annotated as *Novosphingobium* but is an incomplete genome. It was very rare except at the beginning of the experiment. |
| NP3 | Gamma proteobacteria 1 | The genome is indicated as a SAR92/OM6 species, which possesses a Ni/Fe-dependent hydrogenase, a PQQ-dependent glucose dehydrogenase, and genes implicated in sulfur oxidization. It is relatively abundant throughout the experiment and generally evenly distributed between phases (bulk, SSML, and aerosol). |
| NP4 | *Methylophaga sp*. | The assembly indicates a methylotroph, but unlike the closest reference genomes, it appears to lack NO reductase, dissimilatory nitrite reductase, and $N_2O$ reductase. Instead it appears to have assimilatory nitrate and nitrite reductase. This species (bin) is most abundant early in the bloom. |
| NP5 | *Escherichia coli* strain CAICE | The genome is annotated as *E. coli* but does not appear to have a Type III secretion system or many of the hallmarks of pathogenesis. It contains genes for capsular polysaccharide synthesis and multiple siderophore biosynthesis and uptake systems. The species is abundant in aerosols, particularly in the beginning of the experiment but is present throughout the experiment. |
| NP6 | Delta proteobacteria 1 | The genome indicates a basal deltaproteobacteria based on the phylogeny of r proteins. |
| NP8 | *Roseobacter* fragments 1 | This bin is annotated as a *Roseobacter* and is rare during the experiment. |
| NP9 | *Roseobacter* fragments 2 | This bin is very abundant particularly in the aerosol samples towards the end of the bloom. It contains a putative *rbcL*/*rbcS* gene cluster (carbon fixation via ribulose-bisphosphate carboxylase/oxygenase) and aerobic formate dehydrogenase-like protein (often can be hydrocarbon degrading). |
| 7_1 | *Legionella* sp. | Most ORFs have the highest amino acid similarity to *Legionella pneumophila* or *drancourtii* (70–80% identity) and represent a unique species, likely from a sister genus. The genome contains both Type II and Type IV secretion systems (Lsp and Dot/ICM respectively) as well as several ORFs with highest identity to eukaryotes. The genome also contains a Ni/Fe hydrogenase. The species is motile and compentent. It is most abundant early and found throughout the experiment. |
| 7_2_0 | *Roseobacter* fragments 6 | This Roseobacter genome is most abundant in the water on day 8 of the experiment. It contains several elements of denitrification, including nitrite (Cu) reductase, nitric oxide reducatase. It is generally enriched in the aerosol phase. |
| 7_2_1 | *Roseobacter* sp. | The assembly yielded a moderately sized *Roseobacter* genome. It was abundant at the bloom peak, particularly in the aerosols. It contains a putative rbcL/rbcS gene cluster, in addition to nitrite reductase (Cu) and nitric oxide reductase. It may couple denitrification to carbon fixation. |
| 7_2_2 | *Polaribacter* sp. | The genome consistently suggests a basal Flavobacteria. It contains a Ni/Fe hydrogenase. It is mostly water-bourne and is most abundant during middle of the experiment. |
| 7_2_3 | Phage 1 | The assembly is likely a Roseophage (phage of *Roseobacteria*) based on the similarity of auxillary metabolic proteins and the presence of clear orthologs for pelagiphage. The large size of the genome indicates this is probably not a single viral species and reflect many similar viral genomes. |
| 7_2_4 | NCLDV | This genome comprised a large bin with many hits to *Marseillevirus*. |
| 7_2_5 | *Erythrobacter* sp. | This species was abundant throughout the experiment, though most abundant towards the conclusion (Extended Data Fig. 5). It was generally found throughout all sample types. |
| 7_2_6 | *Rosebacter* fragments 3 | This genome is abundant towards end of the experiment and was generally enriched in aerosols. |
| 7_2_7 | *Rosebacter* fragments 4 | This assembly was rare throughout the experiment. |
| 7_2_8 | Phage 3 | This assembly blooms at the end of the experiment in the 0.025 µm fraction. The abundance of *Roseobacter* and alpha-proteobacterial proteins, in addition to the clear phage genes (head, tail, baseplate wedge), indicate it a phage of these bacteria. |
| 7_2_9 | *Rosebacter* fragments 5 | This assembly possibly contains a set of mobile genetic elements like plasmids. For example, much of the machinery for conjugal transfer (pilus, reverse transcriptase, resolvase, endonucleases, mate pair stabilization proteins), are present in this bin. It contains abundant *Roseobacter* elements and nitric oxide reductase and was present throughout the experiment. |
| 7_2_10 | Phage 4 | Assembly indicates a phage with clear orthologs for tail, head, baseplate, but it is difficult to identify the host. A spike in abundance in the >3 µm fraction was followed by being very abundant in viral size fraction (0.025–0.2 µm) after the last two time points, with distributions in pretty much every substrate. This may indicate an early infection and burst event. |
| 7_2_11 | Phage 5 | Assembly indicates a phage with clear orthologs for tail, head, baseplate, but it is difficult to identify the host. An abundance in the 0.025–0.2 µm fraction shifts to an increasing abundance in larger size fractions, and then reverts back to an increased amount in the 0.025–0.2 µm fraction indicating a possible transition from free phage, to infection of the host, and then to a burst releasing progeny phage. |
| 7_2_13 | Phage 2 | Based on the similarity of auxillary metabolic proteins and the presence of clear orthologs for pelagiphage this assembly likely represents a phage for *Roseobacteria*. It is most abundant early in the experiment and is primarily absent from later time points. |
| 7_2_14 | Diatom fragment | This bin represents a diatom genome fragment. It includes several photosystem proteins, indicating it is likely a portion of the chloroplast genome, which is far more abundant than the nuclear chromosomes[7]. It is most abundant during the peak of the bloom in bulk, >3 µm fraction samples. |


## Acknowledgements

Chapter 5 is material that has been submitted for publication, titled "Selective transfer of bacteria and viruses from the ocean to the atmosphere". The dissertation author is the primary author of the work reported, supported by

L. R. Thompson, D. Kaul, J. L. Espinoza, R. A. Richter, Z. Z. Xu, C. Lee, K. M. Pham, C. M. Beall, F. Malfatti, F.Azam, and R. Knight and under the supervision of M. D. Burkart, C. L. Dupont, and K. A. Prather. The dissertation author devised experiment and strategy for analyses and performed aerosol and bulk sampling with assistance from co-authors. Additionally, she extracted, purified, prepared DNA samples for sequencing, performed aerosolization calculations and analysis, and prepared manuscript and chapter.

**Section 5.6 References**

*Main Text References*


1. Fernstrom, A. & Goldblatt, M. Aerobiology and its role in the transmission of infectious diseases. J. Pathog. http://dx.doi.org/10.1155/2013/493960 (2013). doi:10.1155/2013/493960

2. Gralton, J., Tovey, E., McLaws, M. L. & Rawlinson, W. D. The role of particle size in aerosolised pathogen transmission: A review. J. Infect. 62, 1–13 (2011).

3. Tang, J. W. The effect of environmental parameters on the survival of airborne infectious agents. J. R. Soc. Interface 6, S737–S746 (2009).

4. Womack, A. M., Bohannan, B. J. M. & Green, J. L. Biodiversity and biogeography of the atmosphere. Philos. Trans. R. Soc. Lond. B. Biol. Sci. 365, 3645–53 (2010).

5. Mayol, E., Jimenez, M. A., Herndl, G. J., Duarte, C. M. & Arrieta, J. M. Resolving the abundance and air-sea fluxes of airborne microorganisms in the North Atlantic Ocean. Front. Microbiol. 5, 1–9 (2014).

6. Kourtev, P. S., Hill, K. A., Shepson, P. B. & Konopka, A. Atmospheric cloud water contains a diverse bacterial community. Atmos. Environ. 45, 5399–5405 (2011).

7. Joung, Y. S., Ge, Z. & Buie, C. R. Bioaerosol generation by raindrops on soil. Nat. Commun. 8, 14668 (2017).

8. Whitman, W. B., Coleman, D. C. & Wiebe, W. J. Prokaryotes: the unseen majority. Proc. Natl. Acad. Sci. U. S. A. 95, 6578–6583 (1998).

9. Burrows, S. M., Elbert, W., Lawrence, M. G. & Pöschl, U. Bacteria in the global atmosphere – Part 1: Review and synthesis of literature data for different ecosystems. Atmos. Chem. Phys. 9, 9263–9280 (2009).

10. Sharoni, S., Trainic, M., Schatz, D., Lehahn, Y., Flores, M. J., Bidle, K. D., Ben-Dor, S., Rudich, Y., Koren, I. & Vardi, A. Infection of phytoplankton by aerosolized marine viruses. Proc. Natl. Acad. Sci. 112, 6643–6647 (2015).

11. Fröhlich-Nowoisky, J., Kampf, C. J., Weber, B., Huffman, J. A., Pöhlker, C., Andreae, M. O., Lang-Yona, N., Burrows, S. M., Gunthe, S. S., Elbert, W., Su, H., Hoor, P., Thines, E., Hoffmann, T., Després, V. R. & Pöschl, U. Bioaerosols in the Earth System: Climate, Health, and Ecosystem Interactions. Atmos. Res. 182, 346–376 (2016).

12. Christner, B. C. Cloudy with a Chance of Microbes. Microbe Mag. 7, 70–75 (2012).

13. Bauer, H., Giebl, H., Hitzenberger, R., Kasper-Giebl, A., Reischl, G., Zibuska, F. & Puxbaum, H. Airborne bacteria as cloud condensation nuclei. J. Geophys. Res. 108, 1–5 (2003).

14. Collins, D. B., Bertram, T. H., Sultana, C. M., Lee, C., Axson, J. L. & Prather, K. A. Phytoplankton blooms weakly influence the cloud forming ability of sea spray aerosol. Geophys. Res. Lett. 43, 9975–9983 (2016).

15. Creamean, J. M., Suski, K. J., Rosenfeld, D., Cazorla, A., Demott, P. J., Sullivan, R. C., White, A. B., Ralph, F., Minnis, P., Comstock, J. M., Tomlinson, J. M. & Prather, K. A. Dust and Biological Aerosols. Science 339, 1572–1578 (2013).

16. Stetzenbach, L. D. Ch 73: Introduction to Aerobiology. Man. Enivironmental Microbiol. 925–938 (ASM Press, Washington DC (2007). doi:10.1128/9781555815882.ch73

17. Cunliffe, M., Engel, A., Frka, S., Gašparović, B., Guitart, C., Murrell, J. C., Salter, M., Stolle, C., Upstill-Goddard, R. & Wurl, O. Sea surface microlayers: A unified physicochemical and biological perspective of the air-ocean

interface. Prog. Oceanogr. 109, 104–116 (2013).

18. Aller, J. Y., Kuznetsova, M. R., Jahns, C. J. & Kemp, P. F. The sea surface microlayer as a source of viral and bacterial enrichment in marine aerosols. J. Aerosol Sci. 36, 801–812 (2005).

19. Grammatika, M. & Zimmerman, W. B. Microhydrodynamics of flotation processes in the sea surface layer. Dyn. Atmos. Ocean. 34, 327–348 (2001).

20. Leck, C. & Bigg, E. K. Source and evolution of the marine aerosol—A new perspective. Geophys. Res. Lett. 32, L19803, doi:10.1029/2005GL023651 (2005).

21. Hultin, K. A. H., Krejci, R., Pinhassi, J., Gomez-Consarnau, L., Mårtensson, E. M., Hagström, Å. & Nilsson, E. D. Aerosol and bacterial emissions from Baltic Seawater. Atmos. Res. 99, 1–14 (2011).

22. Blanchard, D. C. & Syzdek, L. D. Water-to-air transfer and enrichment of bacteria in drops from bursting bubbles. Appl. Environ. Microbiol. 43, 1001–1005 (1982).

23. Baylor, A. E. R., Baylor, M. B., Blanchard, D. C., Syzdek, L. D. & Appel, C. Virus Transfer from Surf to Wind. Science. 198, 575–580 (1977).

24. Joux, F., Agogué, H., Obernosterer, I., Dupuy, C., Reinthaler, T., Herndl, G. & Lebaron, P. Microbial community structure in the sea surface microlayer at two contrasting coastal sites in the northwestern Mediterranean Sea. Aquat. Microb. Ecol. 42, 91–104 (2006).

25. Bezdek, H. F. & Carlucci, A. F. Surface Concentration of Marine Bacteria. Limnol. Oceanogr. 17, 566–569 (1972).

26. Sieburth, J., Willis, P.-J., Johnson, K. M., Burney, C. M., Lavoie, D. M., Hinga, K. R., Caron, D. A., French, F. W., Johnson, P. W. & Davis, P. G. Dissolved Organic Matter and Heterotrophic Microneuston in the Surface Microlayers of the North Atlantic. Science. 194, 1415–1418 (1976).

27. Wang, X., Deane, G. B., Moore, K. A., Ryder, O. S., Stokes, M. D., Beall, C. M., Collins, D. B., Santander, M. V, Burrows, S. M., Sultana, C. M. & Prather, K. A. The role of jet and film drops in controlling the mixing state of submicron sea spray aerosol particles. Proc. Natl. Acad. Sci. U. S. A. 114, 201702420 (2017).

28. Fahlgren, C., Gómez-Consarnau, L., Zábori, J., Lindh, M. V., Krejci, R.,

Mårtensson, E. M., Nilsson, D. & Pinhassi, J. Seawater mesocosm experiments in the Arctic uncover differential transfer of marine bacteria to aerosols. Environ. Microbiol. Rep. 7, n/a-n/a (2015).

29. Hejkal, T. W., LaRock, P. A. & Winchester, J. W. Water-to-air fractionation of bacteria. Appl. Environ. Microbiol. 39, 335–338 (1980).

30. Amato, P. Clouds Provide Atmospheric Oases for Microbes. Microbe 7, 119–123 (2012).

31. Collins, D. B., Zhao, D. F., Ruppel, M. J., Laskina, O., Grandquist, J. R., Modini, R. L., Stokes, M. D., Russell, L. M., Bertram, T. H., Grassian, V. H., Deane, G. B. & Prather, K. A. Direct aerosol chemical composition measurements to evaluate the physicochemical differences between controlled sea spray aerosol generation schemes. Atmos. Meas. Tech. 7, 3667–3683 (2014).

32. Prather, K. A., Bertram, T. H., Grassian, V. H., Deane, G. B., Stokes, M. D., Demott, P. J., Aluwihare, L. I., Palenik, B. P., Azam, F., Seinfeld, J. H., Moffet, R. C., Molina, M. J., Cappa, C. D., Geiger, F. M., Roberts, G. C., Russell, L. M., Ault, A. P., Baltrusaitis, J., Collins, D. B., Corrigan, C. E., Cuadra-Rodriguez, L. A., Ebben, C. J., Forestieri, S. D., Guasco, T. L., Hersey, S. P., Kim, M. J., Lambert, W. F., Modini, R. L., Mui, W., Pedler, B. E., Ruppel, M. J., Ryder, O. S., Schoepp, N. G., Sullivan, R. C. & Zhao, D. Bringing the ocean into the laboratory to probe the chemical complexity of sea spray aerosol. Proc. Natl. Acad. Sci. U. S. A. 110, 7550–5 (2013).

33. Kim, H., Miller, A. J., McGowan, J. & Carter, M. L. Coastal phytoplankton blooms in the Southern California Bight. Prog. Oceanogr. 82, 137–147 (2009).

34. Turley, C. M. & Mackie, P. J. Biogeochemical significance of attached and free-living bacteria and the flux of particles in the NE Atlantic Ocean. Mar. Ecol. Prog. Ser. 115, 191–204 (1994).

35. Fuhrman, J. A. Marine viruses and their biogeochemical and ecological effects. Nature 399, 541–548 (1999).

36. Wood, D. E. & Salzberg, S. L. Kraken: ultrafast metagenomic sequence classification using exact alignments. Genome Biol. 15, R46 (2014).

37. Dupont, C. L., Rusch, D. B., Yooseph, S., Lombardo, M., Richter, R. A., Valas, R., Novotny, M., Yee-greenbaum, J., Selengut, J. D., Haft, D. H., Halpern, A. L., Lasken, R. S., Nealson, K., Friedman, R. & Venter, J. C. Genomic insights

to SAR86 , an abundant and uncultivated marine bacterial lineage. ISME J. 6, 1186–1199 (2012).

38. Dupont, C. L., Larsson, J., Yooseph, S., Ininbergs, K., Goll, J., Asplund-Samuelsson, J., McCrow, J. P., Celepli, N., Allen, L. Z., Ekman, M., Lucas, A. J., Hagström, Å., Thiagarajan, M., Brindefalk, B., Richter, A. R., Andersson, A. F., Tenney, A., Lundin, D., Tovchigrechko, A., Nylander, J. A. A., Brami, D., Badger, J. H., Allen, A. E., Rusch, D. B., Hoffman, J., Norrby, E., Friedman, R., Pinhassi, J., Venter, J. C. & Bergman, B. Functional tradeoffs underpin salinity-driven divergence in microbial community composition. PLoS One 9, (2014).

39. Buchan, A., LeCleir, G. R., Gulvik, C. a & González, J. M. Master recyclers: features and functions of bacteria associated with phytoplankton blooms. Nat. Rev. Microbiol. 12, 686–698 (2014).

40. Rooney-Varga, J. N., Giewat, M. W., Savin, M. C., Sood, S., Legresley, M. & Martin, J. L. Links between phytoplankton and bacterial community dynamics in a coastal marine environment. Microb. Ecol. 49, 163–175 (2005).

41. Grossart, H. P., Levold, F., Allgaier, M., Simon, M. & Brinkhoff, T. Marine diatom species harbour distinct bacterial communities. Environ. Microbiol. 7, 860–873 (2005).

42. Ishii, S. & Sadowsky, M. J. Escherichia coli in the Environment: Implications for Water Quality and Human Health. Microbes Environ. 23, 101–108 (2008).

43. Rozen, Y. & Belkin, S. Survival of enteric bacteria in seawater: Molecular aspects. Ocean. Heal. Pathog. Mar. Environ. 25, 513–529 (2001).

44. Molofsky, A. B. & Swanson, M. S. Differentiate to thrive : lessons from the Legionella pneumophila life cycle. Mol. Microbiol. 53, 29–40 (2004).

45. Barka, E. A., Vatsa, P., Sanchez, L., Gaveau-vaillant, N., Jacquard, C., Klenk, H.-P., Clément, C., Ouhdouch, Y. & van Wezel, G. P. Taxonomy, Physiology, and Natural Products of Actinobacteria. Microbiol. Mol. Biol. Rev. 80, 1–43 (2016).

46. Gago, G., Diacovich, L., Arabolaza, A., Tsai, S.-C. & Gramajo, H. Fatty acid biosynthesis in actinomycetes. FEMS Microbiol. Rev. 35, 475–97 (2011).

47. Tauch, A., Schneider, J., Szczepanowski, R., Tilker, A., Viehoever, P., Gartemann, K. H., Arnold, W., Blom, J., Brinkrolf, K., Brune, I., Götker, S.,

Weisshaar, B., Goesmann, A., Dröge, M. & Pühler, A. Ultrafast pyrosequencing of Corynebacterium kroppenstedtii DSM44385 revealed insights into the physiology of a lipophilic corynebacterium that lacks mycolic acids. J. Biotechnol. 136, 22–30 (2008).

48. Wells, W. F. On air-borne infection. II. Droplets and droplet nuclei. Am. J. Hyg. 20, 611–618 (1934).

49. Cole, E. C. & Cook, C. E. Characterization of infectious aerosols in health care facilities : An aid to effective engineering controls and preventive strategies. 453–464 (1990).

50. Ackermann, H. W. Bacteriophage observations and evolution. Res. Microbiol. 154, 245–251 (2003).

51. Davison, A. J., Eberle, R., Ehlers, B., Hayward, G. S., McGeoch, D. J., Minson, A. C., Pellett, P. E., Roizman, B., Studdert, M. J. & Thiry, E. The order Herpesvirales. Arch. Virol. 154, 171–177 (2009).

52. Meder, F., Wehling, J., Fink, A., Piel, B., Li, K., Frank, K., Rosenauer, A., Treccani, L., Koeppen, S., Dotzauer, A. & Rezwan, K. The role of surface functionalization of colloidal alumina particles on their controlled interactions with viruses. Biomaterials 34, 4203–4213 (2013).

53. Roberts, I. S. the Biochemistry and Genetics of Capsular Polysaccharide Production in Bacteria. Annu. Rev. Microbiol. 50, 285–315 (1996).

54. Verduin, C. M., Hol, C., Fleer, A., Dijk, H. Van & Belkum, A. Van. Moraxella catarrhalis: from Emerging to Established Pathogen. Clin. Microbiol. Rev. 15, 125–144 (2002).

*Methods References*

1. Wang, X., Sultana, C. M., Trueblood, J., Hill, T. C. J., Malfatti, F., Lee, C., Laskina, O., Moore, K. a., Beall, C. M., McCluskey, C. S., Cornwell, G. C., Zhou, Y., Cox, J. L., Pendergraft, M. a., Santander, M. V., Bertram, T. H., Cappa, C. D., Azam, F., DeMott, P. J., Grassian, V. H. & Prather, K. a. Microbial Control of Sea Spray Aerosol Composition: A Tale of Two Blooms. ACS Cent. Sci. 1, 124–131 (2015).

2. Prather, K. A., Bertram, T. H., Grassian, V. H., Deane, G. B., Stokes, M. D., Demott, P. J., Aluwihare, L. I., Palenik, B. P., Azam, F., Seinfeld, J. H., Moffet,

R. C., Molina, M. J., Cappa, C. D., Geiger, F. M., Roberts, G. C., Russell, L. M., Ault, A. P., Baltrusaitis, J., Collins, D. B., Corrigan, C. E., Cuadra-Rodriguez, L. A., Ebben, C. J., Forestieri, S. D., Guasco, T. L., Hersey, S. P., Kim, M. J., Lambert, W. F., Modini, R. L., Mui, W., Pedler, B. E., Ruppel, M. J., Ryder, O. S., Schoepp, N. G., Sullivan, R. C. & Zhao, D. Bringing the ocean into the laboratory to probe the chemical complexity of sea spray aerosol. Proc. Natl. Acad. Sci. U. S. A. 110, 7550–5 (2013).

3. Guillard, R. R. L. Culture of Phytoplankton for Feeding Marine Invertebrates. in Culture of Marine Invertebrate Animals: Proceedings --- 1st Conference on Culture of Marine Invertebrate Animals Greenport (eds. Smith, W. L. & Chanley, M. H.) 29–60 (Springer US, 1975). doi:10.1007/978-1-4615-8714-9_3

4. Cunliffe, M., Harrison, E., Salter, M., Schäfer, H., Upstill-Goddard, R. & Murrell, J. Comparison and validation of sampling strategies for the molecular microbial analysis of surface microlayers. Aquat. Microb. Ecol. 57, 69–77 (2009).

5. Yooseph, S., Andrews-Pfannkoch, C., Tenney, A., McQuaid, J., Williamson, S., Thiagarajan, M., Brami, D., Zeigler-Allen, L., Hoffman, J., Goll, J. B., Fadrosh, D., Glass, J., Adams, M. D., Friedman, R. & Venter, J. C. A metagenomic framework for the study of airborne microbial communities. PLoS One 8, e81862 (2013).

6. Monger, B. C. & Landry, M. R. Flow Cytometric Analysis of Marine Bacteria with Hoechst 33342t. Appl. Environ. Microbiol. 59, 905–911 (1993).

7. Noble, R. T. & Fuhrman, J. A. Use of SYBR Green I for rapid epifluorescence counts of marine viruses and bacteria. Aquat. Microb. Ecol. 14, 113–118 (1998).

8. Boström, K. H., Simu, K., Hagström, Å. & Riemann, L. Optimization of DNA extraction for quantitative marine bacterioplankton community analysis. Limnol. Oceanogr. Methods 2, 365–373 (2004).

9. Bolger, A. M., Lohse, M. & Usadel, B. Trimmomatic: A flexible trimmer for Illumina sequence data. Bioinformatics 30, 2114–2120 (2014).

10. Wood, D. E. & Salzberg, S. L. Kraken: ultrafast metagenomic sequence classification using exact alignments. Genome Biol. 15, R46 (2014).

11. Sirén, J., Välimäki, N. & Mäkinen, V. Indexing graphs for path queries with applications in genome research. IEEE/ACM Trans. Comput. Biol. Bioinforma. 11, 375–388 (2014).

12. Quinlan, A. R. & Hall, I. M. BEDTools: A flexible suite of utilities for comparing genomic features. Bioinformatics 26, 841–842 (2010).

13. Dupont, C. L., Rusch, D. B., Yooseph, S., Lombardo, M., Richter, R. A., Valas, R., Novotny, M., Yee-greenbaum, J., Selengut, J. D., Haft, D. H., Halpern, A. L., Lasken, R. S., Nealson, K., Friedman, R. & Venter, J. C. Genomic insights to SAR86 , an abundant and uncultivated marine bacterial lineage. ISME J. 6, 1186–1199 (2012).

14. Nurk, S., Meleshko, D., Korobeynikov, A. & Pevzner, P. A. metaSPAdes: a new versatile metagenomics assembler. arXiv Prepr. arXiv1604.03071 1, (2016).

15. Gurevich, A., Saveliev, V., Vyahhi, N. & Tesler, G. QUAST: Quality assessment tool for genome assemblies. Bioinformatics 29, 1072–1075 (2013).

16. Laczny, C. C., Sternal, T., Plugaru, V., Gawron, P., Atashpendar, A., Margossian, H. H., Coronado, S., der Maaten, L. van, Vlassis, N. & Wilmes, P. VizBin - an application for reference-independent visualization and human-augmented binning of metagenomic data. Microbiome 3, 1 (2015).

17. Parks, D. H., Imelfort, M., Skennerton, C. T., Hugenholtz, P. & Tyson, G. W. CheckM: assessing the quality of microbial genomes recovered from. Genome Res. 25, 1043–1055 (2015).

18. Dupont, C. L., Larsson, J., Yooseph, S., Ininbergs, K., Goll, J., Asplund-Samuelsson, J., McCrow, J. P., Celepli, N., Allen, L. Z., Ekman, M., Lucas, A. J., Hagström, Å., Thiagarajan, M., Brindefalk, B., Richter, A. R., Andersson, A. F., Tenney, A., Lundin, D., Tovchigrechko, A., Nylander, J. A. A., Brami, D., Badger, J. H., Allen, A. E., Rusch, D. B., Hoffman, J., Norrby, E., Friedman, R., Pinhassi, J., Venter, J. C. & Bergman, B. Functional tradeoffs underpin salinity-driven divergence in microbial community composition. PLoS One 9, (2014).

19. Letunic, I. & Bork, P. Interactive Tree of Life v2: Online annotation and display of phylogenetic trees made easy. Nucleic Acids Res. 39, 475–478 (2011).

*Supplementary Information References*

1. Kim, H., Miller, A. J., McGowan, J. & Carter, M. L. Coastal phytoplankton blooms in the Southern California Bight. Prog. Oceanogr. 82, 137–147 (2009).

2. Whitman, W. B., Coleman, D. C. & Wiebe, W. J. Prokaryotes: the unseen majority. Proc. Natl. Acad. Sci. U. S. A. 95, 6578–6583 (1998).

3. Bird, D. F. & Kalff, J. Empirical Relationships between Bacterial Abundance and Chlorophyll Concentration in Fresh and Marine Waters. Can. J. Fish. Aquat. Sci. 41, 1015–1023 (1984).

4. Turley, C. M. & Mackie, P. J. Biogeochemical significance of attached and free-living bacteria and the flux of particles in the NE Atlantic Ocean. Mar. Ecol. Prog. Ser. 115, 191–204 (1994).

5. Burrows, S. M., Elbert, W., Lawrence, M. G. & Pöschl, U. Bacteria in the global atmosphere – Part 1: Review and synthesis of literature data for different ecosystems. Atmos. Chem. Phys. 9, 9263–9280 (2009).

6. Dupont, C. L., Larsson, J., Yooseph, S., Ininbergs, K., Goll, J., Asplund-Samuelsson, J., McCrow, J. P., Celepli, N., Allen, L. Z., Ekman, M., Lucas, A. J., Hagström, Å., Thiagarajan, M., Brindefalk, B., Richter, A. R., Andersson, A. F., Tenney, A., Lundin, D., Tovchigrechko, A., Nylander, J. A. A., Brami, D., Badger, J. H., Allen, A. E., Rusch, D. B., Hoffman, J., Norrby, E., Friedman, R., Pinhassi, J., Venter, J. C. & Bergman, B. Functional tradeoffs underpin salinity-driven divergence in microbial community composition. PLoS One 9, (2014).

# Chapter 6. Cultivable halotolerant bacteria and fungi from precipitation and sea spray aerosols indicate a possible missing marine source of atmospheric ice nucleating particles

## Section 6.1 Introduction

Ice nucleating particles (INPs) are crucial to the formation of ice in clouds and precipitation, and primary biological aerosol particles (PBAP) are important to ice nucleation (IN) processes and regulation of precipitation[1–4]. However, the connection between airborne microbial communities and IN properties is ill-defined[5,6]. As ice containing clouds are the predominant sources of global precipitation[7] ice nuclei are of particular importance in climate cooling processes. The lack of the specific connections between species, abundance, IN properties, and precipitation impede accurate prediction and understanding on the role of PBAP in precipitation.

INPs are rare aerosols (1 in $10^5$)[8] that induce freezing of cloud droplets at temperatures above the homogenous freezing point of water (-38 °C), and can influence several mixed-phase optical and microphysical cloud properties including phase, lifetime, and precipitation[1,3,4,9]. As mixed-phase clouds cover 20-30 % of the Earth[10], they have a significant influence on climate. However, numerical representation of in-cloud ice processes remains problematic for global climate models (GCMs). An intercomparison of 19 different GCMs (McCoy et al., 2015) showed that glaciation temperature, the temperature at which ice

and liquid are equally mixed, varies by 40 °C, and that repartitioning between ice and water is responsible for a significant portion of the increase in mixed-phase cloud liquid water paths[11].

Ice processes in mixed-phase clouds are controlled by several parameters including updraft, moisture supply, and INP concentrations[12]. Sometimes moisture supply and updraft can dominate in-cloud ice processes, and the sign and magnitude of the relationship between INP and ice processes remains in question due to limited *in situ* observations of relationships between INP concentrations and cloud macro and microphysical properties[7]. However, there is both observational and simulation-based evidence for a strong influence of INPs on cloud processes. Yun and Penner demonstrated the high sensitivity of GCM simulated TOA longwave flux to the treatment of heterogeneous ice nucleation in mixed phase clouds[13]. From the observational perspective, Ault et al. compared two atmospheric river events in California and found that the presence of dust INPs during an atmospheric river event enhanced precipitation over the Sierra Nevada mountains by 40 %[14].

With freezing temperatures up to 36 °C above the freezing temperature of water, biogenic INPs can have a particularly profound impact on mixed-phase clouds[4]. Though mineral dust is considered to be the dominant source of INPs in many parts of the world[15–18], biogenic INPs remain potentially influential due to their warmer freezing temperatures, particularly in remote ocean regions where dust is less abundant.

PBAP comprise a subset of INPs that have the warmest freezing temperatures. A primary focus of early investigations into biological IN sources was bacteria possessing cell-surface ice nucleation proteins. These ice nucleating proteins can nucleate ice at temperatures as warm as -2 to -8 °C leading to the observations of bioaerosol IN activity at greater than -10 °C. Their low natural abundance and predominance in terrestrial environments have indicated a diminished role of bioaerosols limited to terrestrial systems[19,20], or generally insignificant to precipitation formation[21,22]. However, some of these investigations neglect the contributions of more moderate temperature biological INP sources; IN activation at temperatures > -15 °C has been suggested to be a possible important range for range for PBAP contribution to IN and precipitation[7,23,24].

Precipitation studies have shown that IN properties are influenced by PBAP and can vary according to storm and precipitation event, location, and type. Airborne bacteria and fungi, IN temperatures, and precipitation were found to be tightly correlated in a forest ecosystem, identifying the microorganisms as likely IN activity sources[25]. IN temperatures also demonstrate specificity to storms and precipitation type. Storms can be clustered into groups having similar freeze profiles in mountain snow[19], and compiled comparisons of several precipitation studies[26] demonstrated that snow samples consistently exhibit much warmer IN activation temperatures when to compared to rain and mixed precipitation studies. Additionally, precipitation has also been shown to remove bioaerosols

and INPs from the atmosphere, as shown by 50 % decreases in INPs and bioaerosols when 10 % and 20 % of water vapor is lost respectively[27].

As oceans cover 70 % of the earth, and sea spray aerosol has been shown to be a significant source of INPs[28], marine biological INPs may significantly influence mixed-phase clouds. In simulations of INP populations, marine organic aerosols have been shown to dominate INP populations in the Southern Ocean[29], and when implemented into a coupled aerosol and GCM model, marine organic aerosols contribute more to ice formation than dust or black carbon/organic matter in mixed-phase clouds[30]. Mesocosm studies have linked sea spray aerosol IN activity to the decline of phytoplankton blooms[31], and IN properties have been detected in marine diatoms and green algae[3,32–35]. Marine Antarctic bacteria and those associated with sea-ice have also been identified with IN activity[36,37]. While the ocean seems to be an important source of IN and marine microorganisms have been identified in rain samples[38], examinations of specific IN activity of marine bacterial and fungal isolates in the atmosphere and precipitation are underrepresented and uncharacterized in the literature[39].

In an effort to elaborate on possible underestimated biological sources of marine INPs and to compare potential differences between aerosol and rain we isolated cultivable halotolerant bacteria and fungi from sea spay aerosol (SSA) and precipitation from a coastal subtropical climate in southern California over the course of 9 rainstorms during an El Niño event. Using cultivation in marine medium to guide selection, several bacterial and fungal species were isolated,

identified, and assessed for IN properties using immersion mode spectroscopy. While these methods eliminate species not amenable to cultivation, it allowed examination of the contribution of these isolates to IN properties detected in original samples. We used the FLEXible PARTicle dispersion model (FLEXPART) and the High-Resolution Rapid Refresh atmospheric model (HRRR) to estimate isolate source, identify altitudes, and characterize storm meteorology. Studies that combine precipitation, IN, microbial identity, and weather tracking in diverse precipitation types, regions, and climates are key to unraveling specific contributions to climate patterns.

**Section 6.2 Results and Discussion**

*Subtropical coastal storm properties and origins*

SSA and rain samples were collected from a pier on the coast of La Jolla, CA (32°52'01.4"N 117°15'26.5"W) spanning 9 rainstorms March 6 to May 6, 2016 during an El Niño event. The source of precipitation was determined using 10-day FLEXPART back trajectories (Figure 6.1, Table S6.1). Storms derived from the mid-Pacific Ocean (storms 1, 6, 7, 8, 9) or Bering Sea (storms 2, 3, 4, 5) indicating a marine source of the storms and microorganisms isolated. Storm 7 (Figure 6.1g) may have been additionally influenced by west coast continental sources. SSA INP measurement show IN activity in the range of –9.5 to –21.7 °C (Figure S6.3b) and rain INP measurements were in the range of –6.2 to –19.3 °C (Figure 6.3b). Cloud bottom and top altitudes were estimated using the High-Resolution Rapid

Refresh model (HRRR). Over the 9 storms, cloud altitude ranged from 950 – 600 mb, bottom to top, or 500 – 4000 m, with temperatures ranging from 265 – 288 K (Table S6.1).

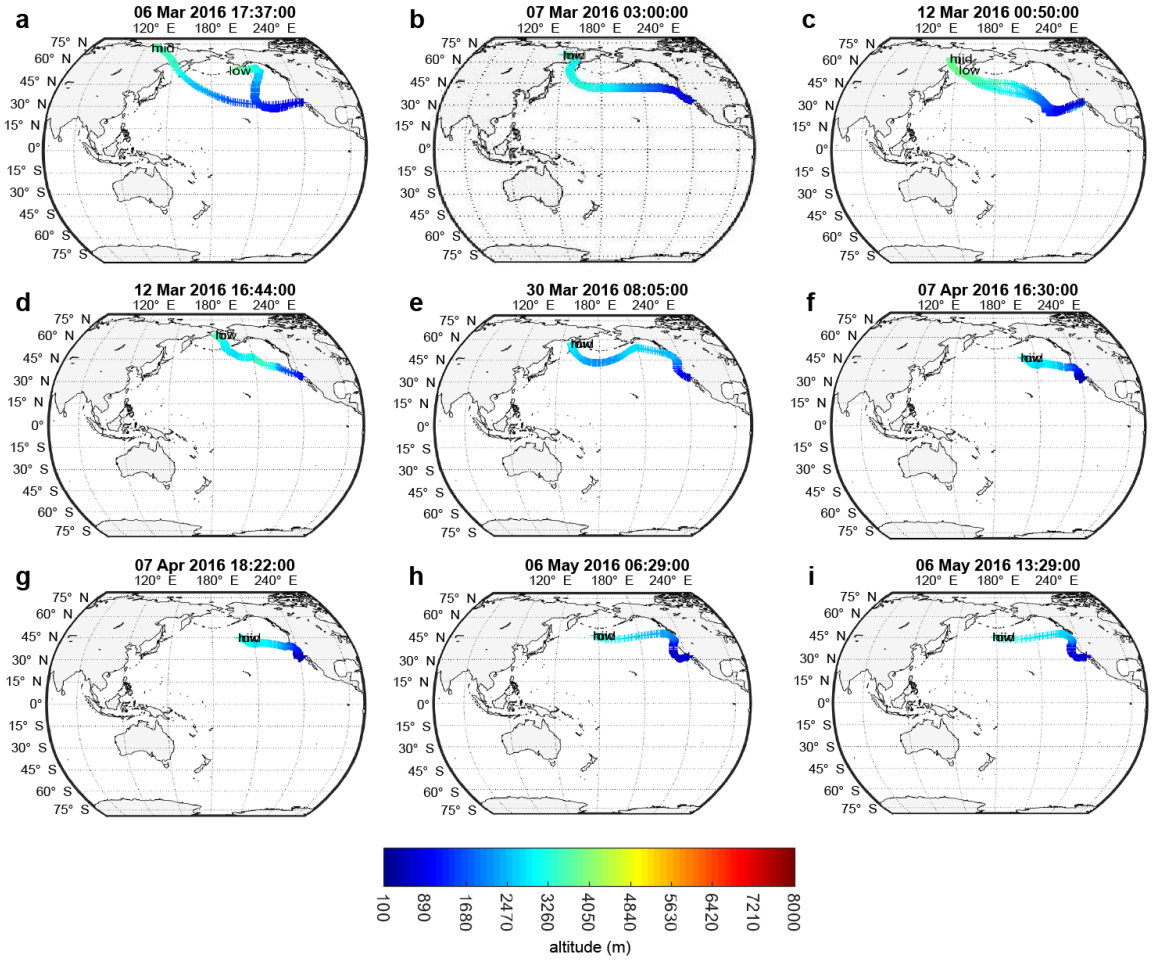


Figure 6.1 10-day back-trajectories from cloud base, mid-cloud, and cloud-top during 9 precipitation events at the SIO Pier (32.8662 °N, 117.2544 °W). FLEXPART back-trajectories were used to estimate potential source regions of INPs to the clouds during precipitation events. Shown are the particle centroids of back-trajectories from three release altitudes within each cloud (see Table S6.1 for details on altitude selection criteria), labeled "high" for cloud top, "mid" for halfway between base and top, and "low" for cloud bottom. Origins of particles in the 10-day simulation are shown to range from 4000 – 8000 m over Russia to 2500 – 3500 m over the Sea of Okhostk, the Bering Sea, and the north Pacific. FLEXPART results suggest a dominance of marine particle sources to clouds.

*Bacterial and fungal taxonomy*

Rain and SSA samples resulted in 37 isolates from rain samples, and 14 isolates from SSA samples with 29 unique OTUs as determined by > 96 % sequence identity of 16S sequences (Table S6.3). The isolates derived from rain and SSA are highly pigmented, presumably to content with high *uv* exposure (Figure S6.1). This pigmentation was especially prevalent in rain samples. More isolates were obtained from rain samples, and this is likely the result of lower SSA bacterial and fungal loads between rain sampling. This supports observations of precipitation deposition and removal of PBAP from the atmosphere[27].

The taxonomy of the SSA and rain isolates differed between the communities with some overlap (Figure 6.2, Table S6.3). While these differences may owe to artificial biases from low SSA isolates recovery, the rain samples had a high proportion of Actinobacteria; while in SSA, Firmicutes, and Proteobacteria were more dominant with no fungal species isolated. However, dominant SSA species such as *Bacillus* sp. and *Psychrobacter* sp. were also isolated from rain samples demonstrating that the rain at least in part derives from a similar source as SSA. *Cellulosimicrobium* sp. and *Microbacterium* sp. were common Actinobacteria found in rain samples. Even with a much warmer climate than commonly examined in similar precipitation studies, the community structure is similar to what is commonly found in precipitation, clouds, or ice and is distinct from other ecological niches[1,39–41]. Their presence in these and other studies may be explained by an increased ability of Actinobacteria, select Proteobacteria and Firmicutes to aerosolize (see Chapter 5). Only one known characteristic IN

bacteria, *Pantoea* sp., known to possess IN proteins[42] was identified in one rain and one SSA sample representing 3.5 % of total isolates. The storm tracking data (Figure 6.1) in conjunction with the use of marine medium and shared community composition between precipitation and SSA samples, suggest a marine origin for many of the rain isolates. However, as several of the species identified in this study have been described in terrestrial, marine, and freshwater systems, it cannot be ruled out that these species are able to adapt to diverse environmental and salinity conditions. While cultivation methods exclude the large amount uncultivable microorganism in the environment, we captured several possible contributors to rain IN activity and through isolation maintain the ability to further characterize them.

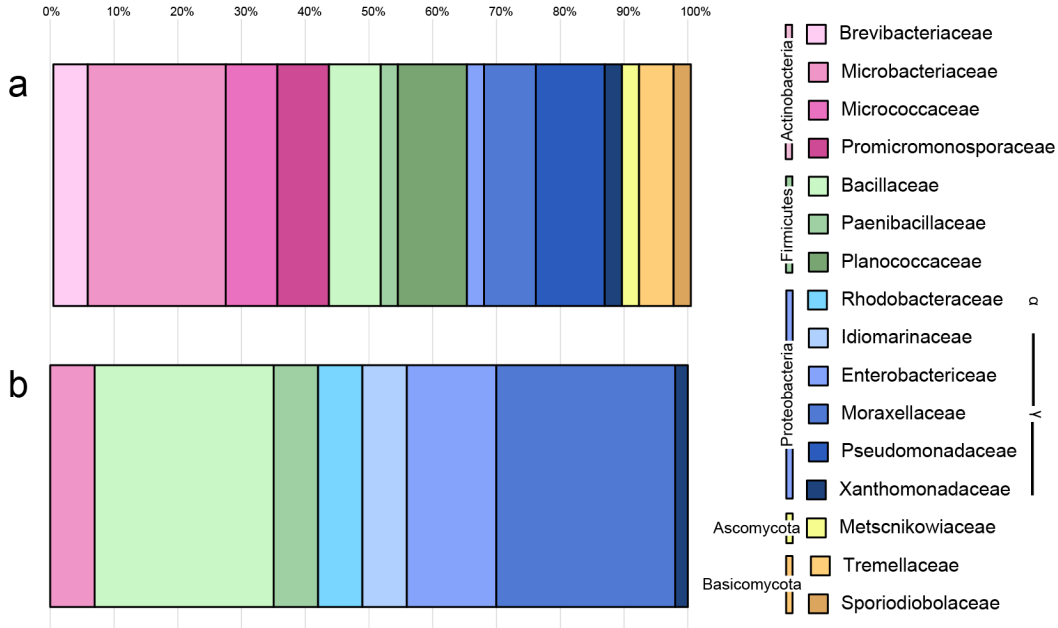

Figure 6.2 Taxonomic distributions of precipitation (a) and SSA (b) isolates.

*IN Properties of Rain and SSA isolates*

The IN properties of rain and SSA isolates show moderate IN activity and specificity according to source and or storm type (Figure 6.3, Figure S6.3). To examine the IN properties of unique strains within samples an effort was made to remove duplicates using multiple sequence alignment analysis (see methods). The relationship between 16S sequences of isolates within their OTUs is shown in (Figure S6.2). All rain isolates freeze between -12.2 and -24.2 (Figure 6.3a). SSA isolates had IN activity between -13.8 and -25.8 °C (Figure S6.3a). Sterile growth media, ZoBell, also demonstrated moderate IN activity, -12.5 to -24.9 °C (Figure S6.4a). To ensure the growth media was not influencing isolate IN properties controls were run on media-free isolates which retain their IN activity in the absence of ZoBell medium (Figure S6.4b). The IN temperature range of these rain isolates follows the trends outlined in Petters and Wright for precipitation samples with rain samples that range from ~ -11 to -37 °C[26]. This could indicate that there are similar sources of IN activity in similar precipitation types and that microorganisms could be contributing to IN activity in this and other systems. The range of IN activity temperatures are shown for storm (Figure 6.3b) and SSA (Figure S6.3b). An overlap in IN freezing temperatures is evident from -12 to -19.25 °C between the IN activity of the raw samples and the isolates derived from them. This indicates a possible shared origin of IN activity; the bacteria and fungi could be a source of the IN activity in the original precipitation and SSA samples in the overlapping range. In Fig. 6.3, the cultures derived from precipitation exhibit IN

activity down to -24 °C, whereas the raw precipitation INP freezing temperatures only extend to -19.25 °C. However, the lack of apparent INP freezing activity beyond -19.25 °C is simply an artifact of the high concentration of INPs in raw precipitation relative to the concentration of INPs in the microbial cultures. As described in Section 6.4, the concentration of INPs measured depends on the fraction of unfrozen wells, so the lack of data beyond the coldest freezing temperature simply reflective of the temperature at which all droplets had frozen, and not of the lack of INPs that activate at colder temperatures. Thus, the overlap in IN freezing temperatures between the two samples regimes (cultures derived from precipitation and the raw precipitation) theoretically range from -12 °C down to the homogenous freezing point of water (-38 °C). While the isolates and their originating raw samples have overlapping IN profiles, other sources like inorganic and organic molecules and detritus, marine microorganisms that were not captured by isolation or amenable to cultivation, or possible freshwater organism of terrestrial origin could be responsible for the activity in raw samples. Though of note, storm 2 and storm 7, the most likely to have terrestrial contributions (Figure 6.1), had colder IN temperature ranges -13.8 to -19.0 °C and -10.9 to -17.0 °C respectively, compared to the entire range for the raw precipitation samples (-6.2 to -19.3 °C).

The IN temperatures of specific isolates trend according to storm demonstrated by similar freezing profiles of isolates from the same storm (Figure 6.3a). To examine this further, we inspected the variance of a storm's isolate IN

spectra compared to the spectra of all the storm isolates observed by comparing the distribution of isolates from the same precipitation event to the distribution of all storm isolates examined by area coverage of 2D plots (Figure S6.5, Table S6.3). Using percent of spread with 100 % representing the coverage of all rain isolates combined, most of the storms had isolates with IN activity low area coverage indicating a tight clustering of data. Seven storms had less than 40 % spread; 6 less than 26%. Storm 9 with 6 isolates representing a spread of 12.46 % was a particularly good example of similar storm-isolate activity. This temperature clustering was not present in SSA isolate data (Figure S6.3). This precipitation / IN temperature relationship has been seen in other studies that observed similar freezing profiles in snow[19]. The temperature selection behavior could be the result of different microbial sources by region, cloud height, or storm fronts. Different IN properties according to storm fronts have been observed in other studies[43]. This could also be explained by selective deposition of microbes by cloud temperature. It could also be the microbes adapting themselves to the temperature of their environment though this is unlikely as an adaptation to cloud temperatures would likely be lost under laboratory conditions.

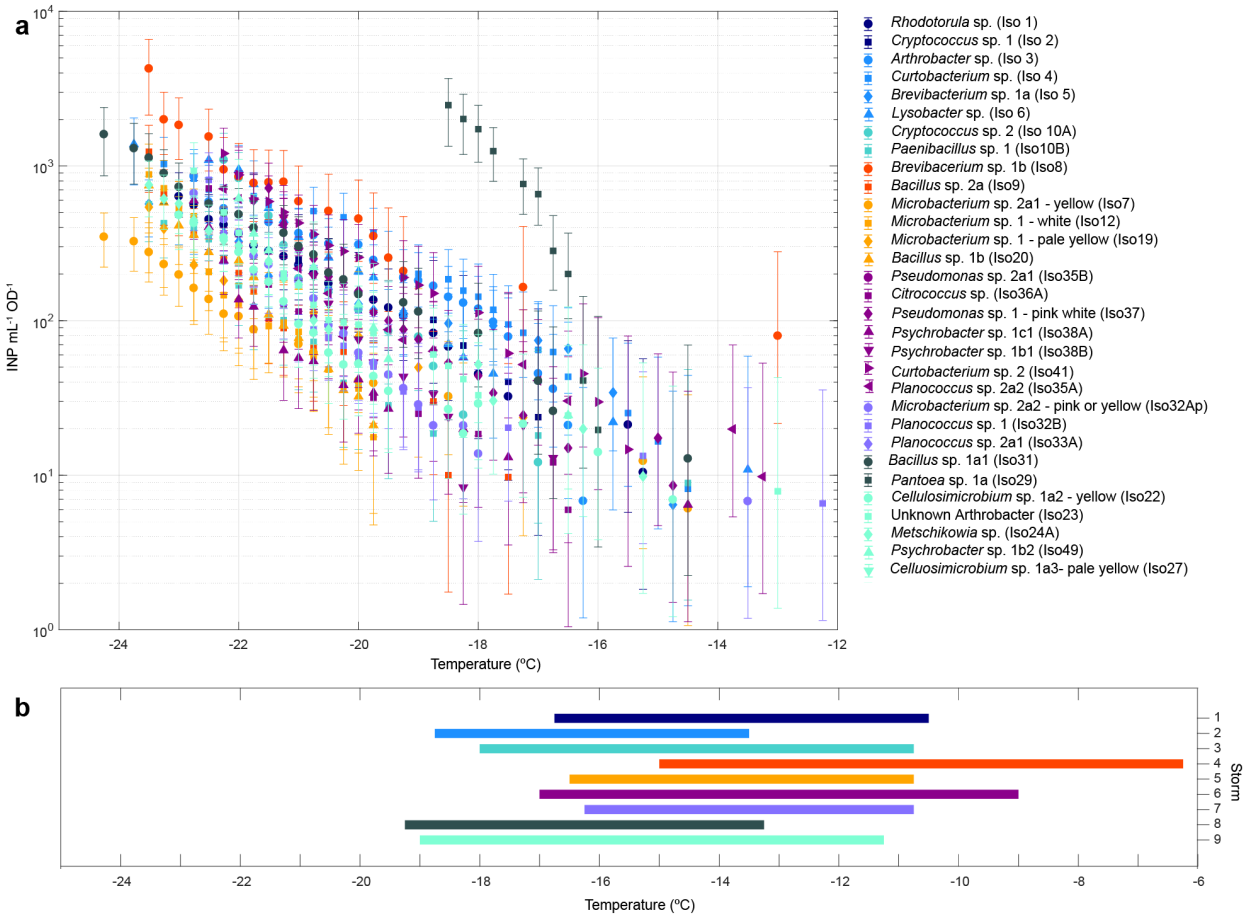


Figure 6.3 (a) IN activity of precipitation isolates by storm. (b) IN activity of storm samples. INP measurements are normalized to culture OD (590nm).

While there is a great deal of overlap of IN properties of rain and SSA isolates, rain isolates generally had warmer IN temperatures (Figure 6.4). The IN activity of SSA isolates is shifted to colder temperatures and precipitation isolates IN measurements have a higher density in the warmest observed temperatures compared to SSA samples. This indicates a temperature specificity in these systems.

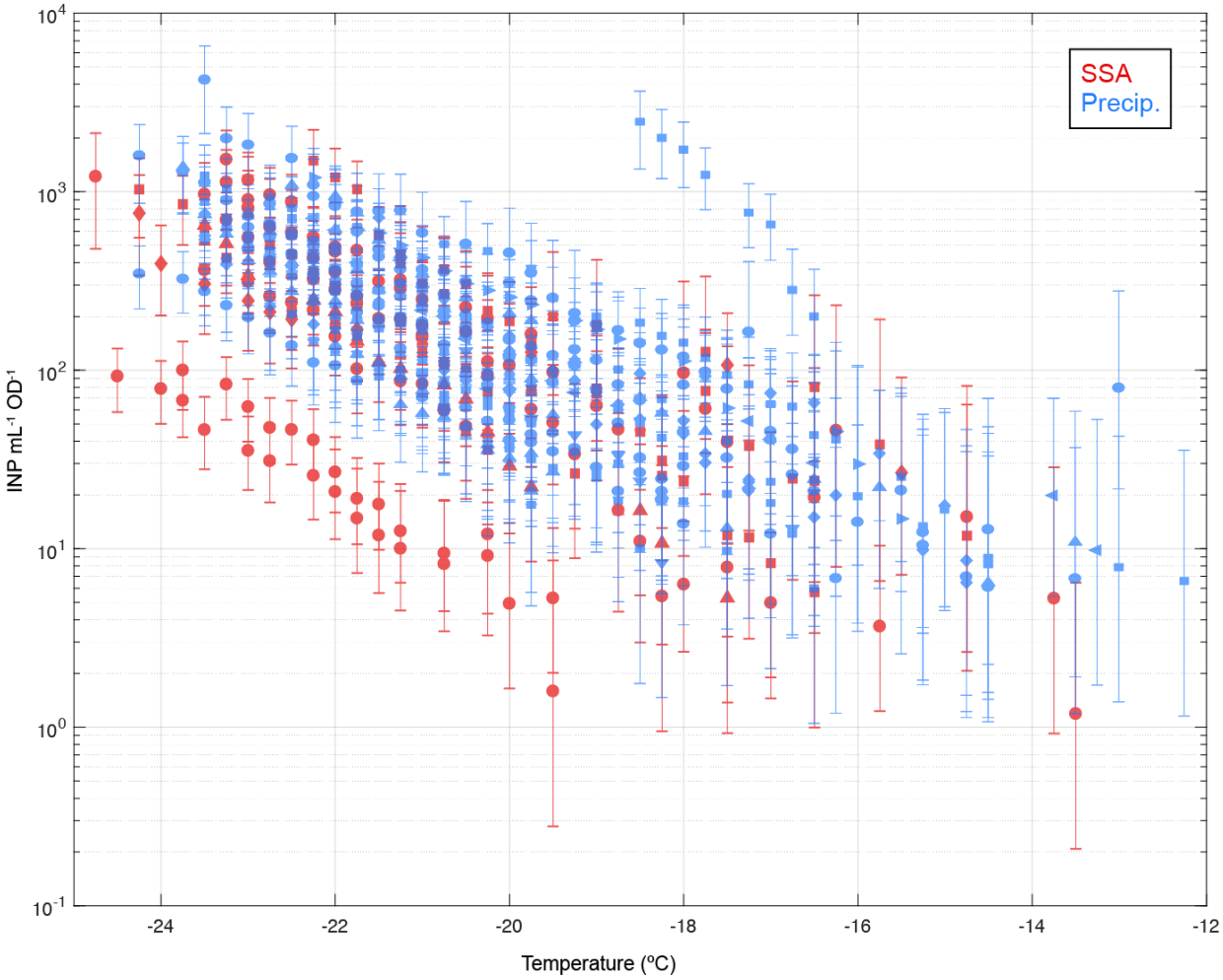


Figure 6.4 Comparison of IN activity of precipitation and SSA. INP measurements are normalized to culture OD (590nm).

## Section 6.3 Conclusions

While cultivation methods limit a complete view of the total bacterial and fungal communities affecting IN properties, we were able to test the specific IN activity of a subset of halotolerant bacterial and fungal species to show that many isolates have moderate IN activity. These rain and SSA isolates have similar IN temperature profiles to their sources indicating that these bioaerosols contribute to IN activity seen in their systems. The IN activity of rain isolates have

colder IN temperatures than studies of snow and ice indicating a possible connection between IN activation temperatures and precipitation type[26]. This temperature specificity is further extended to be also storm specific indicating unique cloud mechanisms that deposit microbes within a narrow range of IN activities. A study of air and snow bacterial and fungal communities in a high elevation region suggest that changes in IN activity were not associated with population changes of the commonly studied ice-nucleating protein containing bacteria[40]. While this data set lacks information regarding abundance in precipitation samples or clouds, our results indicate a presence of several taxonomies of IN active bacteria with moderate freezing temperatures. It is possible that in subtropical, Mediterranean climate zones, an abundance of such moderate marine biogenic INPs could influence ice processes in mixed-phase clouds. Additionally, INP with activation temperatures > -10°C could be more important for snow formation while more moderate IN activation temperatures ( -20 to -10 °C) could be more important to rain formation. As a number of samples derive from the mid-Pacific Ocean and Bering Sea it indicates that several of the isolates are likely of marine origin underlining an possible important source and specific species contribution to precipitation relevant INP for both coastal and open ocean regions.

**Section 6.4 Methods**

*Precipitation and SSA Sample Collection Methods*

Precipitation and Sea Spray Aerosol (SSA) samples were collected on the Ellen Browning Scripps Memorial Pier at Scripps Institution of Oceanography (SIO) (32.8662 °N, 117.2544 °W) from 03/06/16 – 05/17/16. SSA samples were collected on Whatman® Nuclepore 45 mm diameter, 0.2 µm pore-size polycarbonate filters placed inopen-face 150 mL Nalgene ® Analytical Filter Units. After collection, SSA filter samples were immersed in 12 mL of ultrapure water, and particles were shaken off the filter by hand for 20 minutes. The precipitation samples were collected using a modified Teledyne Isco© Full-Size Portable Sampler, fitted with 24 1 L polypropylene bottles. Prior to sampling, the bottles were immersed in 10 % hydrogen peroxide for 10 minutes, then rinsed three times with ultrapure water. The automated sampler would engage when triggered by precipitation of at least 0.05"/hr, and would sample using the first of 24 bottles for 30 minutes, and thereafter switch bottles at hourly intervals. Within one to two hours of sample collection, INP concentrations were measured using the SIO-Automated Ice Spectrometer (SIO-AIS)[46], an automated offline freezing assay technique for measurement of immersion mode INPs. To decrease the effect of interstitial particle sweep out by falling raindrops on measured INP concentration, precipitation from the first 30 minutes was discarded. In Wright and Petters, sweep out was estimated to contribute from 1.2 – 14 % to measured concentrations of INP in a precipitation sample.

The INP measurement technique is described in detail in Beall et al.[46], but briefly, the precipitation samples were distributed in microliter aliquots into a clean 96-well disposable polypropylene sample tray. An equal number and volume of aliquots of ultrapure water accompany each sample in the disposable tray as control for contamination from the loading and/or ultrapure water. The sample trays are then inserted into an aluminum block that is cooled until the samples are frozen. Cumulative INP number concentrations per temperature per volume are calculated using the fraction of unfrozen wells per given temperature interval:

$$\mathrm{INP} = \frac{-\ln(f)}{V_d} \qquad \text{Eq. (1)}$$

where $V_d$ is the volume of the sample in each well, or for SSA samples. For SSA filter samples, cumulative INP number concentrations are calculated using the ratio of the volume used for resuspension of the particles to the volume of SSA sampled:

$$\mathrm{INP} = \frac{-\ln(f)\cdot V_{re}}{V_d \cdot V_{SSA}} \qquad \text{Eq. (2)}$$

The fraction of unfrozen wells "f" is adjusted for contamination by subtracting the number of frozen ultrapure water wells per temperature interval from both the total number of unfrozen wells and total wells of the sample.

Within one to two hours of collection, precipitation and SSA samples were also inoculated in 5 mL ZoBell growth media [47] (5 g peptone, 1 g yeast extract per 1 L) in filtered (0.22 μm) autoclaved seawater and grown under ambient

conditions (21 - 24 ˚C). INP concentrations for cultures were measured 1 day post inoculation and for several days to monitor for sustained IN activity.

*Bacterial and fungal isolation and characterization*

Precipitation and SSA microorganisms were cultivated with Zobell marine growth medium[47]. Isolation was performed by successive plating on ZoBell agar. Liquid cultures were inoculated from single colonies and grown to late exponential phase. DNA was extracted from liquid cultures of isolates after an overnight lysis with proteinaseK and lysozyme (MilliporeSigma)[48] using a QIAamp® kit (QIAGEN). 16S V4 ribosomal DNA fragments were amplified using the primers 515F (GTGYCAGCMGCCGCGGTAA) and 926R (CCGYCAATTCMTTTRAGT)[49]. PCR products were purified using GenElute™ PCR Clean-up kit (MilliporeSigma). 16S fragment DNA sequences were resolved by sanger sequencing (Retrogen, San Diego, CA). OTUs were determined from 16S sequences using SINA[50] and individual sequences were inspected using BLAST (https://www.ncbi.nlm.nih.gov/) for further characterization.

To assess for duplicate isolates within the sample sampling period, 16S sequences were compared. Sequences within the same OTU were adjusted and aligned in DECIPHER(Alignseqs(), AdjustAlignment())[51]. These sequence alignments were used to generate phylogenetic trees using ClustalW2 (UPGMA)[52] and visualized with iTOL[53]. Branch distances were used to evaluate sequence similarity. To facilitate comparisons between organisms assigned to the same OTU,

identity assignments include divisions at distances > 0.1 (e.g. 1, 2, 3…) and further subdivided by distances > 0.01 (e.g. 1a, 1b, 1c…). Nonzero distances < 0.01 were given sub labels (e.g. 1a1, 1a2…). Zero distances were given identical labels. Distances < 0.01 were determined to be possible duplicates. These were removed from relevant analyses if they were collected during the same sampling period unless the organisms had a different phenotype generally indicated by different pigmentation.

*Storm and aerosol source characterization methods*

No radar was available at the sampling site. Cloud altitudes at the time of precipitation sample collection were estimated using the High-Resolution Rapid Refresh model (HRRR). The altitudes and pressure levels of clouds were assumed to be located where RH > 95-100 % in the model. The specific RH criteria applied to each storm are provided in Table S6.1. HRRR model output was compared with RH, pressure, and wind measurements from the SIO pier weather station. Three heights of the cloud, top, middle and bottom were used as release points of FLEXPART 10-day Lagrangian backward trajectories. Back-trajectories were used to identify potential sources of INPs in the precipitation samples, and to indicate potential sources of land-based contamination in SSA and precipitation samples due to local wind patterns or land-sea breezes.

*Isolate measurement and controls*

To measure the IN activity of each isolate, liquid cultures were grown to late exponential phase. Growth was monitored by OD (590 nm). INP concentrations were measured as described on liquid cultures and compared to ZoBell blank as a control. To account for disparate culture densities, INP measurements were normalized to OD measurements. To remove possible influence from ZoBell growth media on INP measurements, late exponential cultures were washed three times with filtered (0.22 µm) autoclaved seawater by successive centrifugation and resuspension. INP measurements were taken as described and compared to sterile seawater controls.

## Section 6.5 Supplementary Information

Table S6.1 Cloud characteristics during 9 precipitation events over the sampling site: SIO Pier (32.8662 °N, 117.2544 °W).

| Storm | Local Date | Local time start | Local time stop | UTC Date | UTC time | UTC Time used for HRRR Hourly Products | RH criteria | Temp (K) | Pressure (mb) | Geopotential Height (m) |
|---|---|---|---|---|---|---|---|---|---|---|
| 1 | 3/6/2016 | 9:07 | 10:07 | 3/6/2016 | 17:07 - 18:07 | 17:00 | >95% | 283 - 274 | 950 - 750 | 800 - 2000 |
| | | | | | | 18:00 | >95% | 288 - 271 | 925 - 725 | 800 - 2000 |
| 2 | 3/7/2016 | 18:30 | 19:30 | 3/8/2016 | 2:30 - 3:30 | 2:00 | >95% | 275 - 268 | 850 - 750 | 1700 - 3000 |
| | | | | | | 3:00 | >95% | 278 - 270 | 875 - 800 | 1500 - 2000 |
| 3 | 3/11/2016 | 16:20 | 17:20 | 3/12/2016 | 00:20 - 1:20 | 12:00 | >95% | 282 - 275 | 950 - 800 | 500 - 2200 |
| | | | | | | 1:00 | >95% | 282 - 262 | 950 - 675 | 800 - 4000 |
| 4 | 3/12/2016 | 8:20 | 9:14 | 3/12/2016 | 16:20 - 17:14 | 16:00 | > 90% | 280 - 278 | 925 - 900 | 1000 - 1100 |
| | | | | | | 17:00 | >90% | 280 | 925 | 1000 |
| 5 | 3/29/2016 | 23:35 | 0:35 | 3/30/2016 | 6:35 - 7:35 | 7:00 | > 90% | 270, 275 | 800, 900 | 2000, 700 |
| | | | | | | 8:00 | > 90% | 278 - 267 | 925 - 750 | 500 - 3000 |
| 6 | 4/7/2016 | 8:15 | 11:00 | 4/7/2016 | 15:15 - 18:00 | 15:00 | > 95% | 278 - 270 | 1000, 750 - 650 | 2200 - 4000 |
| | | | | | | 16:00 | > 95% | 275 - 272 | 725 - 675 | 2200 - 3000 |
| | | | | | | 17:00 | > 95% | 280 - 270 | 775 - 625 | 2000 - 4000 |
| | | | | | | 18:00 | > 95% | 282 - 275 | 850 - 725 | 2500 - 4000 |
| 7 | 4/7/2016 | 12:07 | 13:07 | 4/7/2016 | 19:07 - 20:07 | 19:00 | > 95% | 275 - 265 | 750 - 600 | 2000 - 4000 |
| | | | | | | 20:00 | > 95% | 275 - 265 | 750 - 600 | 3000 - 4000 |
| 8 | 5/5/2016 | 22:59 | 23:59 | 5/6/2016 | 6:00 - 7:00 | 6:00 | > 95% | 275 - 273 | 825 - 750 | 1100 - 2100 |
| | | | | | | 7:00 | > 95% | 278 - 270 | 850 - 750 | 1500 - 2700 |
| 9 | 5/6/2016 | 2:59 | 3:59 | 5/6/2016 | 10:00 - 11:00 | 10:00 | >95% | 282 - 270 | 875 - 700 | 1000 - 3000 |
| | | | | | | 11:00 | > 95% | 278 - 268 | 825 - 700 | 1700 - 3000 |
| 9 | 5/6/2016 | 4:59 | 5:59 | 5/6/2016 | 13:00 - 14:00 | 13:00 | > 95% | 275 - 273 | 825 - 675 | 2000 - 3000 |
| | | | | | | 14:00 | > 95% | 277 - 268 | 850 - 700 | 1500 - 3000 |
| 9 | 5/6/2016 | 8:59 | 9:59 | 5/6/2016 | 17:00 - 18:00 | 17:00 | > 95% | 275 - 270 | 825 - 750 | 1800 - 2800 |
| | | | | | | 18:00 | > 95% | 275 - 271 | 825 - 775 | 1700 - 2900 |

Cloud base and top altitudes were estimated using the RH product of the High-Resolution Rapid Refresh real-time atmospheric model, and three altitudes within the cloud were used as particle release points for FLEXPART back-trajectories (see Figure 6.1): cloud top, cloud base, and middle (halfway between). Regions where RH (Relative Humidity) >95 % were considered for all events except Storm 4 and 5, when a criterion of >90 % was applied. The hourly products closest in time to the precipitation sampling period were used. When cloud depth and altitudes changed over the sampling period, the lowest cloud base and highest cloud altitude were selected as release points for FLEXPART back-trajectories.

Table S6.2 Precipitation (a) and SSA (b) sampling periods

**a** Precipitation

| Event No. | Local Date | Local Time | UTC Date | UTC time |
|---|---|---|---|---|
| 1 | 3/6/2016 | 9:07 - 10:07 | 3/6/2016 | 17:07 - 18:07 |
| 2 | 3/7/2016 | 18:30 - 19:30 | 3/8/2016 | 2:30 - 3:30 |
| 3 | 3/11/2016 | 16:20 - 17:20 | 3/12/2016 | 00:20 - 1:20 |
| 4 | 3/12/2016 | 8:20 - 9:14 | 3/12/2016 | 16:20 - 17:14 |
| 5 | 3/29/2016 | 23:35 - 0:35 | 3/30/2016 | 6:35 - 7:35 |
| 6 | 4/7/2016 | 8:15 - 11:00 | 4/7/2016 | 15:15 - 18:00 |
| 7 | 4/7/2016 | 12:07 - 13:07 | 4/7/2016 | 19:07 - 20:07 |
| 8 | 5/5/2016 | 22:59 - 23:59 | 5/6/2016 | 6:00 - 7:00 |
| 9 | 5/6/2016 | 2:59 - 3:59 | 5/6/2016 | 10:00 - 11:00 |
| 9 | 5/6/2016 | 4:59 - 5:59 | 5/6/2016 | 13:00 - 14:00 |
| 9 | 5/6/2016 | 8:59 - 9:59 | 5/6/2016 | 17:00 - 18:00 |

**b** SSA

| Event No. | Local Date | Local Time | UTC Date | UTC time |
|---|---|---|---|---|
| 20 | 3/5/2016 | 10:40 - 12:15 | 3/5/2016 | 18:40 - 20:15 |
| 21 | 3/7/2016 | 14:58 - 16:52 | 3/7/2016 | 22:58 - 23:52 |
| 22 | 3/8/2016 | 11:34 - 14:42 | 3/8/2016 | 19:34 - 22:42 |
| 23 | 3/28/2016 | 09:09 - 12:22 | 3/28/2016 | 16:09 - 19:22 |
| 24 | 4/28/2016 | 11:45 - 13:22 | 4/28/2016 | 18:45 - 20:22 |
| 25 | 5/5/2016 | 12:00 - 14:23 | 5/5/2016 | 19:00 - 21:23 |
| 26 | 5/6/2016 | 14:15 - 16:37 | 5/6/2016 | 21:15 - 23:37 |

Both precipitation and SSA were collected on Scripps Pier. SSA samples were collected between precipitation events.

Table S6.3 Identity and characteristics of precipitation and SSA isolates

| Isolate ID | Isolate | Storm/ Collection | Isolate IN temp | Isolate T50 | BLAST Identity | % Identity | Phylum | Class | Order | Family |
|---|---|---|---|---|---|---|---|---|---|---|
| Iso1 | Rhodoturula sp | 1 | -17 | -20.5 | Rhodotorula mucilaginosa | 99% | Basidiomycota | Urediniomycetes | Sporidiales | Sporiodiobolaceae |
| Iso2 | Cryptococcus sp. 1 | 1 | -17 | -18.75 | Cryptococcus aureus | 100% | Basidiomycota | Tremellomycetes | Tremellales | Tremellaceae |
| Iso3 | Arthrobacter sp. | 2 | -18 | -19 | Arthrobacter sp.(A. luteolus, A.citreus) | 100% | Actinobacteria | Actinobacteria | Actinomycetales | Micrococcaceae |
| Iso5 | Brevibacterium sp. 1a | 2 | -16.5 | -20 | Brevibacterium sp. (B.linens) | 100% | Actinobacteria | Actinobacteria | Actinomycetales | Brevibacteriaceae |
| Iso4 | Curtobacterium sp. 1 | 2 | -16.25 | -18.375 | Curtobacterium sp. (C. pusillum, C. flaccumfaciens, C. oceanosedimentum) | 100% | Actinobacteria | Actinobacteria | Actinomycetales | Microbacteriaceae |
| Iso6 | Lysobacter sp. | 2 | -15.25 | -20.25 | Lysobacter concretionis | 99% | Proteobacteria | Gammaproteobacteria | Xanthomonadales | Xanthomonadaceae |
| Iso10A | Cryptococcus sp. 2 | 3 | -17 | -20.5 | Cryptococcus sp. (C. flavescens, C. aureus) | 99% | Basidiomycota | Tremellomycetes | Tremellales | Tremellaceae |
| Iso10B | Paenibacillus sp. 1 | 3 | -14.5 | -21.125 | Paenibacillus sp. | 100% | Firmicutes | Bacilli | Bacillales | Paenibacillus |
| Iso9 | Bacillus sp. 2a | 4 | -19.25 | -21.5 | Bacillus sp. (B. baekryungensis, B. hwajinpoensis) | 100% | Firmicutes | Bacilli | Bacillales | Bacilaceae |
| Iso8 | Brevibacterium sp. 1b | 4 | -13 | -21.125 | Brevibacterium sp. (B. luteolum) | 97% | Actinobacteria | Actinobacteria | Actinomycetales | Brevibacteriaceae |
| Iso20 | Bacillus sp. 1b | 5 | -19.75 | -21.5 | Bacillus sp. (B. baekryungensis, B. hwajinpoensis) | 100% | Firmicutes | Bacilli | Bacillales | Bacilaceae |
| Iso12 | Microbacterium sp 1 | 5 | -19.75 | -21.625 | Microbacterium esteraromaticum | 100% | Actinobacteria | Actinobacteria | Actinomycetales | Microbacteriaceae |
| Iso19 | Microbacterium sp 1 | 5 | -17.25 | -22 | Microbacterium esteraromaticum | 100% | Actinobacteria | Actinobacteria | Actinomycetales | Microbacteriaceae |
| Iso7 | Microbacterium sp 2a1 | 5 | -14.5 | -21.875 | Microbacterium esteraromaticum | 100% | Actinobacteria | Actinobacteria | Actinomycetales | Microbacteriaceae |
| Iso36A | Citriococcus sp. | 6 | -16.5 | -20.75 | Citricoccus sp. (C. muralis) | 97% | Actinobacteria | Actinobacteria | Actinomycetales | Micrococcaceae |
| Iso40 | Curtobacterium sp. 2 | 6 | -16 | -19.625 | Curtobacterium sp. | 100% | Actinobacteria | Actinobacteria | Actinomycetales | Microbacteriaceae |
| Iso41 | Curtobacterium sp. 2 | 6 | -15.5 | -20 | Curtobacterium flaccumfaciens | 100% | Actinobacteria | Actinobacteria | Actinomycetales | Microbacteriaceae |
| Iso35A | Planococcus sp. 2a2 | 6 | -13.25 | -19.875 | Planococcus sp.(P. maritimus, P. plakortidis, P. rifietoesis) | 100% | Firmicutes | Bacilli | Bacillales | Planococcaceae |
| Iso36B | Planococcus sp. 2a2 | 6 | -13 | -19.875 | Planococcus sp. | 100% | Firmicutes | Bacilli | Bacillales | Planococcaceae |
| Iso37 | Pseudomonas sp. 1 | 6 | -14.75 | -19.25 | Pseudomonas sp. (P. synxantha, P. grimontii, P. extremaustralis) | 100% | Proteobacteria | Gammaproteobacteria | Pseudomondales | Pseudomonadaceae |
| Iso35B | Pseudomonas sp. 2a1 | 6 | -15 | -20 | Pseudomonas veronii | 100% | Proteobacteria | Gammaproteobacteria | Pseudomondales | Pseudomonadaceae |
| Iso34 | Pseudomonas sp. 2a2 | 6 | -12.75 | -20.625 | Pseudomonas sp. (P. synxantha, P. grimontii, P. extremaustralis) | 100% | Proteobacteria | Gammaproteobacteria | Pseudomondales | Pseudomonadaceae |
| Iso39 | Pseudomonas sp. 2a3 | 6 | -16.25 | -19.625 | Pseudomonas sp. (P. synxantha, P. mucidolens, P. grimontii, ) | 100% | Proteobacteria | Gammaproteobacteria | Pseudomondales | Pseudomonadaceae |
| Iso38B | Psychrobacter sp. 1b1 | 6 | -16.75 | -20 | Psychrobacter sp. (P. maritimus) | 100% | Proteobacteria | Gammaproteobacteria | Pseudomondales | Moraxellaceae |
| Iso38A | Psychrobacter sp. 1c1 | 6 | -14.5 | -20.75 | Psychrobacter sp. | 99% | Proteobacteria | Gammaproteobacteria | Pseudomondales | Moraxellaceae |
| Iso32Ap | Microbacterium sp 2a2 | 7 | -13.5 | -20.375 | Microbacterium esteraromaticum | 99% | Actinobacteria | Actinobacteria | Actinomycetales | Microbacteriaceae |
| Iso33By | Microbacterium sp 2a4 | 7 | -13 | -19.75 | Microbacterium esteraromaticum | 99% | Actinobacteria | Actinobacteria | Actinomycetales | Microbacteriaceae |
| Iso32B | Planococcus sp. 1 | 7 | -12.25 | -20.5 | Planococcus maritimus | 99% | Firmicutes | Bacilli | Bacillales | Planococcaceae |
| Iso33A | Planococcus sp. 2a1 | 7 | -14.75 | -20.125 | Planococcus sp. | 99% | Firmicutes | Bacilli | Bacillales | Planococcaceae |
| Iso33Bp | Unknown Microbacterium | 7 | -12.25 | -20.625 | Unknown Microbacterium sp.? | 89% | Actinobacteria | Actinobacteria | Actinomycetales | Microbacteriaceae |
| Iso31 | Bacillus sp. 1a1 | 8 | -14.5 | -21 | Bacillus halmapalus | 100% | Firmicutes | Bacilli | Bacillales | Bacilaceae |
| Iso29 | Pantoea sp. 1a | 8 | -16 | -17.125 | Pantoea sp. (P. agglomerans, P. ananatis) | 100% | Proteobacteria | Gammaproteobacteria | Enterobacteriales | Enterobacteriaceae |
| Iso30 | Pantoea sp. 1a | 8 | -15.25 | -16.25 | Pantoea sp. (P. agglomerans, P. ananatis) | 100% | Proteobacteria | Gammaproteobacteria | Enterobacteriales | Enterobacteriaceae |
| Iso21 | Cellulosimicrobium sp. 1a1 | 9 | -14 | -21.5 | Cellulosimicrobium sp. (C. funkei, C.cellulans, C. marinum) | 100% | Actinobacteria | Actinobacteria | Actinomycetales | Promicromonosporaceae |
| Iso22 | Cellulosimicrobium sp. 1a2 | 9 | -14.75 | -20.375 | Cellulosimicrobium sp. (C. funkei, C.cellulans, C. marinum) | 99% | Actinobacteria | Actinobacteria | Actinomycetales | Promicromonosporaceae |
| Iso24B | Cellulosimicrobium sp. 1a3 | 9 | -15.75 | -20.625 | Cellulosimicrobium sp. (C. funkei, C.cellulans, C. marinum) | 100% | Actinobacteria | Actinobacteria | Actinomycetales | Promicromonosporaceae |
| Iso28 | Cellulosimicrobium sp. 1a3 | 9 | -16 | -20.75 | Cellulosimicrobium sp. (C. funkei, C.cellulans, C. marinum) | 100% | Actinobacteria | Actinobacteria | Actinomycetales | Promicromonosporaceae |
| Iso24A | Metschikowia sp. | 9 | -15.25 | -21.5 | Metschikowia sp. (M. zobellii, M. krissii, M. reukaufii) | 99% | Ascomycota | Saccharomycetes | Saccharomycetales | Metschikowiaceae |
| Iso49 | Psychrobacter sp. 1b2 | 9 | -18.25 | -20.375 | Psychrobacter sp. (P. pulmonis, P. faecalis) | 99% | Proteobacteria | Gammaproteobacteria | Pseudomondales | Moraxellaceae |
| Iso23 | Unknown Arthrobacter | 9 | -13 | -20.375 | Unknown Arthrobacter sp. | 86% | Actinobacteria | Actinobacteria | Actinomycetales | Micrococcaceae |
| SSA42 | Idiomarina sp. | 20 | -15.5 | -21.25 | Idiomarina fontislapidosi | 100% | Proteobacteria | Gammaproteobacteria | Alteromonadales | Idiomarinaceae |
| SSA14 | Bacillus sp. 1a2 | 21 | -18 | -21.625 | Bacillus sp. (B. aquimaris, B. vietnamensis) | 100% | Firmicutes | Bacilli | Bacillales | Bacilaceae |
| SSA15 | Pantoea sp. 1b | 21 | -15.5 | -20.125 | Pantoea sp. (P. ananatis, P. stewartii, P. agglomerans) | 100% | Proteobacteria | Gammaproteobacteria | Enterobacteriales | Enterobacteriaceae |
| SSA17 | Pantoea sp. 1b | 21 | -15.5 | -21 | Pantoea sp. (P. ananatis, P. stewartii, P. agglomerans) | 100% | Proteobacteria | Gammaproteobacteria | Enterobacteriales | Enterobacteriaceae |
| SSA18 | Pantoea sp. 1b | 21 | -19.25 | -21 | Pantoea sp. (P. ananatis, P. stewartii, P. agglomerans) | 100% | Proteobacteria | Gammaproteobacteria | Enterobacteriales | Enterobacteriaceae |
| SSA16 | Psychrobacter sp. 2a | 21 | -15.5 | -22.625 | Psychrobacter sp. | 93% | Proteobacteria | Gammaproteobacteria | Pseudomondales | Moraxellaceae |
| SSA43 | Bacillus sp. 2b2 | 22 | -16.5 | -21.25 | Bacillus sp. (B. muralis) | 100% | Firmicutes | Bacilli | Bacillales | Bacilaceae |
| SSA44A | Paenibacillus sp. 1 | 23 | -19.25 | -21.125 | Paenibacillus sp. (P. tundrae, P. amyloyticus, P. agarideverons, P. taichungensis) | 100% | Firmicutes | Bacilli | Bacillales | Paenibacillus |
| SSA46 | Bacillus sp. 2b1 | 24 | -18.75 | -21.875 | Bacillus halmapalus | 100% | Firmicutes | Bacilli | Bacillales | Bacilaceae |
| SSA45 | Psychrobacter sp. 1c2 | 24 | -15.25 | -21.5 | Psychrobacter sp. | 100% | Proteobacteria | Gammaproteobacteria | Pseudomondales | Moraxellaceae |
| SSA47 | Bacillus sp. 2b1 | 25 | -18.25 | -21.5 | Bacillus halmapalus | 100% | Firmicutes | Bacilli | Bacillales | Bacilaceae |
| SSA48 | Psychrobacter sp. 1a | 25 | -16.5 | -20 | Psychrobacter sp. (P. pulmonis, P. faecalis) | 96% | Proteobacteria | Gammaproteobacteria | Pseudomondales | Moraxellaceae |
| SSA26 | Microbacterium sp 1 | 26 | -18.25 | -20.5 | Microbacterium esteraromaticum | 99% | Actinobacteria | Actinobacteria | Actinomycetales | Microbacteriaceae |
| SSA25 | Psychrobacter sp. 2b | 26 | -21.25 | -22.125 | Psychrobacter sp. (P. pulmonis, P. faecalis) | 100% | Proteobacteria | Gammaproteobacteria | Pseudomondales | Moraxellaceae |

Storm/collection indicates storm or SSA sampling period. SSA periods after storms periods are denoted with a "2" (eg. SSA period 21 was after storm 1). Taxonomy is denoted by results of BLAST from 16S sequences, percent identity to BLAST assignments, and membership to taxonomic divisions. Isolate identifiers derive from results of multiple sequence alignment analysis (Figure S6.2).

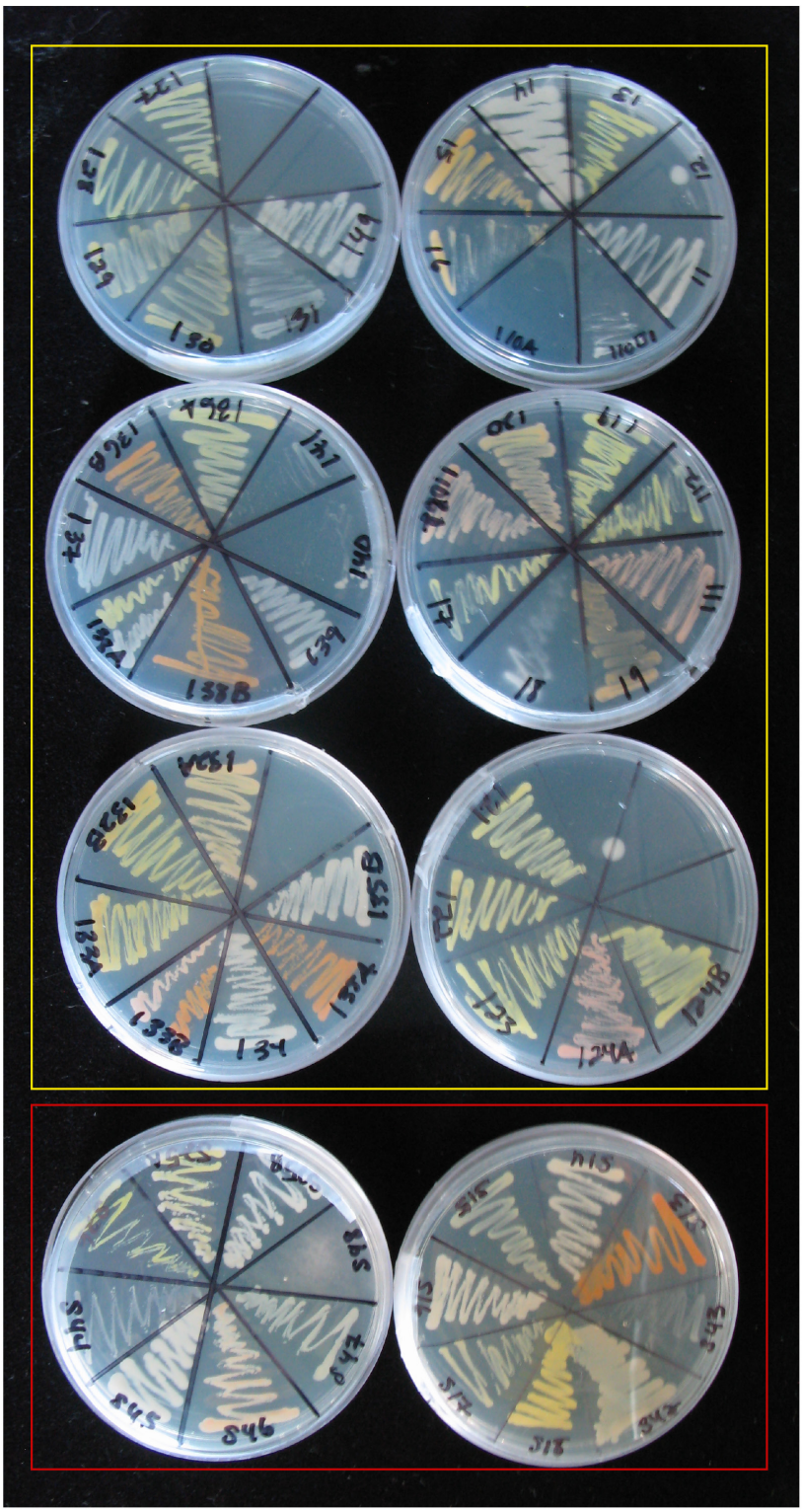

Figure S6.1 Image of SSA (red box) and precipitation (yellow box) isolates on agar plates. Isolates derived from cultivation based isolation.

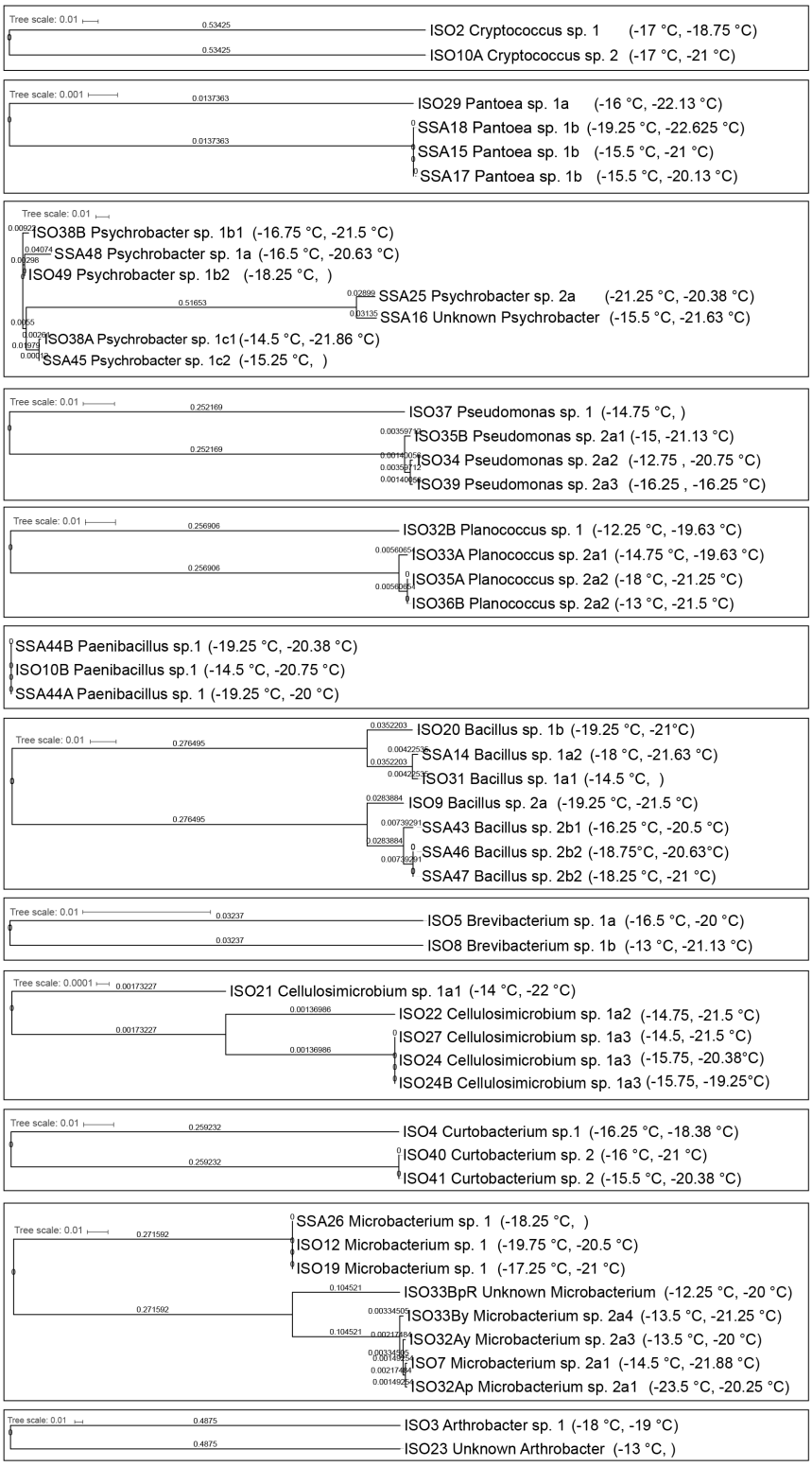


Figure S6.2 Relationship of isolates within the same OTUs using multiple sequence alignments of 16S sequences. Multiple sequence alignments were used to generate phylogenetic trees. The resulting branch distances were used to label isolates within the same OTU. Distances > 0.1 were given a new number. This division was further subdivided by distances > 0.01 which were given a unique letter. Distances < 0.01 were considered possible duplicates.

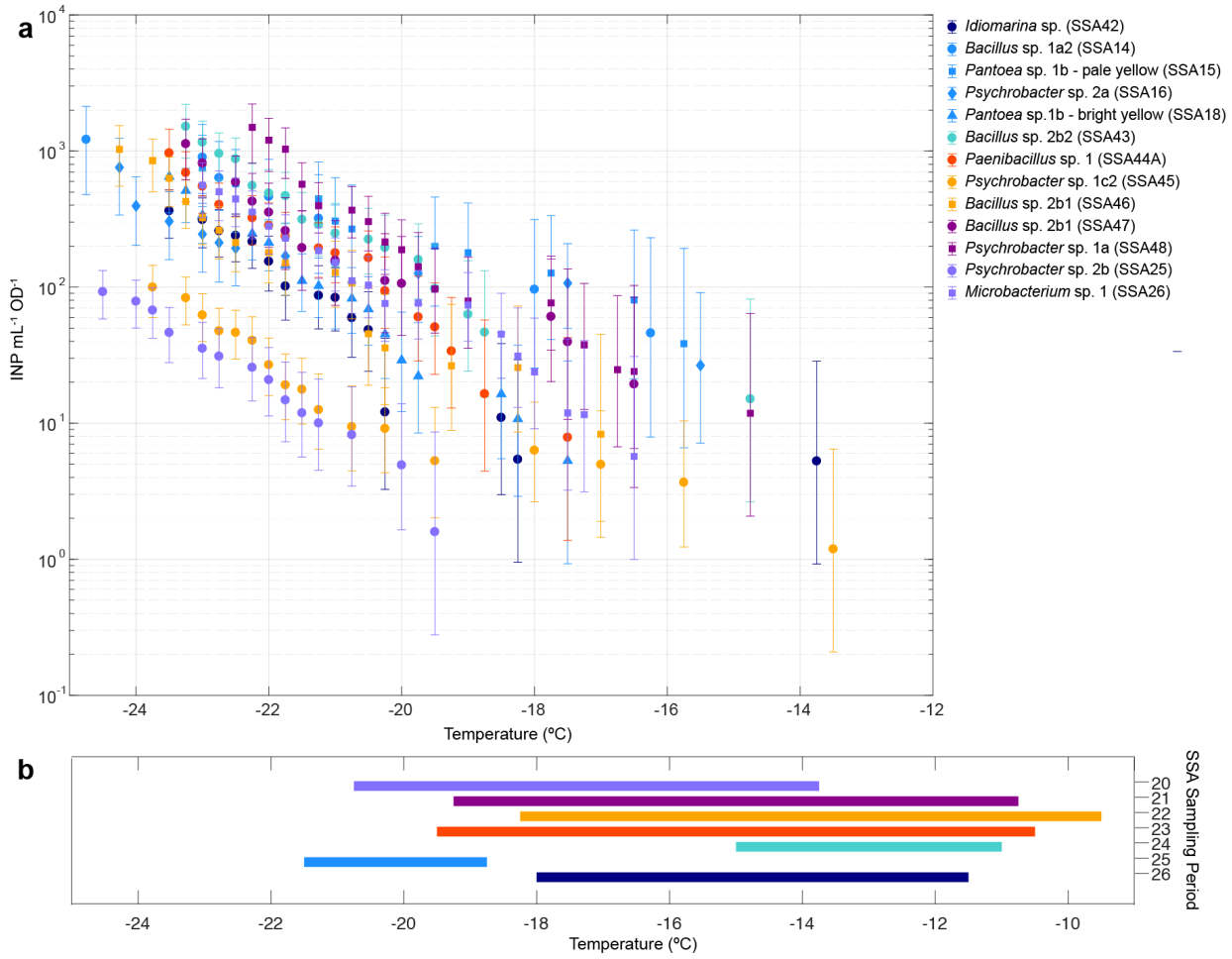


Figure S6.3 IN activity of SSA isolates (a) and SSA samples (b) by collection period. Each color represents a different sampling period indicated on right side of (b). (a) INP measurements are normalized to culture OD (590 nm). SSA sampling period indicates date of sample collection described in Table S6.2.

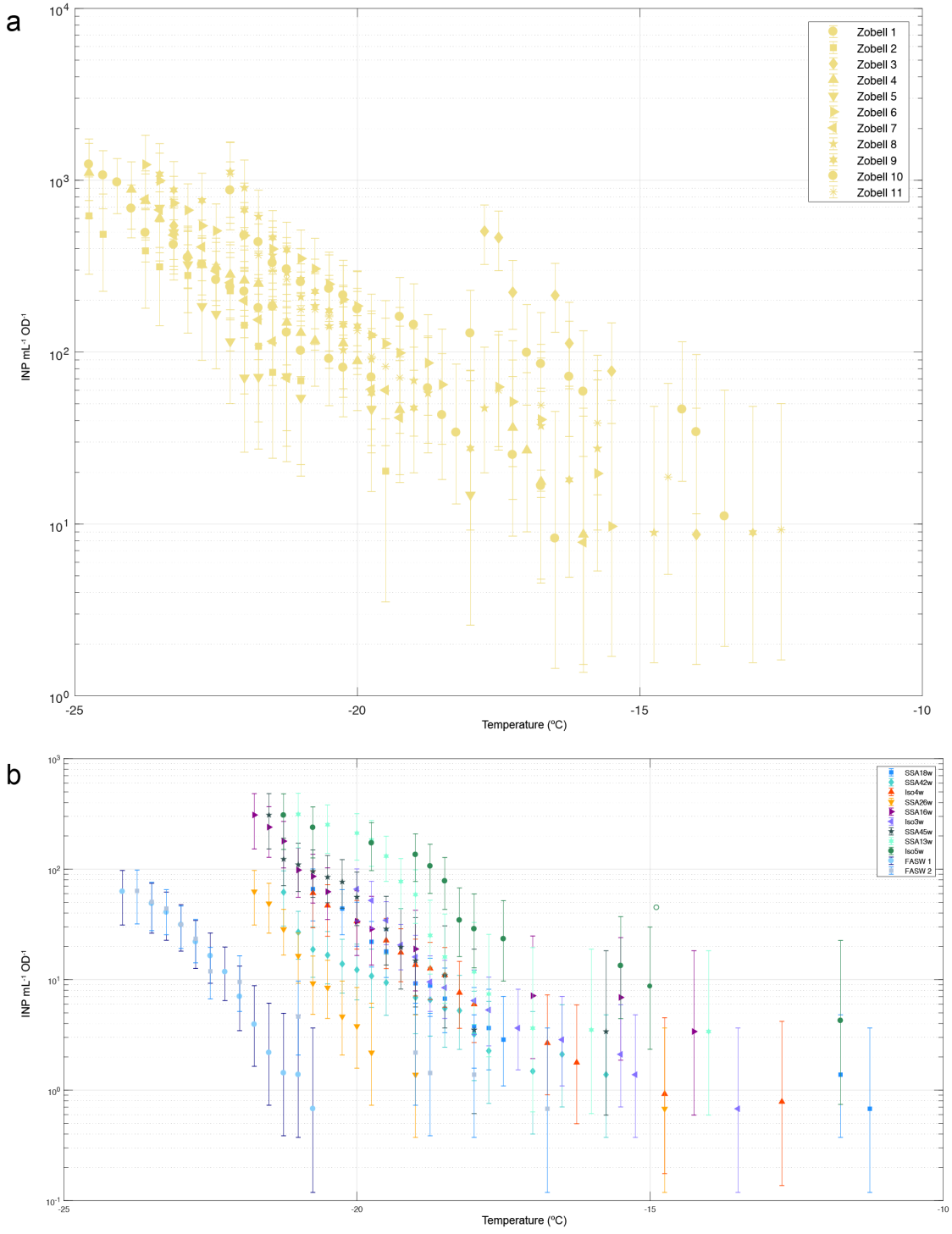


Figure S6.4 Controls of IN measurements. (a) IN activity of ZoBell media blanks. (b) IN activity of selected media–free isolate. INP measurements are normalized to culture OD (590 nm).

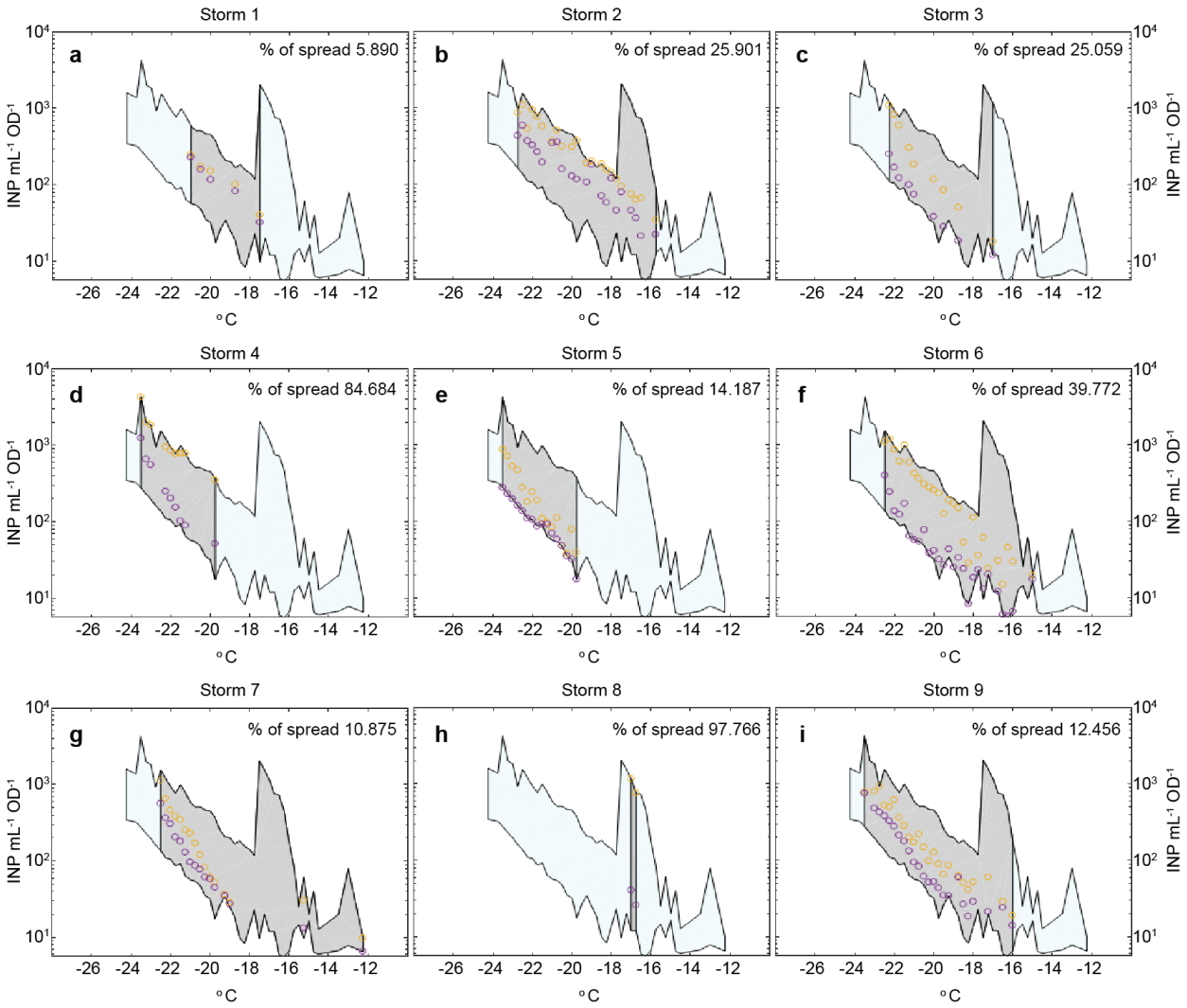


Figure S6.5 Distribution analysis of precipitation isolates for each storm 1-9, (a-i) respectively, compared to total distribution for all storm isolates. Area of all storm isolates indicated (blue). Area in temperature range for comparison, total area considered each storm (gray). Storm isolate area is the area between orange and purple circles which indicate the groups with the highest and lowest IN activity. Spread is calculated as the percentage of this area to total area.

Table S6.3 Comparison of isolate abundance to IN distribution

| storm | # of isolates | Isolate proportion(%) | Spread(%) |
|---|---|---|---|
| 1 | 2 | 5.88 | 5.89 |
| 2 | 4 | 11.76 | 25.90 |
| 3 | 2 | 5.88 | 25.06 |
| 4 | 2 | 5.88 | 84.67 |
| 5 | 4 | 11.76 | 14.19 |
| 6 | 9 | 26.47 | 39.77 |
| 7 | 3 | 8.82 | 10.88 |
| 8 | 2 | 5.88 | 97.77 |
| 9 | 6 | 17.65 | 12.46 |

Isolates Proportion for the storm indicated is by number of organisms isolated for the storm of the total over all storms. Spread as determined by area analysis (Figure S6.5).

**Acknowledgements**

Chapter 6, is material currently being prepared for submission: C. M. Beall, J.M. Michaud, M. Fish, M. D. Stokes, M. D. Burkart, K. A. Prather. "Cultivable halotolerant bacteria and fungi from precipitation and sea spray aerosols indicate a possible missing marine source of atmospheric ice nucleating particles". The dissertation author and C. M. Beall and co-primary authors of this work under the supervision of M. D. Burkart and K. A. Prather. The dissertation author devised isolation and testing strategy, performed isolation of bacterial and fungal species with assistance of C. M. Beall, extracted DNA from isolates, performed species identification and phylogenetic analyses, and prepared manuscript and chapter with assistance from C. M. Beall.

**Section 6.6 References**


1. Fröhlich-Nowoisky, J., Kampf, C. J., Weber, B., Huffman, J. A., Pöhlker, C., Andreae, M. O., Lang-Yona, N., Burrows, S. M., Gunthe, S. S., Elbert, W., Su, H., Hoor, P., Thines, E., Hoffmann, T., Després, V. R. & Pöschl, U. Bioaerosols in the Earth system: Climate, health, and ecosystem interactions. *Atmos. Res.* **182,** 346–376 (2016).

2. DeLeon-Rodriguez, N., Lathem, T. L., Rodriguez-R, L. M., Barazesh, J. M., Anderson, B. E., Beyersdorf, A. J., Ziemba, L. D., Bergin, M., Nenes, A. & Konstantinidis, K. T. Microbiome of the upper troposphere: species composition and prevalence, effects of tropical storms, and atmospheric implications. *Proc. Natl. Acad. Sci. U. S. A.* **110,** 2575–80 (2013).

3. Ladino, L. A., Yakobi-Hancock, J. D., Kilthau, W. P., Mason, R. H., Si, M., Li, J., Miller, L. A., Schiller, C. L., Huffman, J. A., Aller, J. Y., Knopf, D. A., Bertram, A. K. & Abbatt, J. P. D. Addressing the ice nucleating abilities of marine aerosol: A combination of deposition mode laboratory and field measurements. *Atmos. Environ.* **132,** 1–10 (2016).

4. Creamean, J. M., Suski, K. J., Rosenfeld, D., Cazorla, A., Demott, P. J., Sullivan, R. C., White, A. B., Ralph, F., Minnis, P., Comstock, J. M., Tomlinson, J. M. & Prather, K. A. Dust and Biological Aerosols. *Science* **339,** 1572–1578 (2013).

5. Fröhlich-nowoisky, J., Kampf, C. J., Weber, B., Huffman, J. A., Pöhlker, C., Andreae, M. O., Lang-yona, N., Burrows, S. M., Gunthe, S. S., Elbert, W., Su, H., Hoor, P., Thines, E., Hoffmann, T., Després, V. R. & Pöschl, U. Bioaerosols in the Earth system : Climate , health , and ecosystem interactions. *Atmos. Res.* **182,** 346–376 (2016).

6. DeMott, P. J. & Prenni, A. J. New Directions: Need for defining the numbers and sources of biological aerosols acting as ice nuclei. *Atmos. Environ.* **44,** 1944–1945 (2010).

7. DeMott, P. J., Prenni, A. J., Liu, X., Kreidenweis, S. M., Petters, M. D., Twohy, C. H., Richardson, M. S., Eidhammer, T. & Rogers, D. C. Predicting global atmospheric ice nuclei distributions and their impacts on climate. *Proc. Natl. Acad. Sci. U. S. A.* **107,** 11217–22 (2010).

8. Rogers, D. C., DeMott, P. J., Kreidenweis, S. M. & Chen, Y. Measurements of ice nucleating aerosols during SUCCESS. *Geophys. Res. Lett.* **25,** 1383–1386 (1998).

9. DeLeon-Rodriguez, N., Lathem, T. L., Rodriguez-R, L. M., Barazesh, J. M., Anderson, B. E., Beyersdorf, A. J., Ziemba, L. D., Bergin, M., Nenes, A. & Konstantinidis, K. T. Microbiome of the upper troposphere: species composition and prevalence, effects of tropical storms, and atmospheric implications. *Proc. Natl. Acad. Sci. U. S. A.* **110,** 2575–80 (2013).

10. Warren, S. G., Hahn, C. J., London, J., Chervin, R. M. & Jenne, R. L. *Global Distribution of Total Cloud Cover and Cloud Amounts over the Ocean*. (1988).

11. McCoy, D. T., Hartmann, D. L., Zelinka, M. D., Ceppi, P. & Grosvenor, D. P. Journal of Geophysical Research : Atmospheres. *J. Geophys. Res. Atmos.* **120,** 9539–9554 (2015).

12. Seinfeld, J. H., Bretherton, C., Carslaw, K. S., Coe, H., DeMott, P. J., Dunlea, E. J., Feingold, G., Ghan, S., Guenther, A. B., Kahn, R., Kraucunas, I., Kreidenweis, S. M., Molina, M. J., Nenes, A., Penner, J. E., Prather, K. A., Ramanathan, V., Ramaswamy, V., Rasch, P. J., Ravishankara, A. R., Rosenfeld, D., Stephens, G. & Wood, R. Improving our fundamental understanding of the role of aerosol−cloud interactions in the climate system. *Proc. Natl. Acad. Sci.* **113,** 5781–5790 (2016).

13. Yun, Y. & Penner, J. E. Global model comparison of heterogeneous ice nucleation parameterizations in mixed phase clouds. *J. Geophys. Res. Atmos.* **117,** 1–23 (2012).

14. Ault, A. P., Williams, C. R., White, A. B., Neiman, P. J., Creamean, J. M., Gaston, C. J., Ralph, F. M. & Prather, K. A. Detection of Asian dust in California orographic precipitation. *J. Geophys. Res. Atmos.* **116,** 1–15 (2011).

15. Hoose, C., Kristjánsson, J. E., Chen, J.-P. & Hazra, A. A Classical-Theory-Based Parameterization of Heterogeneous Ice Nucleation by Mineral Dust, Soot, and Biological Particles in a Global Climate Model. *J. Atmos. Sci.* **67,** 2483–2503 (2010).

16. Ardon-Dryer, K. & Levin, Z. Ground-based measurements of immersion freezing in the eastern Mediterranean. *Atmos. Chem. Phys.* **14,** 5217–5231 (2014).

17. Demott, P. J., Prenni, A. J., McMeeking, G. R., Sullivan, R. C., Petters, M. D., Tobo, Y., Niemand, M., M??hler, O., Snider, J. R., Wang, Z. & Kreidenweis, S. M. Integrating laboratory and field data to quantify the immersion freezing ice nucleation activity of mineral dust particles. *Atmos. Chem. Phys.* **15,** 393–

409 (2015).

18. Boose, Y., Sierau, B., Isabel García, M., Rodríguez, S., Alastuey, A., Linke, C., Schnaiter, M., Kupiszewski, P., Kanji, Z. A. & Lohmann, U. Ice nucleating particles in the Saharan Air Layer. *Atmos. Chem. Phys.* **16,** 9067–9087 (2016).

19. Christner, B. C., Cai, R., Morris, C. E., McCarter, K. S., Foreman, C. M., Skidmore, M. L., Montross, S. N. & Sands, D. C. Geographic, seasonal, and precipitation chemistry influence on the abundance and activity of biological ice nucleators in rain and snow. *Proc. Natl. Acad. Sci. U. S. A.* **105,** 18854–18859 (2008).

20. Christner, B. C. Cloudy with a Chance of Microbes. *Microbe Mag.* **7,** 70–75 (2012).

21. Lu, Z., Du, P., Du, R., Liang, Z., Qin, S., Li, Z. & Wang, Y. The diversity and role of bacterial ice nuclei in rainwater from mountain sites in China. *Aerosol Air Qual. Res.* **16,** 640–652 (2016).

22. Hoose, C., Kristjánsson, J. E. & Burrows, S. M. How important is biological ice nucleation in clouds on a global scale? *Environ. Res. Lett.* **5,** 24009 (2010).

23. Morris, C. E., Conen, F., Alex Huffman, J., Phillips, V., Pöschl, U. & Sands, D. C. Bioprecipitation: A feedback cycle linking Earth history, ecosystem dynamics and land use through biological ice nucleators in the atmosphere. *Glob. Chang. Biol.* **20,** 341–351 (2014).

24. Murray, B. J., O'Sullivan, D., Atkinson, J. D. & Webb, M. E. Ice nucleation by particles immersed in supercooled cloud droplets. *Chem. Soc. Rev.* **41,** 6519–54 (2012).

25. Huffman, J. A., Prenni, A. J., Demott, P. J., Pöhlker, C., Mason, R. H., Robinson, N. H., Fröhlich-Nowoisky, J., Tobo, Y., Després, V. R., Garcia, E., Gochis, D. J., Harris, E., Müller-Germann, I., Ruzene, C., Schmer, B., Sinha, B., Day, D. A., Andreae, M. O., Jimenez, J. L., Gallagher, M., Kreidenweis, S. M., Bertram, A. K. & Pöschl, U. High concentrations of biological aerosol particles and ice nuclei during and after rain. *Atmos. Chem. Phys.* **13,** 6151–6164 (2013).

26. Petters, M. D. & Wright, T. P. Revisiting ice nucleation from precipitation samples. *Geophys. Res. Lett.* **42,** 8758–8766 (2015).

27. Stopelli, E., Conen, F., Morris, C. E., Herrmann, E., Bukowiecki, N. & Alewell, C. Ice nucleation active particles are efficiently removed by precipitating clouds. *Sci. Rep.* **5,** 16433 (2015).

28. Demott, P. J., Hill, T. C. J., Mccluskey, C. S., Prather, K. A., Collins, D. B., Sullivan, R. C., Ruppel, M. J., Mason, R. H., Irish, V. E., Lee, T., Yeon, C., Siek, T., Snider, J. R., Mcmeeking, G. R., Dhaniyala, S., Lewis, E. R. & Wentzell, J. J. B. Sea spray aerosol as a unique source of ice nucleating particles. **113,** (2016).

29. Vergara-Temprado, J., Murray, B. J., Wilson, T. W., O'Sullivan, D., Browse, J., Pringle, K. J., Ardon-Dryer, K., Bertram, A. K., Burrows, S. M., Ceburnis, D., Demott, P. J., Mason, R. H., O'Dowd, C. D., Rinaldi, M. & Carslaw, K. S. Contribution of feldspar and marine organic aerosols to global ice nucleating particle concentrations. *Atmos. Chem. Phys.* **17,** 3637–3658 (2017).

30. Yun, Y. & Penner, J. E. An evaluation of the potential radiative forcing and climatic impact of marine organic aerosols as heterogeneous ice nuclei. *Geophys. Res. Lett.* **40,** 4121–4126 (2013).

31. McCluskey, C. S., Hill, T. C. J., Malfatti, F., Sultana, C. M., Lee, C., Santander, M. V., Beall, C. M., Moore, K. A., Cornwell, G. C., Collins, D. B., Prather, K. A., Jayarathne, T., Stone, E. A., Azam, F., Kreidenweis, S. M. & DeMott, P. J. A Dynamic Link between Ice Nucleating Particles Released in Nascent Sea Spray Aerosol and Oceanic Biological Activity during Two Mesocosm Experiments. *J. Atmos. Sci.* **74,** 151–166 (2017).

32. Wilson, T. W., Ladino, L. a., Alpert, P. a., Breckels, M. N., Brooks, I. M., Browse, J., Burrows, S. M., Carslaw, K. S., Huffman, J. A., Judd, C., Kilthau, W. P., Mason, R. H., McFiggans, G., Miller, L. a., Nájera, J. J., Polishchuk, E., Rae, S., Schiller, C. L., Si, M., Temprado, J. V., Whale, T. F., Wong, J. P. S., Wurl, O., Yakobi-Hancock, J. D., Abbatt, J. P. D., Aller, J. Y., Bertram, A. K., Knopf, D. a. & Murray, B. J. A marine biogenic source of atmospheric ice-nucleating particles. *Nature* **525,** 234–238 (2015).

33. Alpert, P. A., Aller, J. Y. & Knopf, D. A. Ice nucleation from aqueous NaCl droplets with and without marine diatoms. *Atmos. Chem. Phys. Discuss.* **11,** 8291–8336 (2011).

34. Knopf, D. A., Alpert, P. A., Wang, B. & Aller, J. Y. Stimulation of ice nucleation by marine diatoms. *Nat. Geosci.* **4,** 88–90 (2011).

35. Alpert, P. A., Aller, J. Y. & Knopf, D. A. Initiation of the ice phase by marine biogenic surfaces in supersaturated gas and supercooled aqueous phases. *Phys. Chem. Chem. Phys.* **13,** 19882 (2011).

36. Parker, L., Sullivan, C., Forest, T. & Ackley, S. Ice nucleation activity of

antarctic marine microorganisms. *Antarct. J.* **20,** 126–127 (1985).

37. Junge, K. & Swanson, B. D. High-resolution ice nucleation spectra of sea-ice bacteria: implications for cloud formation and life in frozen environments. *Biogeosciences Discuss.* **4,** 4261–4282 (2007).

38. Hu, W., Murata, K., Horikawa, Y., Naganuma, A. & Zhang, D. Bacterial community composition in rainwater associated with synoptic weather in an area downwind of the Asian continent. *Sci. Total Environ.* **601–602,** 1775–1784 (2017).

39. Santl-Temkiv, T., Sahyoun, M., Finster, K., Hartmann, S., Augustin-Bauditz, S., Stratmann, F., Wex, H., Clauss, T., Nielsen, N. W., Sorensen, J. H., Korsholm, U. S., Wick, L. Y. & Karlson, U. G. Characterization of airborne ice-nucleation-active bacteria and bacterial fragments. *Atmos. Environ.* **109,** 105–117 (2015).

40. Bowers, R. M., Lauber, C. L., Wiedinmyer, C., Hamady, M., Hallar, A. G., Fall, R., Knight, R. & Fierer, N. Characterization of airborne microbial communities at a high-elevation site and their potential to act as atmospheric ice nuclei. *Appl. Environ. Microbiol.* **75,** 5121–5130 (2009).

41. Vaïtilingom, M., Attard, E., Gaiani, N., Sancelme, M., Deguillaume, L., Flossmann, A. I., Amato, P. & Delort, A. M. Long-term features of cloud microbiology at the puy de Dôme (France). *Atmos. Environ.* **56,** 88–100 (2012).

42. Hill, T. C. J., Moffett, B. F., Demott, P. J., Georgakopoulos, D. G., Stump, W. L. & Franc, G. D. Measurement of ice nucleation-active bacteria on plants and in precipitation by quantitative PCR. *Appl. Environ. Microbiol.* **80,** 1256–67 (2014).

43. Stopelli, E., Conen, F., Morris, C. E., Herrmann, E., Henne, S., Steinbacher, M. & Alewell, C. Predicting abundance and variability of ice nucleating particles in precipitation at the high-altitude observatory Jungfraujoch. *Atmos. Chem. Phys.* **16,** 8341–8351 (2016).

44. Lorv, J. S. H., Rose, D. R. & Glick, B. R. Bacterial ice crystal controlling proteins. *Scientifica (Cairo).* **2014,** 976895 (2014).

45. Hill, T. C. J., Moffett, B. F., DeMott, P. J., Georgakopoulos, D. G., Stump, W. L. & Franc, G. D. Measurement of ice nucleation-active bacteria on plants and in precipitation by quantitative PCR. *Appl. Environ. Microbiol.* **80,** 1256–1267 (2014).

46. Beall, C. M., Stokes, M. D., Hill, T. C., Demott, P. J., Dewald, J. T., Prather, K. A., Jolla, L., Collins, F., Jolla, L. & Jolla, L. Automation and heat transfer characterization of immersion mode spectroscopy for analysis of ice nucleating particles. 2613–2626 (2017).

47. ZoBell, C. E. Marine Bacteriology. *Annu. Rev. Biochem.* **16,** 565–586 (1947).

48. Boström, K. H., Simu, K., Hagström, Å. & Riemann, L. Optimization of DNA extraction for quantitative marine bacterioplankton community analysis. *Limnol. Oceanogr. Methods* **2,** 365–373 (2004).

49. Walters, W., Hyde, E. R., Berg-lyons, D., Ackermann, G., Humphrey, G., Parada, A., Gilbert, J. a & Jansson, J. K. Improved bacterial 16S rRNA gene (V4 and V4-5) and fungal internal transcribed spacer marker gene primers for microbial community surveys. *mSystems* **1,** e0009-15 (2015).

50. Pruesse, E., Peplies, J. & Glöckner, F. O. SINA: Accurate high-throughput multiple sequence alignment of ribosomal RNA genes. *Bioinformatics* **28,** 1823–1829 (2012).

51. Wright, E. S. DECIPHER: harnessing local sequence context to improve protein multiple sequence alignment. *BMC Bioinformatics* **16,** 322 (2015).

52. McWilliam, H., Li, W., Uludag, M., Squizzato, S., Park, Y. M., Buso, N., Cowley, A. P. & Lopez, R. Analysis Tool Web Services from the EMBL-EBI. *Nucleic Acids Res.* **41,** 597–600 (2013).

53. Letunic, I. & Bork, P. Interactive Tree of Life v2: Online annotation and display of phylogenetic trees made easy. *Nucleic Acids Res.* **39,** 475–478 (2011).

# Chapter 7. Fluorescent Probes to Profile Fatty Acid and Polyketide Acyl-Carrier Protein Transacylase Domains

## Section 2.1 Introduction

Natural products are privileged structural and functional scaffolds produced by microorganisms as agents of microbial warfare, virulence factors, signaling molecules, and clinically viable therapeutics.[1] The biosynthesis of many natural products is catalyzed by polyketide synthases (PKS) and nonribosomal peptide synthetases (NRPS), multi-modular enzymatic assembly lines that are functionally and structurally analogous to fatty acid synthases (FAS). Notably, targeting enzymes within these complex protein assemblies has emerged as a strategy to tackle multidrug resistant bacteria[2–4], cancer[5], and various other health-related malignancies[6]. Over the past fifteen years, our laboratory has embarked on studies to isolate, characterize, and identify these modular synthases to complement genomic investigations aimed at characterizing novel natural product biosynthetic gene clusters. In particular, we have developed fluorescent activity-based probes to profile and identify acyl and peptidyl carrier proteins,[7–12] ketosynthases,[13] dehydratases,[14] thioesterases,[13,15] and flavin-dependent oxidases[16]. Such probes offer possibilities for the development of new drug leads. Herein, we report the design, synthesis, and evaluation of novel fluorescent probes to interrogate PKS and FAS acyl-carrier protein transacylase (AT) domains.

Polyketide and fatty acid biosynthesis is primed by AT domains that select and load acyl-CoA substrates onto *holo*-acyl carrier protein (ACP) via transient acylation of an AT active site serine or cysteine (Figure 7.1).

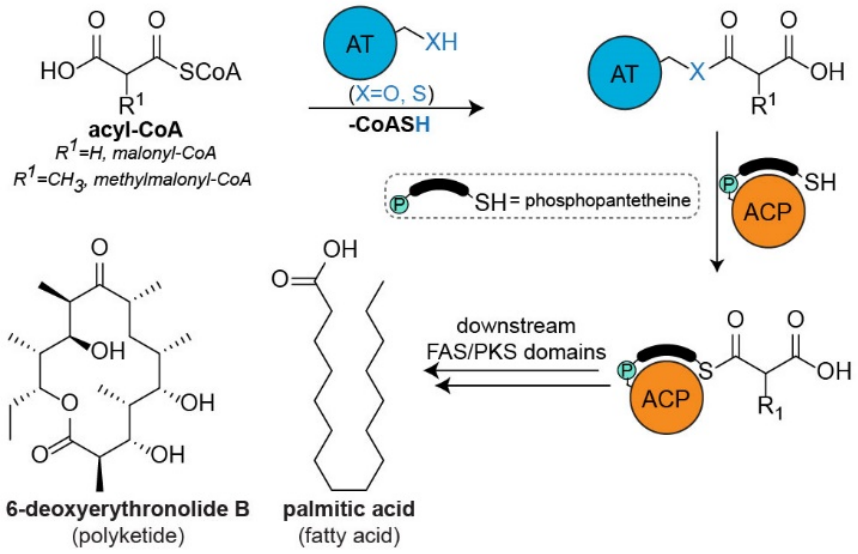


Figure 7.1 Acyl-carrier protein transacylase (AT) domains in fatty acid synthases (FAS) and polyketide synthases (PKS). The AT domain (blue sphere) initiates biosynthesis through transient acylation of an active site serine or cysteine by acyl-CoA. The acyl group is then transferred to the phosphopantetheinyl arm of holo-acyl-carrier protein (ACP) (orange sphere). Downstream domains catalyze chain extension, modification, and offloading of the product from the catalytic machinery. Palmitic acid and 6-deoxyerythronolide are representative examples of fatty acids and polyketides, respectively.

In particular, malonyl-CoA acyl-carrier protein transacylase (MCAT) is a serine α/β-hydrolase present in numerous FAS and PKS. During fatty acid biosynthesis in *Escherichia coli*, the MCAT domain FabD catalyzes two half reactions: (1) loading of malonyl from malonyl-CoA onto an active site serine and (2) transthioesterification onto *holo*-ACP. Importantly, truncated FabD arrested *E. coli* growth under physiological conditions and demonstrated defects in overall fatty acid composition[17]. Thus, drugs targeting bacterial AT domains and other FAS

enzymes in Gram-negative bacteria and mycobacteria offer tractable alternatives to the growing threat of multi-drug resistance[18,19]. In contrast, during polyketide biosynthesis, AT enzymes select, load, and transfer a wider array of acyl-CoA substrates, thereby providing an avenue to engineer PKS to incorporate alternative acyl extender units to expand polyketide structural diversity[20,21].

In spite of the importance of AT domains in FAS and PKS, only a handful of inhibitors have been discovered, many of which are derived from *in silico* computational studies or from natural sources that demonstrate low micromolar enzyme inhibition that poorly translates to bacterial growth inhibition. The paucity of inhibitors presents a particular challenge to developing AT-selective activity-based probes.

To determine the feasibility of profiling AT domains, we examined labeling of *E. coli* FabD with commercially available affinity and fluorescent fluorophosphonate probes (Figure S7.1a). Fluorophosphonates are privileged warheads used extensively to profile α/β serine hydrolases.[22,23] Fluorophosphonate electrophiles strongly labeled FabD and several enzymes from bacterial cellular lysates, including other serine hydrolases and a FabD homolog from a *Flavobacteria* isolate, BBFL7 (Figure S7.1b-c). The tedious nature of affinity-based labeling assays, lack of FabD specificity, and short half-life of fluorophosphonates highlighted the need to develop stable fluorescent probes for rapid and selective FabD labeling.

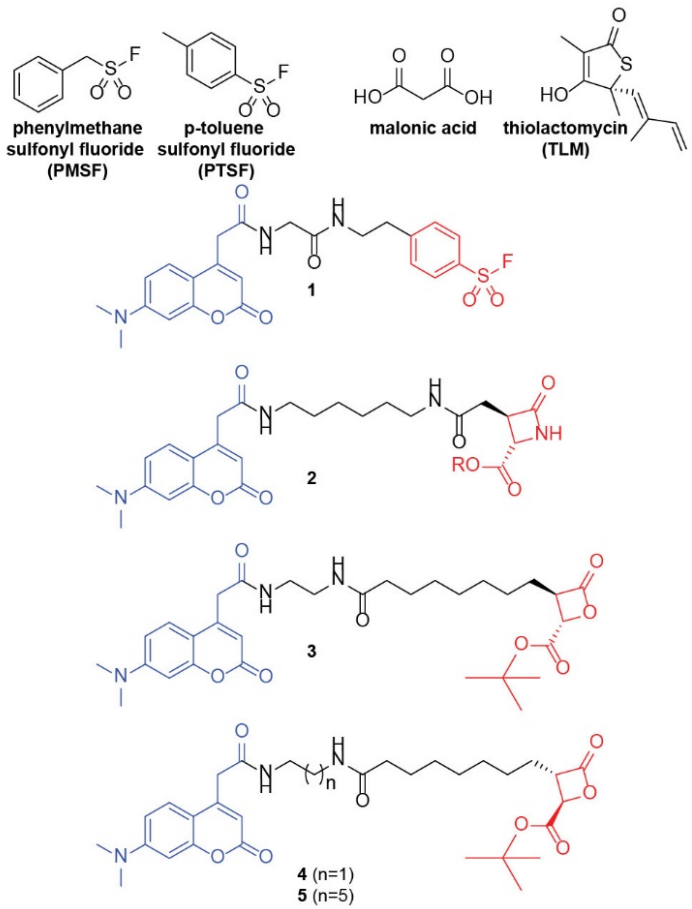


Figure 7.2 Structures of inhibitors and fluorescent probes for AT domain profiling studies. Fluorescent analogue **1** was designed as a mimic of phenylmethane sulfonyl fluoride (PMSF) and p-toluene sulfonyl fluoride (PTSF). Second generation lactam probe **2** and lactone probes **3–5** were designed as malonic acid and thiolactomycin (TLM) mimics with improved hydrolytic stability and enhanced reactivity with active site residues. The functional units in each inhibitor are indicated by color: the reactive warhead (red), the linker (black), and the fluorescent tag (blue).

## Section 7.2 Results and Discussion

Previously, our activity-based probes targeting PKS, NRPS, and FAS domains were designed based on known active site inhibitors[7-16]. Phenylmethane sulfonyl fluoride (PMSF) (Figure 7.2) inactivates FabD by covalent modification at the active site serine and *para*-toluene sulfonyl fluoride (PTSF) (Figure 7.2) docks into the active site of a FabD homolog of *Plasmodium falciparum* forming hydrogen

bonds with the side chains of active site serine and arginine residues[24,25]. Given the activity of PMSF and PTSF and literature providing support for using sulfonyl fluorides as privileged warheads for activity-based protein profiling[26–28], we hypothesized that fluorescent aryl sulfonyl fluoride **1** might serve as a suitable electrophile to irreversibly label FabD (Figure 7.2). Moreover, docking studies of thiolactomycin (TLM), an inhibitor of *E. coli* ketosynthases and acetyl-ACP acyltransferase[29,30], revealed critical hydrogen bonds with catalytic residues of *P. falciparum* FabD[25], inspiring us to design lactam and lactone activity-based probes. Strained β-lactones and β-lactams are privileged pharmacophores found in clinical therapeutics and are emerging as activity-based probes[31–33]. Thus, we envisioned that fluorescent β-lactam **2** and β-lactones **3–5** might selectively react with FabD as mimics of the three-carbon malonate core of malonyl-CoA (Figure 7.2). Further evidence for the suitability of lactams and lactones as reactive warheads was demonstrated through docking studies with FabD in which the warheads oriented themselves in the catalytic site poised for nucleophilic attack by serine (Figure S7.2).

With these new probes in hand, we first optimized conditions for labeling *E. coli* FabD using aryl sulfonyl fluoride probe **1**. We observed labeling by SDS-PAGE with as little as 5 μM FabD and 10 μM probe, with labeling intensity saturating at 50 μM **1** (Figure S7.3). To maximize labeling and minimize probe hydrolysis, we investigated the influence of buffer on labeling efficiency. The composition of buffer had a modest effect on labeling, as labeling was more pronounced in

phosphate buffered saline (PBS) than in HEPES at pH ~ 7.0, and abrogated in Tris buffer, presumably due to nonspecific reactivity (Figure S7.4).

Next, with our optimized conditions (10 μM FabD, 50 μM probe, PBS, 12 h), we assessed whether probes **2–5** labeled FabD. Indeed, we observed robust labeling of FabD with all probes (Figure 7.3a-d, Figure S7.5), except for lactam **2**, even at 500 μM for 12 h at 37 ºC (data not shown), presumably due to the stability of amides relative to esters and aryl sulfonyl fluorides. Labeling of FabD with aryl sulfonyl fluoride **1** was pH-dependent, with minimal labeling observed at acidic pHs (5–6), and labeling intensity reaching a maximum at pH 7, whereas labeling with lactones **3–5** was minimally impacted by pH. At acidic pHs, non-specific labeling with all probes decreased when FabD was denatured by heating at 95 ºC in the presence of 1% sodium dodecyl sulfate (SDS). In contrast, at higher pH values (7–9), probes **4–5** demonstrated increased non-specific labeling, whereas non-specific labeling with probes **1** and **3** were less impacted, highlighting the influence that stereochemistry and linker length have on non-specific labeling. Probe **5** is the most hydrophobic of all probes examined (logP = 4.08).

Next, we conducted time-course studies to assess FabD labeling time-scales (10 μM FabD, 50 μM probe, PBS, pH 7). Aryl sulfonyl fluoride **1** was moderately reactive, with labeling levels reaching a maximum at 12 h and sustained at those levels for up to 24 h (Figure 7.3e, Figure S7.6a). Lactones **3–4** were most reactive, labeling FabD as quickly as 1 h and being sustained at those levels

throughout the experiment (Figures 7.3f-g, Figure S7.6b-c). Lastly, lactone **5** was the least reactive, taking 24 h to maximally label FabD (Figure 7.3h, Figure S7.6d), suggesting that longer linker lengths are suboptimal for FabD labeling. All probes demonstrated increased non-specific labeling under SDS-denaturing conditions as the time-course ensued.

To determine whether our probes targeted the active site serine of FabD, we generated FabD S92C, in which the catalytic serine was mutated to cysteine. As expected, given the enhanced nucleophlicity of thiols, we observed slightly enhanced labeling of FabD S92C with our lactone probes (Figure S7.7a), suggesting that irreversible covalent modification occurs in the active site, although off-target effects are also likely. Consistent with FabD, FabD S92C is differentially labeled by lactones (**4>3>5**), further highlighting the influence of stereochemistry and linker length on mutant labeling. Labeling of both wildtype and mutant FabD with **1** did not differ substantially.

To confirm active site targeting, pretreating FabD S92C with *N*-ethylmaleimide (NEM) to block cysteine residues showed decreased labeling of all probes (Figure S7.7b), while NEM pretreatment of wildtype FabD did not affect labeling intensity (Figure S7.7c).

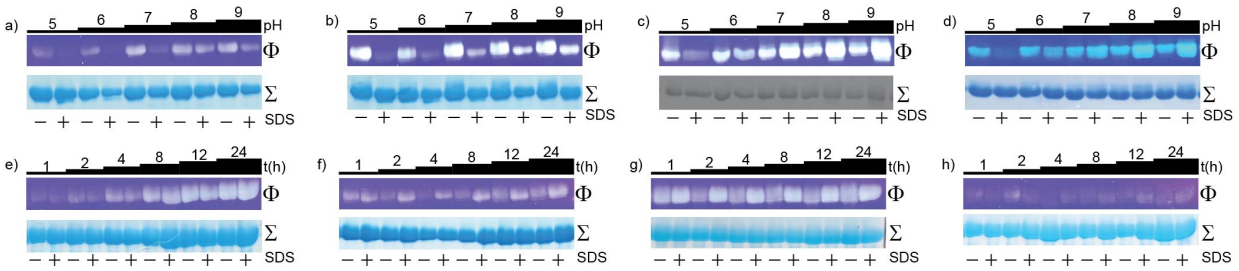


Figure 7.3 In vitro labeling of E. coli FabD with fluorescent probes 1 and 3–5. (a–d) In-gel fluorescent SDS-PAGE analysis denoting pH-dependent labeling of FabD (10 μM, PBS, 12 h, 37 °C) with 50 μM (a) **1**, (b) **3**, (c) **4**, or (d) **5**. (e–h) In-gel fluorescent SDS-PAGE analysis denoting time-dependent labeling of FabD (10 μM, PBS, pH 7, 37 °C) with 50 μM (e) **1**, (f) **3**, (g) **4**, or (h) **5**. For each panel, **Φ** depicts gel visualized under UV at 365 nm and **Σ** depicts the total protein content by staining with colloidal Coomassie Brilliant Blue. Full images of the gels are provided in Figures S7.5–S7.6

Next, we evaluated labeling specificity by examining whether our probes labeled enzymes downstream of FabD in *E. coli* FAS, many of which contain nucleophilic residues in their active site. Although probes **1** and **3–5** labeled ketosynthases FabF and FabH, ketoreductase FabG, and dehydratase (DH) FabA (Figure S7.8–S7.9), we investigated whether they selectively labeled FabD in competition experiments (5 μM FabD, 5 μM FAS enzyme, 25 μM probe, PBS, pH 7, 37 °C, 4 h). Aryl sulfonyl fluoride **1** preferentially labeled FabF and FabG over FabD, (Figure 7.4a, Figure S7.10a). Moreover, lactones **3–5** preferentially labeled both FabF and FabA over FabD to varying intensities (**4>3>5**), whereas FabD was preferred over FabG (Figure 7.4b-d, Figure S7.10b-d). The preference of our lactone probes for FabA was surprising, given number of buried nucleophilic residues in the protein (11 K, 2 C, 4 S, 2 H).

To determine if our fluorescent probes target the active sites of FabF, FabH, and FabA we utilized mechanism-based inhibitors and crosslinkers. In particular,

cerulenin is a covalent inhibitor of FabF and FabH[19], and crosslinker sulfonyl-alkyne **6** irreversibly reacts with FabA $His_{70}$ after formation of an electrophilic allene intermediate (Figure 7.4e)[34]. We pretreated FabF (10 μM) with cerulenin (10 μM, 18 h, 37 ºC), then added FabD (10 μM) and fluorescent probe (50 μM, 4 h). As expected, cerulenin pretreatment abrogated FabF labeling with sulfonyl fluoride **1**, suggestive of active site targeting, albeit modest changes in FabD labeling were observed (Figure 7.4f, Figure S7.11). Interestingly, cerulenin pretreatment enhanced FabF labeling with lactones **3–5**, indicating that labeling occurs outside of the active site and is likely promoted due to conformational changes in FabF. Cerulenin treatment of FabH decreased FabH labeling of all probes, suggesting FabH active site targeting (data not shown). To determine whether our fluorescent probes target the catalytic site of FabA, we preincubated FabA (10 μM) with **6** (100 μM, 18 h, 37 ºC), then added FabD (10 μM) and fluorescent probes (50 μM, 4 h). Pretreatment with **6** abrogated FabA labeling with all probes (Figure 7.4g, Figure S7.12), suggesting active site FabA targeting, and also increased FabD labeling by **3** and **5**, while labeling with **1** and **4** was not substantially impacted by pretreatment with **6**. Taken together, these data suggest that specificity for FabD can be modulated by pretreatment or co-treatment with known inhibitors or crosslinkers.

To further investigate FabD labeling specificity, we examined reactivity with various hydrolases. We first surveyed *in vitro* cross-reactivity with TesA, a multifunctional SGNH hydrolase that hydrolyzes long chain acyl-CoA and acyl-ACP

thioesters[35,36]. To our delight, sulfonyl fluoride **1** weakly labeled TesA, with no labeling observed by the lactones (Figure S7.13). Intriguingly, competition experiments between FabD and TesA neutralized FabD labeling with the lactones, likely via nucleophilic attack of the active site serine at the lactone carbonyl, followed by rapid hydrolysis. Next, we examined whether our probes labeled well-characterized serine hydrolases, including proteases and esterases known to react with fluorophosphonates. Sulfonyl fluoride **1** was most promiscuous and labeled both thrombin and pig liver esterase (Figure S7.14). In contrast, lactones **3–5** selectively labeled FabD, leaving all hydrolases tested untouched (Figure S7.15).

As a final demonstration of scope, we wondered whether PKS AT domains could be labeled, especially in light of earlier docking studies demonstrating favorable interactions with both FAS and PKS AT domains (Figure S7.2). Thus, we tested whether CazM, a starter AT domain from the chaetidovirdin PKS and ZmaA, a *trans* acting AT domain from the zwittermicin NRPS-PKS hybrid pathway could be labeled with our probes. TAMRA-FP showed limited utility and strongly labeled CazM under non-denaturing conditions (Figure S7.16). Aryl sulfonyl fluoride **1** labeled all AT domains, showing selectivity for CazM, which contains a native cysteine in the catalytic site (Figure 7.5a, Figure S7.17a). Interestingly, **1** also labeled the ZmaA S192C mutant more strongly than the ZmaA wildtype enzyme, which suggests that **1** selectively targets catalytic residues.

The lactone probes strongly and selectively labeled enzymes containing an active site cysteine (Figures 7.5b-d). Both CazM and ZmaA S192C were more strongly labeled by all lactone probes in comparison to aryl sulfonyl fluoride. The lactones demonstrated modest differences in CazM labeling dependent on stereochemistry (**4>3**) and linker length (**4>5**). In contrast, ZmaA S192C labeling was also influenced by stereochemistry (**3>4**) and linker length (**4>5**). Although **5** demonstrated the least labeling of ZmaA S192C of the lactones tested, labeling of wt ZmaA was completely abrogated, suggesting that linker lengths can be tuned to achieve selective labeling at the catalytic site. We surmise that the small amounts of background labeling of wt ZmaA with shorter lactones **3** and **4** is due to labeling of non-catalytic residues. Taken together, our data suggests that the reactivity and specificity of lactone probes can be modulated by adjusting the linker length, with longer lengths showing abrogated activity. Our shorter lactones contain 11 atoms separating the coumarin core from the proposed site of nucleophilic attack, which is approximately the same length as the pantetheine prosthetic group and leading to optimal labeling activity.

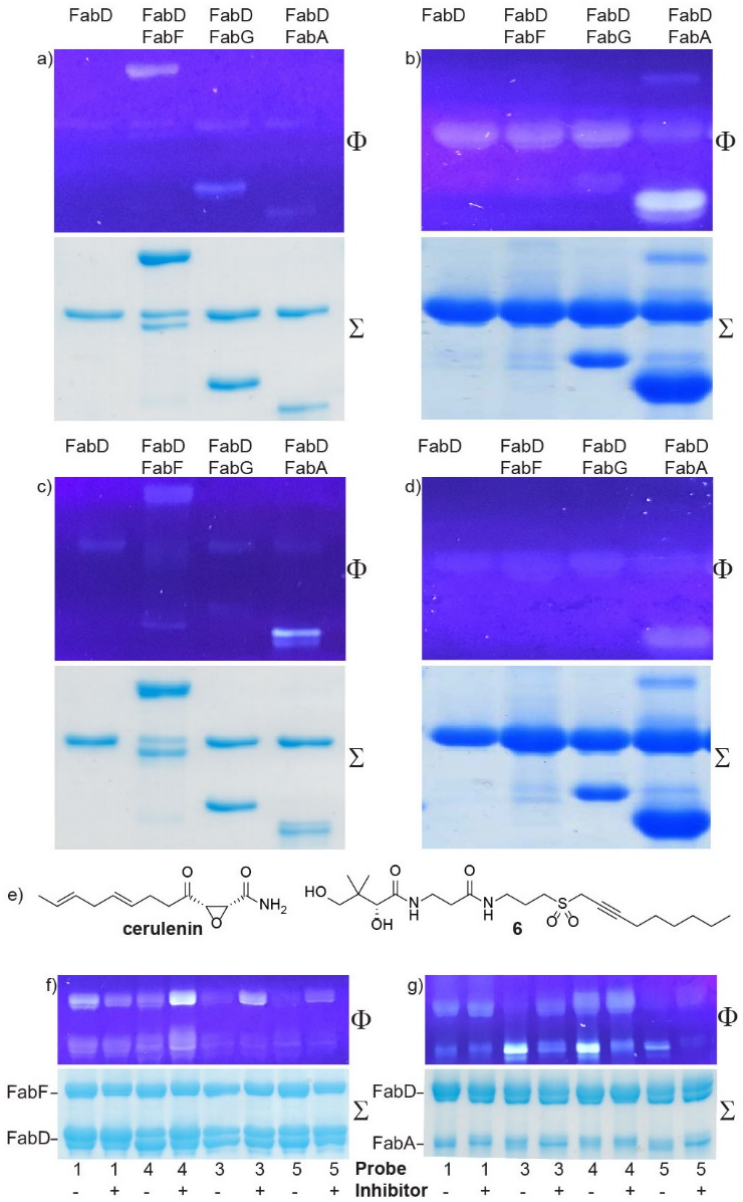


Figure 7.4 Evaluation and modulation of labeling specificity with fluorescent probes and inhibitors. (a–d) In-gel fluorescent SDS-PAGE analysis denoting competitive labeling between equimolar amounts of FabD and FAS enzymes (5 μM, PBS, pH 7, 4 h, 37 ºC) with 25 μM (a) **1**, (b) **3**, (c) **4**, or (d) **5**. (e) Structures of cerulenin and sulfonyl alkyne **6**, mechanism-based inhibitors of FabF and FabA, respectively. (f) Modulation of FabD versus FabF fluorescent probe labeling specificity by pretreating FabF (10 μM) with cerulenin (10 μM, 18 h, 37 º) prior to addition of FabD (10 μM) and probes (50 μM). (g**)** Modulation of FabD versus FabA fluorescent probe labeling specificity by pretreating FabA (10 μM) with sulfonyl alkyne **6** (1 mM, 18 h, 37 ºC) prior to addition of FabD (10 μM) and probes (50 μM). For each panel, Φ depicts gel visualized under UV at 365 nm and Σ depicts the total protein content by staining with colloidal Coomassie Brilliant Blue. Full gel images are provided in Figures S7.10–S7.12.

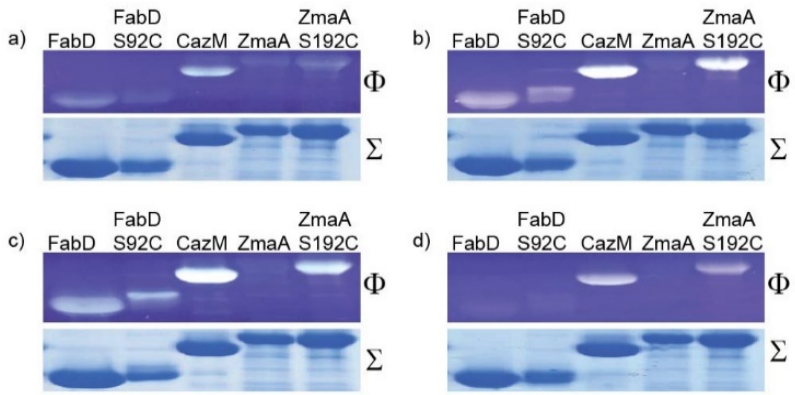


Figure 7.5 Labeling of AT domains derived from polyketide (CazM, ZmaA, ZmaA S192C) biosynthetic pathways. In-gel fluorescent SDS-PAGE analysis denoting labeling of polyketide AT domains (10 μM, PBS, pH 7, 12 h, 37 ºC) with 50 μM: (a) **1**, (b) **3**, (c) **4**, or (d) **5**. For each panel, **Φ** depicts gel visualized under UV at 365 nm and **Σ** depicts the total protein content by staining with colloidal Coomassie Brilliant Blue. Full images of the gels are provided in Figure S7.17.

## Section 7.3 Conclusions

In conclusion, herein, we have developed broad-scope fluorescent sulfonyl fluoride and lactone reactive probes that irreversibly label the active sites of both FAS and PKS AT domains. We demonstrated that labeling intensity can be modulated by slight changes in stereochemistry and linker length and specificity can tuned to bias labeling of AT domains by inhibiting the activity of promiscuous partners. The probes developed herein are promising tools that will inspire the elaboration of new AT domains inhibitors as potential therapeutics, and provide valuable insights that can be leveraged to identify and engineer ACP-containing pathways in various organisms.

**Section 7.4 Methods**

*Chemical Biology Materials and Methods*

*FabD, CazM SAT, and ZmaA AT Protein Expression and Purification*

Recombinant FabD was expressed from a pET-28b construct with an N-terminal 6x His tag. Recombinant CazM SAT from *Chaetomium globusum* was expressed from a pHis8 construct with and N-terminal 8x His tag[37]. Recombinant ZmaA from *Bacillus cereus* was expressed from a pET-28b construct with an N-terminal 6x His tag[38]. BL21 (DE3) cells were cultured at 37 ºC in Luria-Bertani (LB) broth supplemented with 50 µg/mL kanamycin to an $OD_{600}$ of 0.8. The cells were cooled to 0 ºC on ice and induced with 1 mM isopropyl β-D-1-thiogalactopyranoside (IPTG) and grown overnight (~20 h) at 16 ºC. Cells were harvested via centrifugation at 1,000 RCF, 30 min, 4 ºC and the pellet was resuspended in lysis buffer (25 mM HEPES, pH 7.4, 150 mM NaCl, 10% glycerol, 1 µg/mL DNase, 1 µg/mL RNase, and 1 µg/mL lysozyme) and lysed by passage through a French pressure cell. The lysate was clarified by centrifugation at 12,000 RCF, 1 h, 4 ºC. $His_6$-tagged FabD was purified using Ni-NTA resin (Novagen), washing the resin with wash buffer (25 mM HEPES, pH 7.4, 150 mM NaCl, 10% glycerol, 25 mM imidazole), and eluting the protein with elution buffer (25 mM HEPES, pH 7.4, 150 mM NaCl, 10% glycerol, 250 mM imidazole). Eluted proteins were visualized by 12% SDS-PAGE with Coomassie Brilliant Blue staining and quantified via nanodrop. Imidazole was removed using either a PD-10 desalting column (GE

Healthcare Life Sciences) or a 10 kDa molecular weight cutoff Amicon ultra centrifugation filter and stored at -20 ºC.

*Site-directed Mutagenesis of FabD S92C and ZmaA AT S192C*

Site directed mutagenesis was performed using methods described in Liu and Naismith (2008)[39] to mutate Ser 92 to Cys in FabD and Ser 192 to Cys in ZmaA AT S192C in the pET28b constructs. Primers used for FabD S92C were forward primer- TCACTGCCTGGGGGAATACTCCGCGCT, reverse primer- CCCAGGCAGTGACCGGCCATCATTGC and for ZmaA AT S192C were forward primer- GAATTAAACCTGAAGCAATGATTGGATATTGTTTTGGCGAATATGTGG, reverse primer- AATCATTGCTTCAGGTTTAATTCCCCAACCCATTAATAGTTTCG Q5 polymerase (neb.com) reagents and PCR parameters were followed according to manufacturer's recommendations except for the addition of GC-enhancer and 5mM 7-deaza-dGTP (FabD S92C only). FabD S92C and ZmaA AT S192C was expressed and purified as described above for FabD wt.

*In vitro Labeling of Recombinant FabD by Fluorescent AT Domain Reactive Probes 1, and 3-5*

Optimized conditions for fluorescent probes 1, and 3–5 recombinant FabD reactions were as follows: recombinant FabD (10 μM) was treated with fluorescent probes 1 or 3–5 (50 μM from a 1.5 mM stock in DMSO; final DMSO concentration < 5%) for 12 h at 37 ºC in PBS containing 10 % glycerol, pH 5, 6, 7, 8, and 9.

Controls were performed by pre-denaturation of FabD by addition of 1 % SDS and heating at 95 ºC for 5 min. In time course studies, FabD (10 μM) was treated with probe (50 μM) at 37 ºC in PBS, 10 % glycerol, pH 7 for 1–24 h. Assays were quenched with 5x SDS loading buffer, boiled at 95 ºC, 5 min, and subjected to SDS-PAGE. Gels were visualized at 365 nm using a UV lamp and stained with Coomassie Brilliant Blue.

*In vitro Labeling of FabD S92C by Fluorescent AT Domain Reactive Probes 1, and 3–5*

FabD S92C (30 μM) was treated with fluorescent probe 1 or 3–5 (60 μM from a 1.5 mM stock in DMSO; final DMSO concentration < 5%) for 24 h at 37 ºC in PBS containing 10 % glycerol, pH 7. Assays were quenched with 5x SDS loading buffer, boiled at 95 ºC, 5 min, and subjected to SDS-PAGE. Gels were visualized first at 365 nm using a UV lamp and then stained with Coomassie Brilliant Blue.

*In vitro Labeling of FAS enzymes by Fluorescent AT Domain Reactive Probes 1, and 3–5*

FAS enzymes (10 μM, ACP transacylases FabD and FabD S92C, ketosynthases FabF and FabH, ketoreductase FabG, and dehydratase FabA) were treated with fluorescent probes 1 or 3–5 (50 μM from a 1.5 mM stock in DMSO; final DMSO concentration < 5 %) for 1 h at 37 ºC in PBS containing 10 % glycerol, pH 7. Assays were quenched with 5x SDS loading buffer, incubated at 21 ºC, 2 h,

and subjected to SDS-PAGE. Gels were visualized at 365 nm using a UV lamp and stained with Coomassie Brilliant Blue.

*In vitro Competitive Labeling between FabD and FAS enzymes by Fluorescent AT Domain Reactive Probes 1, and 3–5*

FabD (5 μM) and an FAS enzyme (5 μM of either ketosynthase FabF, ketoreductase FabG, dehydratase FabA, or thioesterase TesA) were treated with fluorescent probes 1 or 3–5 (25 μM from a 1.5 mM stock in DMSO; final DMSO concentration < 5 %) for 4 h at 37 ºC in PBS containing 10 % glycerol, pH 7. Assays were quenched with 5x SDS loading buffer, boiled at 95 ºC, 5 min, and subjected to SDS-PAGE. Gels were visualized at 365 nm using a UV lamp and stained with Coomassie Brilliant Blue.

*Effect of N-ethyl-maleimide on labeling of FabD and FabD S92C by Fluorescent AT Domain Reactive Probes 1, and 3–5*

FabD or FabD S92C (10 μM) were pretreated with *N*-ethyl maleimide (1 mM, from a 20 mM stock in DMSO) for 1h at 37 ºC in PBS containing 10 % glycerol, pH. This was followed by the addition of fluorescent probes 1 or 3–5 (50 μM from a 1.5 mM stock in DMSO; final DMSO concentration < 10 %) for 4 h at 37 ºC. Controls were performed in the absence of *N*-ethyl maleimide, in which vehicle (DMSO) was added. Assays were quenched with 5x SDS loading buffer, boiled

at 95 ºC, 5 min, and subjected to SDS-PAGE. Gels were visualized at 365 nm using a UV lamp and stained with Coomassie Brilliant Blue.

*Effect of cerulenin on competitive labeling of FabD and FabF Fluorescent AT Domain Reactive Probes 1, and 3–5*

Ketosynthase FabF (10 μM) and cerulenin (10 μM, from 448 μM stock in DMSO) were coincubated for 18 h at 37 ºC in PBS containing 10 % glycerol, pH. This was followed by the addition of FabD (10 μM) and fluorescent probes 1 or 3–5 (50 μM from a 1.5 mM stock in DMSO; final DMSO concentration < 10 %) and incubation was continued for 4 h at 37 ºC. Controls were performed in the absence of *N*-ethyl maleimide, in which vehicle (DMSO) was added. Assays were quenched with 5x SDS loading buffer, boiled at 95 ºC, 5 min, and subjected to SDS-PAGE. Gels were visualized at 365 nm using a UV lamp and stained with Coomassie Brilliant Blue.

*Effect of cerulenin on labeling of FabF Fluorescent AT Domain Reactive Probes 1, and 3–5*

Ketosynthase FabF (5 μM) and cerulenin (25 μM, from 448 μM stock in DMSO) were coincubated for 18 h at 37 ºC in PBS containing 10 % glycerol, pH. This was followed by the addition of fluorescent probes 1 or 3–5 (25 μM from a 1.5 mM stock in DMSO; final DMSO concentration < 10 %) and incubation was

continued for 4 h at 37 ºC. Controls were performed in the absence of *N*-ethyl maleimide, in which vehicle (DMSO) was added. Assays were quenched with 5x SDS loading buffer, boiled at 95 ºC, 5 min, and subjected to SDS-PAGE. Gels were visualized at 365 nm using a UV lamp and stained with Coomassie Brilliant Blue.

*Effect of sulfonyl-alkyne crosslinker 6 on competitive labeling of FabA and FabF Fluorescent AT Domain Reactive Probes **1**, and **3–5***

Dehydratase FabA (10 μM) and sulfonyl alkyne crosslinker 6 (100 μM, from 2 mM stock in DMSO) were coincubated for 18 h at 37 ºC in PBS containing 10 % glycerol, pH. This was followed by the addition of FabD (10 μM) and fluorescent probes 1 or 3–5 (50 μM from a 1.5 mM stock in DMSO; final DMSO concentration < 10 %) and incubation was continued for 4 h at 37 ºC. Controls were performed in the absence of 6 in which vehicle (DMSO) was added. Assays were quenched with 5x SDS loading buffer, boiled at 95 ºC, 5 min, and subjected to SDS-PAGE. Gels were visualized at 365 nm using a UV lamp and stained with Coomassie Brilliant Blue.

*Docking analyses*

Molecular docking was performed with small molecule ligands representative of native malonyl and methylmalonyl AT substrates and probe mimics including a

partial pantetheinyl arm. Docking used available crystal structures of FabD from *Xanthomonas oryzae* (PDB: 3K89) and a PKS AT domain from module 5 of DEBS from *Saccharopolyspora erythaea* (PDB: 2HG4) and Autodock Vina (http://vina.scripps.edu). Docking utilized constrained proteins except for three active site residues in the AT domain[40].

*Synthetic Materials and Methods*

*Reagents*

Chemical reagents were purchased from Acros, Fluka, Sigma-Aldrich, or TCI and used without further purification. Deuterated NMR solvents were purchased from Cambridge Isotope Laboratories.

*Reactions*

All reactions were conducted with rigorously dried anhydrous solvents that were obtained by passing through a solvent column composed of activated A1 alumina. Anhydrous *N*,*N*-dimethylformamide was obtained by passage over activated molecular sieves and a subsequent NaOCN column to remove traces of dimethylamine. Triethylamine (Et3N) was dried over Na and freshly distilled. Ethyl-*N*,*N*-diisopropylamine (Et*N*i*P*r2) was distilled from ninhydrin, then from potassium hydroxide. Anhydrous CH3CN was obtained by distillation from CaH2. All reactions were performed under positive pressure of Ar in oven-dried glassware

sealed with septa, with stirring from a Teflon coated stir bars using an IKAMAG RCT-basic mechanical stirrer (IKA GmbH). Solutions were heated using either a sand or silicon oil bath.

*Chromatography*

Analytical Thin Layer Chromatography (TLC) was performed on Silica Gel 60 F254 precoated glass plates (EMSciences). Preparative TLC (pTLC) was conducted on Silica Gel 60 plates (EM Sciences). Visualization was achieved with UV light and/or an appropriate stain (I2 on SiO2, KMnO4, bromocresol green, dinitrophenylhydrazine, ninhydrin, and ceric ammonium molybdate). Flash chromatography was carried out Geduran Silica Gel 60 (40-63 mesh) from EM Biosciences. Yields and characterization data correspond to isolated, chromatographically and spectroscopically homogeneous materials.

*Analytical Instrumentation*

$^{1}H$ NMR spectra were recorded on Varian Mercury 300, Varian Mercury 400 spectrometers, Varian Mercury Plus 400, a JEOL ECA500, or a Varian VX500 spectrometer. $^{13}C$ NMR spectra were recorded at 125 MHz on a Varian VX500 spectrometer equipped with an Xsens Cold probe or at 125 MHz on a JEOL ECA 500, 100 MHz on a Varian Mercury 400 or 100 MHz on a Varian Mercury Plus 400 spectrometer. Chemical shifts for $^{1}H$ NMR and $^{13}C$ NMR analyses were referenced to

the reported values of Gottlieb[41] using the signal from the residual solvent for $^{1}H$ spectra, or to the $^{13}C$ signal from the deuterated solvent. Chemical shift δ values for $^{1}H$ and $^{13}C$ spectra are reported in parts per million (ppm) relative to these referenced values, and multiplicities are abbreviated as s = singlet, d = doublet, t = triplet, q = quartet, m = multiplet, br = broad. All $^{13}C$ NMR spectra were recorded with complete proton decoupling. FID files were processed using MestraNova 6.0.2. (MestreLab Research). Electrospray (ESI) mass spectrometric analyses were performed using a ThermoFinnigan LCQ Deca spectrometer, and high-resolution analyses were conducted using a ThermoFinnigan MAT900XL mass spectrometer with electron impact (EI) ionization. A Thermo Scientific LTQ Orbitrap XL mass spectrometer was used for high-resolution electrospray ionization mass spectrometry analysis (HR-ESI-MS). Spectral data and procedures are provided for all new compounds and copies of select spectra have been provided.

*Nomenclature*

Atom numbers shown in chemical structures herein correspond to the numbering system used in the text of the article and Supporting Information and not to IUPAC nomenclature, which was used solely to name each compound. Compounds not cited in the paper are numbered herein from **S1**.

## Section 7.5 Supplementary Information

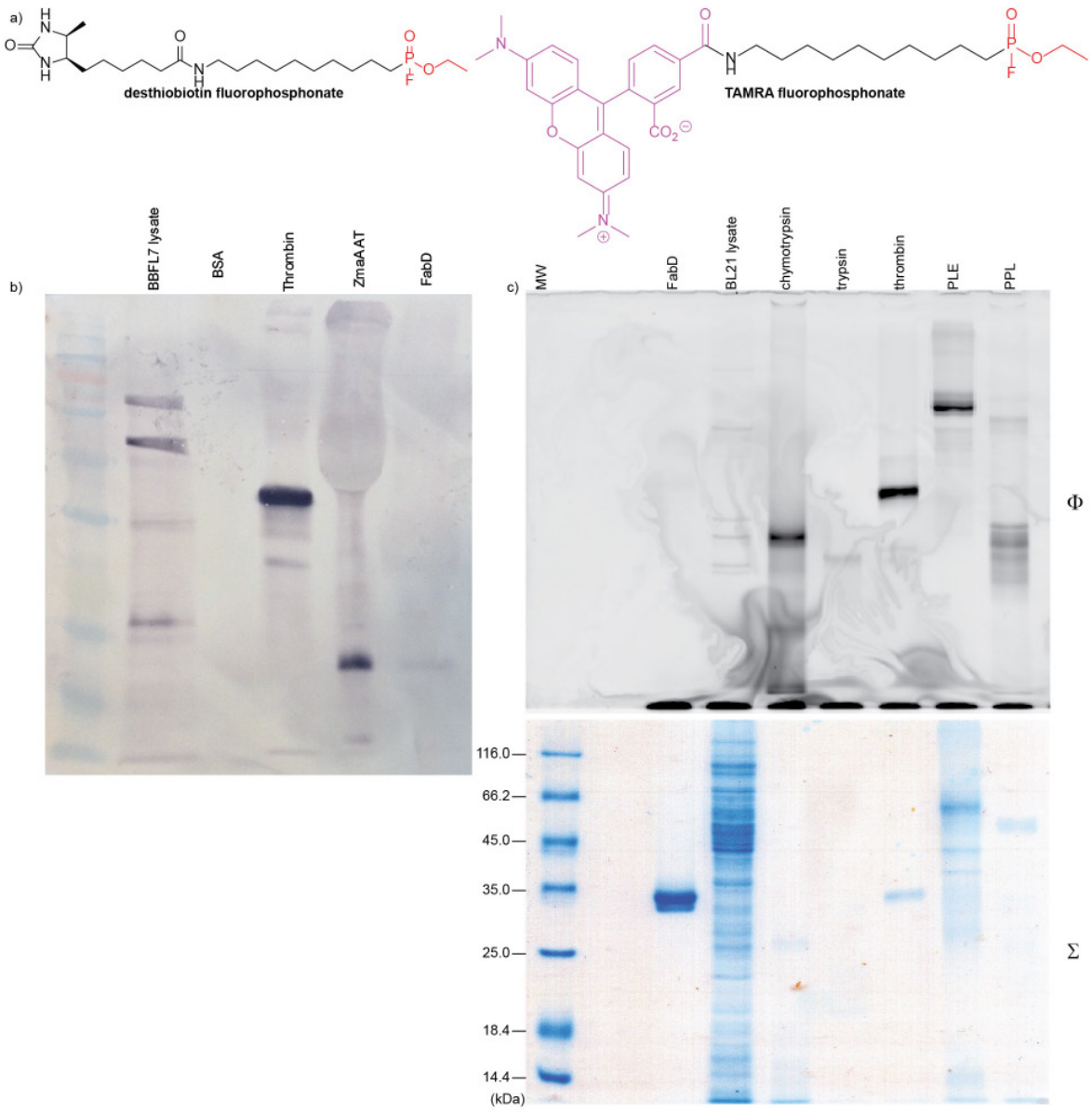


Figure S7.1 Pilot labeling studies of Escherichia coli FabD and other serine hydrolases with commercially available fluorophosphonate probes. (A) Chemical structures of desthiobiotin fluorophosphonate (FP) and TAMRA-FP. (B) Western blot analysis denoting labeling of serine hydrolases FabD, thrombin, ZmaA AT, (2 - 8 mg/mL) and BBFL7 cellular lysate (1.5 mg/mL), with desthiobiotin FP (12 μM, pH 7.5, 2.5 hours, ambient temperature). (C) In-gel fluorescent SDS-PAGE analysis denoting labeling of serine hydrolases FabD, chymotrypsin, trypsin, thrombin, pig liver esterase (PLE), or pig pancreas lipase (2–5 μM) with TAMRA-FP (2–5 μM, 1 equiv., PBS, pH 7, 2 h, 37 □C). E. coli cellular lysate (2.5 mg/mL) was treated with 5 μM TAMRA-FP under the same conditions. Φ depicts SDS-PAGE gel imaged with Typhoon FLA9500 (fluorescence mode, Cy3 green laser, 532 nm) and Σ depicts the total protein content by staining with colloidal Coomassie Brilliant Blue.

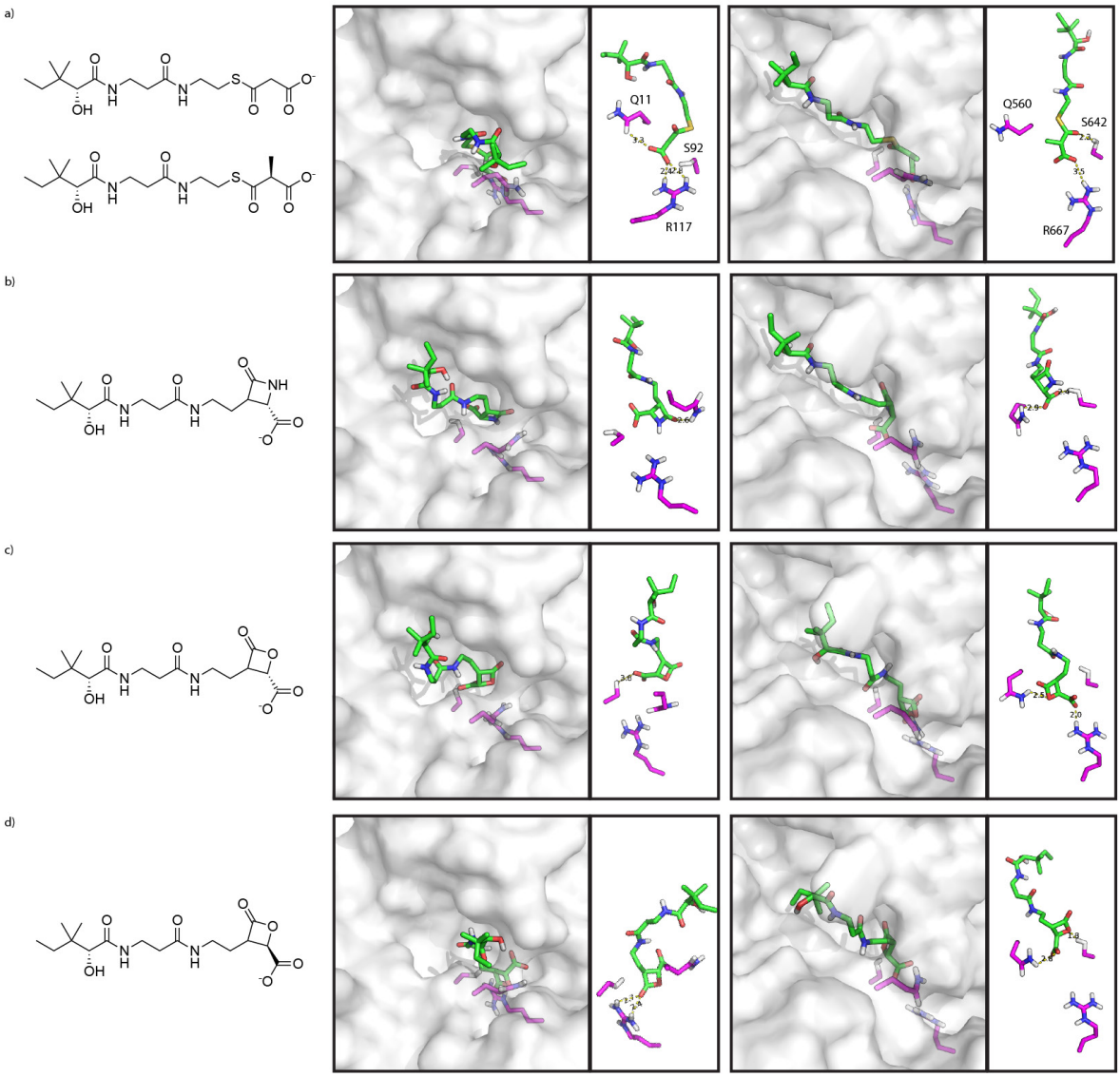


Figure S7.2 Computational docking of lactams and lactones into acyl-carrier protein transacylase (AT) domains derived from fatty acid synthases (FAS) and polyketide synthases (PKS). Chemical structures of pantetheine analogues with docking poses for FabD FAS AT domain from *Xanthomonas oryzae* (PDB: 3K89) (left) and DEBS module 5 PKS AT domain from *Saccharopolyspora erythaea* (PDB: 2HG4) (right) using pantheine mimic structures for (a) native malonyl and methylmalonyl substrates for FabD and DEBS AT respectively (a) lactam probe (b) and lactone probes (c–d).

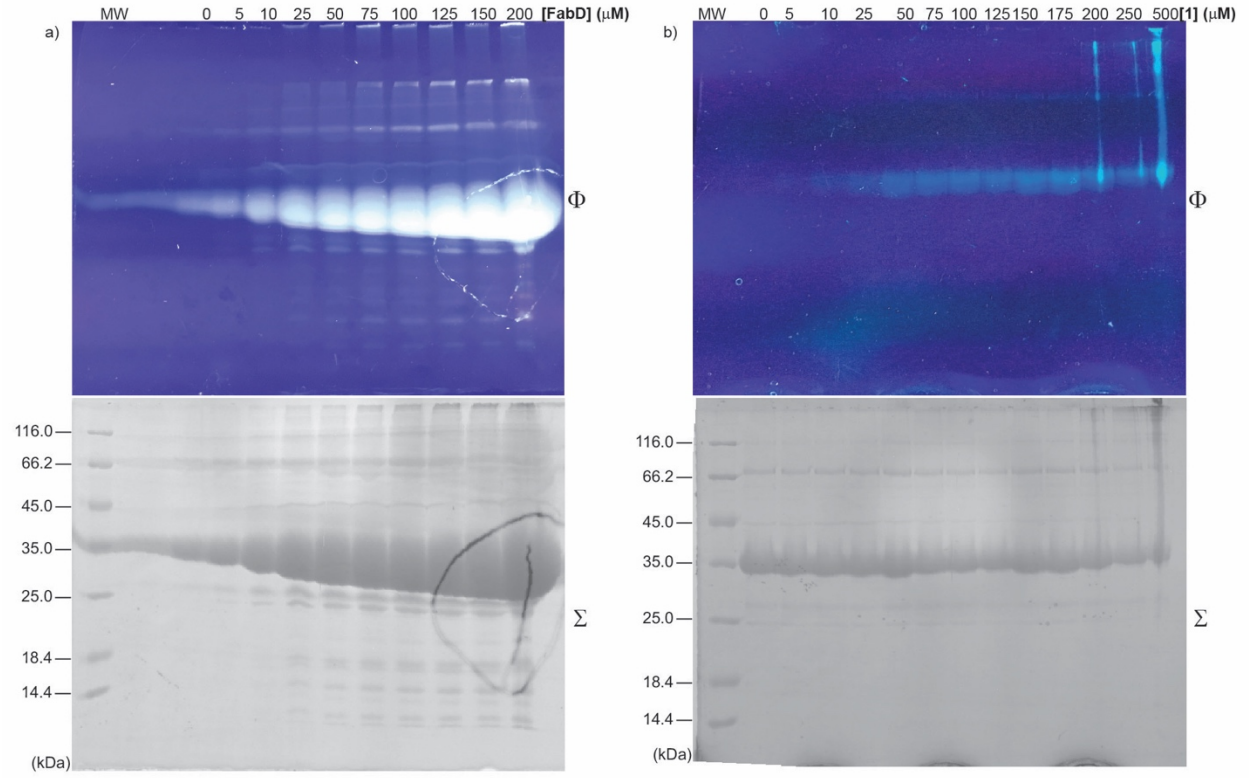


Figure S7.3 Pilot concentration-dependent labeling studies of *E. coli* FabD to assess sensitivity and labeling limits of detection. (a) In-gel fluorescent SDS-PAGE analysis denoting labeling of FabD (0–200 μM) with 1 (100 μM, PBS, pH 7.6, 12 h, 37 □C). (b) In-gel fluorescent SDS-PAGE analysis denoting labeling of FabD (10 μM) with 1 (0–500 μM, PBS, pH 7.6, 12 h, 37 □C). For each panel, Φ depicts gel visualized under UV at 365 nm and Σ depicts the total protein content by staining with colloidal Coomassie Brilliant Blue.

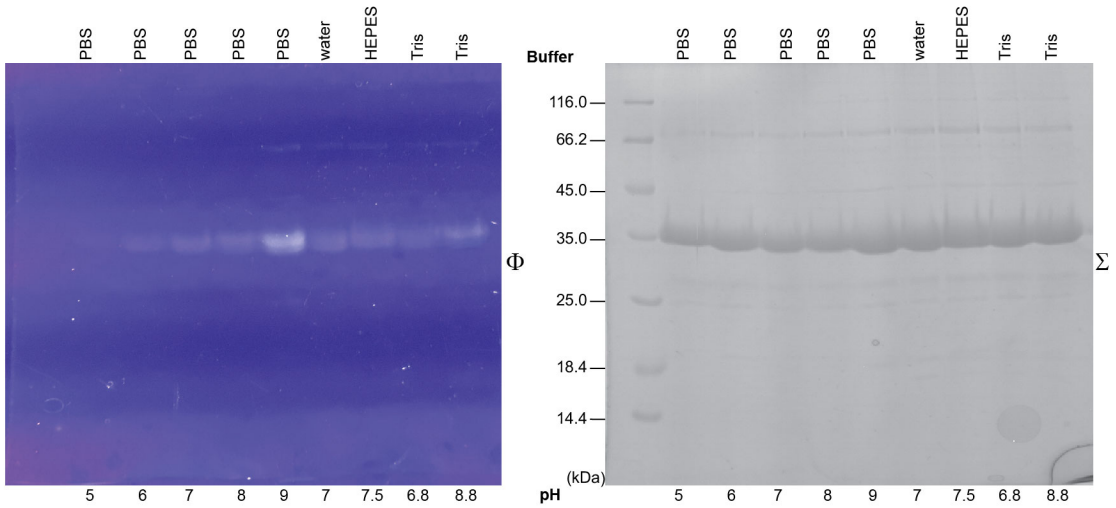


Figure S7.4 Pilot labeling studies of *E. coli* FabD to evaluate the influence of buffer on labeling. In-gel fluorescent SDS-PAGE analysis denoting labeling of FabD (10 μM) with 1 (50 μM, 12 h, 37 □C) in various buffers. Φ depicts gel visualized under UV at 365 nm and Σ depicts the total protein content by staining with colloidal Coomassie Brilliant Blue.

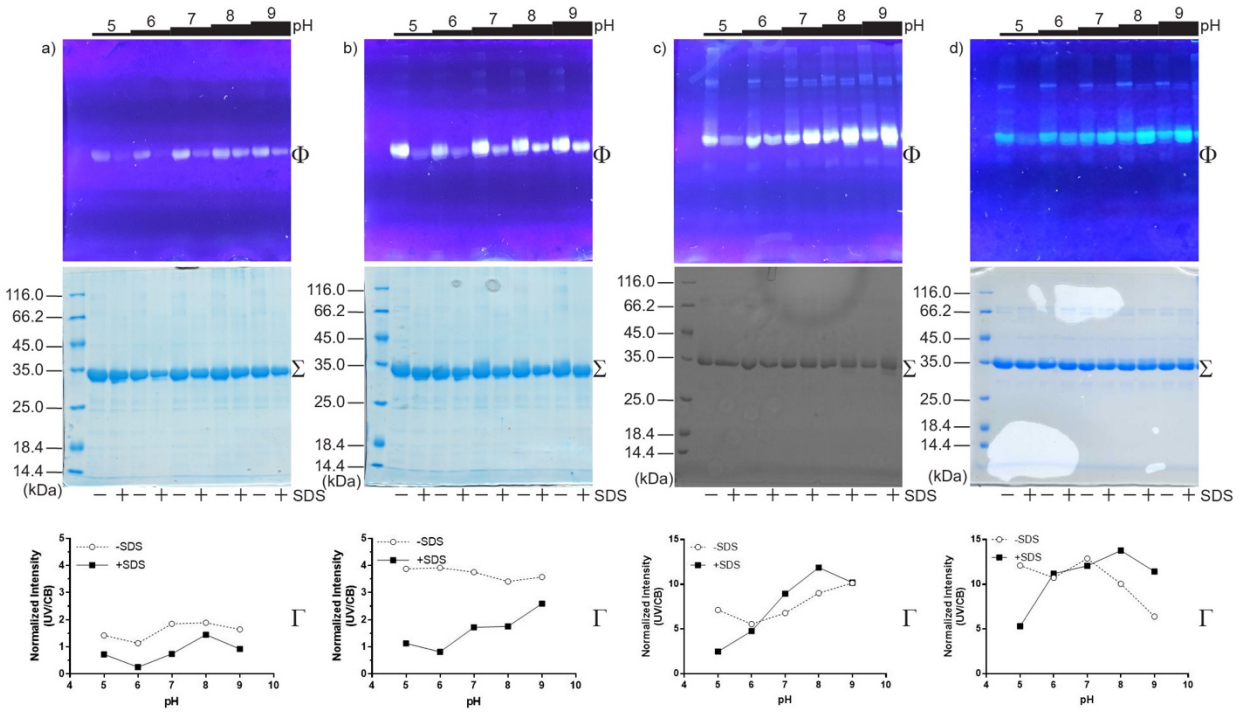


Figure S7.5 Full depiction of gels shown in Figures 3a–d. In-gel fluorescent SDS-PAGE analysis denoting pH-dependent labeling of FabD (10 μM, PBS, 12 h, 37 □C) with 50 μM (a) 1, (b) 3, (c) 4, or (d) 5. For each panel, Φ depicts gel visualized under UV at 365 nm, Σ depicts the total protein content by staining with colloidal Coomassie Brilliant Blue, and Γ depicts semi-quantitation of fluorescence using ImageJ software in which intensities were normalized to total protein content.

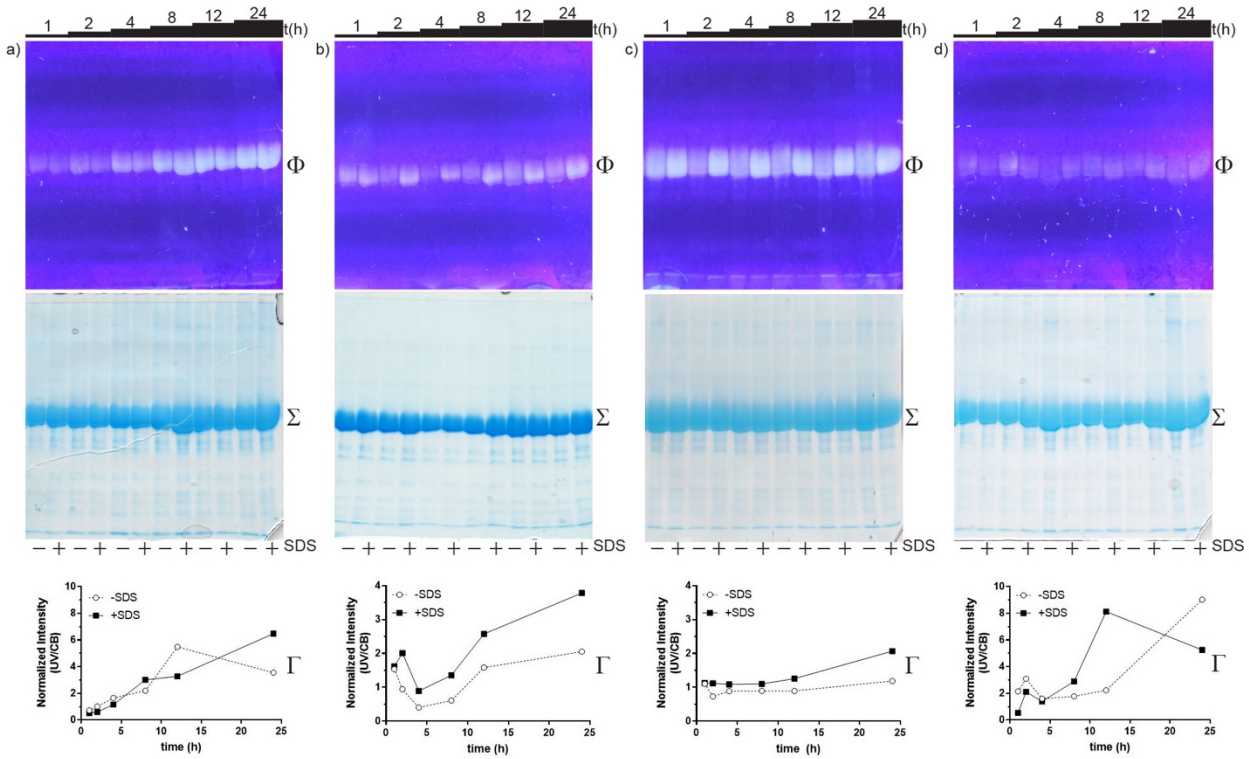


Figure S7.6 Full depiction of gels shown in Figures 3e–h. In-gel fluorescent SDS-PAGE analysis denoting time-dependent labeling of FabD (10 μM, PBS, pH 7, 37 □C) with 50 μM (e) 1, (f) 3, (g) 4, or (h) 5. For each panel, Φ depicts gel visualized under UV at 365 nm, Σ depicts the total protein content by staining with colloidal Coomassie Brilliant Blue, and Γ depicts semi-quantitation of fluorescence using ImageJ software in which intensities were normalized to total protein content.

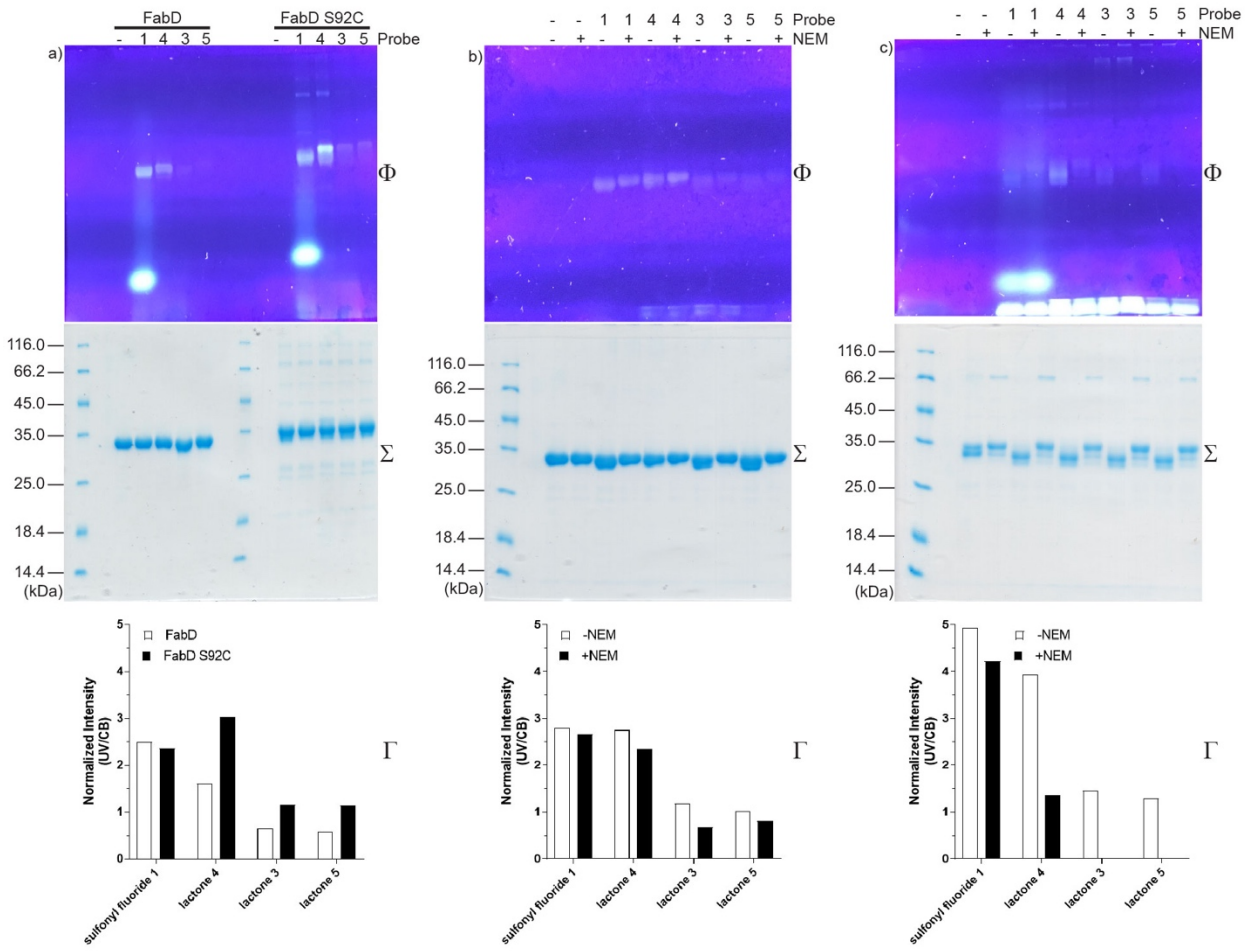


Figure S7.7 Labeling of FabD S92C. (a) In-gel SDS-PAGE analysis denoting labeling of FabD S92C (30 μM, PBS, pH 7, 37 □C, 24 h) with fluorescent probe (60 μM). (b–c) In gel SDS-PAGE analysis denoting the effects of N-ethyl maleimide (NEM) pretreatment (1 mM, 1 h, 37 □C) on labeling of (b) FabD (10 μM, PBS, pH 7, 50 μM probe, 4 h, 37 □C) and (c) FabD S92C (10 μM, PBS, pH 7, 50 μM probe, 4 h, 37 □C). For each panel, Φ depicts gel visualized under UV at 365 nm, Σ depicts the total protein content by staining with colloidal Coomassie Brilliant Blue, and Γ depicts semi-quantitation of fluorescence using ImageJ software in which intensities were normalized to total protein content.

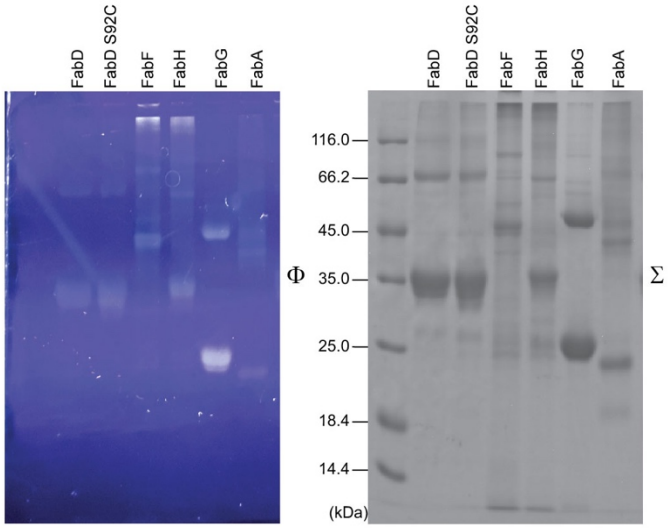


Figure S7.8 Labeling specificity of aryl sulfonyl fluoride probe. In-gel SDS-PAGE analysis denoting aryl sulfonyl fluoride cross-reactivity with other FAS enzymes (10 μM, PBS, pH 9, 37 □C, 24 h) with 50 μM 1. Φ depicts gel visualized under UV at 365 nm and Σ depicts the total protein content by staining with colloidal Coomassie Brilliant Blue.

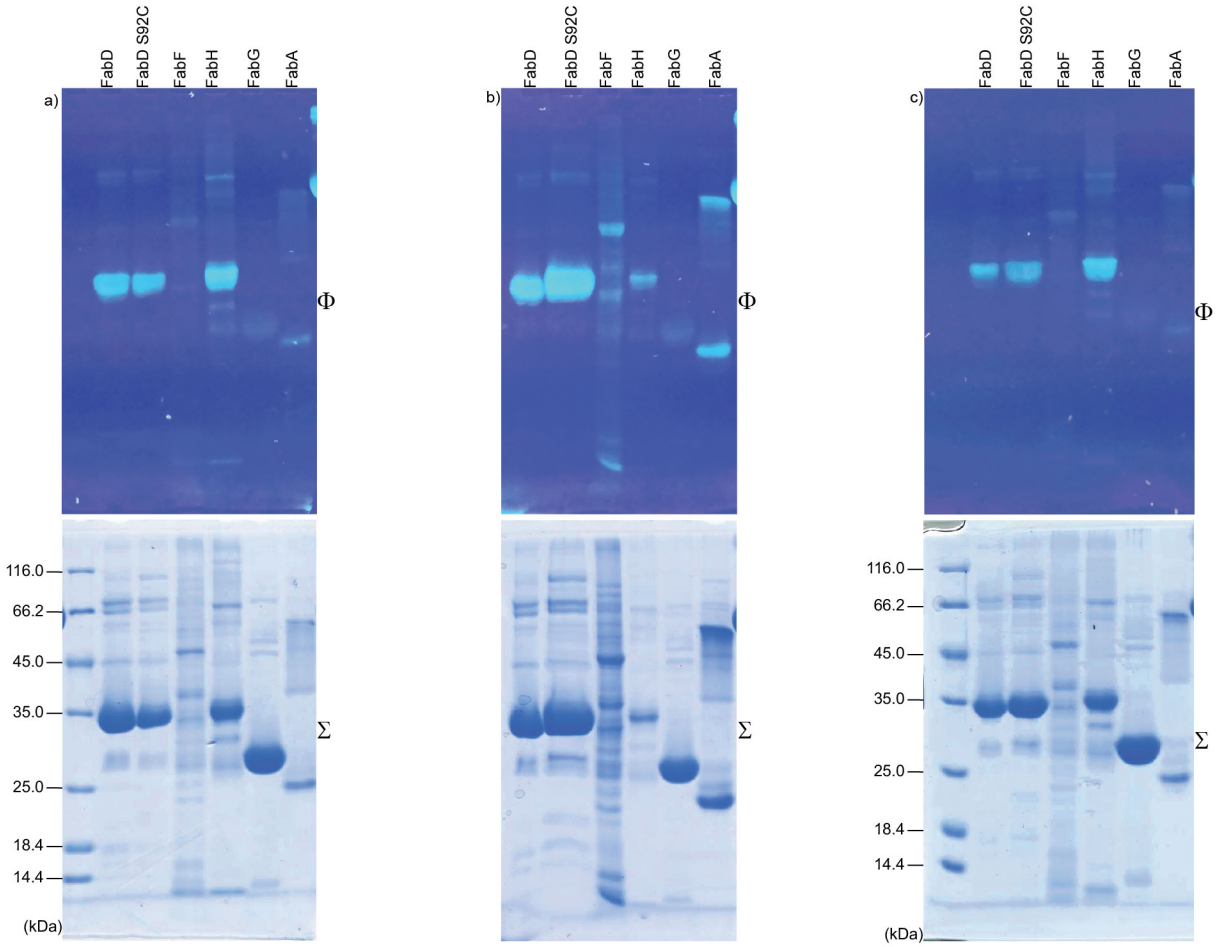


Figure S7.9 Labeling specificity of lactone probes. In-gel SDS-PAGE analysis denoting lactone cross-reactivity with other FAS enzymes (10 μM, PBS, pH 7, 37 □C, 1 h) with 50 μM (a) 3, (b) 4, or (c) 5. For each panel, Φ depicts gel visualized under UV at 365 nm and Σ depicts the total protein content by staining with colloidal Coomassie Brilliant Blue.

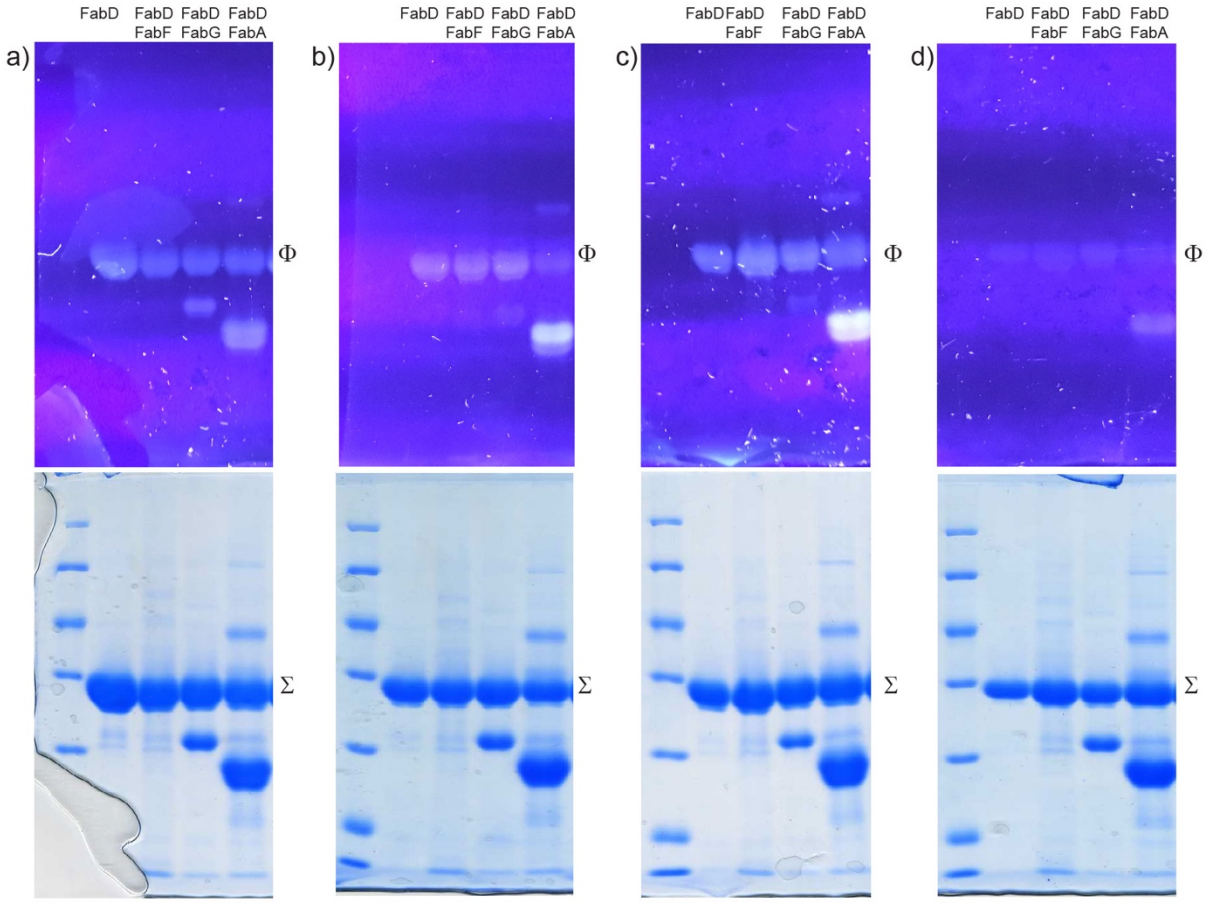


Figure S7.10 Full depiction of gels shown in Figures 4a–d. In-gel fluorescent SDS-PAGE analysis denoting competitive labeling between equimolar amounts of FabD and FAS enzymes (5 μM, PBS, pH 7, 4 h, 37 □C) with 25 μM (a) **1**, (b) **3**, (c) **4**, or (d) **5**. For each panel, Φ depicts gel visualized under UV at 365 nm and Σ depicts the total protein content by staining with colloidal Coomassie Brilliant Blue.

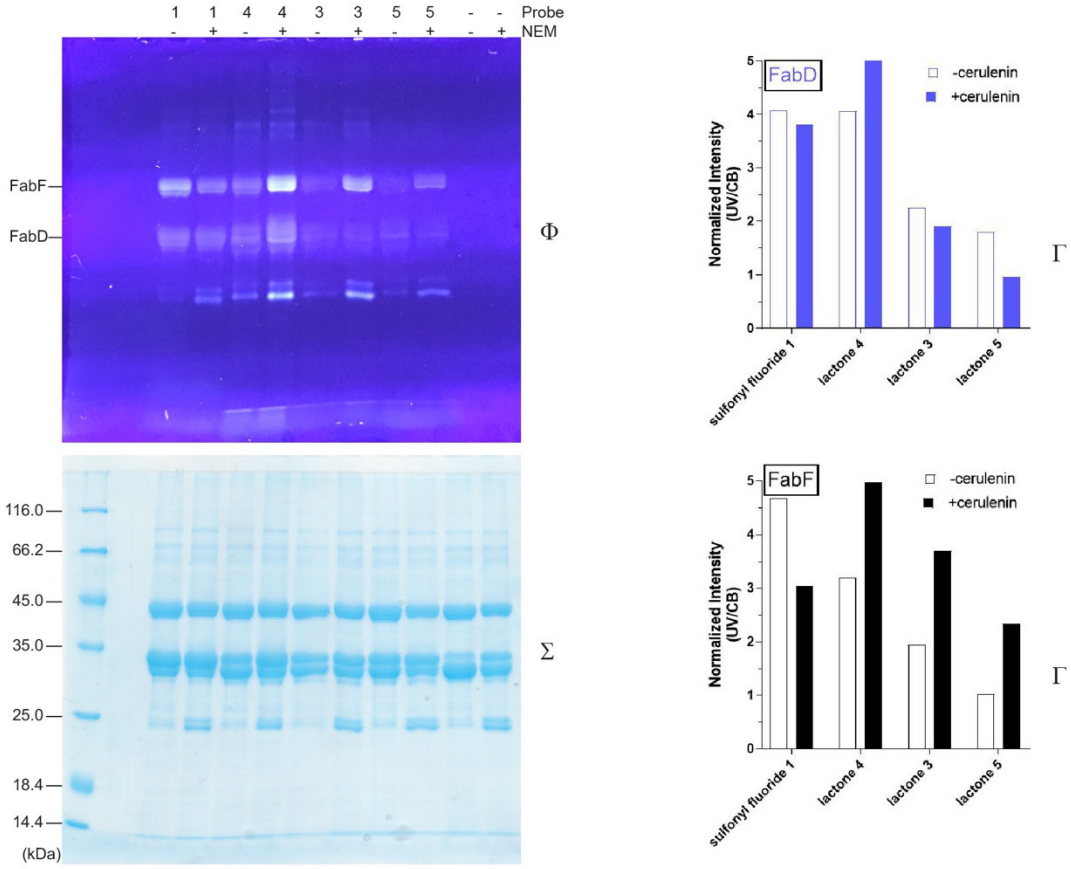


Figure S7.11 Full depiction of gels shown in Figure 4f. Modulation of FabD versus FabF fluorescent probe labeling specificity by pretreating FabF (10 μM) with cerulenin (10 μM, 18 h, 37 □) prior to addition of FabD (10 μM) and probes (50 μM). For each panel, Φ depicts gel visualized under UV at 365 nm, Σ depicts the total protein content by staining with colloidal Coomassie Brilliant Blue, and Γ depicts semi-quantitation of fluorescence using ImageJ software in which intensities were normalized to total protein content.

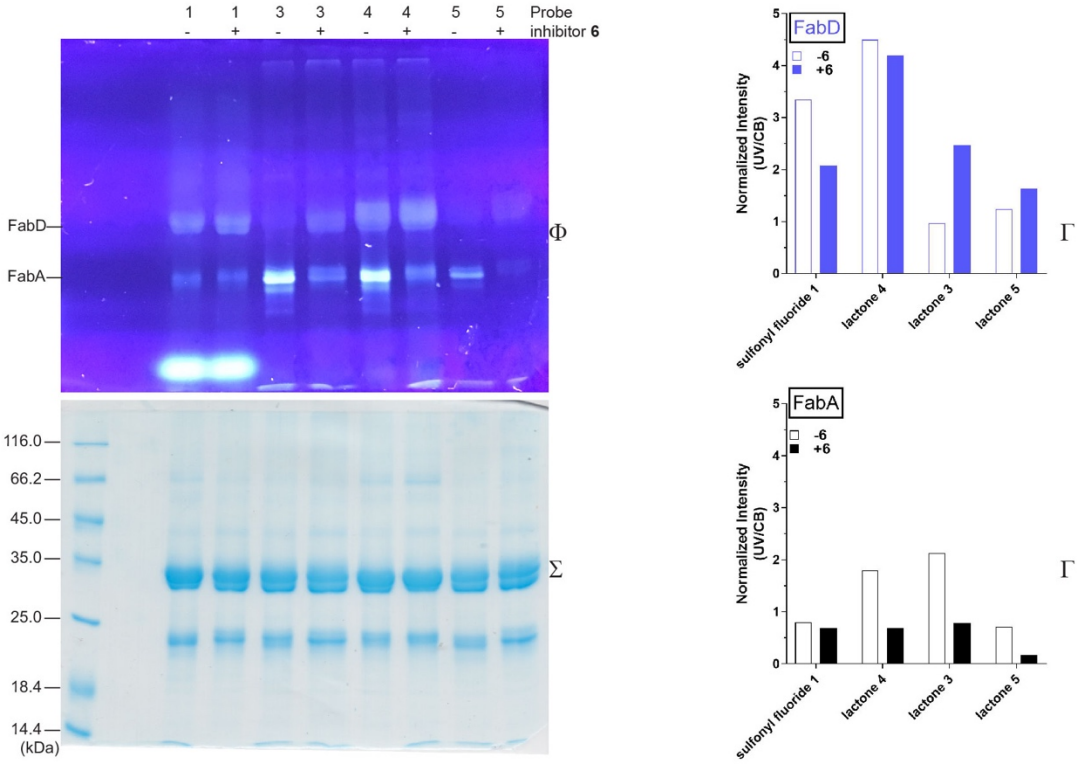


Figure S7.12 Full depiction of gels shown in Figure 4g. Modulation of FabD versus FabA fluorescent probe labeling specificity by pretreating FabA (10 μM) with sulfonyl alkyne 6 (100 μM, 18 h, 37 □C) prior to addition of FabD (10 μM) and probes (50 μM). For each panel, Φ depicts gel visualized under UV at 365 nm, Σ depicts the total protein content by staining with colloidal Coomassie Brilliant Blue, and Γ depicts semi-quantitation of fluorescence using ImageJ software in which intensities were normalized to total protein content.

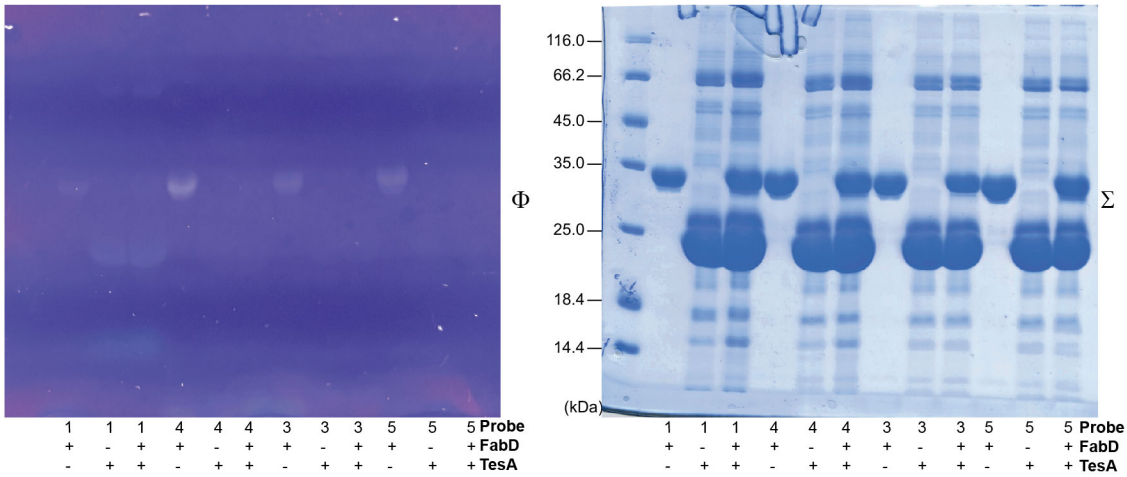


Figure S7.13 Evaluation of labeling specificity between serine hydrolases FabD and TesA. In-gel SDS-PAGE analysis denoting competitive labeling between equimolar amounts of FabD and TesA (5 μM, PBS, pH 7, 4 h, 37 □C, 25 μM fluorescent probe). For each panel, Φ depicts gel visualized under UV at 365 nm and Σ depicts the total protein content by staining with colloidal Coomassie Brilliant Blue.

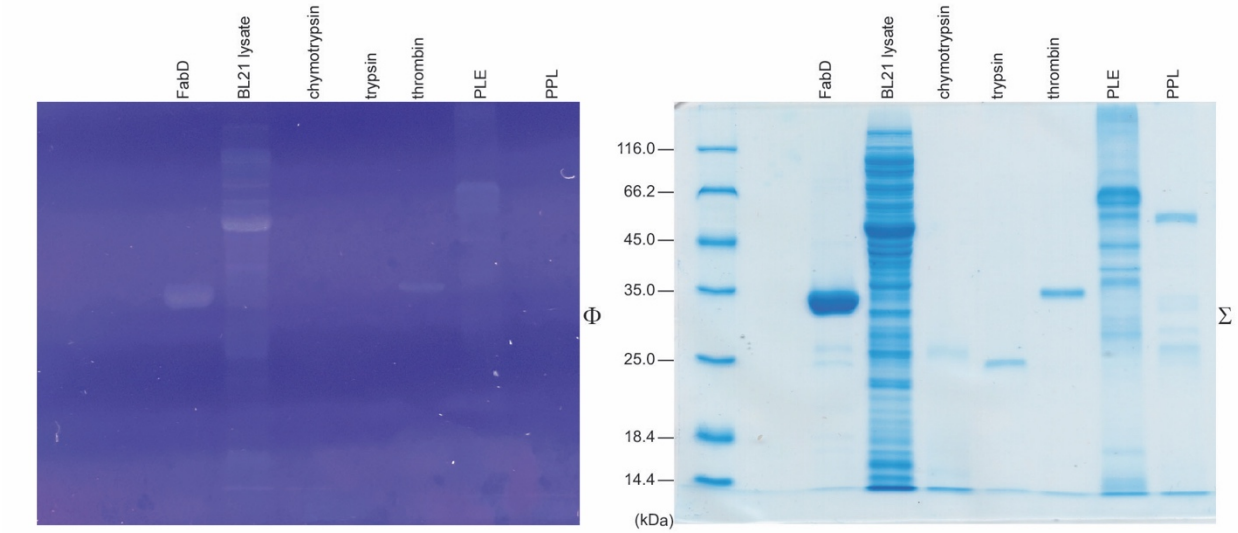


Figure S7.14 Evaluation of aryl sulfonyl fluoride promiscuity with additional serine hydrolases. In-gel SDS-PAGE analysis denoting labeling of serine hydrolases FabD, chymotrypsin, trypsin, thrombin, pig liver esterase (PLE), or pig pancreas lipase (PPL) (2–10 μM) with 1 (50 μM, PBS, pH 7, 4 h, 37 □). E. coli BL21 lysate (5 mg/mL) was treated with 1 under the same conditions. For each panel, Φ depicts gel visualized under UV at 365 nm and Σ depicts the total protein content by staining with colloidal Coomassie Brilliant Blue.

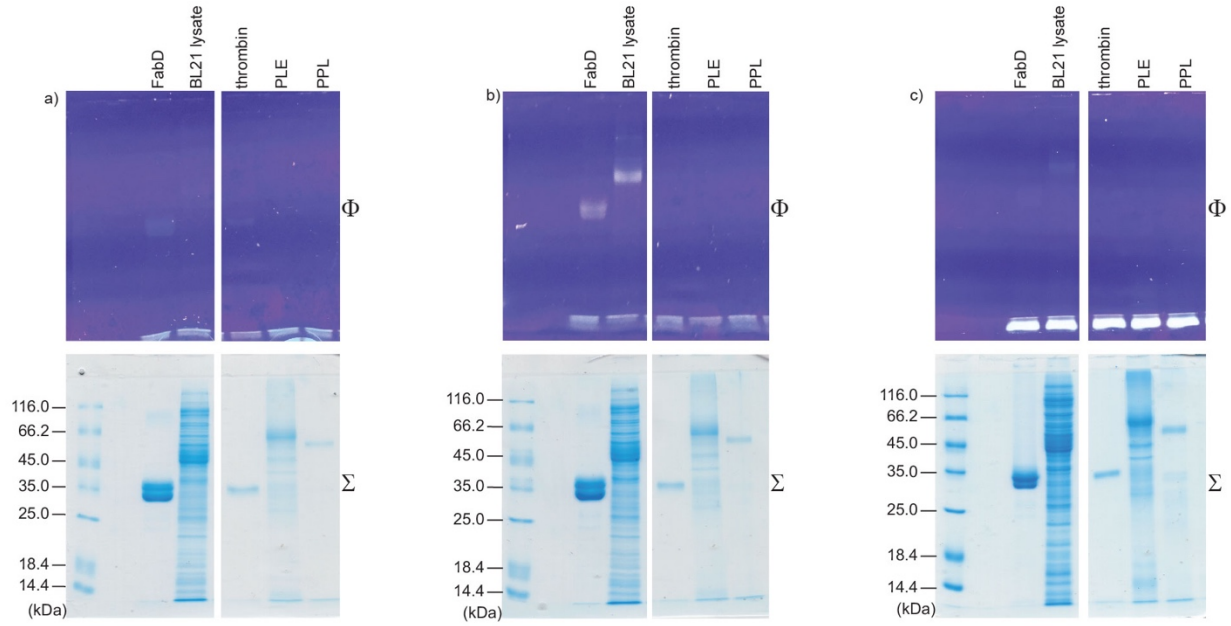


Figure S7.15 Evaluation of lactone promiscuity with additional serine hydrolases. In-gel SDS-PAGE analysis denoting labeling of serine hydrolases FabD, thrombin, pig liver esterase (PLE), or pig pancreas lipase (PPL) (2–10 μM, fluorescent probe , PBS, pH 7, 4 h, 37 □) with 50 μM: (a) 3, (b) 4, or (c) 5. E. coli BL21 lysate (5 mg/mL) was treated with 3–5 under the same conditions. For each panel, Φ depicts gel visualized under UV at 365 nm and Σ depicts the total protein content by staining with colloidal Coomassie Brilliant Blue.

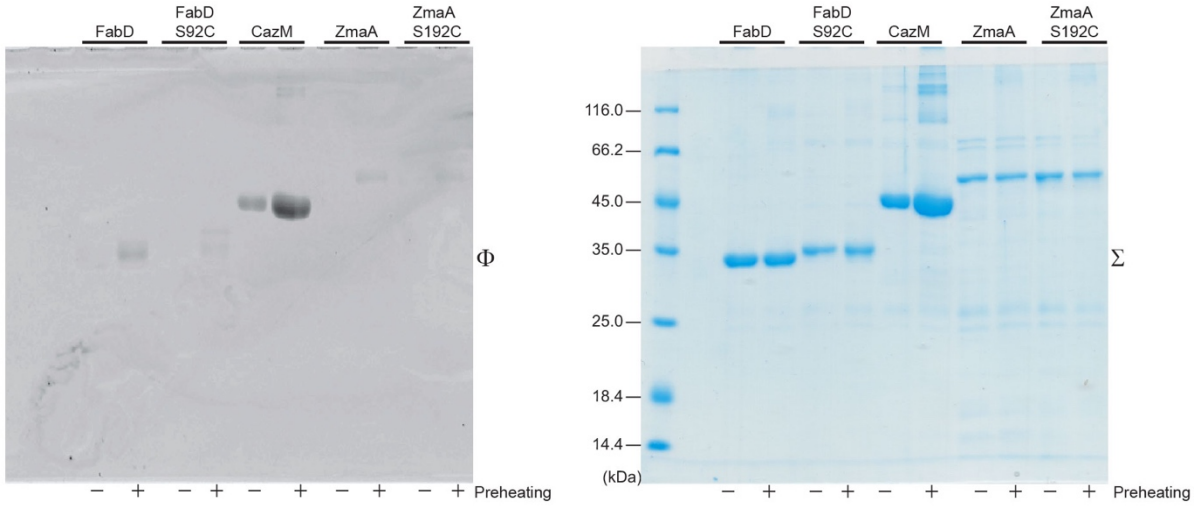


Figure S7.16 Labeling of AT domains derived from polyketide biosynthetic pathways with TAMRA-FP. In-gel SDS-PAGE analysis denoting labeling of polyketide AT domains (5 μM) with TAMRA-FP (5 μM, PBS, pH 7, 2 h, 37 □C). For each panel, Φ depicts SDS-PAGE gel imaged with Typhoon FLA9500 (fluorescence mode, Cy3 green laser, 532 nm) and Σ depicts the total protein content by staining with colloidal Coomassie Brilliant Blue.

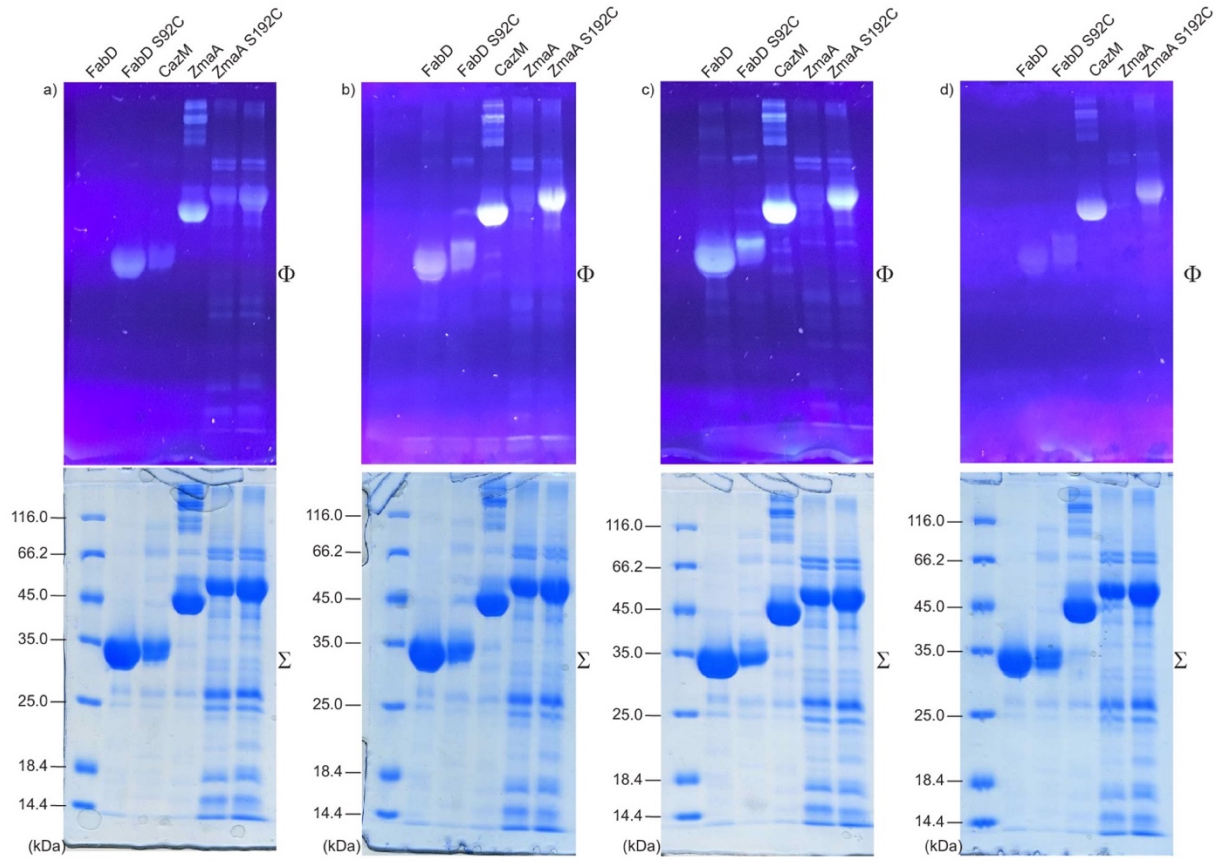


Figure S7.17 Full depiction of gels shown in Figure 5. In-gel fluorescent SDS-PAGE analysis denoting labeling of polyketide AT domains (10 μM, PBS, pH 7, 12 h, 37 □C) with 50 μM: (a) 1, (b) 3, (c) 4, or (d) 5. For each panel, Φ depicts gel visualized under UV at 365 nm and Σ depicts the total protein content by staining with colloidal Coomassie Brilliant Blue.

*Synthesis of fluorescent aryl-sulfonyl fluoride **1***

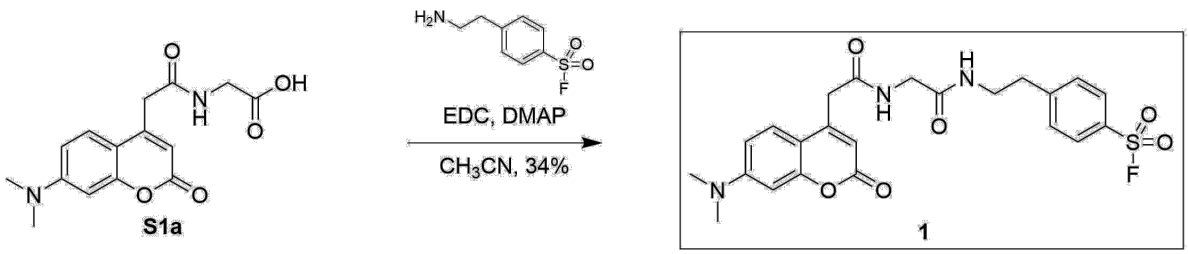


Scheme S7.1 General synthetic approach to access fluorescent aryl-sulfonyl fluoride **1**. (EDC=1-Ethy-3-(3-dimethylaminopropyl)carbodiimide); DMAP=4-(dimethylamino)-pyridine).

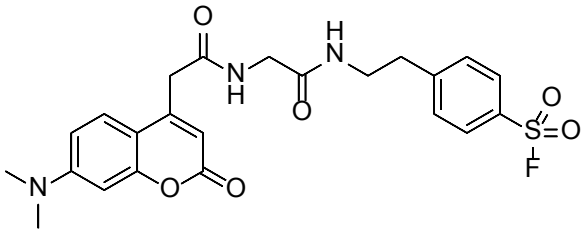

**4-(2-(2-(2-(7-(dimethylamino)-2-oxo-2H-chromen-4-yl)acetamido)acetamido)ethyl)benzene- sulfonyl fluoride propanoate (1).** In a 20 mL scintillation vial, *N*-7-diemthylaminocoumarin-4-acetyl-glycine **S1a**[42] (12.8 mg, 0.0423 mmol, 1.0 equiv.) and 1.5 mL acetonitrile were added. To the suspension was added EDC•HCl (24.8 mg, 0.129 mmol, 5.6 equiv.) and DMAP (1.0 mg, 0.0082 mmol, 0.19 equiv.). After 30 min, 2-aminoethylbenzenesulfonyl fluoride (10.8 mg, 0.0451 mmol, 1.1 equiv.). After 23 h, the reaction was quenched with saturated aq. $NH_4Cl$ (10 mL) and extracted with EtOAc (3x25 mL). The combined organic extracts were dried ($MgSO_4$), filtered, and concentrated by rotary evaporation. Purification by silica flash chromatography (19:1 → 4:1 $CH_2Cl_2$/MeOH) afforded **1** (7.0 mg, 34%) as a pale yellow solid.

**TLC**: $R_f$ 0.18 (19:1 $CH_2Cl_2$/MeOH). **$^1$H-NMR** (400 MHz, $CD_3CN$): 7.95 (d, *J* = 8.4 Hz, 2H), 7.50 (dd, *J* = 14.3, 8.6 Hz, 4H), 6.87 (s, 1H), 6.68 (dd, *J* = 9.0, 2.6 Hz, 1H), 6.54 (d, *J* = 2.5 Hz, 1H), 6.49 (s, 1H), 6.01 (s, 1H), 3.68 – 3.63 (m, 4H), 3.41 (q, *J* = 6.9 Hz, 2H), 3.02 (s, 6H), 2.85 (t, *J* = 7.0 Hz, 2H). **ESI-MS** *m/z* (rel int): (pos) 512.88 ($[M+Na]^+$, 100), 489.48 ($[M+H]^+$, 80), 527.58 ($[M+K]^+$, 40).

*Synthesis of fluorescent lactam* ***2***

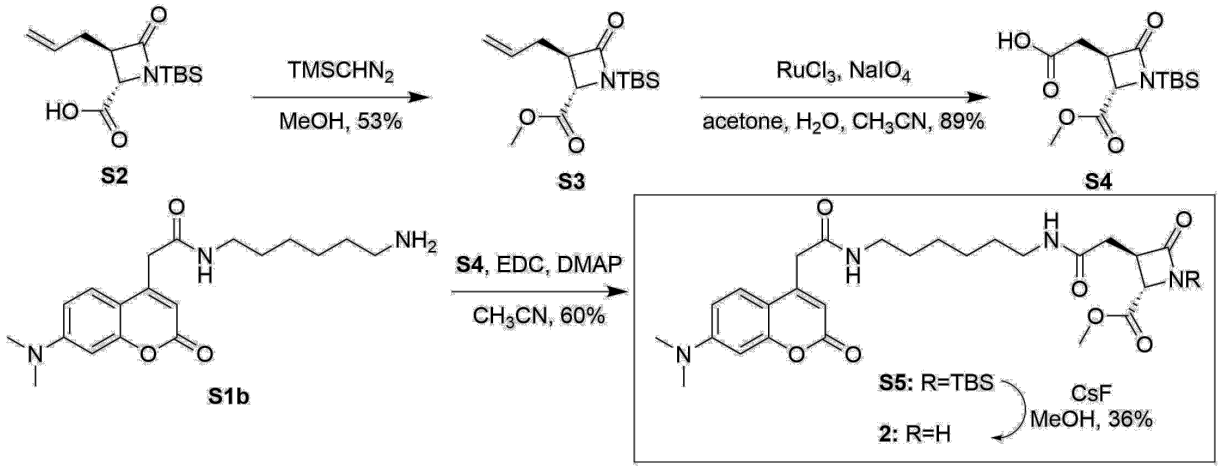


Scheme S7.2 General synthetic approach to access fluorescent lactam **2**. (TMS=trimethylsilyl; EDC=1-Ethy-3-(3-dimethylaminopropyl)carbodiimide; DMAP=4-(dimethylamino)-pyridine; TBS=tert-butyl-dimethylsilyl).

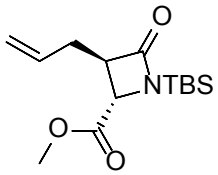

**Methyl (2*S*,3*R*)-3-allyl-1-(*tert*-butyldimethylsilyl)-4-oxoazetidine-2-carboxylate (S3).** In a 10 mL pear-shaped flask, (2*S*,3*R*)-3-allyl-1-(*tert*-butyldimethylsilyl)-4-oxoazetidine-2-carboxylic acid **S2**[43] (56.2 mg, 0.2086 mmol, 1.0 equiv.) and 2.1 mL methanol were added. The vessel was cooled to 0 ºC and 0.42 mL $TMSCHN_2$ was added and the reaction was warmed to 21 ºC. After 13.5 h, the volatiles were removed by rotary evaporation. Purification by silica flash chromatography (3:1 → 1:1 hexanes/EtOAc) afforded **S3** (31.3 mg, 53%) as a clear residue.

**$^1$H-NMR** (400 MHz, $CDCl_3$): δ 5.81 (m, 1H), 5.22–5.11 (m, 2H), 3.78 (d, *J* = 2.7 Hz, 1H), 3.76 (s, 3H), 3.35 (m, 1H), 2.49 (m, 2H), 0.95 (s, 9H), 0.28 (s, 3H), 0.09 (s, 3H). **ESI-MS** *m/z* (rel int): (pos) 284.14 ($[M+H]^+$, 100), 306.09 ($[M+Na]^+$, 70).

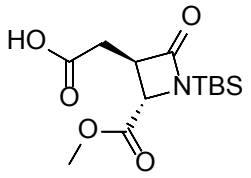


**2-((2*S*,3*R*)-1-(*tert*-butyldimethylsilyl)-2-(methoxycarbonyl)-4-oxoazetidin-3-yl)acetic acid carboxylate (S4).** In a 20 mL scintillation vial, methyl-(2*S*,3*R*)-3-allyl-1-(*tert*-butyldimethylsilyl)-4-oxoazetidine-2-carboxylate **S3** (14.9 mg, 0.0523 mmol, 1.0 equiv.), 1 mL $CCl_4$, 1 mL $CH_3CN$, and 1.5 mL $H_2O$ were added. To the clear solution was added $NaIO_4$ (59.3 mg, 0.2772 mmol, 5.3 equiv.) and $RuCl_3 \bullet (H_2O)n$ (0.2 mg, 0.0012 mmol, 0.022 equiv.). After 2 h, the reaction was extracted with $CH_2Cl_2$ (3x10 mL), dried ($MgSO_4$), filtered through a pad of celite, and concen-

trated by rotary evaporation to afford **S4** (14.0 mg, 89%) as a brown solid. The crude material was >95% pure and advanced to the next step without further purification.

**$^1$H-NMR** (400 MHz, $CDCl_3$): δ 3.94 (d, 1H), 3.77 (s, 3H), 3.63–3.56 (m, 1H), 2.82 (ddd, *J* = 56.8, 17.6, 6.8 Hz, 2H), 0.96 (s, 9H), 0.28 (s, 3H), 0.12 (s, 3H).

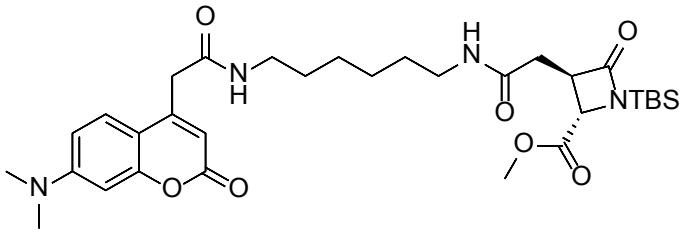


**Methyl (*2S,3R*)-1-(*tert*-butyldimethylsilyl)-3-(2-((6-(2-(7-(dimethylamino)-2-oxo-2H-chromen-4-yl)acetamido)hexyl)amino)-2-oxoethyl)-4-oxoazetidine-2-carboxylate (S5).** In a 10 round bottom flask, 2-((*2S,3R*)-1-(*tert*-butyldimethylsilyl)-2-(methoxycarbonyl)-4-oxoazetidin-3-yl)acetic acid carboxylate **S4** (5.9 mg, 0.0196 mmol, 1.0 equiv.) and 1.5 mL acetonitrile were added. To the suspension was added EDC•HCl (7.0 mg, 0.0365 mmol, 1.9 equiv.) and DMAP (3.1 mg, 0.0254 mmol, 1.3 equiv.). After 30 min, hexanediamine-containing coumarin **S1b**[7] (6.8 mg, 0.0196 mmol, 1.0 equiv.) was added as a solution in 2.4 mL acetonitrile. After 24 h, the reaction was quenched with saturated aq. $NH_4Cl$ (5 mL) and extracted with EtOAc (3x15 mL). The combined organic extracts were dried ($MgSO_4$), filtered, and concentrated by rotary evaporation. Purification by silica

flash chromatography (EtOAc → 1:1 EtOAc/MeOH) afforded **S5** (6.3 mg, 60%) as a pale yellow oil.

**TLC**: $R_f$ 0.44 (19:1 EtOAc/MeOH). **$^1$H-NMR** (400 MHz, $CD_3OD$): 7.58 (d, *J* = 9.1 Hz, 1H), 6.76 (dd, *J* = 9.1, 2.5 Hz, 1H), 6.57 (d, *J* = 2.5 Hz, 1H), 6.05 (s, 1H), 4.05 (d, *J* = 2.6 Hz, 1H), 3.75 (s, 3H), 3.68 (s, 1H), 3.55 (ddd, *J* = 9.1, 5.3, 3.0 Hz, 1H), 3.23–3.18 (m, 2H), 3.15–3.11 (m, 2H), 3.08 (s, 6H), 2.59 (ddd, *J* = 42.5, 15.1, 7.2 Hz, 2H), 1.57–1.43 (m, 4H), 1.39–1.27 (m, 4H), 0.96 (s, 9H), 0.26 (s, 3H), 0.14 (s, 3H). **ESI-MS** *m/z* (rel int): (pos) 651.43 ($[M+Na]^+$, 100), 537.54 ($[M-TBS+Na]^+$, 20).

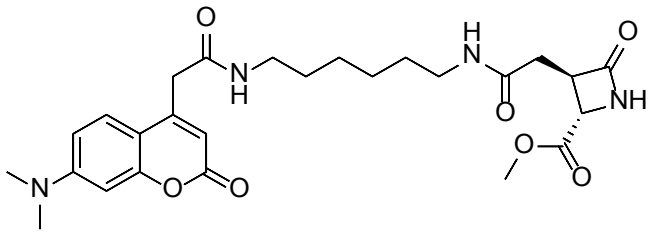

**Methyl (2S,3R)-3-(2-((6-(2-(7-(dimethylamino)-2-oxo-2H-chromen-4-yl)acetamido)hexyl)amino)-2-oxoethyl)-4-oxoazetidine-2-carboxylate (2).** In a 20 mL vial, **S5** (2.7 mg, 0.0043 mmol, 1.0 equiv.) and 2 mL methanol were added. To the solution was added CsF (2.5 mg, 0.0165 mmol, 3.8 equiv.). After 1 h, the volatiles were removed by rotary evaporation. Purification by silica flash chromatography (19:1 → 9:1 $CH_2Cl_2$/MeOH) afforded **2** (0.8 mg, 36%) as a clear oily residue.

**$^1$H-NMR** (400 MHz, $CD_3OD$): 7.59 (d, *J* = 9.3 Hz, 1H), 6.77 (d, *J* = 5.4 Hz, 1H), 6.58 (d, *J* = 3.0 Hz, 1H), 6.05 (s, 1H), 4.78 (d, *J* = 4.9 Hz, 3H), 4.05 (d, *J* = 2.1 Hz, 1H), 3.75 (s, 2H), 3.68 (s, 2H), 3.24–3.18 (m, 6H), 3.17–3.11 (m, 5H), 3.08 (s, 4H), 2.16 (s, 2H), 1.90 (s, 2H), 1.51 (d, *J* = 17.8 Hz, 6H). **ESI-MS** *m/z* (rel int): (pos) 537.43 ($[M+Na]^+$, 100).

*Synthesis of lactones* ***3–5***

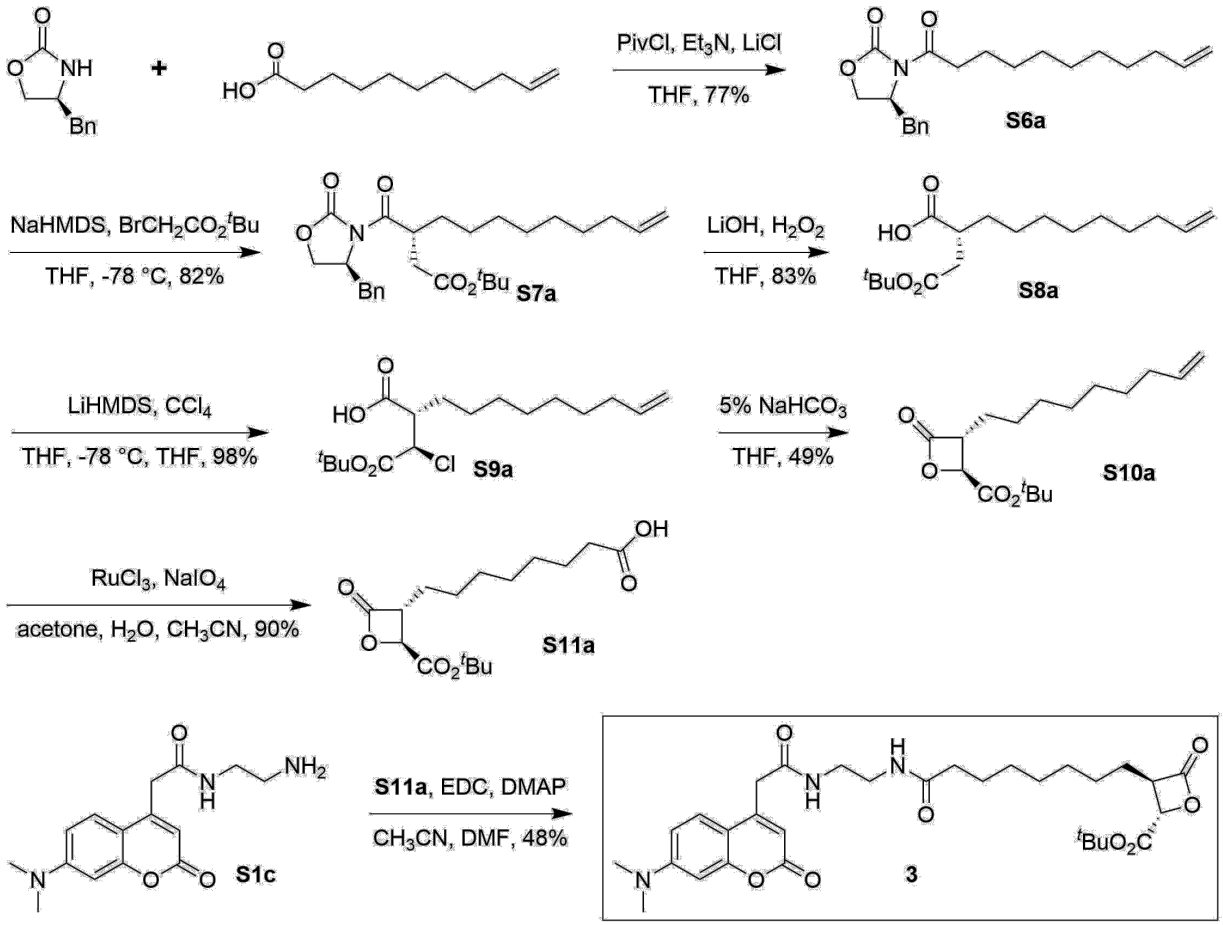


Scheme S7.3 General synthetic approach to access fluorescent lactone **3**. (PivCl=trimethyacetyl chloride; NaHMDS=sodium bis(trimethylsilyl)amide; LiHMDS=lithium bis(trimethylsilyl)amide; EDC=1-Ethy-3-(3-dimethylaminopropyl)carbodiimide); DMAP=4-(dimethylamino)-pyridine).

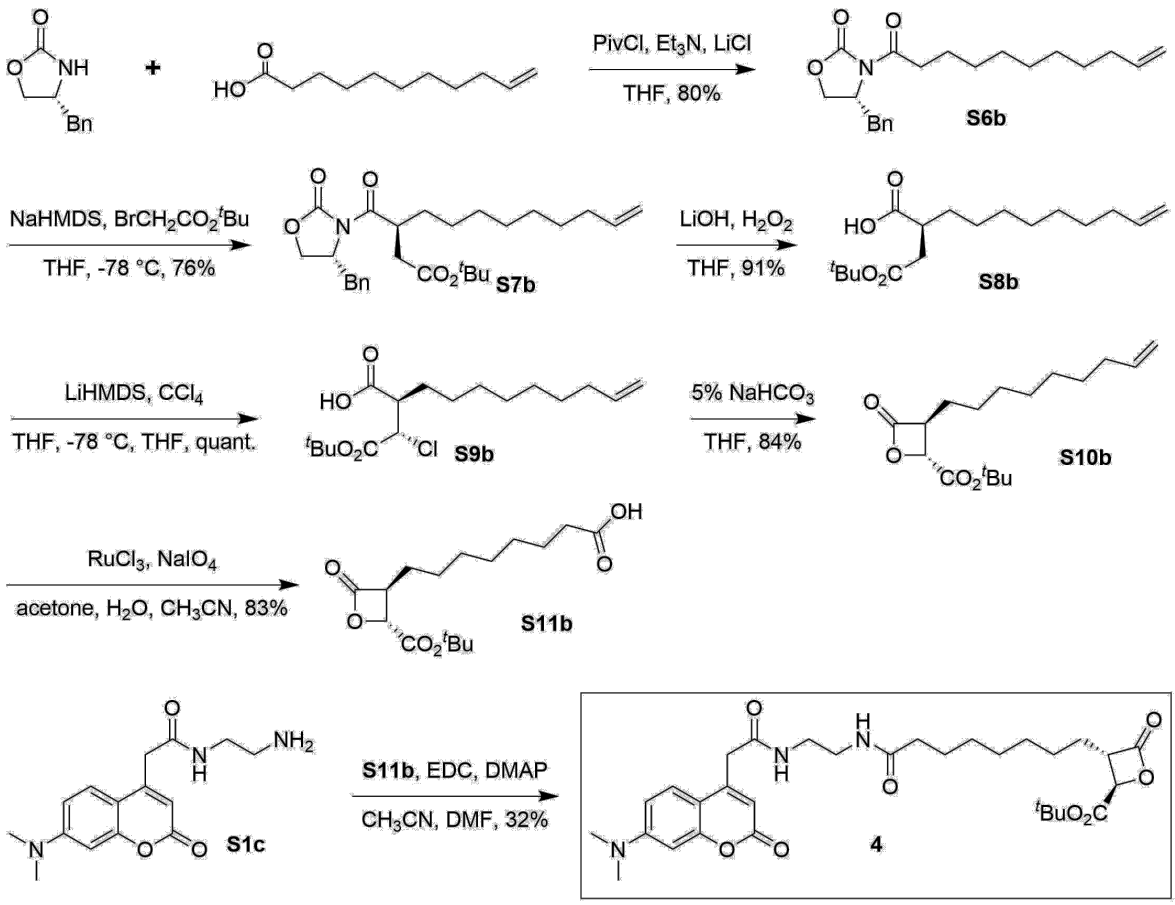


Scheme S7.4 General synthetic approach to access fluorescent lactone **4**. (PivCl=trimethyacetyl chloride; NaHMDS=sodium bis(trimethylsilyl)amide; LiHMDS=lithium bis(trimethylsilyl)amide; EDC=1-Ethy-3-(3-dimethylaminopropyl)carbodiimide); DMAP=4-(dimethylamino)-pyridine).

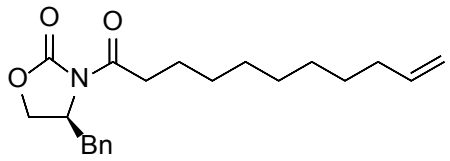

**(*S*)-4-benzyl-3-(undec-10-enoyl)oxazolidin-2-one (S6a).** In a 100 mL pear-shaped flask, 10-undecenoic acid (1.0023 g, 5.4390 mmol, 1.0 equiv.) and 50 mL THF were added. The solution was cooled to 0 ºC before the addition of trimethylamine (2.4 mL, 17.2191 mmol, 3.5 equiv.) and trimethyl acetyl chloride (0.67 mL, 5.4398 mmol, 1.0 equiv.). After 1 h at 0 ºC, to the cloudy suspension was

added LiCl (261.2 mg, 6.1618 mmol, 1.1 equiv.) and (*S*)-(-)-4-benzyl-2-oxazolidinone (1.0652, 6.0113 mmol, 1.1 equiv.). The reaction was warmed to 21 ºC and stirred for 16 h. The volatiles were removed by rotary evaporation and the resulting white solid was dissolved in EtOAc (100 mL), washed with 1 M HCl (25 mL), satd $NaHCO_3$ (25 mL), and brine (25 mL). The organic phase was dried ($MgSO_4$), filtered, and concentrated by rotary evaporation. Purification by silica flash chromatography (85:15 → 4:1 hexanes/diethyl ether) afforded **S6a** (1.4373 g, 77%) as a clear oil.

**TLC**: $R_f$ 0.32 (3:1 hexanes/diethyl ether). **$^1$H-NMR** (400 MHz, $CDCl_3$): δ 7.37–7.26 (m, 3H), 7.21 (d, *J* = 6.8 Hz, 2H), 5.81 (td, *J* = 16.9, 6.7 Hz, 1H), 4.96 (dd, *J* = 25.6, 13.6 Hz, 2H), 4.72–4.63 (m, 1H), 4.23–4.13 (m, 2H), 3.30 (d, *J* = 13.3 Hz, 1H), 2.93 (qt, *J* = 16.9, 7.6 Hz, 2H), 2.76 (dd, *J* = 13.2, 9.7 Hz, 1H), 2.04 (q, *J* = 6.5 Hz, 2H), 1.67 (dt, *J* = 15.8, 7.4 Hz, 2H), 1.44–1.25 (m, 10H). **$^{13}$C-NMR** (100 MHz, $CDCl_3$): δ 173.55, 153.58, 139.32, 135.45, 129.54, 129.07, 127.45, 114.26, 77.48, 77.16, 76.84, 66.27, 55.28, 38.06, 35.66, 33.92, 29.46, 29.44, 29.24, 29.20, 29.03, 24.38. **ESI-MS** *m*/*z* (rel int): (pos) 460.89 ($[M+NH_4]^+$, 100), 366.12 ($[M+Na]^+$, 15), 344.14 ($[M+H]^+$, 10).

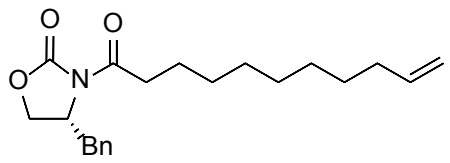

**(*R*)-4-benzyl-3-(undec-10-enoyl)oxazolidin-2-one (S6b).** Prepared as described for **S6a** from (*R*)-(-)-4-benzyl-2-oxazolidinone, to give **S6b** (1.2727 g, 80%) as a clear oil.

**TLC**: $R_f$ 0.23 (4:1 hexanes/diethyl ether). **$^1$H-NMR** (400 MHz, $CDCl_3$): δ 7.31 (dd, *J* = 18.0, 7.0 Hz, 3H), 7.21 (d, *J* = 6.5 Hz, 2H), 5.81 (ddt, *J* = 16.7, 12.4, 6.0 Hz, 1H), 4.96 (dd, *J* = 25.1, 13.2 Hz, 2H), 4.67 (dt, *J* = 9.5, 3.9 Hz, 1H), 4.18 (p, *J* = 7.5, 5.9 Hz, 2H), 3.30 (d, *J* = 13.2 Hz, 1H), 2.92 (tq, *J* = 19.2, 9.4 Hz, 2H), 2.76 (t, *J* = 11.4 Hz, 1H), 2.09–2.00 (m, 2H), 1.75–1.61 (m, 2H), 1.45–1.19 (m, 10H). **$^{13}$C-NMR** (100 MHz, $CDCl_3$): δ 173.53, 153.56, 139.27, 135.42, 129.51, 129.03, 127.42, 114.24, 77.48, 77.16, 76.84, 66.24, 55.24, 38.01, 35.63, 33.89, 29.43, 29.41, 29.35, 29.28, 29.21, 29.17, 29.13, 29.00, 28.97, 27.09, 24.35. **ESI-MS** *m*/*z* (rel int): (pos) 344.31 ($[M+H]^+$, 100), 366.31 ($[M+Na]^+$, 80).

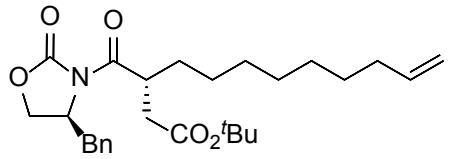


***tert*-Butyl (*R*)-3-((*S*)-4-benzyl-2-oxooxazolidine-3-carbonyl)dodec-11-enoate (S7a).** In a 15 mL 3-necked flask, (*S*)-4-benzyl-3-(undec-10-enoyl)oxazolidin-2-one **S6a** (779.1 mg, 2.2683 mmol, 1.0 equiv.) and 5 mL tetrahydrofuran were added. The reaction vessel was cooled to -78 ºC before the slow, dropwise addition of

NaHMDS (1.4 mL, 2.0 M in THF, 2.8 mmol, 1.2 equiv.). After stirring for 2 h at -78 ºC, tert-butyl-bromoacetate (0.90 mL, 6.1369 mmol, 2.7 equiv.) was added dropwise and stirring was continued for 2 h at -78 ºC. The reaction was quenched with saturated aq. $NH_4Cl$ (10 mL) and extracted with EtOAc (4x25 mL). The combined organic extracts were dried ($MgSO_4$), filtered, and concentrated by rotary evaporation. Purification by silica flash chromatography (19:1 → 4:1 hexanes/diethyl ether) afforded **S7a** (847.8 mg, 82%) as a clear oil.

**TLC**: $R_f$ 0.30 (4:1 hexanes/diethyl ether). **$^1$H-NMR** (400 MHz, $CDCl_3$): δ 7.39–7.23 (m, 5H), 5.86–5.73 (m, 1H), 4.95 (dd, *J* = 24.5, 13.5 Hz, 2H), 4.72–4.61 (m, 1H), 4.23–4.12 (m, 3H), 3.34 (d, *J* = 13.0 Hz, 1H), 2.77 (dq, *J* = 23.4, 13.2, 11.9 Hz, 2H), 2.53–2.43 (m, 1H), 2.08–1.98 (m, 2H), 1.63 (dd, *J* = 14.1, 7.5 Hz, 2H), 1.43 (s, 9 H), 1.37–1.23 (m, 10H). **$^{13}$C-NMR** (100 MHz, $CDCl_3$): δ 176.17, 171.55, 153.15, 139.27, 135.89, 129.62, 129.03, 127.31, 114.28, 80.79, 77.48, 77.16, 76.84, 65.98, 55.70, 39.42, 37.65, 37.21, 33.88, 32.09, 29.63, 29.39, 29.13, 28.98, 28.19, 26.94. **ESI-MS** *m/z* (rel int): (pos) 480.25 ([M+Na]$^+$, 100).

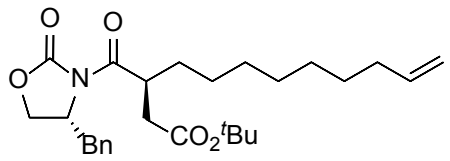

***tert*-Butyl (*S*)-3-((*R*)-4-benzyl-2-oxooxazolidine-3-carbonyl)dodec-11-enoate (S7b).** Prepared as described for **S7a** from (*R*)-4-benzyl-3-(undec-10-enoyl)oxazolidin-2-one **S6b**, to give **S7b** (347.3 mg, 76%) as a clear oil.

**TLC**: $R_f$ 0.37 (4:1 hexanes/diethyl ether). **$^1$H-NMR** (400 MHz, $CDCl_3$): δ 7.37–7.30 (m, 2H), 7.27 (d, *J* = 6.2 Hz, 3H), 5.87–5.73 (m, 1H), 5.03–4.88 (m, 2H), 4.70–4.61 (m, 1H), 4.21–4.12 (m, 3H), 3.38–3.30 (m, 1H), 2.77 (dddd, *J* = 23.3, 13.5, 10.3, 1.4 Hz, 2H), 2.53–2.43 (m, 1H), 2.03 (ddd, *J* = 7.7, 5.0, 1.5 Hz, 2H), 1.64 (dt, *J* = 13.9, 6.6 Hz, 2H), 1.42 (d, *J* = 1.5 Hz, 9H), 1.38–1.31 (m, 5H), 1.27 (s, 7H). **$^{13}$C-NMR** (100 MHz, $CDCl_3$): δ 176.23, 171.62, 153.21, 139.35, 135.96, 129.69, 129.10, 127.38, 114.36, 80.86, 77.55, 77.23, 76.91, 66.06, 55.77, 39.49, 37.72, 37.28, 33.95, 32.16, 29.70, 29.45, 29.20, 29.05, 28.26, 27.01. **ESI-MS** *m*/*z* (rel int): (pos) 480.22 ([M+Na]$^+$, 100).

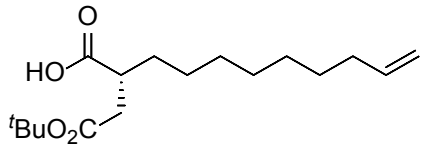


**(*R*)-2-(2-(*tert*-butoxy)-2-oxoethyl)undec-10-enoic acid (S8a).** In a 20 mL vial, *tert*-Butyl (*R*)-3-((*S*)-4-benzyl-2-oxooxazolidine-3-carbonyl)dodec-11-enoate **S7a** (368.1 mg, 0.8044 mmol, 1.0 equiv.), 6 mL tetrahydrofuran, and 2 mL w, ,ater were added. The reaction vessel was cooled to 0 ºC before adding $H_2O_2$ (0.41 mL, 4.0220 mmol, 5.0 equiv.) and LiOH•$H_2O$ (78.3 mg, 1.8661 mmol, 2.3 equiv.).

The reaction stirred at 0 ºC for 15 min. before being warmed to 21 ºC. After 1.5 h, the reaction was quenched with saturated aq. $NaS_2O_3$ (10 mL), brine (10 mL), and saturated aq. $NH_4Cl$ (10 mL) and extracted with $CH_2Cl_2$ (4x25 mL). The combined organic extracts were dried ($MgSO_4$), filtered, and concentrated by rotary evaporation. Purification by silica flash chromatography (3:1 → 1:1 hexanes/diethyl ether + 1% acetic acid) afforded **S8a** (460.9 mg, 83%) as a clear oil.

**TLC**: $R_f$ 0.18 (3:1 hexanes/diethyl ether + 1% acetic acid). **$^1$H-NMR** (400 MHz, $CDCl_3$): δ 5.86–5.73 (m, 1H), 5.03–4.89 (m, 2H), 2.78 (dt, *J* = 12.5, 6.6 Hz, 1H), 2.61 (dd, *J* = 16.4, 9.4 Hz, 1H), 2.37 (dd, *J* = 16.4, 5.1 Hz, 1H), 2.02 (q, *J* = 6.6 Hz, 2H), 1.65 (dq, *J* = 14.2, 7.0 Hz, 2H), 1.50 (dd, *J* = 14.6, 6.8 Hz, 2H), 1.43 (s, 9H), 1.39–1.25 (m, 10H). **$^{13}$C-NMR** (100 MHz, $CDCl_3$): δ 181.62, 171.26, 139.26, 114.31, 81.11, 77.48, 77.16, 76.84, 41.48, 37.20, 33.90, 31.77, 29.48, 29.35, 29.13, 28.99, 28.11, 27.01. **ESI-MS** *m/z* (rel int): (pos) 321.15 ($[M+Na]^+$, 100), 343.14 ($[M-H+2Na]^+$, 35); (neg) 297.16 ($[M-H]^-$, 100).

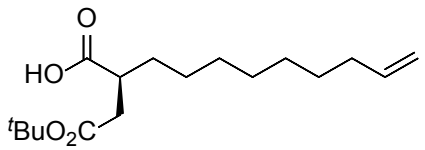

**(*S*)-2-(2-(*tert*-butoxy)-2-oxoethyl)undec-10-enoic acid (S8b).** Prepared as described for **S8a**, from *tert*-Butyl (*R*)-3-((*S*)-4-benzyl-2-oxooxazolidine-3-carbonyl)dodec-11-enoate **S7b**, to give **S8b** (538.5 mg, 91%) as a clear oil.

**TLC**: $R_f$ 0.46 (1:1 hexanes/diethyl ether + 1% acetic acid). **$^1$H-NMR** (400 MHz, $CDCl_3$): δ 5.79 (ddt, *J* = 17.1, 9.9, 6.7 Hz, 1H), 5.08–4.87 (m, 2H), 2.79 (ddd, *J* = 9.7, 5.0, 2.3 Hz, 1H), 2.60 (dd, *J* = 16.1, 9.4 Hz, 1H), 2.37 (dt, *J* = 16.4, 3.5 Hz, 1H), 2.02 (d, *J* = 7.5 Hz, 2H), 1.65 (q, *J* = 7.6 Hz, 1H), 1.42 (s, 10H), 1.39–1.21 (m, 10H). **$^{13}$C-NMR** (100 MHz, $CDCl_3$): δ 181.60, 171.33, 139.34, 114.38, 81.18, 77.55, 77.23, 76.91, 41.54, 37.28, 33.97, 31.85, 29.56, 29.43, 29.21, 29.06, 28.19, 27.09. **ESI-MS** *m*/*z* (rel int): (pos) 321.15 ($[M+Na]^+$, 100), 343.16 ($[M-H+Na]^+$, 30); 297.16 ($[M-H]^-$, 100).

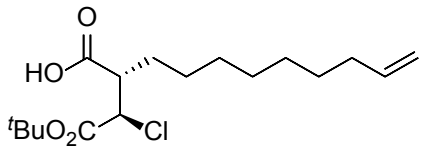


**(*S*)-2-((*R*)-2-(*tert*-butoxy)-1-chloro-2-oxoethyl)undec-10-enoic acid (S9a).** In a 25 mL pear-shaped flask, (*R*)-2-(2-(*tert*-butoxy)-2-oxoethyl)undec-10-enoic acid **S8a** (151.9 mg, 0.5090 mmol, 1.0 equiv.) and 5 mL tetrahydrofuran were added. The reaction vessel was cooled to -78 ºC before the slow, dropwise addition of LiHMDS (0.75 mL, 1.5 M in THF, 1.1198 mmol, 2.2 equiv.). The reaction was maintained at -78 ºC for 1 h before the addition of $CCl_4$ (0.60 mL of a 0.94 M solution

in THF, 0.5599 mmol, 1.1 equiv.). After stirring at -78 ºC for an additional 1.5 h, the reaction was quenched with glacial acetic acid (0.1 mL) and the volatiles were removed by rotary evaporation. The resulting white solid was dissolved in EtOAc (100 mL) and washed with 1 M HCl (10 mL) and brine (10 mL). The organic phases were dried ($MgSO_4$), filtered, and concentrated by rotary evaporation to afford **S9a** (351.0 mg, 98%) as a white solid. The material was >95% pure and was carried forward to the next step without additional purification.

**TLC**: $R_f$ 0.18 (3:2 hexanes/diethyl ether + 1% acetic acid). **$^1$H-NMR** (400 MHz, $CDCl_3$): δ 5.88–5.74 (m, 1H), 5.06–4.90 (m, 2H), 4.37 (d, *J* = 9.2 Hz, 1H), 3.03 (td, *J* = 9.1, 8.4, 4.6 Hz, 1H), 2.03 (q, *J* = 7.9, 7.2 Hz, 3H), 1.86–1.77 (m, 2H), 1.47 (s, 6H), 1.40–1.23 (m, 12H). **ESI-MS** *m*/*z* (rel int): (pos) 355.13 ([M+Na]$^+$, 100).

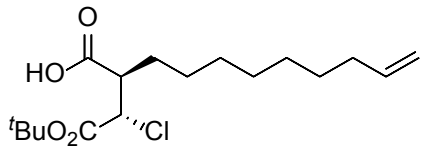


**(*R*)-2-((*S*)-2-(*tert*-butoxy)-1-chloro-2-oxoethyl)undec-10-enoic acid acid (S9b).** Prepared as described for **S9a**, from (*S*)-2-(2-(*tert*-butoxy)-2-oxoethyl)undec-10-enoic acid **S8b**, to give **S9b** (213.3 mg, quant.) as an oil.

**TLC**: $R_f$ 0.29 (3:2 hexanes/diethyl ether + 1% acetic acid). **$^1$H-NMR** (400 MHz, $CDCl_3$): δ 10.67 (s, 2H), 5.95–5.70 (m, 1H), 5.14–4.82 (m, 2H), 4.36 (d, *J* = 9.1 Hz, 1H), 3.02 (td, *J* = 8.8, 8.4, 4.4 Hz, 1H), 2.03 (q, *J* = 8.0, 7.4 Hz, 2H), 1.82 (d, *J* = 9.6 Hz, 2H), 1.49 (d, *J* = 20.3 Hz, 9H), 1.29 (s, 10H). **$^{13}$C-NMR** (100 MHz): δ 179.28, 167.77, 139.32, 114.42, 83.35, 77.55, 77.23, 76.91, 57.63, 48.71, 33.96, 29.57, 29.44, 29.37, 29.20, 29.07, 29.06, 28.56, 28.09, 27.87, 27.63, 26.26. **ESI-MS** *m*/z (rel int): (pos) 355.20 ($[M+Na]^+$, 100); (neg) 663.43 ($[2M-H]^-$, 100), 699.14 ($[2M+Cl]^-$, 30).

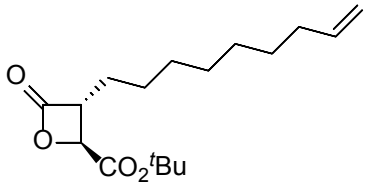


***tert*-Butyl (2*S*,3*R*)-3-(non-8-en-1-yl)-4-oxooxetane-2-carboxylate (S10a).** In a 25 mL round bottom flask, (*S*)-2-((*R*)-2-(*tert*-butoxy)-1-chloro-2-oxoethyl)undec-10-enoic acid **S9a** (84.7 mg, 0.2545 mmol, 1.0 equiv.), 5 mL tetrahydrofuran, and 5 mL 5% aq. $NaHCO_3$ were added. After stirring for 16 h, the reaction was diluted with EtOAc (50 mL) and the aqueous and organic phases were separated. The organic phase was washed with brine (5 mL), dried ($MgSO_4$), filtered, and concentrated by rotary evaporation. Purification by silica flash chromatography (19:1 → 9:1 hexanes/diethyl ether) afforded **S10a** (152.5 mg, 49%) as a clear oil.

**$^1$H-NMR** (400 MHz, $CDCl_3$): δ 5.83–5.68 (m, 1H), 4.91 (dd, *J* = 24.0, 13.6 Hz, 2H), 4.49–4.40 (m, 1H), 3.68–3.56 (m, 1H), 2.08–1.94 (m, 2H), 1.92–1.71 (m, 2H), 1.46 (s, 9H), 1.41 (s, 2H), 1.27 (s, 8H). **$^{13}$C-NMR** (100 MHz, $CDCl_3$): δ 169.42, 167.23, 138.95, 114.24, 83.46, 77.48, 77.16, 76.84, 71.83, 57.11, 33.70, 29.10, 28.90, 28.78, 27.86, 27.62, 26.61. **ESI-MS** *m*/*z* (rel int): (pos) 314.17 ($[M+NH_4]^+$, 100), 319.16 ($[M+Na]^+$, 70), 297.24 ($[M+H]^+$, 35).

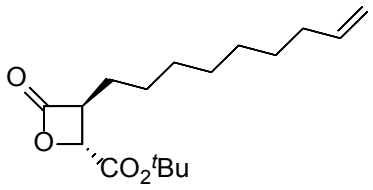


***tert*-Butyl (*2R,3S*)-3-(non-8-en-1-yl)-4-oxooxetane-2-carboxylate (S10b).** Prepared as described for **S10a**, from (*R*)-2-((*S*)-2-(*tert*-butoxy)-1-chloro-2-oxoethyl)undec-10-enoic acid **S9b**, to give **S10b** (15.0 mg, 84%) as a clear oil.

**TLC**: $R_f$ 0.27 (9:1 hexanes/diethyl ether). **$^1$H-NMR** (400 MHz, $CDCl_3$): δ 5.80 (td, *J* = 16.9, 6.7 Hz, 1H), 5.03–4.90 (m, 2H), 4.47 (d, *J* = 4.3 Hz, 1H), 3.70–3.61 (m, 1H), 2.04 (q, *J* = 7.2 Hz, 3H), 1.86 (m, 4H), 1.51 (s, 9H), 1.41–1.26 (m, 10H). **$^{13}$C-NMR** (100 MHz, $CDCl_3$): δ 139.17, 114.41, 77.48, 72.07, 57.31, 33.86, 29.27, 29.08, 28.95, 28.07, 27.82, 26.78. **ESI-MS** *m*/*z* (rel int): (pos) 319.27 ($[M+Na]^+$, 100), 314.24 ($[M+NH_4]^+$, 35).

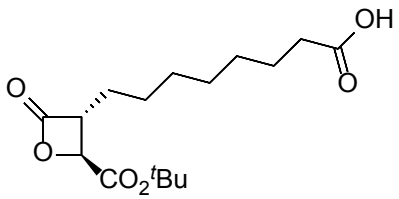


**8-((*2S,3R*)-2-(*tert*-butoxycarbonyl)-4-oxooxetan-3-yl)octanoic acid (S11a).** In a 20 mL vial, *tert*-Butyl (*2S,3R*)-3-(non-8-en-1-yl)-4-oxooxetane-2-carboxylate **S10a** (61.8 mg, 0.2085 mmol, 1.0 equiv.), 1 mL $CCl_4$, 1 mL $CH_3CN$, and 1.5 mL $H_2O$ were added. To the clear solution was added $NaIO_4$ (180.9 mg, 0.8458 mmol, 4.1 equiv.) and $RuCl_3 \bullet (H_2O)_n$. After 1.5 h, the reaction was diluted with $H_2O$ (5 mL) and extracted with $CH_2Cl_2$ (3x10 mL). The combined organic extracts were dried (MgS 1.5 mL methanol were added. The combined organic extracts were dried ($MgSO_4$), filtered over a pad of celite, and concentrated by rotary evaporation to afford **S11a** (59.2 mg, 90%) as a dark grey solid. The product was >95% pure; therefore, carried forward to the next step without additional purification.

**TLC**: $R_f$ 0.46 (1:1 hexanes/EtOAc + 1% acetic acid). **$^1$H-NMR** (400 MHz, $CDCl_3$): δ 4.46 (d, *J* = 4.3 Hz, 1H), 3.63 (ddd, *J* = 10.6, 6.4, 4.4 Hz, 1H), 2.33 (t, *J* = 7.4 Hz, 2H), 1.94–1.74 (m, 2H), 1.61 (dt, *J* = 13.8, 7.3 Hz, 2H), 1.49 (s, 9H), 1.46–1.39 (m, 2H), 1.32 (s, 6H).**$^{13}$C-NMR** (100 MHz, $CDCl_3$): δ 180.16, 169.53, 167.36, 83.73, 77.48, 77.16, 76.84, 71.95, 57.18, 34.06, 28.97, 28.91, 28.86, 27.98, 27.71, 26.65, 24.61. **ESI-MS** *m/z* (rel int): (pos) 337.11 ($[M+Na]^+$, 100), 332.18 ($[M+NH_4]^+$, 70); (neg) 313.03 ($[M-H]^-$, 100).

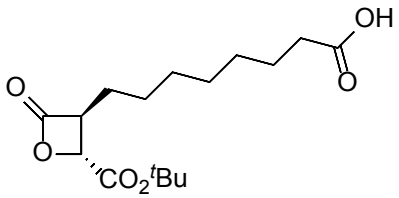


**8-((*2R,3S*)-2-(*tert*-butoxycarbonyl)-4-oxooxetan-3-yl)octanoic acid (S11b).** Prepared as described for **S11a**, from *tert*-butyl (*2R,3S*)-3-(non-8-en-1-yl)-4-oxooxetane-2-carboxylate **S10b**, to give **S11b** (32.1 mg, 83%) as a dark oil.

**TLC**: $R_f$ 0.19 (3:1 hexanes/EtOAc + 1% acetic acid). **$^1$H-NMR** (400 MHz, $CDCl_3$): δ 4.46 (d, *J* = 4.3 Hz, 1H), 3.68–3.61 (m, 1H), 2.34 (t, *J* = 7.0 Hz, 2H), 1.84 (ddq, *J* = 29.3, 14.2, 7.3 Hz, 2H), 1.67–1.58 (m, 2H), 1.50 (s, 9H), 1.48–1.41 (m, 2H), 1.33 (s, 5H). **$^{13}$C-NMR** (100 MHz, $CDCl_3$): δ 179.92, 169.53, 167.40, 83.77, 77.48, 77.16, 76.85, 72.02, 57.25, 34.07, 29.01, 28.96, 28.91, 28.05, 27.78, 26.69, 24.67. **ESI-MS** *m/z* (rel int): (pos) 337.34 ($[M+Na]^+$, 100), 332.33 ($[M+NH_4]^+$, 50); (neg) 313.08 ($[M-H]^-$, 100).

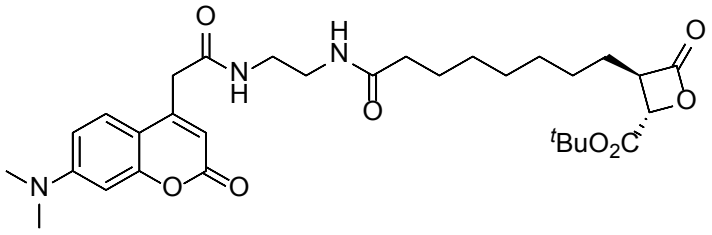


***tert*-Butyl (*2S,3R*)-3-(8-((2-(2-(7-(dimethylamino)-2-oxo-2H-chromen-4-yl)acetamido)ethyl)amino)-8-oxooctyl)-4-oxooxetane-2-carboxylate (3).** In a 25 mL pear-shaped flask, ethylenediamine-containing coumarin **S1c**[8] (9.5 mg,

0.0236 mmol, 1.0 equiv.), 8-((2*S*,3*R*)-2-(*tert*-butoxycarbonyl)-4-oxooxetan-3-yl)octanoic acid **S11a** (7.4 mg, 0.0236 mmol, 1.0 equiv.), 2.4 mL acetonitrile, and 0.1 mL DMF were added. To the solution was added EDC•HCl (6.7 mg, 0.0350 mmol, 1.5 equiv.) and DMAP (1.9 mg, 0.0156 mmol, 0.7 equiv.). After 20 h, the reaction was quenched with saturated aq. $NH_4Cl$ (10 mL) and extracted with EtOAc (4x25 mL). The combined organic extracts were dried ($MgSO_4$), filtered, and concentrated by rotary evaporation. Purification by preparatory TLC (19:1 EtOAc/MeOH) afforded **3** (6.6 mg, 48%) as a white solid.

**TLC**: $R_f$ 0.44 (19:1 EtOAc/MeOH). **$^1$H-NMR** (400 MHz, $CD_3OD$): δ 7.89 (s, 1H), 7.55 (d, *J* = 9.0 Hz, 1H), 6.77 (d, *J* = 11.5 Hz, 1H), 6.57 (s, 1H), 6.05 (s, 1H), 4.66 (d, *J* = 4.3 Hz, 1H), 3.80–3.71 (m, 1H), 3.68 (s, 2H), 3.08 (s, 7H), 2.16–2.07 (m, 2H), 1.84 (dt, *J* = 14.8, 7.2 Hz, 3H), 1.51 (s, 9H), 1.29 – 1.32 (m, *J* = 10.0 Hz, 10H). **ESI-MS** *m*/z (rel int): (pos) 1172.78 ($[2M+H]^+$, 100), 1194.87 ($[2M+Na]^+$, 50), 586.70 ($[M+H]^+$, 40).

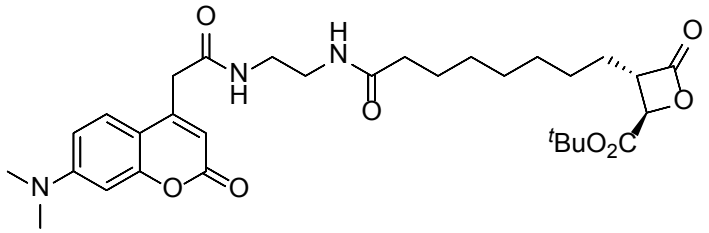


***tert*-Butyl (2*R*,3*S*)-3-(8-((2-(2-(7-(dimethylamino)-2-oxo-2H-chromen-4-yl)acetamido)ethyl)amino)-8-oxooctyl)-4-oxooxetane-2-carboxylate (4).** Pre-

pared as described for **3**, from ethylenediamine-containing coumarin **S1c**[44] and 8-((2*R*,3*S*)-2-(*tert*-butoxycarbonyl)-4-oxooxetan-3-yl)octanoic acid **S11b**, to give **4** (5.6 mg, 32%) as a white solid.

**$^1$H-NMR** (400 MHz, $CD_3OD$): δ 7.55 (d, *J* = 8.9 Hz, 1H), 6.77 (d, *J* = 9.0 Hz, 1H), 6.57 (s, 1H), 6.05 (s, 1H), 4.18 (d, *J* = 5.4 Hz, 1H), 3.68 (s, 1H), 3.66 (s, 2H), 3.35 (s, 2H), 3.08 (s, 6H), 2.76 (dt, *J* = 10.1, 5.2 Hz, 1H), 2.18–2.06 (m, 2H), 1.47 (s, 8H), 1.30 (s, 11H). **ESI-MS** *m/z* (rel int): (pos) 586.40 ([M+H]$^+$, 100), 1171.88 ([2M+H]$^+$, 30).

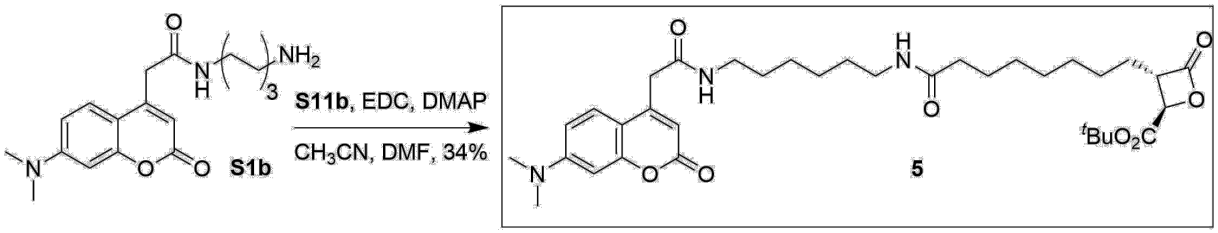


Scheme S7.5 General synthetic approach to access fluorescent lactone **5**. EDC=1-Ethy-3-(3-dimethylaminopropyl)carbodiimide); DMAP=4-(dimethylamino)-pyridine).

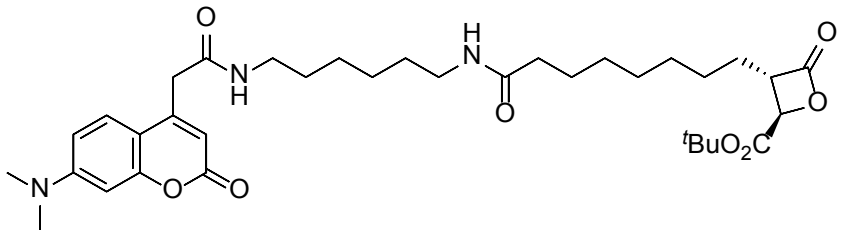

***tert*-Butyl (2*R*,3*S*)-3-(8-((6-(2-(7-(dimethylamino)-2-oxo-2H-chromen-4-yl)acetamido)hexyl)amino)-8-oxooctyl)-4-oxooxetane-2-carboxylate (5).** Prepared as described for **3–4**, from hexanediamine-containing coumarin **S1b**[7] and 8-((2*R*,3*S*)-2-(*tert*-butoxycarbonyl)-4-oxooxetan-3-yl)octanoic acid **S11b**, to give ***5*** (5.3 mg, 34%) as a pale yellow solid.

**$^1$H-NMR** (400 MHz, $CD_3OD$): δ 7.90 (s, 1H), 7.58 (d, *J* = 9.0 Hz, 1H), 6.76 (d, *J* = 9.0 Hz, 1H), 6.57 (s, 1H), 6.04 (s, 1H), 4.66 (d, *J* = 3.7 Hz, 1H), 3.75 (s, 1H), 3.67 (s, 2H), 3.19 (d, *J* = 6.7 Hz, 2H), 3.16–3.10 (m, 2H), 3.07 (s, 4H), 2.16 (t, *J* = 7.1 Hz, 2H), 1.84 (dt, *J* = 11.8, 5.4 Hz, 2H), 1.66–1.57 (m, 3H), 1.51 (s, 8H), 1.46 (s, 4H), 1.41–1.27 (m, 13H), 0.98–0.81 (m, 2H).

**Acknowledgements**

Chapter 7, is material currently being prepared for submission: T. D. Davis, J. M. Michaud, M. D. Burkart. "Fluorescent probes to profile fatty acid and polyketide acyl-carrier protein transacylase domains". T. D. Davis is the primary author of the work reported, supported by the dissertation author and under the supervision of M. D. Burkart. The dissertation author performed site-directed mutagenesis and cloning of *E. coli* strains, performed docking analyses, expressed and isolated protein samples with assistance from T. D. Davis, and assisted with manuscript and chapter preparation.

**Section 7.6 References**

1. Newman, D. J. & Cragg, G. M. Natural Products as Sources of New Drugs from 1981 to 2014. *J Nat Prod* **79,** 629–661 (2016).
2. Aggarwal, A., Parai, M. K., Shetty, N., Wallis, D., Woolhiser, L., Hastings, C., Dutta, N. K., Galaviz, S., Dhakal, R. C., Shrestha, R., Wakabayashi, S., Walpole, C., Matthews, D., Floyd, D., Scullion, P., Riley, J., Epemolu, O., Norval, S., Snavely, T., Robertson, G. T., Rubin, E. J., Ioerger, T. R., Sirgel, F. A., van der Merwe, R., van Helden, P. D., Keller, P., Bottger, E. C., Karakousis, P. C., Lenaerts, A. J. & Sacchettini, J. C. Development of a Novel Lead that Targets M. tuberculosis Polyketide Synthase 13. *Cell* **170,** 249–259 e25 (2017).
3. Li, J. W.-H. & Vederas, J. C. Drug Discovery and Natural Products: End of an Era or an Endless Frontier? *Science*. **325,** 161–165 (2009).
4. Hughes, D. Microbial genetics: Exploiting genomics, genetics and chemistry to combat antibiotic resistance. *Nat. Rev. Genet.* **4,** 432–441

(2003).

5. Shen, B., Du, L., Sanchez, C., Edwards, D. J., Chen, M. & Murrell, J. M. The biosynthetic gene cluster for the anticancer drug bleomycin from Streptomyces verticillus ATCC15003 as a model for hybrid peptide-polyketide natural product biosynthesis. *J. Ind. Microbiol. Biotechnol.* **27,** 378–385 (2001).

6. Ma, G., Zancanella, M., Oyola, Y., Richardson, R. D., Smith, J. W. & Romo, D. Total synthesis and comparative analysis of orlistat, valilactone, and a transposed orlistat derivative: Inhibitors of fatty acid synthase. *Org. Lett.* **8,** 4497–4500 (2006).

7. Clarke, K. M., Mercer, A. C., La Clair, J. J. & Burkart, M. D. In vivo reporter labeling of proteins via metabolic delivery of coenzyme A analogues. *J. Am. Chem. Soc.* **127,** 11234–11235 (2005).

8. Worthington, A. S. & Burkart, M. D. One-pot chemo-enzymatic synthesis of reporter-modified proteins. *Org. Biomol. Chem.* **4,** 44–46 (2006).

9. Meier, J. L., Mercer, A. C., Rivera Jr., H. & Burkart, M. D. Synthesis and evaluation of bioorthogonal pantetheine analogues for in vivo protein modification. *J Am Chem Soc* **128,** 12174–12184 (2006).

10. Hur, G. H., Meier, J. L., Baskin, J., Codelli, J. A., Bertozzi, C. R., Marahiel, M. A. & Burkart, M. D. Crosslinking studies of protein-protein interactions in nonribosomal peptide biosynthesis. *Chem Biol* **16,** 372–381 (2009).

11. Worthington, A. S., Hur, G. H. & Burkart, M. D. Activity-guided engineering of natural product carrier proteins. *Mol Biosyst* **7,** 365–370 (2011).

12. Yu, W. L., Jones, B. D., Kang, M., Hammons, J. C., La Clair, J. J. & Burkart, M. D. Spirohexenolide A targets human macrophage migration inhibitory factor (hMIF). *J Nat Prod* **76,** 817–823 (2013).

13. Meier, J. L., Mercer, A. C. & Burkart, M. D. Fluorescent profiling of modular biosynthetic enzymes by complementary metabolic and activity based probes. *J Am Chem Soc* **130,** 5443–5445 (2008).

14. Ishikawa, F., Haushalter, R. W. & Burkart, M. D. Dehydratase-specific probes for fatty acid and polyketide synthases. *J Am Chem Soc* **134,** 769–772 (2012).

15. Meier, J. L., Barrows-Yano, T., Foley, T. L., Wike, C. L. & Burkart, M. D. The unusual macrocycle forming thioesterase of mycolactone. *Mol Biosyst* **4,** 663–671 (2008).

16. McCulloch, I. P., La Clair, J. J., Jaremko, M. J. & Burkart, M. D. Fluorescent Mechanism-Based Probe for Aerobic Flavin-Dependent Enzyme Activity. *Chembiochem* **17,** 1598–1601 (2016).

17. Harder, M. E., Ladenson, R. C., Schimmel, S. D. & Silbert, D. F. Mutants of Escherichia coli with temperature-sensitive malonyl coenzyme A-acyl carrier protein transacylase. *J Biol Chem* **249,** 7468–7475 (1974).

18. Wright, H. T. & Reynolds, K. A. Antibacterial targets in fatty acid biosynthesis. *Curr. Opin. Microbiol.* **10,** 447–453 (2007).

19. Price, A. C., Choi, K. H., Heath, R. J., Li, Z., White, S. W. & Rock, C. O. Inhibition of β-ketoacyl-acyl carrier protein synthases by thiolactomycin and cerulenin: Structure and mechanism. *J. Biol. Chem.* **276,** 6551–6559 (2001).

20. Chan, Y. A. & Thomas, M. G. *Chapter 7 Formation and Characterization of Acyl Carrier Protein-Linked Polyketide Synthase Extender Units*. *Methods in Enzymology* **459,** (Elsevier Inc., 2009).

21. Winter, J. M., Cascio, D., Dietrich, D., Sato, M., Watanabe, K., Sawaya, M. R., Vederas, J. C. & Tang, Y. Biochemical and Structural Basis for Controlling Chemical Modularity in Fungal Polyketide Biosynthesis. *J. Am. Chem. Soc.* **137,** 9885–9893 (2015).

22. Kidd, D., Liu, Y. & Cravatt, B. F. Profiling serine hydrolase activities in complex proteomes. *Biochemistry* **40,** 4005–15 (2001).

23. Liu, Y., Patricelli, M. P. & Cravatt, B. F. Activity-based protein profiling: The serine hydrolases. *Proc. Natl. Acad. Sci.* **96,** 14694–14699 (1999).

24. Joshi, V. C. & Wakil, S. J. Studies on the mechanism of fatty acid synthesis. XXVI. Purification and properties of malonyl-coenzyme A--acyl carrier protein transacylase of Escherichia coli. *Arch Biochem Biophys* **143,** 493–505 (1971).

25. Sreshty, M. A., Surolia, A., Sastry, G. N. & Murty, U. S. Deorphanization of Malonyl CoA:ACP Transacylase Drug Target in Plasmodium falciparum (PfFabD) Using Bacterial Antagonists: A 'Piggyback' Approach for Antimalarial Drug Discovery. *Mol Inf.* **31,** 281–299 (2012).

26. Grimster, N. P., Connelly, S., Baranczak, A., Dong, J., Krasnova, L. B., Sharpless, K. B., Powers, E. T., Wilson, I. A. & Kelly, J. W. Aromatic sulfonyl fluorides covalently kinetically stabilize transthyretin to prevent amyloidogenesis while affording a fluorescent conjugate. *J Am Chem Soc* **135,** 5656–5668 (2013).

27. Dong, J., Krasnova, L., Finn, M. G. & Sharpless, K. B. Sulfur(VI) fluoride exchange (SuFEx): another good reaction for click chemistry. *Angew Chem Int Ed Engl* **53,** 9430–9448 (2014).

28. Narayanan, A. & Jones, L. H. Sulfonyl fluorides as privileged warheads in chemical biology. *Chem Sci* **6,** 2650–2659 (2015).

29. Nishida, I., Kawaguchi, A. & Yamada, M. Effect of thiolactomycin on the individual enzymes of the fatty acid synthase system in Escherichia coli. *J Biochem* **99,** 1447–1454 (1986).

30. Jackowski, S., Murphy, C. M., Cronan Jr., J. E. & Rock, C. O. Acetoacetyl-acyl carrier protein synthase. A target for the antibiotic thiolactomycin. *J Biol Chem* **264,** 7624–7629 (1989).

31. Kluge, A. F. & Petter, R. C. Acylating drugs: redesigning natural covalent inhibitors. *Curr Opin Chem Biol* **14,** 421–427 (2010).

32. Bottcher, T. & Sieber, S. A. Beta-lactones as privileged structures for the active-site labeling of versatile bacterial enzyme classes. *Angew Chem Int Ed Engl* **47,** 4600–4603 (2008).

33. Bottcher, T. & Sieber, S. A. beta-Lactams and beta-lactones as activity-based probes in chemical biology. *Medchemcomm* **3,** 408–417 (2012).

34. Ishikawa, F., Haushalter, R. W., Lee, D. J., Finzel, K. & Burkart, M. D. Sulfonyl 3-alkynyl pantetheinamides as mechanism-based cross-linkers of acyl carrier protein dehydratase. *J Am Chem Soc* **135,** 8846–8849 (2013).

35. Jeon, E., Lee, S., Won, J. I., Han, S. O., Kim, J. & Lee, J. Development of Escherichia coli MG1655 strains to produce long chain fatty acids by engineering fatty acid synthesis (FAS) metabolism. *Enzyme Microb. Technol.* **49,** 44–51 (2011).

36. Cho, H. & Cronan, J. E. 'Protease I' of Escherichia coli functions as a thioesterase in vivo. *J. Bacteriol.* **176,** 1793–1795 (1994).

37. Winter, J. M., Sato, M., Sugimoto, S., Chiou, G., Garg, N. K., Tang, Y. & Watanabe, K. Identification and characterization of the chaetoviridin and chaetomugilin gene cluster in chaetomium globosum reveal dual functions of an iterative highly-reducing polyketide synthase. *J. Am. Chem. Soc.* **134,** 17900–17903 (2012).

38. Chan, Y. a & Thomas, M. G. Recognition of (2S)-aminomalonyl-acyl carrier protein (ACP) and (2R)-hydroxymalonyl-ACP by acyltransferases in zwittermicin A biosynthesis. *Biochemistry* **49,** 3667–77 (2010).

39. Liu, H. & Naismith, J. H. An efficient one-step site-directed deletion, insertion, single and multiple-site plasmid mutagenesis protocol. *BMC Biotechnol.* **8,** 91 (2008).

40. Beld, J., Cang, H. & Burkart, M. D. Visualizing the chain-flipping mechanism in Fatty-Acid biosynthesis. *Angew. Chem. Int. Ed. Engl.* **53,** 14456–61 (2014).

41. Gottlieb, H. E., Kotlyar, V. & Nudelman, A. NMR Chemical Shifts of Common Laboratory Solvents as Trace Impurities. *J. Org. Chem.* **62,** 7512–7515 (1997).

42. Alexander, M. D., Burkart, M. D., Leonard, M. S., Portonovo, P., Liang, B., Ding, X., Joullie, M. M., Gulledge, B. M., Aggen, J. B., Chamberlin, A. R., Sandler, J., Fenical, W., Cui, J., Gharpure, S. J., Polosukhin, A., Zhang, H. R., Evans, P. A., Richardson, A. D., Harper, M. K., Ireland, C. M., Vong, B. G., Brady, T. P., Theodorakis, E. A. & La Clair, J. J. A central strategy for converting natural products into fluorescent probes. *Chembiochem* **7,** 409–416 (2006).

43. Baldwin, J. E., Adlington, R. M., Gollins, D. W. & Schofield, C. J. Stereospecific synthesis of dealanylalahopcin. *Tetrahedron* **46,** 4733–4748 (1990).

44. Sandler, J. S., Fenical, W., Gulledge, B. M., Chamberlin, A. R. & La Clair, J. J. Fluorescent profiling of natural product producers. *J. Am. Chem. Soc.* **127,** 9320–9321 (2005).